PULSED EPR DIPOLAR SPECTROSCOPY WITH NOVEL PARAMAGNETIC TAGS

Dissertation

for attaining the PhD degree

of Natural Sciences

Submitted to the Department 14

of the Johann Wolfgang Goethe University

in Frankfurt am Main

by

Dmitry Akhmetzyanov

from Zelenodolsk, Russia

Frankfurt am Main 2016

(D30)

Accepted by Department 14: Biochemistry, Chemistry and Pharmacy
of the Johann Wolfgang Goethe University as a dissertation

Dean:	Prof. Dr. Michael Karas
First expert assessor:	Prof. Dr. Thomas F. Prisner
Second expert assessor:	Dr. Björn Corzilius
Date of the disputation:	……..

Dedicated to loving memory of my grandfather
Boris Akhmetzyanov,
who inspired me and instilled in my younger self
a curious mindset and who always sincerely
supported and helped me in every situation.

Table of contents

A. Acknowledgements

I would like start the thesis with the acknowledgements section, since without help and support of these people this work would not be possible.

Firstly I would like to express a deep gratitude to my supervisor Prof. Thomas Prisner for his continuous support and many useful discussions we had. His excellent knowledge of magnetic resonance and enthusiasm in science always inspires me. It has been an honor for me to work in his group. Dr. Vasyl Denysenkov is greatly acknowledged for introducing me to high-frequency EPR spectrometers and microwave electronics. He has always lends a hand to help and been open for discussions regardless of how busy he is. His knowledge of microwave technique and instrumentation impresses me all the time. I would like to express many thanks to Dr. Björn Corzilius, who has always found time for discussions, answering my questions and helping me to rationalize the experimental results. He has not only helped me with understanding of theoretical questions and experimental results, but also introduced me to DNP, which was a new topic for me. I very much appreciated this. Dr. Burkhard Endeward is very much acknowledged for his great support with low frequency EPR instrumentation, with performing Q-band PELDOR measurements on manganese-nitroxide system and with the Mn-based distance measurements project in general. Moreover, he has been eager to discuss the results and always gave me good advices. I would like to thank Dr. Sun Un from CEA Saclay in France, whose group was a part of the joint Mn-based distance measurements project. I very much enjoyed collaboration with Sun and his group. We had many hours of interesting discussions when I was visiting CEA, when he was visiting us in Frankfurt and by telephone. His great support on Mn-RIDME studies and Tikhonov regularization analysis with modified kernels is very much acknowledged. The big help of Dr. Hong Yue Vincent Ching, who was a post-doc in Sun's group during this time, is also gratefully acknowledged. We started to perform the Mn-based RIDME measurements together in CEA which were successfully continued by Vincent. Moreover, he performed 94 GHz Mn-based PELDOR measurements, supported 263 GHz measurements in Frankfurt and played a key role in the success of the whole joint project. Also, he corrected English of this thesis. Another scientist in Sun's group Dr. Leandro Tabares is acknowledged for his support with the project and useful discussion of the results. Leandro also prepared all necessary documentation that made my visit to CEA possible. I would like to acknowledge Dr. Jörn Plackmeyer, a chemist in our group, for the synthesis of the manganese-nitroxide model system and his support to the project.

Dr. Paul Demay-Drouhard, Dr. Helene Bertrand and Prof. Clotilde Policar, who were the third part of the joint project, are gratefully acknowledged for the synthesis of the bis-manganese model system and many useful discussions.

Dr. Philipp Spindler is thanked for support with distance measurements on manganese nitroxide system at initial steps of the project.

Dr. Nitin Kunjir and Prof. Snorri Sigurdsson from University of Iceland in Reykjavik are acknowledged for the synthesis of the bis-trityl model system. Similarly to collaboration with Sun's group, I enjoyed this collaboration very much. Nitin and Snorri were always helpful, responded very quickly if problem or questions appeared and were open for discussions of the results. Philipp van Os (born Schöps), who was involved in trityl-based distance measurements project, is acknowledged for performance of Q-band DQC and SIFTER measurements and for lots of useful discussions. The half of the trityl-based distance measurements manuscript was prepared by Philipp. The support of Dr. Andriy Marko in analysis of high-frequency PELDOR data is also acknowledged.

Dr. Alice Bowen is acknowledged for proofreading the manganese-nitroxide and trityl-based distance measurements manuscripts and for giving very useful scientific comments.

Dr. Jiafei Mao, Prof. Clemens Glaubitz (Goethe University), Dr. Olivier Ouari (Aix-Marseille University), Dr. Marcella Orwick-Rydmark, Michel-Andreas Geiger and Prof. Hartmut Oschkinat (FMP Berlin) are acknowledged for collaborations on exciting DNP projects.

I would like to acknowledge Nicole Erlenbach, Claudia Grytz and Eva Jaumann for a great help with the German summary of the thesis. Eva has also checked layout and design of the whole thesis and gave valuable advices how to improve it. Nicole is acknowledged for creating very nice microclimate and bringing good mood into our office and providing "Notfall-Schokolade" when my brain was overloaded by science. Katja Barth is also acknowledged for providing "Notfall-Schokolade" and organizing social evenings for the group. Markus Gränz and Denise Schütz have always helped me with layout and design of presentations and posters for conferences and other meetings and gave valuable advices. Additionally, Markus was encouraging us to participate in different sport and cultural events and Denise organized dinners in Frankfurt cuisine restaurants and other nice events. Thilo Hetzke introduced me to ELDOR detected NMR with manganese centers. Also he organized going to the football games of the local Frankfurt team Eintracht. I would also like to thank the former group members, Dr. Ivan Krstic, Dr. Reza Dastvan and Dr. Jan Krummenacker, for help with my initial scientific and other steps in the group.

The help from Charlotte Börner, Silke Schneider, Sigrid Kämmerer and Bisera Krstic with all the administrative questions is very much acknowledged. The support from Bernhard Thiem regarding the issues with electronics is much appreciated.

I would like to thank the whole Prisner and Corzilius group for very nice, friendly and helpful atmosphere and for everyday team building. The group of Prof. Mike Heilemann is acknowledged for friendliness (especially for "Nach 18Uhr-Zugehörigkeit zur Heilemannschaft") and for many nice events I experienced with them.

Special gratitude is expressed to my first supervisor Prof. Valery Fedorovich Tarasov from Kazan Zavoisky Physical Technical Institute in Russia, where I did my bachelor and master thesis and worked as research engineer in the laboratory of radiospectroscopy of dielectrics. Valery Fedorovich taught me many aspects of experimental EPR spectroscopy as well as magnetic resonance theory and was very supportive to my ideas. The knowledge and skills, learned from him, have been very valuable for me.

The last but not least, I am infinitely and sincerely grateful to my mother, grandmother and grandfather Guzel, Zagira and Boris Akhmetzyanovs for everything they did for me. Their belief and support has always gave me strength to go.

This thesis is dedicated to my grandfather, Boris Akhmetzyanov, who taught and supported me in significantly more ways than anyone else.

B. Acronyms and Symbols

AWG	arbitrary waveform generator
CPMG	Car-Purcell-Meiboom-Gill
Cryo-EM	cryogenic electron microscopy
CW	continuous wave
DEER	double electron-electron resonance
DNP	dynamic nuclear polarization
DOTA	1,4,7,10-tetraazacyclododecane-1,4,7,10-tetraacetic acid
DQ	double quantum
DQC	double quantum coherence
EDTA	ethylenediaminetetraacetic acid
EPR	electron paramagnetic resonance
ESEEM	electron spin echo envelope modulation
FRET	Förster (fluorescence) resonance energy transfer
FWHM	full width at half maximum
His	histidine
IA-PROXYL	3-(2-iodoacetamido)-2,2,5,5-tetramethyl-1-pyrrolidinyloxy
IDA	iminodiacetic acid
MAS	magic angle spinning
MMDPA	4-mercaptomethyl dipicolinic acid
MQC	multiple quantum coherence
MTSL	S-(1-oxyl-2,2,5,5-tetramethyl-2,5-dihydro-1H-pyrrol-3-yl)methyl methanesulfonothioate
NMR	nuclear magnetic resonance
PELDOR	pulsed electron electron double resonance
PyMTA	2,2',2",2"'-[2,6-Pyridinediylbis(methylenenitrilo)]tetraacetic acid
RIDME	relaxation-induced dipolar modulation enhancement
SAXS	small angle X-ray scattering
SDSL	site-directed spin labelling
SIFTER	single frequency technique for refocussing dipolar couplings
SNR	signal-to-noise ratio
SQ	single quantum
SVD	singular value decomposition
TAM	triarylmethyl (trityl)
TEMPO	2,2,6,6-tetramethylpiperidinyloxyl
TETAC	1,4,7,10-tetraazacyclododecane
ZFS	zero-field splitting
ZQC	zero quantum coherence

$\hat{A}$	secular part of electron dipole-dipole coupling Hamilton operator
$\overline{\boldsymbol{A}}$	hyperfine coupling tensor
a_{iso}	isotropic hyperfine coupling constant
$\hat{B}$	pseudo-secular part of electron dipole-dipole coupling Hamilton operator
$\boldsymbol{B_0}$	external permanent magnetic field
B_1	amplitude of magnetic component of electromagnetic wave
$\hat{C}$ - $\hat{F}$	non-secular part of electron dipole-dipole coupling Hamilton operator
δ_{ij}	Kronecker delta
$\delta(x)$	Dirac delta function
$\overline{\boldsymbol{D}}$	second-order ZFS tensor
$\overline{\boldsymbol{D}}_{dip}$	electron dipole-dipole coupling tensor
D	axial ZFS constant
D_{dip}	electron dipole-dipole coupling constant
$\mathcal{E}$	energy of electron spin sublevel (eigenvalue of Hamilton operator)
E	ZFS-asymmetry (rhombocity) constant
$\boldsymbol{e}_i$	unit basis vector
g_e	g-value of a free electron, ≈ 2.0023
$\hat{\mathcal{H}}$	electron spin Hamilton operator
$\hat{\mathcal{H}}_{\mathcal{EZ}}$	electron Zeeman term of the electron spin Hamilton operator
$\hat{\mathcal{H}}_{\mathcal{NZ}}$	nuclear Zeeman term
$\hat{\mathcal{H}}_{\mathcal{HF}}$	hyperfine coupling term
$\hat{\mathcal{H}}_{\mathcal{F}}$	Fermi-contact part of the hyperfine coupling term
$\hat{\mathcal{H}}_{\mathcal{NDD}}$	electron nuclear dipole-dipole coupling part of the hyperfine coupling term
$\hat{\mathcal{H}}_{\mathcal{NQ}}$	nuclear quadrupolar coupling term
$\hat{\mathcal{H}}_{\mathcal{DD}}$	electron dipole-dipole coupling term
$\hat{\mathcal{H}}_{exchange}$	electron exchange interaction term
$\hat{\mathcal{H}}_{\mathrm{MW}}$	microwave field term
h	Planck constant, ≈ $6.626 \cdot 10^{-34}$ J·s

$\hbar$	reduced Planck constant (Dirac constant), $1.055 \cdot 10^{-34}$ J·s
$\hat{\boldsymbol{I}}$	nuclear spin vector operator
I	nuclear spin
$\overline{\boldsymbol{J}}$	exchange interaction tensor
J	isotropic exchange interaction constant
$K(T,R)$	kernel function of Fredholm integral equation of the first kind
$\boldsymbol{M}$	macroscopic magnetization vector
m_I	nuclear spin magnetic quantum number
m_S	electron spin magnetic quantum number
$\overline{\boldsymbol{P}}$	nuclear spin quadrupolar coupling tensor
P	electron spin transition probability
$P(R)$	distance distribution
$\boldsymbol{R}$	distance vector between two magnetic dipole moments
R_{max}	the most probable distance
S	electron spin
$\hat{\boldsymbol{S}}$	electron spin vector operator
$\overline{\boldsymbol{T}}$	electron nuclear dipole-dipole coupling tensor
$T_{l,m}$	spherical tensor operator
α	regularization parameter of Tikhonov regularization
β_e	Bohr magneton, $\approx 9.274 \cdot 10^{-24}$ J/T
γ_N	gyromagnetic ratio of a nucleus
λ	dipolar modulation depth (amplitude of dipolar oscillation)
$\boldsymbol{\mu}$ and $\hat{\boldsymbol{\mu}}$	magnetic dipole moment and corresponding operator
μ_0	vacuum permeability or magnetic constant, $4\pi \cdot 10^{-7}$ N/A^2
ν_{MW}	frequency of electromagnetic wave
σ	density matrix
ψ	electron wave function
ω_{dd}	electron dipole-dipole coupling frequency
ω_{MW}	angular frequency of electromagnetic wave
ω_{larmor}	larmor angular frequency

C. List of Figures, Schemes and Tables

1. Introduction

1.1 EPR among structural biology methods

One of the central structural biology paradigms is that structure defines function. Only by knowing the atom-by-atom arrangement of a biomolecule can one elucidate how it works. For several decades one technique has been almost exclusively used to determine the structure of a biomolecule on this level of detail: X-ray crystallography, in which X-rays are used to produce diffraction patterns of a crystallized biomolecule.[1] Although this has been structural biologists' most powerful tool, it also has major limitations. Proteins, nucleic acids and their complexes have inherent structural flexibility, and, therefore, might be present in multiple conformations that complicates crystallization. Furthermore, crystallization can trap one out of many possible conformations present in solution and lead to artefacts due to crystal packing effects. In order to avoid this, molecules or macromolecular complexes should preferentially be studied in solution and if possible in their native environment.

Over the last three decades advances in instrumentation and computational methods led to new developments in the application of small-angle scattering of X-rays (SAXS)[2] to structural biology.[3] In this method the patterns of X-rays, elastically scattered by the studied biomolecules, are analyzed and thus the structure of molecules is deduced. The use of the SAXS method enables the study of macromolecules in solution with the high speed of both data collection and further structural characterization. Thus, on a modern synchrotron, scattering data can be obtained in seconds, allowing for an almost immediate characterization of the sample and the sample quality.[3] However, the impressive advantages of this method come at a price of lower resolution with respect to X-ray crystallography.

Recent developments in detector hardware and image-processing software have revolutionized another structural biology method, cryo-electron microscopy (cryo-EM).[4,5] In this method a beam of electrons, fired at a flash frozen solution of a sample of interest, is used to create a scattering pattern, which is converted to a three dimensional image of the molecule. A major advantage of this method is that the molecule of interest does not have to be crystallized and high resolution can be obtained (up to 2.2Å).[6] Today the lower molecular size limitation for cryo-EM is about 300 kDa. However, it is predicted that with such rapid development of the method[7] this limitation will be significantly improved.

Another powerful biophysical method for structural biology studies on biomolecules in liquid solution is nuclear magnetic resonance (NMR) spectroscopy.[8,9] Structure determination

in NMR spectroscopy relies on the determination of short range restrains between atoms, *e.g.* in the form of short inter-proton distances (usually less than 0.5 nm). However, for obtaining high resolution structures of complex biological systems, additional labelling with ^{13}C and ^{15}N nuclear isotopes is often required. Thus, by a combination of homonuclear and heteronuclear NMR correlation spectroscopy methods[10–12] it is possible to obtain structures of biomolecules with the same level of details as X-ray crystallography, and additionally conformational dynamics can be revealed. However, liquid state NMR spectroscopy is limited to molecules smaller than about 50 kDa in size.[13]

The biophysical methods that do not have intrinsic size limitations of the studied system are solid-state NMR, fluorescence resonance energy transfer (FRET) and electron paramagnetic resonance spectroscopy (EPR).

Solid-state NMR spectroscopy in combination with magic angle spinning (MAS)[14] is well-suited for studying membrane-embedded proteins, fibriles and oligomers. Intrinsically low sensitivity of solid-state NMR can be improved by application of dynamic nuclear polarization (DNP).[15] In DNP high polarization of the electron spin system, carried by polarizing agents mixed with the sample, is transferred to the nuclear spin system, thus significantly increasing the intensity of NMR signals.[16]

FRET method can determine long-range distance constrains in macromolecules in liquid solutions.[17] For performing this study two different fluorophore labels have to be specifically attached onto the molecule of interest. This method is based on determining the resonance energy transfer efficiency between acceptor and donor fluorophores. From this information the fluorophore distance can be then estimated. FRET has very high sensitivity that allows the performance of experiments at a single molecular level.[18,19] Due to large size and degree of flexibility of commonly used fluorophores as well as other experimental factors (*e.g.* mutual fluorophore orientation), the accuracy of distance determination by FRET is often lower compared to the biophysical methods described above, often allowing more qualitative type of deduced structural information.

The method that is able to determine highly accurate long-range distance constrains in the range of 1.5 to 10 nm is EPR (or sometimes called electron spin resonance, ESR).[20,21] As most biomolecules are diamagnetic, EPR experiments are usually performed using paramagnetic tags based on nitroxide radicals,[22] which have been site-specifically attached to biomolecules of interest.[23] Nitroxide radicals are significantly smaller compared to the fluorophore labels used in FRET making EPR-based distance measurements more accurate, although having intrinsically lower sensitivity. Distance constrains in EPR are determined by

measuring the magnitude of the magnetic dipolar coupling between pairs of paramagnetic tags. Modern biological applications promote the development of novel paramagnetic tags, spin labelling strategies as well as new EPR methodological approaches. Among the novel paramagnetic tags, carbon-based organic radicals, like triarylmethyl (abbreviated as TAM or trityl),[24] and paramagnetic metal ions are of particular interest.

This thesis is focused on EPR-based distance determinations with novel trityl and manganese paramagnetic tags. These tags are highly relevant in structural biology applications, but due to their novelty they have not been fully exploited for distance measurements.

1.2 Motivation and aim of the thesis

Novel trityl and manganese paramagnetic tags have numerous advantages compared to conventionally used nitroxide tags. Trityl has higher chemical stability in the reducing environment of the cell, enhanced relaxation times at room temperature and significantly narrower EPR spectrum. These properties make this paramagnetic tag well suited for studying biological systems in their native environment under physiological conditions. Similarly, paramagnetic metal centers with appropriate ligand spheres are also chemically stable towards redox processes. Manganese is a natural paramagnetic center that occurs as a cofactor in enzymes. Additionally, due to similar properties, it can readily substitute diamagnetic magnesium, an essential cofactor for many enzymes, nucleic acids and nucleotide binding domains of proteins. Therefore, the use of manganese for EPR-based distance measurements is a powerful tool for structural characterization of intrinsic metal sites in biomolecules. However, manganese center is a complex paramagnetic system which has slowed the development of its applications for distance measurements.

The first aim of the thesis was to study the performance of EPR-based distance measurements using trityl paramagnetic tags. For this aim low-frequency (34 GHz) double quantum coherence (DQC) and single frequency technique for refocussing dipolar couplings (SIFTER) as well as high-frequency (180 GHz) pulsed electron electron double resonance (PELDOR or also called DEER) experiments were performed on a model compound doubly-labelled with trityl radicals. These experiments have been performed in order to study the peculiarities of different techniques with these tags and to optimize the EPR experiment in terms of sensitivity and robustness.

The second aim of the thesis was to study the influence of the high-spin multiplicities of Mn^{2+} ions (electron and nuclear spins equal to 5/2) on distance measurements. For this aim, a model system containing Mn^{2+} ion coupled to nitroxide radical was studied by multi-frequency

PELDOR spectroscopy. Another model system with two Mn^{2+} ions was studied by high-frequency (94 GHz) PELDOR and multi-frequency (94 and 263 GHz) relaxation induced dipolar modulation enhancement (RIDME) experiments. This study was performed in order to optimize sensitivity of the PELDOR and RIDME-based distance measurements with Mn^{2+} centers and robustness of the data analysis.

1.3 List of publications

The results presented in this thesis have been published in peer-reviewed scientific journals and presented at international conferences as oral or poster presentations.

The list of publications that are relevant for the thesis

1) **D. Akhmetzyanov**[*], H. Y. V. Ching[*], V. Denysenkov, P. Demay-Drouhard, H. C. Bertrand, L. C. Tabares, C. Policar, T. F Prisner, S. Un, "RIDME Spectroscopy on High-Spin Mn^{2+} Centers" (2016) *Phys. Chem. Chem. Phys.*, **18**, 30857.

The author contribution was preparation of the manuscript, performance of the part of 94 and 263 GHz RIDME measurements and analysis of the data.

2) P. Demay-Drouhard, H. Y. V. Ching, **D. Akhmetzyanov**, R. Guillot, L. C. Tabares, H. C. Bertrand, C. Policar, "A bis-MnII-DOTA complex for pulsed dipolar spectroscopy" (2016) *Chem. Phys. Chem*., **17**, 2066.

The author contribution was performance of Q-band PELDOR measurements with nitroxide radicals, their data analysis, preparation of the corresponding part of the manuscript and critical reading of the whole manuscript.

3) **D. Akhmetzyanov**[*], P. Schöps[*], A. Marko, N. Kunjir, S. Th. Sigurdsson, T. F. Prisner, "Pulsed EPR Dipolar Spectroscopy at Q- and G-band on a Trityl Biradical" (2015) *Phys. Chem. Chem. Phys*., **17**, 24446.

The author contribution was preparation of 50% of the manuscript, performance of 180 GHz PELDOR measurements and analysis of 50% of the data.

4) **D. Akhmetzyanov**, J. Plackmeyer, B. Endeward, V. Denysenkov, T. F. Prisner, "Pulsed electron–electron double resonance spectroscopy between a high-spin Mn^{2+} ion and a nitroxide spin label" (2015) *Phys. Chem. Chem. Phys*., **17**, 6760.

The author contribution was preparation of the manuscript, performance of the measurements and data analysis.

[*] Authors contributed equally to the work

The list of publications that were obtained during the doctoral studies

5) M.-A. Geiger, M. Orwick-Rydmark, K. Märker, W. T. Franks, **D. Akhmetzyanov**, D. Stöppler, M. Zinke, E. Specker, M. Nazaré, A. Diehl, B.-J. van Rossum, F. Aussenac, T. Prisner, Ü. Akbey, H. Oschkinat, "Temperature dependence of cross-effect dynamic nuclear polarization in rotating solids: advantages of elevated temperatures" (2016) *Phys. Chem. Chem. Phys.*, **18**, 30696.

The author contribution was performance of the EPR measurements, EPR-data analysis, preparation of the corresponding part of the manuscript and critical reading of the whole manuscript.

6) B. Joseph, V. M. Tormyshev, O. Yu. Rogozhnikova, **D. Akhmetzyanov**, E. G. Bagryanskaya, T. F. Prisner, "Selective Detection of Membrane Protein-Ligand Interaction at High Resolution in Native Membranes using Trityl - Nitroxide PELDOR" (2016) *Angew. Chem. Int. Ed.*, **128**, 11710.

The author contribution was discussion of the experimental data and critical reading of the manuscript.

7) C. Sauvée, G. Casano, S. Abel, A. Rockenbauer, **D. Akhmetzyanov**, H. Karoui, D. Siri, F. Aussenac, W. Maas, R. T. Weber, T. Prisner, M. Rosay, O. Ouari, P. Tordo, "Tailoring of polarizing agents in the bTurea series for Cross Effect Dynamic Nuclear Polarization in aqueous media" (2016) *Chem. Eur. J.*, **22**, 5598.

The author contribution was performance of the 263 GHz EPR measurements and corresponding data analysis.

8) J. Mao, **D. Akhmetzyanov**, O. Ouari, V. Denysenkov, B. Corzilius, J. Plackmeyer, P. Tordo, T. F. Prisner and C. Glaubitz. "Host-Guest Complexes as Water-Soluble High-Perfomance DNP Polarizing Agents" (2013) *J. Am. Chem. Soc.*, **135**, 19275.

The author contribution was performance of the EPR measurements, EPR-data analysis, preparation of the corresponding part of the manuscript and critical reading of the whole manuscript.

Oral presentations given by author

1) Pulse EPR Dipolar Spectroscopy with High-Spin Mn^{2+} Ions.
The 49th Annual International Meeting of the ESR Spectroscopy Group of the Royal Society of Chemistry, Colchester, England, 2016 (Also given as poster presentation).

2) Pulsed Electron-Electron Double Resonance Spectroscopy on a High-Spin Mn^{2+} Ion coupled with a nitroxide radical.

The 36th Discussion Meeting of the GDCh-Division of "Magnetic Resonance" (FGMR), Berlin, Germany, 2014 (Also given as poster presentation).

3) Pulsed Electron-Electron Double Resonance Spectroscopy on a High-Spin Mn^{2+} Ion non-covalently attached to a Nitroxide Radical.

Modern Development of Magnetic Resonance (MDMR), Kazan, Russia, 2014.

4) Pulsed Electron-Electron Double Resonance Spectroscopy on a High-Spin Mn^{2+} Ion non-covalently attached to a Nitroxide Radical.

Rocky Mountain EPR Symposium, Colorado, USA, 2014

Poster presentations given by author

1) Pulsed EPR Dipolar Spectroscopy at Q- and G-band on a Trityl Biradical.

The 37th Discussion Meeting of the GDCh-Division of "Magnetic Resonance" (FGMR), Darmstadt, Germany, 2015.

2) Pulsed EPR Dipolar Spectroscopy with High-Spin Mn^{2+} Ions.

The 37th Discussion Meeting of the GDCh-Division of "Magnetic Resonance" (FGMR), Darmstadt, Germany, 2015.

3) Pulsed EPR Dipolar Spectroscopy at Q- and G-band on a Trityl Biradical.

European congress on Magnetic Resonance (EUROMAR), Prague, Czech Republic, 2015.

2. Paramagnetic tags available for distance measurements

2.1 Organic radicals

Stable organic radicals are the most widely used spin tag for EPR based distance measurements. Some of the important tags are summarized in Figure 1.

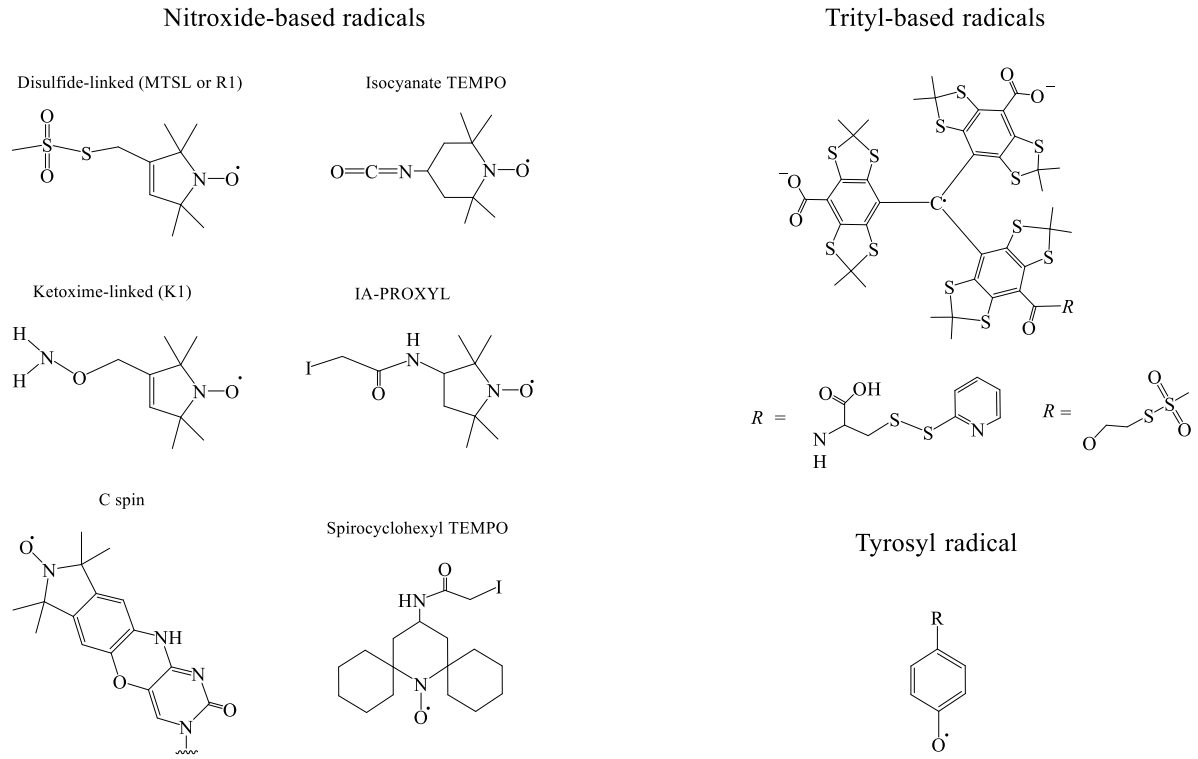

Figure 1. Nitroxide, trityl and tyrosyl organic radicals used in dipolar spectroscopy.

The stable nitroxide radicals are attached to the cysteine via *site-directed spin labelling* (*SDSL*), pioneered in the group of W. Hubbell.[23,25] Thus, in conventional SDSL, a unique cysteine residue is introduced into a protein via site-directed mutagenesis that subsequently reacted with sulfhydryl-specific nitroxide reagent to generate a covalently linked nitroxide side chain. A number of different nitroxides have been used in SDSL, but *methanethiosulfonate* nitroxide radical (MTSL that forms so called side-chain R1) is the most widely used.[23] Labelling of a cysteine residue using this tag is shown in Scheme 1.

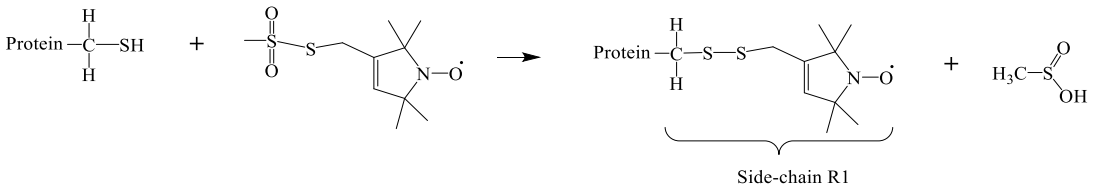

Scheme 1. SDSL of protein with MTSL nitroxide radical.

Introduction of R1 side-chain did not lead to considerable perturbations of the backbone fold, stability and function for the majority of investigated protein systems. As can be seen in Scheme 1, the nitroxide moiety is attached to proteins via flexible linker, leading to the unpaired electron being displaced from the protein backbone by about 0.7 nm. Thus, interpretation of the EPR data in terms of protein structure and conformational flexibility requires knowledge of the radical *rotamers*[26,27] and the internal dynamics of the side-chain by itself. This information has been the most developed for the simple case R1 chain, however, recently it has been extended to other radical side-chains.

The traditional SDSL, which uses cysteine residues and sulfhydryl-reactive nitroxide reagent, can be challenging for proteins that contain functionally important native cysteine residues or disulfide bonds. In this case, a labelling strategy that does not rely on the sulfhydryl or any other reactive functional group present in the standard amino acids is useful. Thus, SDSL has been extended by genetic incorporation of an unnatural amino acids that has unique reactive properties.[28] An example that demonstrates this strategy is given in Scheme 2. In this scheme the unnatural amino acid *p-acetyl-L-phenylalanine*, incorporated into a protein of interest, is reacted with a k*etoxime nitroxide radical*[a].

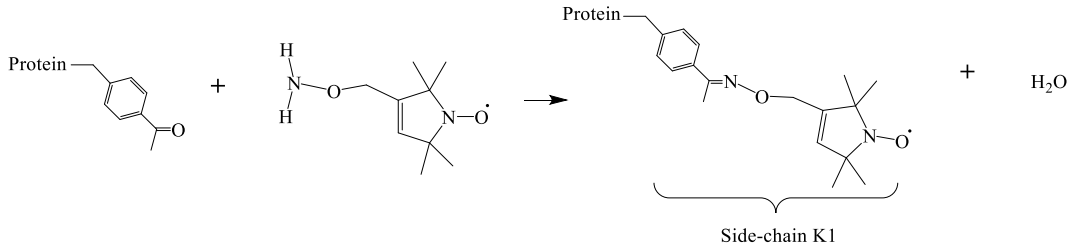

Scheme 2. SDSL of with ketoxime nitroxide radical with genetically encoded p-acetyl-L-phenylalanine into the protein of interest.

Nucleic acids differ from proteins in their basic chemical (nucleotides and amino acids) and structural (A/B-helices and α-helix/β-strand) units. Therefore, SDSL strategies and data interpretation algorithms differ significantly for nucleic acids and can be more complicated than for protein systems. Nucleic acid SDSL employs nitroxides, covalently attached to a backbone, 2' position of sugar (*e.g. isocyanata-TEMPO* radical shown in Figure 1 can be used), specific nucleotide within a target nucleic acid strand (*e.g.* rigid *C spin*[29] or flexible *IA-Proxyl*[30] can be used) as well as non-covalently bound nitroxide radicals to specific sites of nucleic acid duplexes.[31,32] The four naturally occurring nucleotides are not reactive enough at physiological

[a] Referred as nitroxide side chain K1.

temperatures to allow direct coupling to nitroxides, thus, necessitating the use of modified nucleotides that are often incorporated by solid-phase chemical synthesis.[33,34]

For nitroxide radicals N−O radical moiety is often sterically shielded by two-gem-dimethyl-substituted quaternary carbons to provide a radical stability. At temperatures above 80 K rotation of these methyl groups modulates the hyperfine couplings of the unpaired electron to the protons that decreases the electron spin transversal relaxation time. This defines the temperatures at which EPR-based distance measurements are performed with optimum efficiency (typically 50-80 K).[35] Replacing these methyl groups by *spirocyclohexyl groups* (radical is shown in Figure 1) allowed EPR-based distance measurements to be performed on immobilized protein at physiological temperatures.[36]

Another paramagnetic tag with long electron spin transversal relaxation times at room temperature[37,38] is carbon-based trityl radical (Figure 1 right).[24,39] The electron spin carried by this radical does not experience considerable hyperfine[a] and spin-orbit couplings, making its EPR spectrum very narrow. The use of this radical has allowed distance measurements to be performed on immobilized DNA[40] and lysozyme systems[41] at physiological temperatures. Due to relatively complex synthesis, bulkiness and in some cases solubility issues, the trityl radicals have remained underexplored in the EPR-based distance measurements, despite their impressive advantages over conventional nitroxide radicals. The methanethiosulfonate derivative of trityl radical (Figure 1), which can selectively reacts with a cysteine residue like MTSL, has been introduced in 2016.[42] This significantly extends the applicability of the radical in distance measurements.

It is worth noting, that naturally occurring radicals (*e.g.* amino-acid radicals being a cofactor in some enzymes) have also been used in distance measurements for specific biological objects. One of the examples has been an application of *tyrosyl radical* (tyrosine amino acid radical) in EPR dipolar spectroscopy for studying protein-protein interactions.[43]

2.2 Paramagnetic metals

Paramagnetic metals have been introduced for EPR-based distance measurements relatively recently. An important advantage of metal complexes compared to nitroxide radicals is chemical stability in reducing environments. Paramagnetic metals can naturally occur in some biological objects as cofactors, replace diamagnetic metals in binding sites or be site-specifically engineered as a spin tags into the molecule of interest. In this section Cu^{2+}, Mn^{2+}

[a] Nitroxide radicals experience hyperfine couplings with nitrogen and proton nuclei.

and Gd^{3+} paramagnetic tags, which have been site-specifically incorporated into biomolecules, are described (some of the metal complexes are summarized in Figure 2).

The most metal complexes are more bulky compared to nitroxide-based tags. However, not in all cases it leads to increased intrinsic flexibility of the label. As mentioned in previous section, the linker of commonly used MTSL label is relatively flexible, that can lead to ambiguity in associating the distance measurements to the protein structure. Thus, several different nitroxides with rigid linkers have been introduced (e.g. *C*-spin), but, another approach has been the use of copper spin tag, based on the double-histidine Cu^{2+} binding motif (dHis-Cu^{2+}-IDA spin label is shown in Figure 2).[44] This site specific tag has been assembled *in situ* from natural amino acid residues and a metal salt. It did not require post expression modification and provided significantly higher rigidity in binding to the protein compared to MTSL. This copper-based tag can be incorporated in both α-helix and β-sheet by the use of natural amino acids and further utilized in protein systems in which cysteine incorporation and labelling is problematic. The copper spin labels which are cysteine specific has also been developed in the group of S. Saxena. This kind of paramagnetic tags, which are based on the chelate complexes, are shown in Figure 2 (Cu^{2+} - TETAC and Cu^{2+} - EDTA).[45]

In terms of EPR properties, copper is more challenging spin system with respect to organic radicals, despite the fact that both have an elementary electron spin of 1/2. The copper ion exhibits spin-orbit coupling, which leads to significant anisotropy of the $\bar{\boldsymbol{g}}$-tensor.[46] Additionally, this electron spin system experiences strongly anisotropic hyperfine couplings with ^{63}Cu (abundance of 69.17%) and ^{65}Cu (30.83%) nuclei, both having nuclear spin of 3/2, and hyperfine coupling with multiple ^{14}N nuclei coordinating the copper ion. As a result, the EPR spectrum of copper systems is significantly broader than that of organic radicals. Another consequence of spin-orbit coupling is reduction of the transversal electron spin relaxation times. Thus, sensitivity of EPR-experiments with the paramagnetic center is lower with respect to organic radicals. Application of higher frequencies, that can potentially provide higher sensitivity, does not lead to considerable improvement, since the width EPR spectrum proportionally scales due to higher impact of large anisotropy of the $\bar{\boldsymbol{g}}$-tensor.

The metal complexes, which benefit from being used at higher frequencies, are based on high-spin Mn^{2+} and Gd^{3+} systems. Detailed description of EPR properties and peculiarities of these paramagnetic centers is given in section 3.1.2. The Gd^{3+} system has been introduced for EPR-based distance measurements by the group of D. Goldfarb in 2007[47] and has been the most used paramagnetic metal tag. In most cases the $\bar{\boldsymbol{g}}$-tensor of the spin system is isotropic and *zero-field splitting* (ZFS) parameter *D* varies typically in the range of 0.6 till 2.2 GHz with

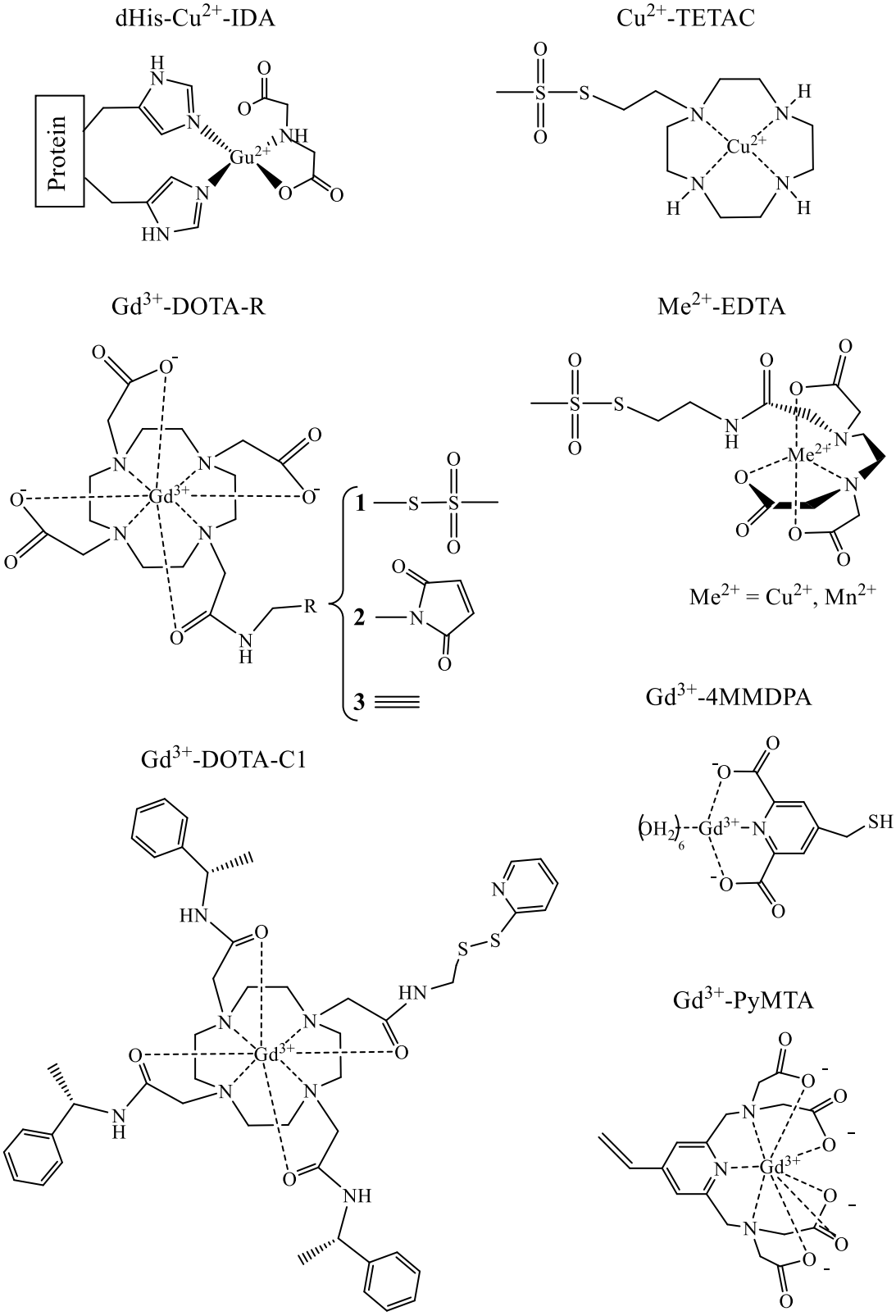

Figure 2. Cu^{2+}, Gd^{3+} and Mn^{2+} complexes used in dipolar spectroscopy.

large statistical distribution.[48,49] Thus, application of higher frequencies and correspondingly higher magnetic fields leads to the single line of the central transition of Gd^{3+} to be narrower and more intense. Additionally it leads to higher polarization of the *spin-sublevels*. This allows the use of significant less amount of sample in EPR-based distance measurements that is an important consideration for biological applications, making Gd^{3+} tags an interesting alternative to organic radicals. In Figure 2 some of Gd^{3+} paramagnetic tags are shown. The distance measurements have been performed *in vitro* on various biological systems including peptides,[50] protein assemblies[51] and trans-membrane helices,[52] where Gd^{3+} tags have been attached via SDSL into cysteine residues (DOTA-R1, DOTA-C1 and 4MMDPA labels) as well as on DNA, where attachment has been based on click chemistry reaction (DOTA-R3 label).[53] Recently, *in-cell* measurements have been performed on a protein (DOTA-R2 label),[54] proline rich peptide (PyMTA label),[55] and a 3-helix bundle[56] where corresponding paramagnetic tags were introduced to cysteine residue, and on peptides with genetically encodable lanthanide-binding tags. Thus, very broad variety of biological problems can be addressed using the Gd^{3+} tags. However, this paramagnetic system is relatively toxic for living systems. Additionally, the typical coordination number of 8-9 of Gd^{3+} leads to relatively large sizes of the tags that should be accounted for in data analysis.

Mn^{2+} is an interesting alternative to Gd^{3+} in terms of a biological perspective. It shares many EPR properties with Gd^{3+}. Although manganese is a more complex spin system, it has smaller coordination number (typically 6), allowing the design of smaller tags. It occurs naturally in enzymes and is widely utilized in EPR as substitution for diamagnetic Mg^{2+}.[48] Having interesting properties, Mn^{2+} has not been widely used in EPR-based distance measurements. The first experiments with cysteine-specific Mn^{2+}-EDTA spin tags (Figure 2) was reported by the group of D. Goldfarb only in 2012.[57]

It is important to note that in recent EPR literature paramagnetic tags with different properties (nitroxide, trityl, Mn^{2+}, Gd^{3+}, Cu^{2+} and other tags) are often referred to as *orthogonal tags (orthogonal spin labels).* One of the reasons for using such terms in EPR spectroscopy is associated with the possibility of measuring many different distance constraints within a single macromolecule or assembly by selectively measuring the dipolar coupling between different combinatory pairs of paramagnetic tags with different properties (*e.g.* nitroxide-nitroxide, trityl-trityl, Mn-Mn, nitroxide-trityl, nitroxide-Mn and trityl-Mn).

3. EPR Theory

A theoretical description starts with the simplest spin system with an electron spin of S = 1/2, an important case for EPR-based distance measurements. A majority of the biologically relevant paramagnetic tags, such as nitroxides, other stable and transiently generated organic radicals, Cu^{2+}, low spin Fe^{3+} (*e.g.* present in heme molecules) and other centers have such electron spin state. For interpretation of the EPR spectra an effective spin Hamiltonian operator formalism is introduced. The spectra of the spin system with isotropic and anisotropic properties are explained with the help of perturbation theory. In the following section more complex spin systems, which have higher electron spin multiplicities, are introduced. The perturbation theory approach, introduced for the simple spin 1/2 case, is used for these systems as well. Although the detailed description is given mainly for high-spin Mn^{2+} ions (S = 5/2), the presented theoretical approach is applicable for more frequently used in distance measurements Gd^{3+} ions (S = 7/2) and other high-spin systems. This is followed by a section that describes magnetic dipole-dipole coupling, a central phenomenon for EPR-based distance measurements. In the final sections of this introduction to pulsed EPR theory, common EPR techniques for distance measurements and data analysis methods are described.

3.1 EPR Spectrum and electron spin Hamiltonian

3.1.1 Electron spin 1/2 systems

One of the most powerful approach to characterize and interpret the spectra in EPR spectroscopy has been the use of a concept of the *effective spin Hamilton operator* $\hat{\mathcal{H}}$ which has been introduced by M. Pryce and A. Abragam in 1951.[58] The *effective spin*, *S*, describes the low-lying ground energy levels[a], which are largely separated from the excited ones. For the stable organic radicals and most transition metal ions, the *effective spin* coincides with the *real spin*, and therefore, in the following the term *effective* is omitted. Thus, the total number of the electron spin sublevels is equal to (2*S*+1), and the EPR spectrum is the superposition of transitions between the levels that are induced by microwave fields with appropriate frequencies. The energy of the spin sublevels is defined as the eigenvalues of the matrix corresponding to the spin Hamilton operator $\hat{\mathcal{H}}$ (referred to in the following as *Hamiltonian*).

[a] Referred to in the following as *electron spin sublevels* that split only by few tenths to a few hundreds of GHz.

The Hamiltonian contains the terms that describe interactions of the electron and nuclear spin magnetic dipole moments with the external magnetic field $\boldsymbol{B}_0$ and various field-independent spin-spin interactions. For an electron spin of $S = 1/2$ the spin Hamiltonian[58–60] is given by:

$$\hat{\mathcal{H}} = \hat{\mathcal{H}}_{EZ} + \hat{\mathcal{H}}_{NZ} + \hat{\mathcal{H}}_{HF} + \hat{\mathcal{H}}_{NQ} + \hat{\mathcal{H}}_{DD} = \\ = \beta_e \hat{\boldsymbol{S}} \cdot \overline{\boldsymbol{g}} \cdot \boldsymbol{B}_0 / \hbar - \sum_j \gamma_j \hat{\boldsymbol{I}}_j \boldsymbol{B}_0 + \sum_j \hat{\boldsymbol{S}} \cdot \overline{\boldsymbol{A}}_j \cdot \hat{\boldsymbol{I}}_j + \sum_j \hat{\boldsymbol{I}}_j \cdot \overline{\boldsymbol{P}}_j \cdot \hat{\boldsymbol{I}}_j + \hat{\boldsymbol{S}} \cdot \overline{\boldsymbol{D}}_{dip} \cdot \hat{\boldsymbol{S}} \quad (3.1.1)$$

The first term $\hat{\mathcal{H}}_{EZ}$ describes the interaction of the electron spin magnetic dipole moment of $\hat{\boldsymbol{\mu}}_e = \beta_e \overline{\boldsymbol{g}} \hat{\boldsymbol{S}} / \hbar$ with the external magnetic field $\boldsymbol{B}_0$ (called *electron Zeeman interaction*), where $\hat{\boldsymbol{S}}$ is the *electron spin vector operator*. The electron Zeeman interaction is usually the dominant term in the spin Hamiltonian for spin 1/2 system. The principal values of the $\overline{\boldsymbol{g}}$-tensor can deviate from the g_e value of 2.0023 (corresponds to the free electron) when contribution from the spin-orbit coupling is non-zero and the $\overline{\boldsymbol{g}}$-tensor can be strongly anisotropic. The spin-orbit coupling originates from the mixing of ground and excited electronic states. The closer the excited states to the ground state, the larger the spin-orbit coupling and the stronger deviation of principal values of $\overline{\boldsymbol{g}}$-tensor from 2.0023. However, for most stable organic radicals and even for high-spin Mn^{2+} complexes the excited states are high in energy and difference of the principal values of the $\overline{\boldsymbol{g}}$-tensor is less than 1%.

The second term $\hat{\mathcal{H}}_{NZ}$ is the interaction of the nuclear spin magnetic dipole moment(s) $\hat{\boldsymbol{\mu}}_{Nj} = -\gamma_{Nj} \hat{\boldsymbol{I}}_j$ with the external magnetic field (nuclear Zeeman interaction), where $\hat{\boldsymbol{I}}_j$ is the *nuclear spin vector operator*.

The third, hyperfine interaction term, $\hat{\mathcal{H}}_{HF}$ results from the interaction of the electron spin magnetic moment with the nuclear spin magnetic moment(s). $\overline{\boldsymbol{A}}$ is the hyperfine coupling tensor that characterizes the energy of this interaction. In general case, the Hamiltonian term $\hat{\mathcal{H}}_{HF}$ comprises of two contributions: isotropic or *Fermi contact interaction* $\hat{\mathcal{H}}_F$ and the *electron nuclear magnetic dipole-dipole coupling* $\hat{\mathcal{H}}_{NDD}$ (spatial interaction).

The Fermi contact interaction is given by:

$$\hat{\mathcal{H}}_F = a_{iso} \hat{\boldsymbol{S}} \hat{\boldsymbol{I}} \quad (3.1.2)$$

The isotropic hyperfine-coupling constant a_{iso} is given as:

$$a_{iso} = \frac{2}{3}\frac{\mu_0}{\hbar^2} g_e \beta_e \gamma_N |\psi_0(0)|^2 \tag{3.1.3}$$

in which $|\psi_0(0)|^2$ is the electron spin density at the nucleus.

The electron-nuclear magnetic dipole-dipole coupling is given as:

$$\hat{\mathcal{H}}_{\mathcal{END}} = \hat{\boldsymbol{S}}\overline{\boldsymbol{T}}\hat{\boldsymbol{I}} \tag{3.1.4}$$

where $\overline{\boldsymbol{T}}$ is the electron-nuclear spin dipolar coupling tensor. The term $\hat{\mathcal{H}}_{\mathcal{END}}$ of the Hamiltonian is analogous to the electron magnetic dipole-dipole coupling term, which is described in detail in section 3.1.3.

The forth, nuclear quadrupole interaction term $\hat{\mathcal{H}}_{\mathcal{NQ}}$ accounts for the interaction of the non-spherical nucleus (in cases of nuclear spin of $I > 1/2$) with the asymmetrically distributed electric fields. $\overline{\boldsymbol{P}}$ is the nuclear quadrupole tensor. This term did not have a significant contribution to the experiments given in the thesis, therefore is not discussed in more detail.

The last, magnetic dipole-dipole coupling term $\hat{\mathcal{H}}_{\mathcal{DD}}$ accounts for the interaction between the two electron spin magnetic dipole moments. This term is crucial for EPR-based distance measurements and is discussed in detail in the separate section 3.1.3.

In order to understand how the terms listed above influence the spin 1/2 system, the *spin sublevel diagram* is given for a nitroxide radical with isotropic $\bar{\boldsymbol{g}}$- and $\overline{\boldsymbol{A}}$-tensors (Figure 3)[a]. The electron spin of this system experiences hyperfine coupling with a ^{14}N nucleus (nuclear spin $I = 1$) with a_{iso} of about 47 MHz and with g_{iso} of about 2.0057.[61,62]

The spin Hamiltonian (eq. 3.1.1) for this system can be simplified to the form, given as:

$$\hat{\mathcal{H}} = \beta_e g_{iso} B_0 \hat{S}_z / \hbar - \gamma_{^{14}N} B_0 \hat{I}_z + a_{iso}\left(\hat{S}_x\hat{I}_x + \hat{S}_y\hat{I}_y + \hat{S}_z\hat{I}_z\right) \tag{3.1.5}$$

where the spin operators $\hat{S}_x$ and $\hat{S}_y$ can be represented by the raising $\hat{S}_+$ and lowering $\hat{S}_-$ operators:

$$\hat{S}_x = \frac{\hat{S}_+ + \hat{S}_-}{2}, \qquad \hat{S}_y = \frac{\hat{S}_+ - \hat{S}_-}{2i} \tag{3.1.6}$$

[a] The isotropic tensors correspond to a nitroxide radical in liquid solution in *isotropic limit*, where all anisotropic properties are averaged out by extremely fast tumbling of the paramagnetic molecules.

The raising and lowering operators are defined as:

$$\hat{S}_{\pm}\left|S,m_S\right\rangle=\sqrt{S(S+1)-m_S(m_S\pm1)}\left|S,m_S\pm1\right\rangle \tag{3.1.7}$$

where m_S, an *electron spin magnetic quantum number*, is the eigenvalue of the spin operator $\hat{S}_z$ and given as:

$$\hat{S}_z\left|S,m_S\right\rangle=m_S\left|S,m_S\right\rangle \tag{3.1.8}$$

The values of m_S are varied in the range [-*S*, -*S*+1, … , *S*-1, *S*]. For a spin of *S* = 1/2 it can have only two values of -1/2 or 1/2. Analogously the nuclear spin operators are defined.

The eigenvalues of the Hamiltonian (eq. 3.1.5) are determined either by full diagonalization of the corresponding matrix or by the *perturbation theory*,[63] in which $\hat{\mathcal{H}}_{\text{perturb}}=\hat{\mathcal{H}}_{\mathcal{HF}}+\hat{\mathcal{H}}_{\mathcal{NZ}}$ is considered as a small perturbation to the electron Zeeman $\hat{\mathcal{H}}_0=\hat{\mathcal{H}}_{\mathcal{EZ}}$ term. Thus, in the perturbation approximation (up to the second order), the eigenvalues can be approximated as:

$$\mathcal{E}(m_S,m_I)\approx\mathcal{E}^{(0)}_{m_S}+\mathcal{E}^{(1)}_{m_S,m_I}+\mathcal{E}^{(2)}_{m_S,m_I} \tag{3.1.9}$$

where $\mathcal{E}^{(1)}_{m_S,m_I}$ and $\mathcal{E}^{(2)}_{m_S,m_I}$ are the first and second *order perturbation corrections* to the spin sublevel energies $\mathcal{E}^{(0)}_{m_S}$, which are the eigenvalues of the electron Zeeman term $\hat{\mathcal{H}}_0=\hat{\mathcal{H}}_{\mathcal{EZ}}$. Thus, the eigenvalues of the Hamiltonian (eq. 3.1.5) can be approximated:

$$\begin{aligned}
&\mathcal{E}(m_S,m_I)\approx\beta_e g_{iso}B_0m_S/\hbar+\left\langle m_S,m_I\left|\hat{\mathcal{H}}_{\text{perturb}}\right|m_S,m_I\right\rangle+\\
&\quad+\sum_{m'_S}\frac{\left|\left\langle m_S,m_I\left|\hat{\mathcal{H}}_{\text{perturb}}\right|m'_S,m_I\right\rangle\right|^2}{\mathcal{E}^{(0)}_{m_S}-\mathcal{E}^{(0)}_{m'_S}}\\
&\mathcal{E}(m_S,m_I)\approx\beta_e g_{iso}B_0m_S/\hbar+a_{iso}m_Sm_I-\gamma_{^{14}N}B_0m_I+\\
&\quad+\frac{a^2_{iso}}{2\beta_e g_{iso}B_0}\left[m_SI(I+1)-m_IS(S+1)+m_S^2m_I-m_Sm_I^2\right]
\end{aligned} \tag{3.1.10}$$

The nuclear Zeeman term is small, such that only the first order perturbation term $-\gamma_{^{14}\text{N}}B_0m_I$ can be retained.

The EPR transitions are the result of interaction of the spin system with continuous-wave, linear polarized and monochromatic microwave irradiation. For the allowed EPR transitions, where $\Delta m_S=\pm1$ (for the absorption $\Delta m_S=+1$) and $\Delta m_I=0$, the resonance conditions for the spin system are given in (eq. 3.1.11).

$$\hbar\omega_{\text{MW}} = \mathcal{E}(m_S, m_I) - \mathcal{E}(m_S - 1, m_I) = \beta_e g_{iso} B_0 / \hbar + a_{iso} m_I + \\ + \frac{a_{iso}^2}{2\beta_e g_{iso} B_0}\left[I(I+1) - m_I^2 + m_I(2m_S - 1)\right] \tag{3.1.11}$$

For the spin $S = 1/2$ system $m_S = 1/2$ and the resonance condition takes the simpler form:

$$\hbar\omega_{\text{MW}} = \beta_e g_{iso} B_0 / \hbar + a_{iso} m_I + \frac{a_{iso}^2}{2\beta_e g_{iso} B_0}\left[I(I+1) - m_I^2\right] \tag{3.1.12}$$

When this condition is fulfilled, the microwave quanta $\hbar\omega_{\text{MW}}$ are absorbed (red lines in Figure 3) by the spin system that is subsequently detected by the microwave diode or quadrature detector of the spectrometer. Due to technical reasons, in most modern EPR spectrometers the spectrum is obtained by sweeping the magnetic field $\boldsymbol{B}_0$ while keeping the microwave frequency ω_{MW} constant. The characteristic EPR absorption spectrum (Figure 3 right) for the spin system consists of the three lines, which are equally separated by a_{iso} when $\beta_e g_{iso} B_0 >> a_{iso}$ [a]. As the detected signals in continuous-wave EPR spectroscopy are very weak, double-modulation schemes are applied to increase the detection sensitivity that also leads to the first derivative of the EPR absorption spectrum being detected (Figure 3).

Absorption of the microwave quanta by the spin system leads to a slight deviation of the spin sublevel population from the equilibrium, which is defined by the Boltzmann distribution. As the spin system is coupled to the phonon bath, the *spin-lattice (longitudinal) relaxation* with a characteristic time of T_{1e} brings this non-equilibrium population back to the Boltzmann distribution. Description of the different longitudinal relaxation mechanisms can be found elsewhere.[59,64,65] Thus, the absorption of the microwave quanta with the following relaxation of the spin system to the equilibrium occurs continuously until the *saturation regime of the EPR transition*[66] is reached[b].

The relative intensity of the resonance lines in the EPR spectrum of the introduced spin system can be found by using the *microwave field Hamiltonian*, which describes the interaction of the spin system with the microwave quanta and given as:

$$\hat{\mathcal{H}}_{\text{MW}}(t) = \beta_e \hat{\boldsymbol{S}} \cdot \bar{\boldsymbol{g}} \cdot \boldsymbol{B}_{\text{MW}}(t) / \hbar \tag{3.1.13}$$

In this Hamiltonian a linearly polarized microwave field is represented by the vector $\boldsymbol{B}_{\text{MW}}(t) = 2B_1 \cos(\omega_{\text{MW}} t) \cdot \boldsymbol{e}_i$, where $2B_1$ is an amplitude and $\boldsymbol{e}_i$ is a unit basis-vector, indicating a direction of the polarization.

[a] In such case the second-order perturbation term, the third term in (eq. 3.1.12), can be neglected.
[b] Saturation depends on the electron spin relaxation times and power of the applied microwave field.

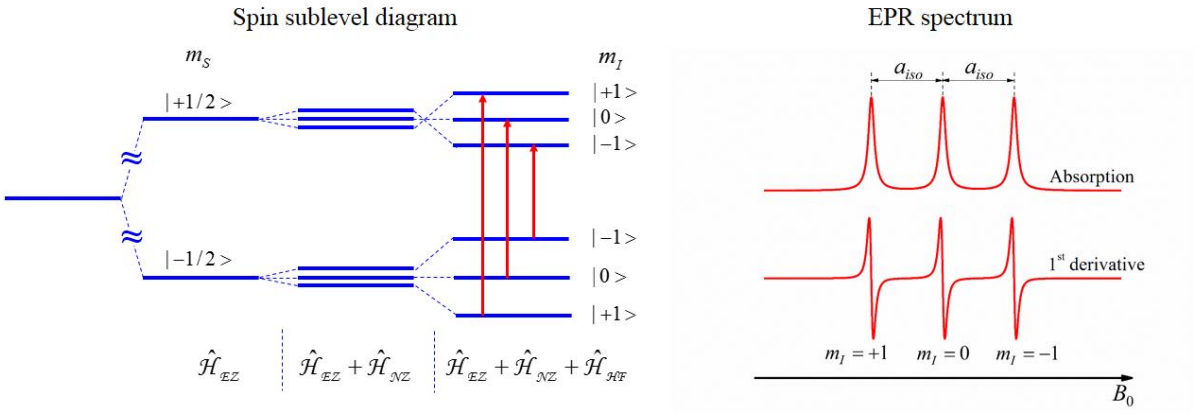

Figure 3. The spin sublevel diagram (left) and corresponding EPR spectrum (right) for spin 1/2 system with isotropic EPR properties.

In terms of simplicity, the Hamiltonian (eq. 3.1.13) is often transformed to *the rotating frame*[a], where it is time-independent. Thus, the relative intensity of the EPR lines can be defined by the transition probabilities:

$$P\left(\left|m_S-1,m_I\right\rangle\rightarrow\left|m_S,m_I\right\rangle\right)=\left(2\left\langle m_S,m_I\left|\beta_e\hat{\boldsymbol{S}}\cdot\bar{\boldsymbol{g}}\cdot\boldsymbol{B}_1\right|m_S-1,m_I\right\rangle/\hbar\right)^2 \tag{3.1.14}$$

In the vast majority of cases polarization of the microwave field is set to be orthogonal (aligned along *x*-axis or *y*-axis) to the direction of external magnetic field $\boldsymbol{B}_0$ (aligned along *z*-axis). Therefore, the transition probabilities (eq. 3.1.14) can be simplified to the form:

$$P=\left[S(S+1)-(m_S-1)m_S\right]\cdot\left(g_{xx}\beta_e B_1\right)^2 \tag{3.1.15}$$

Thus, for the spin system described above the relative intensities of all the lines in the spectrum are equal (see Figure 3).

The spin system considered so far exhibits isotropic EPR-properties[b]. However, EPR-based distance measurements are performed with immobilized tags in order to avoid averaging out of the dipolar coupling. The EPR spectra of the immobilized systems in amorphous samples (frozen solution of powders) reveal anisotropy of the $\bar{\boldsymbol{g}}$- and $\bar{\boldsymbol{A}}$-tensors. For example, the tensors for the nitroxide paramagnetic tag are given with their typical principal values of (2.0090, 2.0061, 2.0021) and (18.5, 18.9, 102.5) MHz,[61,62] respectively. Thus, the paramagnetic molecules with different orientations with respect to the external magnetic field have different resonance spectral positions and different excitation probabilities. In the following description anisotropy of the tensors will be considered.

[a] It is a Cartesian coordinate frame, rotating around the external magnetic field axis with the frequency of ω_{mw}.
[b] A nitroxide radical in liquid solution.

The electron Zeeman term of the spin Hamiltonian is represented as:

$$\begin{aligned}\hat{\mathcal{H}}_{EZ} &= \beta_e \hat{\mathbf{S}} \cdot \bar{\mathbf{g}} \cdot \mathbf{B}_0 / \hbar = \beta_e B_0 \mathbf{n} \cdot \bar{\mathbf{g}} \cdot \hat{\mathbf{S}} / \hbar = \\ &= \beta_e B_0 \left(g_x \sin\theta\cos\varphi \cdot \hat{S}_x + g_y \sin\theta\sin\varphi \cdot \hat{S}_y + g_z \cos\theta \cdot \hat{S}_z \right) / \hbar\end{aligned} \tag{3.1.16}$$

where $\mathbf{n} = (\sin\theta\cos\varphi,\ \sin\theta\sin\varphi,\ \cos\theta) = (0\ \ 0\ \ 1)\mathbf{R}$ is the unit vector, describing the orientation of the external magnetic field vector in the molecular frame. $\mathbf{R}$ is the rotation matrix which transforms the laboratory frame into the molecular frame.

The Hamiltonian $\hat{\mathcal{H}}_{EZ}$ (eq. 3.1.16) can be diagonalized by rotating of the electron spin subspace with the matrix $\mathbf{R}_S$ [67]:

$$\hat{\mathcal{H}}_{EZ}^{diag} = \beta_e B_0 \mathbf{n} \cdot \bar{\mathbf{g}} \cdot \mathbf{R}_S \hat{\mathbf{S}} / \hbar \tag{3.1.17}$$

such that $\mathbf{n} \cdot \bar{\mathbf{g}} \cdot \mathbf{R}_S = (0\ \ 0\ \ g)$. The resulted Zeeman interaction is represented as:

$$\hat{\mathcal{H}}_{EZ} = g \beta_e B_0 \hat{S}_z / \hbar \tag{3.1.18}$$

with an effective value of the $\bar{\mathbf{g}}$-tensor:

$$g(\theta,\varphi) = \sqrt{g_x^2 \sin^2\theta\cos^2\varphi + g_y^2 \sin^2\theta\sin^2\varphi + g_z^2 \cos^2\theta} \tag{3.1.19}$$

By applying rotations of both electron and nuclear spin subspaces for $\hat{\mathcal{H}}_{HF}$ and rotation of nuclear spin subspace for $\hat{\mathcal{H}}_{NZ}$ terms of the Hamiltonian (eq. 3.1.1), these operators can also be diagonalized. Thus, an effective value of the hyperfine coupling is given as:

$$A(\theta,\varphi) = \frac{\sqrt{g_x^2 A_x^2 \sin^2\theta\cos^2\varphi + g_y^2 A_y^2 \sin^2\theta\sin^2\varphi + g_z^2 A_z^2 \cos^2\theta}}{g(\theta,\varphi)} \tag{3.1.20}$$

The EPR resonance condition (eq. 3.1.12) is then modified as (in a first order perturbation theory):

$$\hbar\omega_{MW} = \beta_e g(\theta,\varphi) B_0 / \hbar + A(\theta,\varphi) m_I \tag{3.1.21}$$

The powder EPR spectrum is the weighted sum of the sub-spectra from all molecular orientations. Thus, in the general case the *spectral shape function* is calculated as:

$$F(B) = \sum_{m_I=-1,0,1} \int_0^{2\pi} \int_0^{\pi} G\left[B_0(m_I,\theta,\varphi), B\right] \cdot P(\theta,\varphi) \sin\theta \, d\theta \, d\varphi \tag{3.1.22}$$

where, $G\left[B_0(m_I,\theta,\varphi), B\right]$ is a *line shape function* (*Gaussian* or *Lorentz*), $B_0(m_I,\theta,\varphi)$ is the resonance field position, as defined in (eq. 3.1.21) and which is dependent on molecular orientation, and $P(\theta,\varphi)$ is the transition probability, defined by corresponding modification of

(eq. 3.1.14) and that equals to $\left(g(\theta,\varphi)\beta_e B_1\right)^2$. At low magnetic fields the dependence of transition probability on the molecular orientation is very weak and therefore it can be omitted in the spectral shape calculation (eq. 3.1.22). Often, the spectral shape function $F(B)$ is calculated numerically, but analytical expressions for *axial* and *rhombic* $\bar{\boldsymbol{g}}$-tensors can be found elsewhere.[68,69]

In order to visualize the influence of anisotropic properties of the nitroxide radical spin system to the EPR powder spectrum, simulations are performed for the different microwave frequencies: X - (9.4 GHz), Q - (34 GHz) and G - (180 GHz) bands (Figure 4) using the EasySpin toolbox, developed by S. Stoll.[70]

At X-band frequencies the EPR spectral shape (eq. 3.1.22) is purely defined by the hyperfine coupling anisotropy (Figure 4 top). The whole width of the EPR spectrum can be approximated then by $2A_{zz}$. In the insets of this figure the excited molecular orientations at a given field position are shown (the molecular axes definition and color code explanation are given in Figure 5). This is useful for qualitative understanding the orientational resolution of the corresponding field position.

With increasing the microwave frequency, the $\bar{\boldsymbol{g}}$-tensor anisotropy starts to contribute to the spectral shape and the whole width of the EPR spectrum. Thus, at Q-band frequency the *z*-component of the $\bar{\boldsymbol{g}}$-tensor becomes partially resolved (Figure 4 middle). But this frequency is not large enough to clearly distinguish the *x* and *y* components and completely resolve the *z* component. As a result, orientational resolution for the corresponding region of the EPR spectrum is weak. Furthermore, the orientational resolution of g_{zz} position, marked in the Q-band EPR spectrum, is relatively poor and this assignment has more qualitative meaning (therefore shown as "g_{zz}" in Figure 4).

With both, X and Q-band frequencies, orientational resolution is weak due to the overlap of multiple molecular orientations and/or m_I with identical resonance fields. However, by applying frequencies higher than Q-band (*e.g.* the frequency of G-band as presented in Figure 4), the $\bar{\boldsymbol{g}}$-tensor anisotropy is completely resolved, and the width of the EPR spectrum is determined by the anisotropy of the $\bar{\boldsymbol{g}}$-tensor to a large extent. As a result, the orientational resolution for many spectral positions is significantly higher than for X- and Q-band frequencies (see the insets in Figure 4). Thus, one of the advantages of using higher frequencies is high resolution of the $\bar{\boldsymbol{g}}$-tensor anisotropy and associated high orientational resolution.

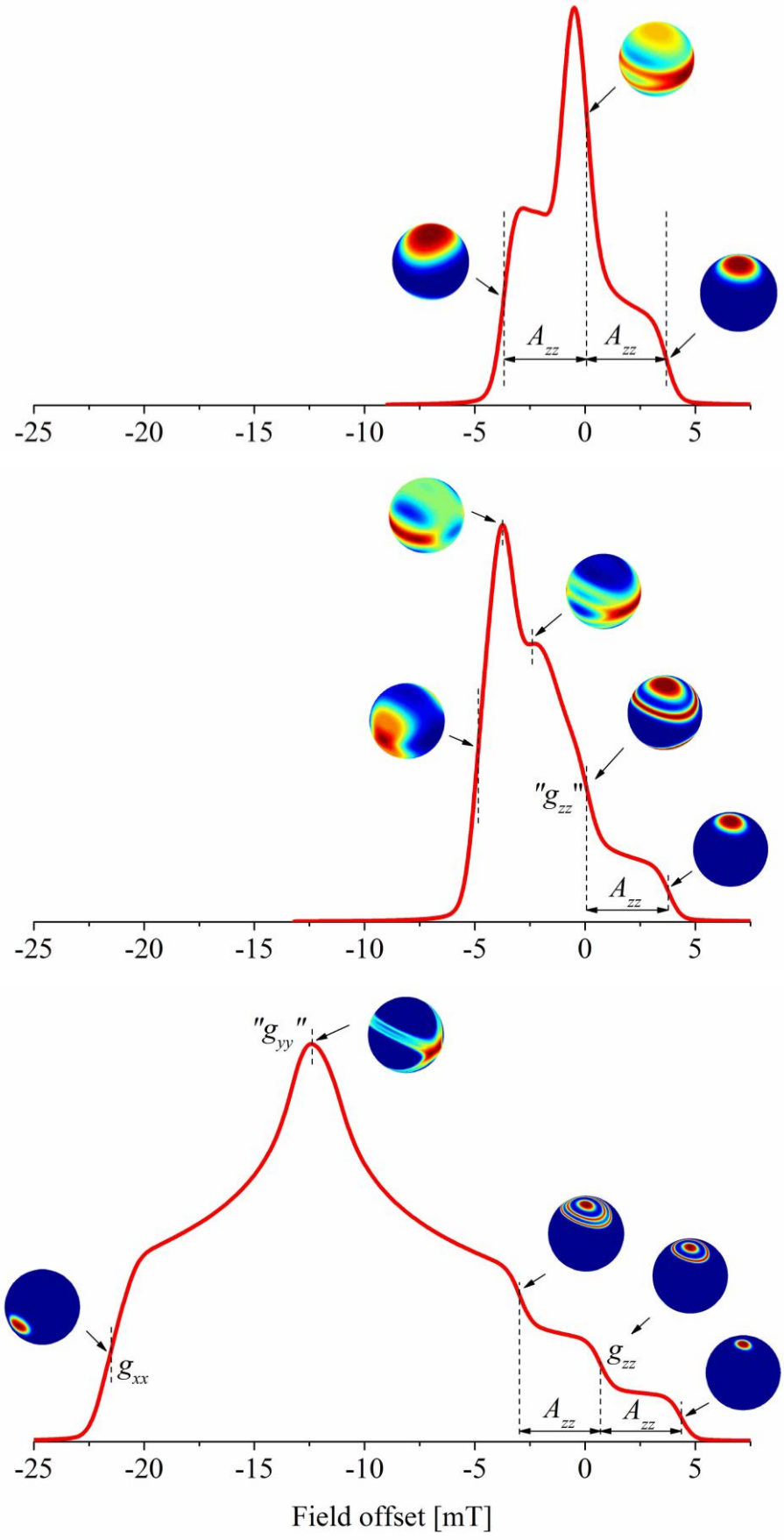

Figure 4. EPR absorption spectra at X- (top), Q- (middle) and G- band (bottom) frequencies of TEMPO in frozen solution. The field offset is with respect to the g_e position at a given frequency.

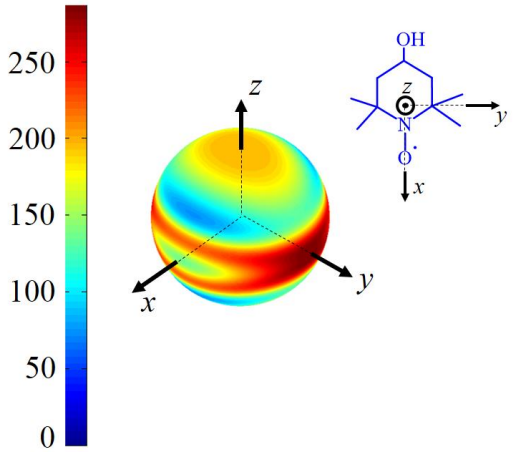

Figure 5. Definition of the molecular axes of a nitroxide radical and the corresponding axes on the sphere of the excited orientations. The weights of the excited molecular orientations (within the excitation bandwidth of 30 MHz) are given in the color-code bar (the example is given for the sphere of the excited molecular orientations for X-band spectrum for the position with an offset of about 0 mT, as indicated in Figure 4 -top).

3.1.2 High electron spin systems

After considering the basic theory for simple spin 1/2 system, we approach more complex high-spin systems. For these systems, additional splitting of the spin sublevels appears due to the indirect effect of the *crystal (ligand) field* to the interaction between the unpaired electrons. This splitting is magnetic field independent and therefore called *Zero-Field Splitting* (*ZFS*). The form of the corresponding spin Hamiltonian is established using *symmetry* considerations,[59,60] since the symmetry and magnitude of the crystal field, interacting with the high-spin system, defines its EPR properties.

For the *cubic symmetry* crystal fields, the fourth-order ZFS spin Hamiltonian (*cubic ZFS term*) has been established[a]. Due to very high symmetry of the cubic ligand field, the corresponding Hamiltonian term is small. Therefore it has only minor contribution and is often neglected in analysis of the EPR spectra in amorphous samples. In contrast to the cubic symmetry, the ligand field with lower symmetry (*e.g. trigonal*, *rhombic* and lower symmetries) gives rise to the second-order ZFS term (also called *quadratic* or *quadrupole ZFS term*)[b]. This term is significantly larger than the fourth-order ZFS term and for some cases can even be the dominant term of the electron spin Hamiltonian, especially at low magnetic fields.

The second-order ZFS Hamiltonian term $\hat{\mathcal{H}}_{ZFS}$ is given as[59,67]

$$\hat{\mathcal{H}}_{ZFS} = \hat{\boldsymbol{S}}' \cdot \overline{\boldsymbol{D}} \cdot \hat{\boldsymbol{S}} \tag{3.1.23}$$

[a] This term is relevant for the spin systems with $S > 3/2$
[b] Relevant in the case of $S > 1/2$

where $\overline{\boldsymbol{D}}$ is the symmetric and traceless ZFS tensor. In the principal axes system of the $\overline{\boldsymbol{D}}$ tensor, the Hamiltonian $\hat{\mathcal{H}}_{ZFS}$ (eq. 3.1.23) takes form of

$$\hat{\mathcal{H}}_{ZFS} = D_{x'}\hat{S}_{x'}^2 + D_{y'}\hat{S}_{y'}^2 + D_{z'}\hat{S}_{z'}^2 = D\left(\hat{S}_{z'}^2 - \frac{1}{3}S(S+1)\hat{\mathbf{1}}\right) + E\left(S_{x'}^2 - S_{y'}^2\right) \tag{3.1.24}$$

with $D = 3D_{z'}/2$ and $E = (D_{x'} - D_{y'})/2$. These parameters are called *second-order ZFS parameters* and given as:

$$\begin{aligned} D &= \frac{3}{4}g^2\beta_e^2\left\langle\frac{r^2-3z^2}{r^5}\right\rangle \\ E &= \frac{3}{4}g^2\beta_e^2\left\langle\frac{y^2-x^2}{r^5}\right\rangle \end{aligned} \tag{3.1.25}$$

where averaging is performed over the crystal field *spherical wave functions*. With the second-order ZFS-parameters D and E the zero-field splitting of the energy levels of Mn^{2+} centers described in the thesis below can be adequately described. The parameter D (axial ZFS parameter) describes the expectation value of the distance between the unpaired electrons in the high spin system, while E represents the deviation of the electron spin density distribution from axial symmetric (*ZFS asymmetry* or *rhombic* parameter). For the cubic symmetry the parameters $D = E = 0$, for the axial symmetry $D \neq 0$ and $E = 0$ and for the rhombic and lower symmetries $D \neq 0$ and $E \neq 0$. Depending on the spin system and symmetry of the ligand field the parameter D can vary from a few hundreds of MHz to a few hundreds of GHz, and the parameter E has its maximum value of $D/3$ (for rhombic and lower symmetries).

As the high-spin Mn^{2+} complexes are the central spin systems in the thesis, the properties of this system are directly introduced into the full Hamiltonian. Furthermore, some of these properties are also relevant for other high-spin metal ions, including Gd^{3+} complexes ($S = 7/2$). Thus, the $\bar{\boldsymbol{g}}$- and hyperfine coupling[a] tensors of Mn^{2+} centers are isotropic in many cases. For Gd^{3+} complexes the hyperfine couplings with ^{155}Gd (14.8% abundance) and ^{157}Gd (15.65% abundance) are usually small (on the order of 10 MHz) and often neglected.[49]

[a] Mn^{2+} electron spin is coupled to the naturally abundant ^{55}Mn nuclear spin with $I = 5/2$.

The full spin Hamiltonian for high-spin Mn^{2+} system is represented as:

$$\hat{\mathcal{H}}_{Mn^{2+}} = \beta_e g_{iso} B_0 \hat{S}_z / \hbar - \gamma_{55_{Mn}} B_0 \hat{I}_z + a_{iso}\left[\hat{S}_z\hat{I}_z + \frac{1}{2}\left(\hat{S}_+\hat{I}_- + \hat{S}_-\hat{I}_+\right)\right] + \\ + D\left(\hat{S}_{z'}^2 - \frac{1}{3}S(S+1)\hat{\mathbf{1}}\right) + E\left(S_{x'}^2 - S_{y'}^2\right) \tag{3.1.26}$$

Note, that the nuclear quadrupolar interaction term for ^{55}Mn nucleus is neglected in this Hamiltonian. The electron and nuclear Zeeman terms as well as hyperfine coupling are represented in the laboratory frame, while the ZFS Hamiltonian in its eigenframe (eq. 3.1.26). Therefore, transformation of the eigenframe (molecular frame) to the laboratory frame has to be performed in order to quantify the EPR spectra of amorphous samples. Although the procedure (eq. 3.1.17) is also suitable for transformation of the ZFS Hamiltonian (eq. 3.1.23), we choose a more general approach that is based on the rotation using the *Wigner matrices* applied on the ZFS Hamiltonian, represented in a S*pherical Tensor Operator (STO)* $T_{l,m}(\boldsymbol{S})$[71–74] basis-set.

The second-order ZFS Hamiltonian represented in $T_{l,m}(\boldsymbol{S})$ basis-set is given as:

$$\hat{\mathcal{H}}_{ZFS'} = \sum_{m=-2}^{2} B'_{2,m} T'_{2,-m}(\boldsymbol{S}) \tag{3.1.27}$$

where the prime symbol indicates the eigenframe of the spin Hamiltonian. The relation of STO $T'_{2,m}(\boldsymbol{S})$of rank 2 to the classical spin operators is given as:[48]

$$T'_{2,0} = \left(3\hat{S}'_z - S(S+1)\cdot\mathbf{1}\right) \\ T'_{2,\pm 2} = \frac{\sqrt{6}\hat{S}'^2_{\pm}}{2} \tag{3.1.28}$$

The ligand field parameters $B'_{2,m}$ are related to the second-order ZFS parameters, as

$$B'_{2,0} = \frac{D}{3} \\ B'_{2,\pm 2} = \frac{E}{\sqrt{6}} \tag{3.1.29}$$

Thus, the ZFS Hamiltonian $\hat{\mathcal{H}}_{ZFS'}$ (eq. 3.1.27) transformed to the laboratory frame is given by

$$\hat{\mathcal{H}}_{ZFS}(\text{lab}) = \sum_{m=-2}^{2} B_{2,m} T_{2,-m}(\boldsymbol{S}) \tag{3.1.30}$$

where STO $T_{2,\pm 1}(\boldsymbol{S})$ are non-zero and given by (eq. 3.1.31).

$$
\begin{aligned}
T_{2,0} &= T'_{2,0} \\
T_{2,\pm1} &= \frac{\sqrt{6}}{2}\left(\hat{S}_{\pm}\hat{S}_z + \hat{S}_z\hat{S}_{\pm}\right) \\
T_{2,\pm2} &= T'_{2,\pm2}
\end{aligned}
\tag{3.1.31}
$$

The transformation of the crystal field parameters $B'_{2,m}$ to the laboratory frame are performed using the Wigner rotation matrices $D^{(2)}_{m,m'}$ of rank 2. The list of the 2nd rank Wigner rotation matrices can be found elsewhere.[48,75] Thus, the parameters $B_{2,m}$ in the laboratory frame are given as:[48]

$$
B_{2,m} = \sum_{m'=-2}^{2} D^{(2)}_{m,m'} B'_{2,m'} \tag{3.1.32}
$$

The angular dependent parameters $B_{2,m}$ are related to the second-order ZFS parameters as given:

$$
\begin{aligned}
B_{2,0} &= \frac{D}{3}\left(3\cos^2\theta - 1\right) + \frac{E}{2}\sin^2\theta\cos 2\varphi, \\
B_{2,\pm1} &= \pm\frac{D}{2\sqrt{6}}\sin 2\theta + \frac{E}{\sqrt{6}}\left(\mp\frac{1}{2}\sin 2\theta\cos 2\varphi + i\sin\theta\sin 2\varphi\right) \\
B_{2,\pm2} &= \pm\frac{D}{2\sqrt{6}}\sin^2\theta + \frac{E}{2\sqrt{6}}\left[\left(1+\cos^2\theta\right)\cos 2\varphi \mp 2i\cos\theta\sin 2\varphi\right]
\end{aligned}
\tag{3.1.33}
$$

The geometrical illustration of the angles θ and φ are shown in Figure 6.

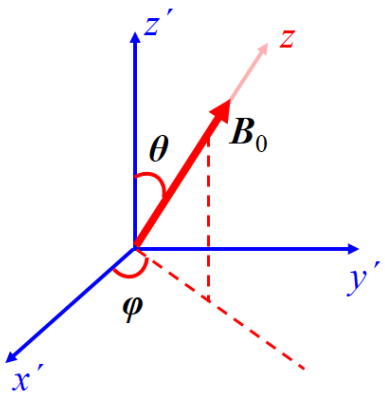

Figure 6. Representation of the angles $\{\theta, \varphi\}$ that relate the eigenframe of the ZFS tensor (molecular frame) $\{x',y',z'\}$ to the applied magnetic field direction $\boldsymbol{B_0}$ and associated with it laboratory frame.

It is convenient to represent the ZFS Hamiltonian (eq. 3.1.30) in the form:[48,76–78]

$$
\begin{aligned}
\hat{\mathcal{H}}_{ZFS}(\text{lab}) &= D_0\left(3\hat{S}_z^2 - S(S+1)\right) + D_1\left(\hat{S}_+\hat{S}_z + \hat{S}_z\hat{S}_+\right) + \\
&+ D_{-1}\left(\hat{S}_-\hat{S}_z + \hat{S}_z\hat{S}_-\right) + D_2\hat{S}_+^2 + D_{-2}\hat{S}_-^2
\end{aligned}
\tag{3.1.34}
$$

where the angular dependent parameters D_m are defined as given in (eq. 3.1.35).

$$D_0 = \frac{D}{6}\left(3\cos^2\theta - 1\right) + \frac{E}{2}\sin^2\theta\cos 2\varphi$$

$$D_{\pm 1} = \frac{1}{4}\sin 2\theta\left(D + E\cos 2\varphi\right) \pm i\frac{E}{2}\sin\theta\sin 2\varphi \tag{3.1.35}$$

$$D_{\pm 2} = \frac{1}{4}\left(D\sin^2\theta + E\cos 2\varphi\left(\cos^2\theta + 1\right)\right) \pm i\frac{E}{2}\cos\theta\sin 2\varphi$$

Thus the Hamiltonian for the Mn^{2+} spin system $\hat{\mathcal{H}}_{Mn^{2+}}$ (eq. 3.1.26) in the laboratory frame is given:

$$\begin{aligned}\hat{\mathcal{H}}_{Mn^{2+}} &= \beta_e g_{iso} B_0 \hat{S}_z/\hbar - \gamma_{55_{Mn}} B_0 \hat{I}_z + a_{iso}\left[\hat{S}_z\hat{I}_z + \frac{1}{2}\left(\hat{S}_+\hat{I}_- + \hat{S}_-\hat{I}_+\right)\right] + \\ &+ D_0\left(3\hat{S}_z^2 - S(S+1)\right) + D_1\left(\hat{S}_+\hat{S}_z + \hat{S}_z\hat{S}_+\right) + D_{-1}\left(\hat{S}_-\hat{S}_z + \hat{S}_z\hat{S}_-\right) + \\ &D_2\hat{S}_+^2 + D_{-2}\hat{S}_-^2\end{aligned} \tag{3.1.36}$$

In order to understand how the high-spin multiplicity of Mn^{2+} influences the EPR spectrum, we apply a first-order perturbation theory to find the eigenvalues of $\hat{\mathcal{H}}_{Mn^{2+}}$ and will consequently examine the spin sublevel diagram. The unperturbed spin Hamiltonian is the electron Zeeman term $\hat{\mathcal{H}}_0 = \hat{\mathcal{H}}_{EZ}$ and the perturbation is $\hat{\mathcal{H}}_{\text{perturb}} = \hat{\mathcal{H}}_{HF} + \hat{\mathcal{H}}_{ZFS} + \hat{\mathcal{H}}_{NZ}$. Importantly, that the first-order perturbation theory can be applied only if the high-field approximation for ZFS, $\beta_e g_{iso} B_0 >> D$ is fulfilled to a very large extent. Thus, the eigenvalues of the spin Hamiltonian $\hat{\mathcal{H}}_{Mn^{2+}}$ (eq. 3.1.36) are given as:

$$\begin{aligned}&\mathcal{E}_{\text{Mn}^{2+}}\left(m_S, m_I, \theta, \varphi\right) \approx \mathcal{E}_{m_S}^{(0)} + \mathcal{E}_{m_S, m_I}^{(1)} \\ &\mathcal{E}_{\text{Mn}^{2+}}\left(m_S, m_I, \theta, \varphi\right) \approx \beta_e g_{iso} B_0 m_S/\hbar - \gamma_{55_{Mn}} B_0 m_I + a_{iso} m_S m_I + \\ &+ \left[\frac{D}{6}\left(3\cos^2\theta - 1\right) + \frac{E}{2}\sin^2\theta\cos 2\varphi\right]\left(3m_S^2 - S(S+1)\right)\end{aligned} \tag{3.1.37}$$

The EPR resonance condition (eq. 3.1.11) takes then the form of

$$\begin{aligned}&\hbar\omega_{\text{MW}} = \mathcal{E}\left(m_S, m_I, \theta, \varphi\right) - \mathcal{E}\left(m_S - 1, m_I, \theta, \varphi\right) = \\ &= \beta_e g_{iso} B_0/\hbar + a_{iso} m_I + \left(D\left(3\cos^2\theta - 1\right) + 3E\sin^2\theta\cos 2\varphi\right)\left(m_S - \frac{1}{2}\right)\end{aligned} \tag{3.1.38}$$

For examining the spin sublevel diagram, we will choose the orientation of the magnetic field $\boldsymbol{B_0}$ aligned along the molecular z' axis (θ = 0, φ = 0). The spin sublevel diagram and corresponding EPR absorption spectrum are given in Figure 7. Effects of the ZFS and hyperfine

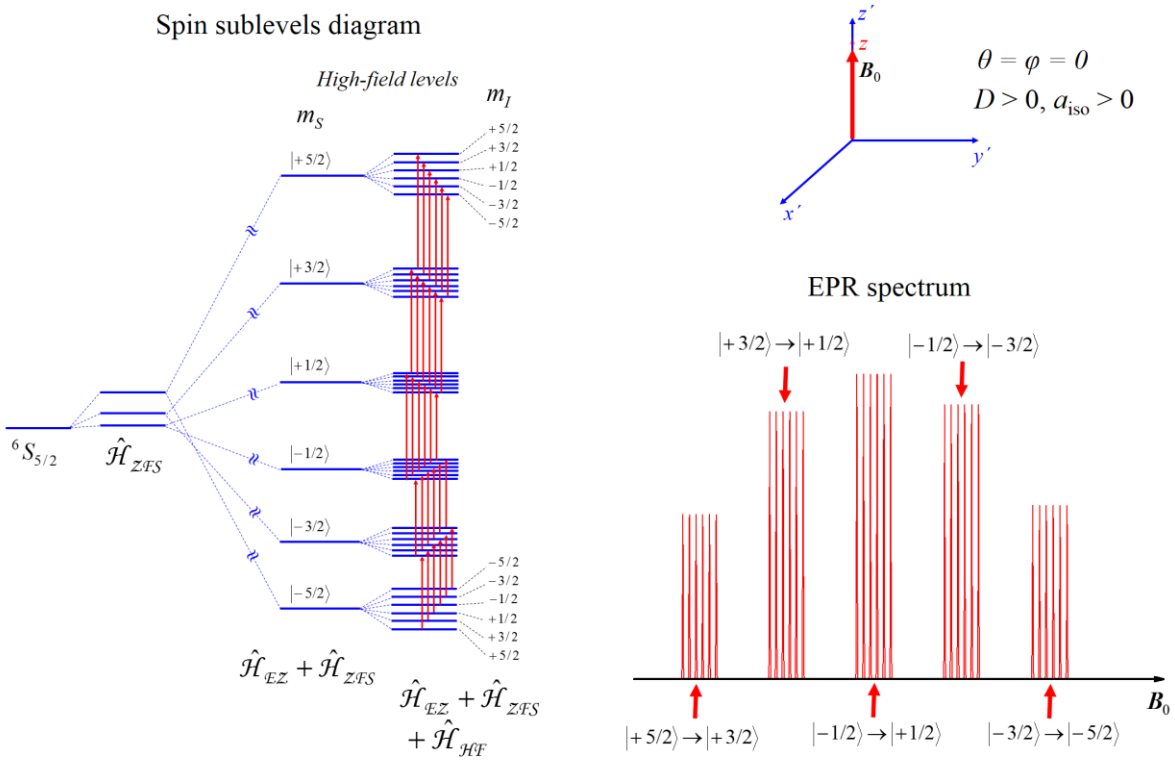

Figure 7. The spin sublevel diagram (left) and corresponding EPR absorption spectrum (right bottom) of Mn^{2+} spin system in the single crystal with an orientation of magnetic field aligned along the molecular *z*' axis (right top). EPR spectrum was simulated in the high temperature approximation.

coupling can be seen in this spin sublevel diagram. Hence, the EPR spectrum consists of 5 fine structure lines $|m_S-1\rangle\rightarrow|m_S\rangle$. Each of these lines is further split into sextet due to the hyperfine coupling that results in the spectrum consisting of 30 lines (see Figure 7). As can be seen from the EPR spectrum, fine structure components have different intensities. This is because the transition probability depends on the electron spin quantum number. In order to calculate the transition probabilities, the modified transition probabilities (eq. 3.1.15) should be used:

$$P\left(|m_S-1,m_I\rangle\rightarrow|m_S,m_I\rangle\right)=\left(S(S+1)-m_S(m_S+1)\right)\cdot P_{S=1/2} \qquad (3.1.39)$$

where, $P_{S=1/2}$ is the transition probability for the spin 1/2 defined in (eq. 3.1.15). In the high-field approximation, the probabilities are given as $5P_{S=1/2}$, $8P_{S=1/2}$ for the EPR lines corresponding to the transitions $|\pm5/2\rangle\rightarrow|\pm3/2\rangle$, $|\pm3/2\rangle\rightarrow|\pm1/2\rangle$ (in the following addressed as *side transitions*), respectively, and $9P_{S=1/2}$ for the transition $|-1/2\rangle\rightarrow|+1/2\rangle$ (*central transition*). For the Gd^{3+} spin system the number of lines in the fine structure is 7 due to its higher electron spin (*S*= 7/2) and the transition probabilities are given as $16P_{S=1/2}$ for the line, corresponding to the central transition and as $15P_{S=1/2}$, $12P_{S=1/2}$ and $7P_{S=1/2}$ for the side

transitions $|\pm 3/2\rangle \rightarrow |\pm 1/2\rangle$, $|\pm 5/2\rangle \rightarrow |\pm 3/2\rangle$ and $|\pm 7/2\rangle \rightarrow |\pm 5/2\rangle$, respectively.

In amorphous samples, the ZFS leads to a significant broadening of the fine structure lines which can be roughly assessed by the first-order perturbation theory (eq. 3.1.38). Thus, the ZFS has a dominant contribution to the width of the EPR spectra of the high-spin systems. However, for the central transition ($m_S = 1/2$) the first-order ZFS dependence disappears (corresponding term equals to zero in (eq. 3.1.38)). Hence, the second- and high-order perturbation theory should be applied. The eigenvalues $\mathcal{E}^{(2)}_{\mathrm{Mn}^{2+}}$ of the spin Hamiltonian $\hat{\mathcal{H}}_{Mn^{2+}}$ (eq. 3.1.48) in the second-order perturbation theory are given as:[77]

$$\mathcal{E}^{(2)}_{\mathrm{Mn}^{2+}}(m_S, m_I, \theta, \varphi) =$$

$$= \frac{a_{iso}^2}{2\beta_e g_{iso} B_0}\left[m_S I(I+1) - m_I S(S+1) + m_S^2 m_I - m_S m_I^2\right] + \tag{3.1.40}$$

$$+ \frac{2D_1 D_{-1}}{\beta_e g_{iso} B_0}\left[8m_S^3 + m_S - 4m_S S(S+1)\right] - \frac{2D_2 D_{-2}}{\beta_e g_{iso} B_0}\left[2m_S^3 + m_S - 2m_S S(S+1)\right]$$

The second-order nuclear Zeeman term is neglected due to its small magnitude. Thus, the resonance condition (eq. 3.1.38) for the central transition up to the second-order perturbation theory takes form:

$$\hbar\omega_{\mathrm{MW}} = \mathcal{E}(+1/2, m_I, \theta, \varphi) - \mathcal{E}(-1/2, m_I, \theta, \varphi) = \beta_e g_{iso} B_0/\hbar + a_{iso} m_I +$$

$$+ \frac{a_{iso}^2}{2\beta_e g_{iso} B_0}\left[I(I+1) - m_I^2\right] - \frac{4S(S+1)-3}{\beta_e g_{iso} B_0}\left(2D_1 D_{-1} - D_2 D_{-2}\right) \tag{3.1.41}$$

As the central transition is only dependent on the ZFS in the second- and higher-order, the width of each line in the sextet is significantly narrower compared to that of the side transitions. This makes the central transition sharp and significantly more intense. The magnitude of the second-order correction *q* scales inversely proportional to the strength of the magnetic field ((eq. 3.1.40) and (eq. 3.1.41)) as given:

$$q \propto \frac{D^2}{\beta_e g_{iso} B_0} \tag{3.1.42}$$

For the side transitions this is a small correction to the width of the corresponding EPR lines compared to that given by the first-order perturbation theory, assuming that the high-field approximation is fulfilled to a large extent. Thus, the side transitions can be considered only in the first-order perturbation theory, while the central transition has to be considered up to the second or higher-order terms.

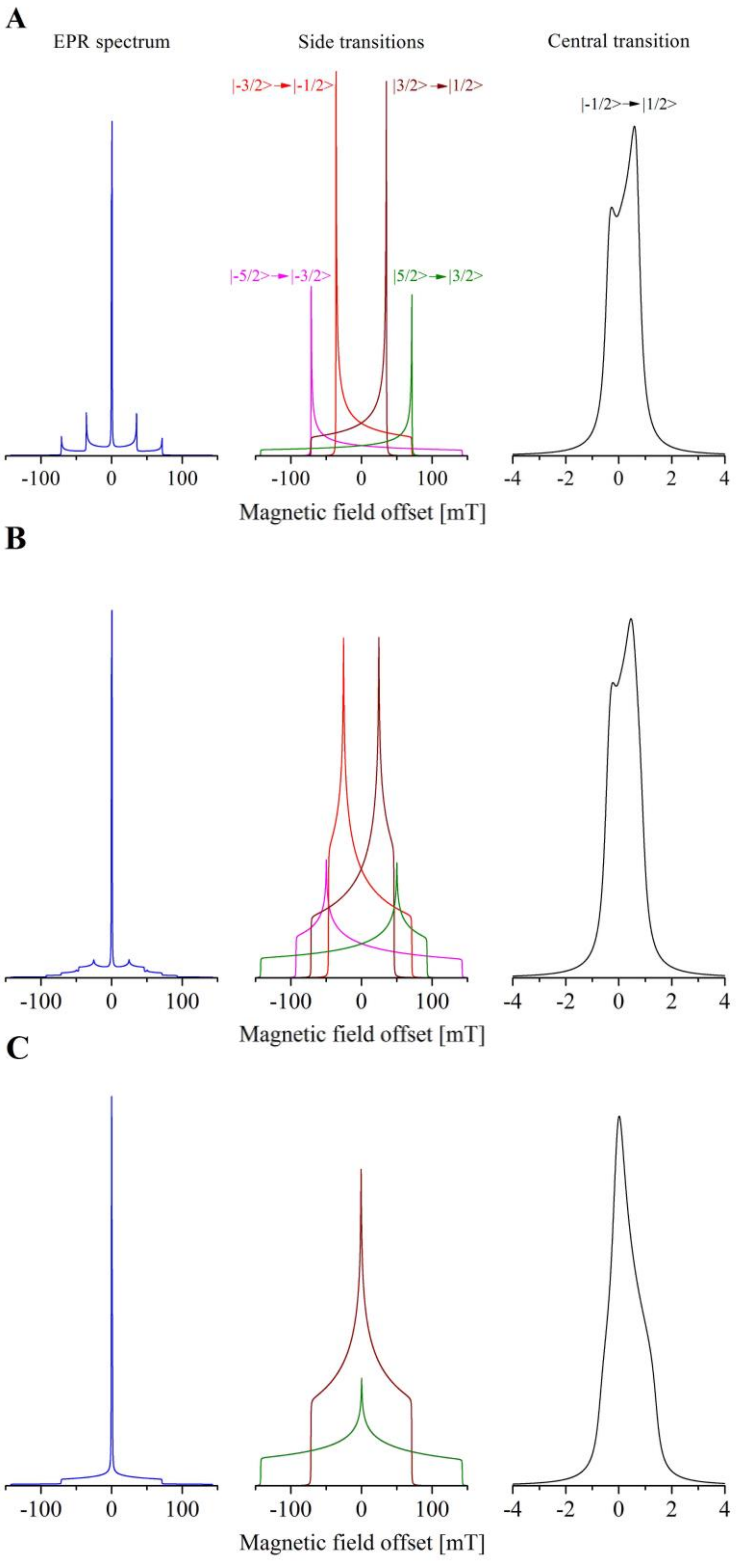

Figure 8. Simulated (full matrix diagonalization) G-band EPR spectra of a spin system with $S = 5/2$ and with ZFS parameter D equals to 1 GHz and various E parameters. A: $E = 0$, B: E =100 MHz and C: $E = D/3$ (note that here some of the side transitions coincide).The magnetic field offset is with respect to the position corresponding to g_{iso} of 2.0023. The intensities of the side transitions are significantly smaller than that of the central transition (can be rationalized from the EPR spectra) and for better visual representation were scaled. The transitions are assigned in pattern A and the color code is retained for B and C. The Lorentzian line broadening of the width of 2 G was applied for the stick spectra and the simulations are performed in high-temperature approximation.

In order to understand the EPR spectrum of the high-spin Mn^{2+} system in amorphous sample, we first assume that the hyperfine coupling equals to 0, set D parameter to 1 GHz and vary parameter E as 0, 100 MHz and $D/3$ and perform the calculations using expressions (eq. 3.1.22) for powder averaging as well as (eq. 3.1.38), (eq. 3.1.39) and (eq. 3.1.41) for assessment of the resonance field positions and transition probabilities. The G-band EPR spectrum of such systems is shown in Figure 8 (left column). As can be seen from this figure the central transition is the dominant transition in the spectrum being at least an order of magnitude more intense than the side transitions. In the middle and right columns the side and central transitions, respectively, are all depicted separately. The intensity of the side transitions were scaled for better visual representation. The top row of Figure 8 represents the axial symmetry case (D = 1 GHz and E = 0), that is encoded in the shape of the EPR lines. The lines corresponding to the side transitions, which are ZFS-dependent in the first-order, reveal the features that correspond to perpendicular (θ = 0, edge of the EPR line with lowest intensity) and parallel orientations (θ = π, edge of the EPR line with highest intensity). The shape of the line corresponding to the central transition is more complicated and less intuitive as a result of its second-order ZFS dependency. With increasing parameter E the side lines take a shape resembling that of the rhombic symmetry (compared to the shape of the nitroxide radical at G-band frequencies, where rhombicity is caused by the $\bar{\boldsymbol{g}}$-tensor anisotropy, see Figure 4) and with E equals to $D/3$ the rhombic symmetry is achieved.

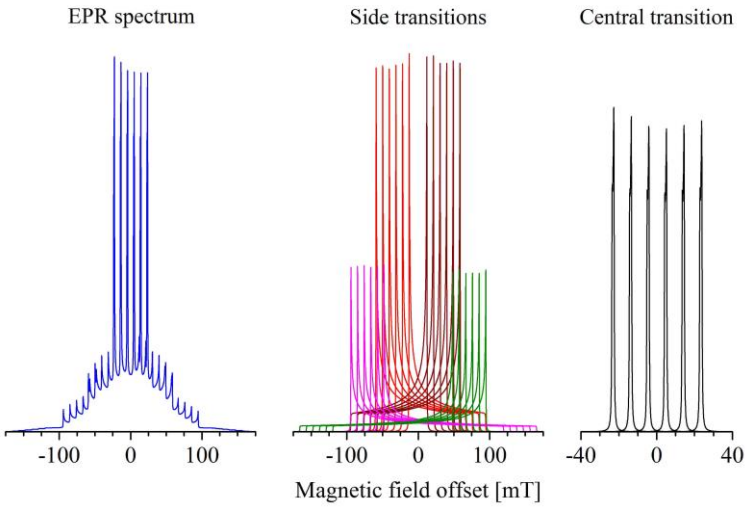

Figure 9. Simulated (full matrix diagonalization) G-band EPR spectra of a Mn^{2+} spin system. The ZFS parameters: D = 1 GHz, E = 0 and the hyperfine coupling constant a_{iso} = 260 MHz.The color code representing different transitions is consistent with Figure 8. The Lorentzian line broadening of the width of 2 G was applied for the stick spectra and the simulations are performed in high-temperature approximation.

As Mn^{2+} spin system has a naturally abundant ^{55}Mn nucleus, the hyperfine coupling has to be taken into account. As a result, each line is split into a sextet and the EPR spectrum becomes significantly more complex. For the simulations, the ZFS parameters are again set to D = 1 GHz and E equals to 0 and the hyperfine coupling of typical value of a_{iso} = 260 MHz (Figure 9).

As the next step, we consider a microwave frequency (and correspondingly resonant magnetic field) dependence of the EPR spectrum, an important consideration for the high-spin systems. The ZFS parameters are retained similar to the ones used before, but the microwave frequency is set to Q-band frequencies (Figure 10). In such case the high field approximation is fulfilled to a lesser degree than at G-band frequencies and the perturbation theory should be used with caution, especially for the central transition. Thus, insignificant changes in the side transitions are observed upon decreasing the microwave frequency (due to a first order ZFS-dependency (eq. 3.1.38)), while the changes in the central transition are significant (see Figure 10). Upon decreasing the microwave frequency the corresponding linewidth increases (eq. 3.1.41) leading to a reduction to its intensity. Additionally the features caused by the second-order effects become significantly more pronounced compared to the 2 G intrinsic Lorenzian linewidth, which was used in the simulations. In the case where ^{55}Mn-hyperfine coupling is absent, the second-order perturbation theory is a good approximation even for the central transition at the frequencies as low as Q-band.

The simulated EPR spectrum of the Mn^{2+} system with hyperfine coupling (D = 1 GHz and E = 0) is shown in Figure 11. At this low frequency the EPR spectrum is significantly more complex than that at G-band. This is not only due to the central transition being broader, but also due to the increased cross-interaction of ZFS and hyperfine coupling terms of the spin Hamiltonian. Thus, by correcting the wave-functions up to the second-order, mixing between the states $|m_S, m_I\rangle$ and $|m_S, m_I \pm 1\rangle$, and between the states $|m_S - 1, m_I \pm 1\rangle$ and $|m_S - 1, m_I\rangle$ occurs due to the cross-terms:

$$\frac{1}{\beta_e g_{iso} B_0}\left(D_{+1}\hat{S}_z\hat{S}_+\right)\left(\frac{a_{iso}}{2}\hat{S}_-\hat{I}_+\right), \quad \frac{1}{\beta_e g_{iso} B_0}\left(D_{-1}\hat{S}_z\hat{S}_-\right)\left(\frac{a_{iso}}{2}\hat{S}_+\hat{I}_-\right) \tag{3.1.43}$$

Thus, the forbidden transitions of the type $|m_S - 1, m_I\rangle \rightarrow |m_S, m_I - 1\rangle$ and $|m_S - 1, m_I - 1\rangle \rightarrow |m_S, m_I\rangle$ become partially allowed, as can be in seen in Figure 11. These transitions are mostly prominent for the central electron spin transition with $m_S = 1/2$ due to

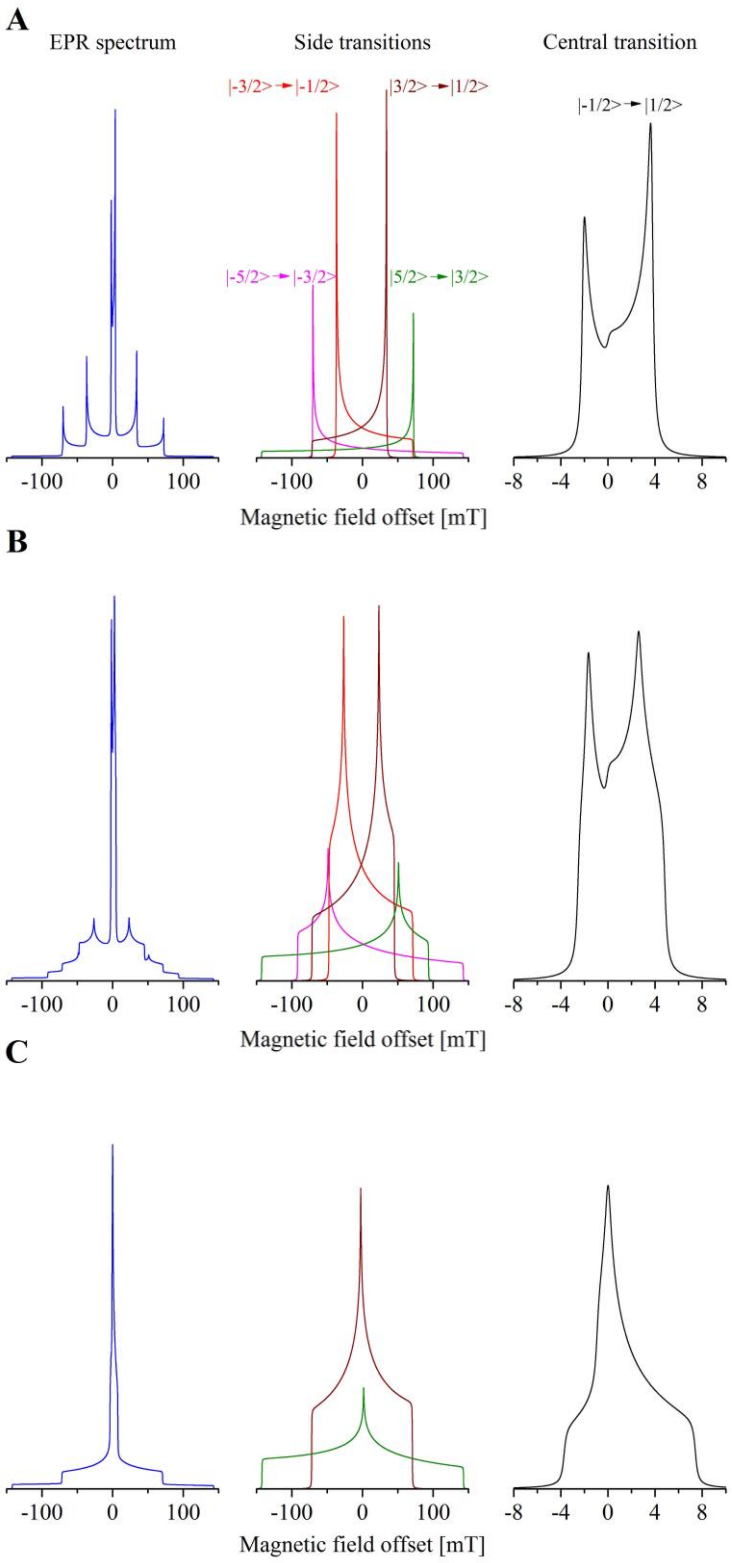

Figure 10. Simulated (full matrix diagonalization) Q-band EPR spectra of a spin system with S = 5/2 and with ZFS parameter D equals to 1 GHz and various E parameters. A: E = 0, B: E =100 MHz and C: $E = D/3$ (note that here some of the side transitions coincide). The magnetic field offset is with respect to the position corresponding to g_{iso} of 2.0023. The intensities of the side transitions are significantly smaller than that of the central transition (can be rationalized from the EPR spectra) and for better visual representation were scaled. The transitions are assigned in pattern A and the color code is retained for B and C. The Lorentzian line broadening of the width of 2 G was applied for the stick spectra and the simulations are performed in high-temperature approximation.

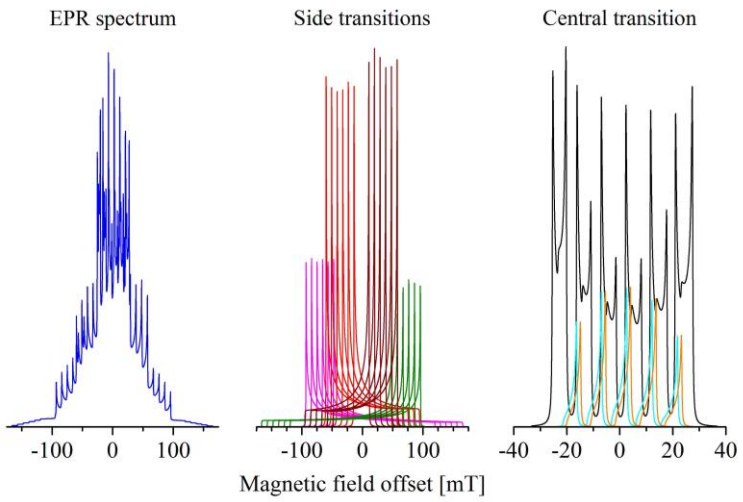

Figure 11. Simulated (full matrix diagonalization) Q-band EPR spectra of a Mn^{2+} spin system. The ZFS parameters: D = 1 GHz, E = 0 and the hyperfine coupling constant a_{iso} = 260 MHz.The color code representing different transitions is consistent with Figure 8. For the central transition, the cyan and orange lines represent the forbidden transitions of the type $|m_S - 1, m_I> \rightarrow |m_S, m_I - 1>$ and $|m_S - 1, m_I - 1> \rightarrow |m_S, m_I>$, respectively. The Lorentzian line broadening of the width of 2 G was applied for the stick spectra and the simulations are performed in high-temperature approximation.

its second-order ZFS-dependency and gain their intensity from the allowed ones ($\Delta m_I = 0$). The relative intensity of the forbidden transitions with respect to the allowed for the central transition is given as:[48,77]

$$I_{rel} = \frac{64}{\left(\beta_e g_{iso} B_0\right)^2} \sin^2 2\theta \left(D - E\cos 2\varphi\right)^2 \left[I(I+1) - m_I^2 + m_I\right] \qquad (3.1.44)$$

For G-band frequencies these transitions have negligibly small amplitude and can be safely neglected, while for Q-band frequencies they cannot be neglected anymore. The situation gets even worse upon applying lower frequencies. Also, the transitions with $\Delta m_S = 1$ and $\Delta m_I = 1$ can have relatively high intensity in such situation. For the simulation given in Figure 11 they have small amplitude and therefore neglected. Such effects are not relevant for Gd^{3+} spin system due to the absence of strong hyperfine couplings.

The last important aspect, which is discussed in this section, is that for amorphous samples, especially for frozen liquid solutions, the ZFS splitting parameters have large (up to the same magnitude as the ZFS parameters by themselves) statistical distribution.[79] This is due to the structural variations of the paramagnetic molecules in frozen solutions. As a result, the features that are typical for the powder-type spectra are smeared out and only the central transition can be distinguished in the EPR spectrum. The simulation of such EPR spectrum at G- and Q-band frequencies is presented in Figure 12.

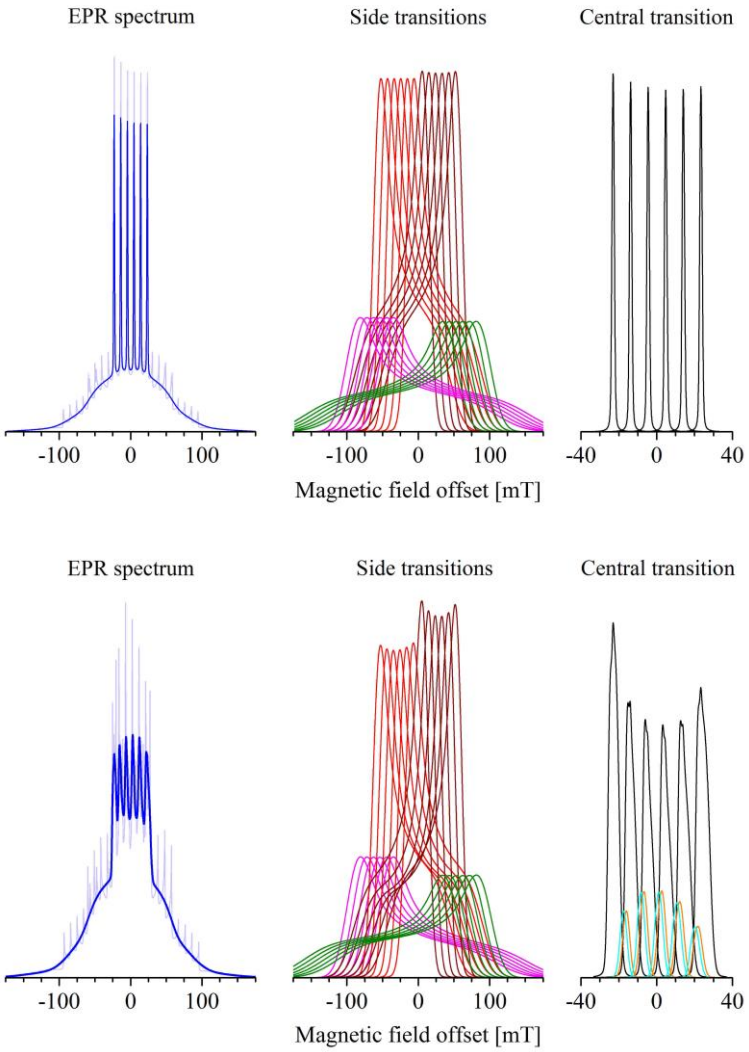

Figure 12. Effect of distribution of the ZFS parameters on the G-band (top) and Q-band (bottom) EPR spectra of a Mn^{2+} spin system. Simulations (full matrix diagonalization) performed with the ZFS parameters: D = 1 GHz with a Gaussian distribution with a width of 500 MHz, E = 0 and the hyperfine coupling constant a_{iso} = 260 MHz. The color code representing different transitions is consistent with previous figures. The light color spectra on the left column represent the spectra with fixed D value of 1 GHz. The Lorentzian line broadening of the width of 2 G as well as Gaussian line broadening of 7 G (due to unresolved hyperfine couplings) were applied for the stick spectra and the simulations are performed in high-temperature approximation.

As can be seen in Figure 12 (statistical distribution of ZFS $\Delta D = D/2$), the side transitions resemble a very broad and smooth signal with sharp and indicative lines from the central transitions superimposed on top of it. The significant broadening of the central transition can be observed upon decreasing the microwave frequency. Such shape of an EPR spectrum is a characteristic peculiarity of Mn^{2+} in biological samples.

In summary of this section, one can appreciate the complexity of the Mn^{2+} spin system, leading to an EPR spectrum that is significantly more complex than that of commonly used stable nitroxide radicals. Upon applications of Mn^{2+} spin system for studying biological samples, an important consideration should be taken into account: the microwave frequency

should be chosen in accordance with the ZFS parameters in a way that a condition $\hbar\omega_{MW} >> D$ is fulfilled to a large extent. If it is not the case, effects of spin sublevels mixing, level energies distortions and appearance of multiple forbidden EPR transitions should be considered in data analysis. This is not trivial due to large dimensionality of the spin Hamiltonian operators of Mn^{2+} and very broad statistical distribution of ZFS parameters. Furthermore, the use of high frequencies with respect to the ZFS lead to narrowing of the central transition, that leads to increased sensitivity of EPR experiments.

3.1.3 Dipolar coupled systems

After having described different spin systems, we approach the central phenomenon for the EPR-based distance measurements. When two paramagnetic centers are located near to each other, *magnetic dipole-dipole coupling* (through-space interaction) between them becomes apparent. The spin Hamiltonian for this interaction is given as:[59]

$$\hat{\mathcal{H}}_{DD} = \hat{\boldsymbol{S}}^A \cdot \overline{\boldsymbol{D}}_{dip} \cdot \hat{\boldsymbol{S}}^B \tag{3.1.45}$$

where $\overline{\boldsymbol{D}}_{dip}$ is the symmetric and traceless magnetic dipole-dipole coupling (for simplicity in the following referred as dipolar coupling) tensor, $\hat{\boldsymbol{S}}^A$ is the spin vector operator corresponding to one paramagnetic center (further referred as center *A*) and $\hat{\boldsymbol{S}}^B$ is the spin vector operator corresponding to another center of the pair (further referred as center *B*). In the point-dipole approximation and in the eigenframe of the dipolar coupling tensor, the Hamiltonian (3.1.45) simplifies to the form:

$$\begin{aligned} \hat{\mathcal{H}}'_{DD} &= D_{dip}\left(\hat{S}_z^A \hat{S}_z^B - 3 \cdot \hat{\boldsymbol{S}}^A \cdot \hat{\boldsymbol{S}}^B\right) \\ D_{dip} &= \frac{\mu_0 g_A g_B \beta_e^2}{4\pi\hbar^2 R^3} \end{aligned} \tag{3.1.46}$$

The D_{dip} is *dipolar coupling constant* represented in angular frequency units.

The dipolar coupling Hamiltonian (eq. 3.1.45) and (eq. 3.1.46) resembles the axially symmetric second-order ZFS spin Hamiltonian (eq. 3.1.23). Thus, the dipolar coupling causes shifts of the spin sublevels of the two-spin system that is identical to that caused by the axial second-order ZFS. Therefore, the dipolar coupling and this ZFS lead to similar effects in the EPR spectra. If the dipolar coupling constant can be determined from EPR experiments, the distance between two paramagnetic centers can be calculated.

The phenomenon of the dipolar coupling originates from the classical theory of magnetism and determined as an energy of interaction of two magnetic dipole moments:[80]

$$\mathcal{E} = \frac{\mu_0}{4\pi}\left(\frac{\boldsymbol{\mu}_\mathrm{A}\boldsymbol{\mu}_\mathrm{B}}{|\boldsymbol{R}|^3} - \frac{3(\boldsymbol{\mu}_\mathrm{A}\cdot\boldsymbol{R})(\boldsymbol{\mu}_\mathrm{B}\cdot\boldsymbol{R})}{|\boldsymbol{R}|^5}\right) \tag{3.1.47}$$

where $\boldsymbol{R}$ is the distance vector between the magnetic dipole moments $\boldsymbol{\mu}_\mathrm{A}$ and $\boldsymbol{\mu}_\mathrm{B}$. In the quantum mechanical formalism, the classical magnetic dipole moments are replaced by the corresponding operators $\hat{\boldsymbol{\mu}}_\mathrm{A}$ and $\hat{\boldsymbol{\mu}}_\mathrm{B}$, which have been introduced in section 3.1.1. Thus, the energy (eq. 3.1.47) takes a quantum mechanical form given by the Hamiltonian:

$$\begin{aligned}
\hat{\mathcal{H}}_{\mathcal{DD}} &= \frac{\mu_0 g_A g_B \beta_e^2}{4\pi\hbar^2 R^3}\left(\hat{\boldsymbol{S}}^A\hat{\boldsymbol{S}}^B - \frac{3\left(\hat{\boldsymbol{S}}^A\cdot\boldsymbol{R}\right)\left(\hat{\boldsymbol{S}}^B\cdot\boldsymbol{R}\right)}{R^2}\right) = \\
&= D_{dip}\Bigg(\hat{S}_z^A\hat{S}_z^B + \frac{1}{2}\left(\hat{S}_+^A\hat{S}_-^B + \hat{S}_-^A\hat{S}_+^B\right) - 3\Big(\sin^2\theta\cos^2\varphi\ \hat{S}_x^A\hat{S}_x^B + \sin^2\theta\sin^2\varphi\ \hat{S}_y^A\hat{S}_y^B + \\
&\quad + \cos^2\theta\ \hat{S}_z^A\hat{S}_z^B + \sin^2\theta\cos\varphi\sin\varphi\left(\hat{S}_x^A\hat{S}_y^B + \hat{S}_y^A\hat{S}_x^B\right) + \\
&\quad + \sin\theta\cos\theta\sin\varphi\left(\hat{S}_x^A\hat{S}_z^B + \hat{S}_z^A\hat{S}_x^B\right) + \\
&\quad + \sin\theta\cos\theta\cos\varphi\left(\hat{S}_y^A\hat{S}_z^B + \hat{S}_z^A\hat{S}_y^B\right)\Big)\Bigg) = \\
&= D_{dip}\left(\hat{A} + \hat{B} + \hat{C} + \hat{D} + \hat{E} + \hat{F}\right)
\end{aligned} \tag{3.1.48}$$

where "dipolar alphabet" operators are defined as:[80]

$$\begin{aligned}
\hat{A} &= \hat{S}_z^A\hat{S}_z^B\left(1 - 3\cos^2\theta\right) \\
\hat{B} &= -\frac{1}{4}\left(\hat{S}_+^A\hat{S}_-^B + \hat{S}_-^B\hat{S}_+^A\right)\left(1 - 3\cos^2\theta\right) \\
\hat{C} &= -\frac{3}{2}\left(\hat{S}_+^A\hat{S}_z^B + \hat{S}_z^B\hat{S}_+^A\right)\sin\theta\cos\theta\ e^{-i\varphi} \\
\hat{D} &= -\frac{3}{2}\left(\hat{S}_-^A\hat{S}_z^B + \hat{S}_z^B\hat{S}_-^A\right)\sin\theta\cos\theta\ e^{-i\varphi} \\
\hat{E} &= -\frac{3}{4}\hat{S}_+^A\hat{S}_+^B\sin^2\theta\ e^{-i2\varphi} \\
\hat{F} &= -\frac{3}{4}\hat{S}_-^A\hat{S}_-^B\sin^2\theta\ e^{i2\varphi}
\end{aligned} \tag{3.1.49}$$

For electron-nuclear hyperfine dipolar coupling (section 3.1.1) one of the electron magnetic dipole moments should be replaced by the nuclear magnetic dipole moment.

Upon application of the external magnetic field $\boldsymbol{B}_0$, a dipolar-coupled system interacts with it. The term $\hat{A}$ commutes with the Zeeman terms of both spins $\hat{\mathcal{H}}_{\mathcal{EZI}}^A = \beta_e g^A B_0 \hat{S}_z^A/\hbar$

and $\hat{\mathcal{H}}^B_{\text{EZI}} = \beta_e g^B B_0 \hat{S}^B_z / \hbar$. This term is called *secular term of* the dipolar coupling Hamiltonian and is crucial for distance measurements.

The term $\hat{B}$ commutes only with the summed Zeeman term when the Zeeman energies of both spins are equal $\hat{\mathcal{H}} = \beta_e g B_0 \left(\hat{S}^A_z + \hat{S}^B_z\right) / \hbar$. This term is called *pseudo-secular term* (*also called flip-flop term*) of the dipolar coupling Hamiltonian. In general case this term causes the mixing of the *adjacent spin sublevels* (the two levels for which the sum of the magnetic quantum numbers of the individual spins $M_S = m^A_S + m^B_S$ is the same). The influence of this term on the dipolar coupled system is unwanted, since it significantly complicates the analysis of EPR-based distance measurements. This term can be neglected only when both following conditions are fulfilled:

(1) High-field approximation for the dipolar coupling (D_{dip} being significantly smaller than the individual electron Zeeman energies of both electron spins).

(2) Weak coupling regime (difference between the resonance energies of the spins being significantly larger than D_{dip}).

It worth noting, that fulfillment of the second condition for a dipolar-coupled high-spin system is less trivial compared to a spin 1/2 system. This is due to the increased impact of the $\hat{S}^{A,B}_{\pm}$ operators for high-spin systems and isotropy of the $\bar{\boldsymbol{g}}$-tensor. The latter leads to the difference in the Zeeman energies of the coupled spins to be zero.[a] For more details of the pseudo-secular term influence on the performance of Gd-based distance measurements, the reader is referred to other studies.[81–83]

The terms $\hat{C}$ till $\hat{F}$ does not commute with the Zeeman term(s) and called *non-secular terms* of the dipolar coupling Hamiltonian. They cause mixing of the spin sublevels with ΔM_S equals ±1 ($\hat{C}$ and $\hat{D}$) and ±2 ($\hat{E}$ and $\hat{F}$). The influence of this term to the dipolar-coupled system can be neglected when condition (1) is fulfilled, that is usually the case in distance measurements.

Further theoretical treatment is performed for the dipolar-coupled spin 1/2 system when both conditions are fulfilled (only the secular term of the dipolar coupling Hamiltonian is relevant and the first-order perturbation theory is an adequate approximation). The spin Hamiltonian $\hat{\mathcal{H}}$ of such system is given by (eq. 3.1.50).

[a] For Mn^{2+} ions large hyperfine coupling contributes to the difference between the Zeeman energies that reduces the influence of the pseudo-secular term.

$$\hat{\mathcal{H}} = \hat{\mathcal{H}}^A_{EZ} + \hat{\mathcal{H}}^B_{EZ} + \hat{\mathcal{H}}_{DD} = \beta_e g_A B_0 \hat{S}^A_z + \beta_e g_B B_0 \hat{S}^B_z + \\ + a_A \hat{S}^A_z \hat{I}^A_z + a_B \hat{S}^B_z \hat{I}^B_z + \omega_{dd} \hat{S}^A_z \hat{S}^B_z \tag{3.1.50}$$

where $\omega_{dd} = D_{dip}\left(1 - 3\cos^2\theta\right)$ is the dipolar coupling frequency in the laboratory frame; θ defines the angle between the vectors $\boldsymbol{R}$ and $\boldsymbol{B_0}$; g_A and g_B are the effective values of the $\bar{\boldsymbol{g}}$-tensor corresponding to the spins *A* and *B*; a_A and a_B are the respective effective values of the $\bar{A}$-tensor. For simplicity only the diagonal term of the hyperfine coupling Hamiltonian is retained and the nuclear Zeeman terms are neglected in the Hamiltonian (eq. 3.1.50). The eigenvalues of the Hamiltonian, determined by the first-order perturbation theory, are given as:

$$\mathcal{E}\left(m_S^A, m_S^B, m_I^A, m_I^B, \theta\right) = \beta_e g_A B_0 m_S^A + \beta_e g_B B_0 m_S^B + a_A m_S^A m_I^A + a_B m_S^B m_I^B + \omega_{dd} m_S^A m_S^B \tag{3.1.51}$$

The corresponding resonance conditions are defined:

$$\hbar\omega_{MW} = \mathcal{E}\left(m_S^A, m_S^B, m_I, \theta\right) - \mathcal{E}\left(m_S^A - 1, m_S^B, m_I, \theta\right) = \beta_e g_A B_0 / \hbar + a_A m_I + \omega_{dd} m_S^B$$

and (3.1.52)

$$\hbar\omega_{MW} = \mathcal{E}\left(m_S^A, m_S^B, m_I, \theta\right) - \mathcal{E}\left(m_S^A, m_S^B - 1, m_I, \theta\right) = \beta_e g_B B_0 / \hbar + a_B m_I + \omega_{dd} m_S^A$$

In order to visualize the shifts of the spin sublevels and the dipolar spectra, the hyperfine coupling is neglected, as it splits the spin sublevels and correspondingly the EPR lines in the manner as was descried in detail in previous sections. The corresponding spin sublevel diagram and schematic EPR spectrum of the dipolar coupled spin 1/2 system in single-crystal sample (fixed θ angle) is given in Figure 13. Thus, the EPR lines corresponding to the spins *A* and *B* are split by ω_{dd}.

For amorphous sample, all θ orientations are present and, therefore, powder-averaging similar as given by (eq. 3.1.22) should be performed:

$$F(B) = \sum_{j=A,B} \int_0^{\pi} G\left[B_0\left(m_S^j, \theta\right), B\right] \sin\theta d\theta \tag{3.1.53}$$

where in general case $B_0\left(m_S^j, \theta\right)$ are the resonance fields, as defined in (eq. 3.1.52); g_A, g_B and a_A, a_B are the orientation-dependent effective values of $\bar{\boldsymbol{g}}$- and $\bar{A}$-tensors, respectively. For simplicity the hyperfine couplings are assumed to be zero and $\bar{\boldsymbol{g}}$-tensors of both spin species to be isotropic and the lineshape function is given as a Dirac delta function:

$$G\left(B_0\left(m_S^j, \theta\right), B\right) = \delta\left(B - B_0\left(m_S^j, \theta\right)\right) \tag{3.1.54}$$

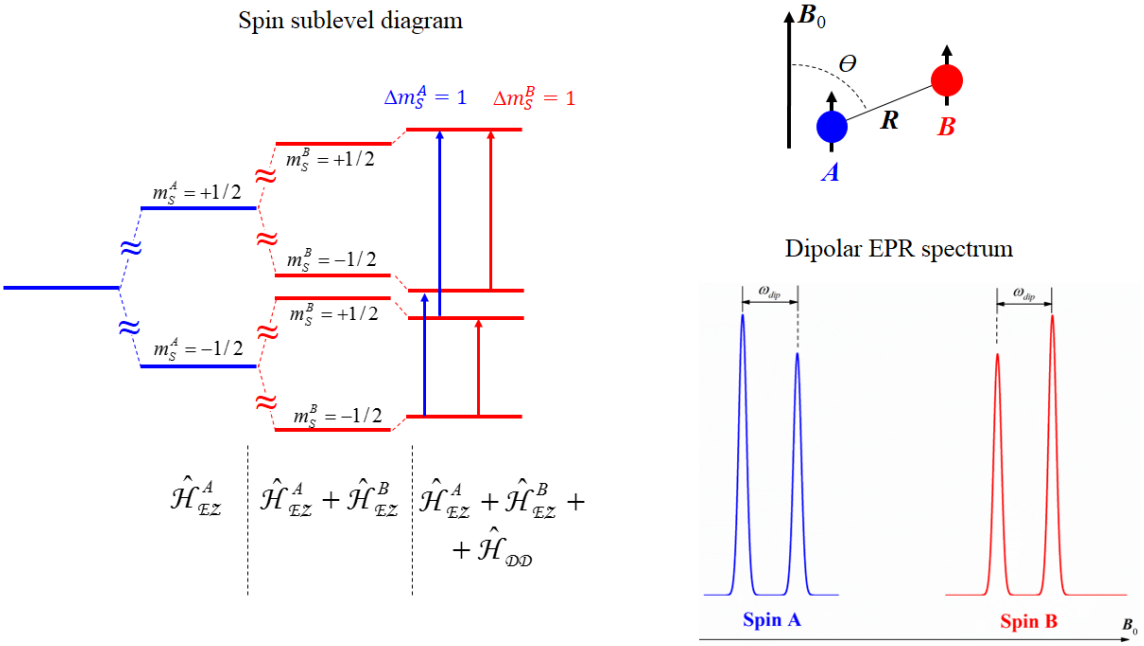

Figure 13. The spin sublevel diagram (left) and dipolar EPR absorption spectrum (right bottom) of the weakly dipolar coupled spin 1/2 system (right top) in single-crystal sample. For simplicity hyperfine coupling is assumed to 0.

The resulting dipolar EPR spectrum consists of the two *Pake doublets* (Figure 14).[84] Two kind of features can be distinguished in the Pake doublets: perpendicular, $\theta = \pi/2$, (highest intensity peaks) and parallel, $\theta = 0$, (lowest intensity features) orientations, which resonance positions are split by D_{dip} and $2D_{dip}$, respectively (see Figure 14).

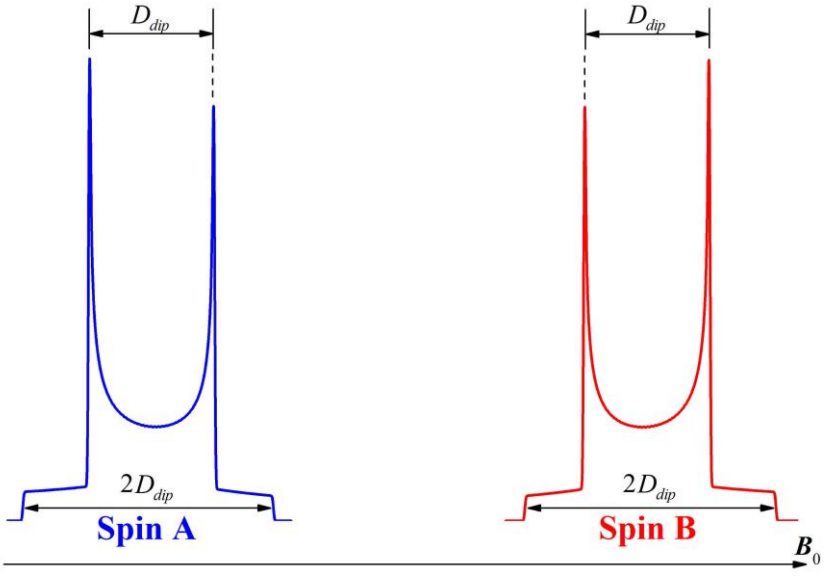

Figure 14. The dipolar EPR absorption spectrum (right bottom) of the weakly dipolar coupled spin 1/2 system (right top) in amorphous sample. For simplicity hyperfine coupling is assumed to 0.

It is worth noting that if the spin centers are too close to each other (R < 1.5 nm) such that there is a significant overlap of the spin-density functions of both spins, the exchange

interaction appears.[85] The spin Hamiltonian corresponding to the exchange interaction in general case is given as:

$$\hat{\mathcal{H}}_{exchange} = \hat{\boldsymbol{S}}^{A} \cdot \bar{\boldsymbol{J}} \cdot \hat{\boldsymbol{S}}^{B} \tag{3.1.55}$$

where $\bar{\boldsymbol{J}}$ is an exchange interaction tensor, which, in contrast to the dipolar coupling tensor, is not traceless. For the most cases $\bar{\boldsymbol{J}}$ is an isotropic tensor. Thus, in the high-field approximation and in week coupling regime the Hamiltonian (eq. 3.1.55) is diagonal:

$$\hat{\mathcal{H}}_{exchange} = J \cdot \hat{S}_z^A \hat{S}_z^B \tag{3.1.56}$$

Thus, the parallel and perpendicular features of the Pake doublets are split by:[67]

$$\begin{aligned} \omega_{dd}\left(D_{dip}, J, \theta = 90^\circ\right) &= \left|D_{dip} + J\right| \\ \omega_{dd}\left(D_{dip}, J, \theta = 0^\circ\right) &= \left|-2D_{dip} + J\right| \end{aligned} \tag{3.1.57}$$

In summary of this section, the dipolar coupling constants are typically very small (*e.g.* 0.8 MHz for R = 4 nm), such that they cannot be resolved in EPR spectra due to inhomogeneous line broadening. In such cases pulsed EPR experiments, which are capable to refocus inhomogeneous broadenings, have to be used.

3.2 Introduction to pulsed EPR

In pulsed EPR spectroscopy very short microwave pulses of the order of 10 ns are used to manipulate the macroscopic magnetization of a spin ensemble. Theoretically, in order to follow the time evolution of a spin system during or after the pulses, the Liouville von Neumann equation has to be solved:[67,86]

$$\frac{d\sigma(t)}{dt} = -i\left[\hat{\mathcal{H}}, \sigma(t)\right] \tag{3.2.1}$$

where, $\sigma(t)$ is the *density matrix operator* and $\hat{\mathcal{H}}$ is the full Hamiltonian of the system (Hamiltonian given in (eq. 3.1.1) with addition of the microwave Hamiltonian (eq. 3.1.13) during the acting of microwave pulses). The full spin Hamiltonian is usually represented in a rotating frame. Thus, the solution of Liouville von Neumann equation (eq. 3.2.1) is given as:

$$\sigma(t) = \exp\left(-i\hat{\mathcal{H}}t\right) \cdot \sigma(0) \cdot \exp\left(i\hat{\mathcal{H}}t\right) \tag{3.2.2}$$

where an exponential operator:

$$U(t) = \exp\left(-i\hat{\mathcal{H}}t\right) \tag{3.2.3}$$

is called *a propagator*, a *unitary operator* that propagates the density operator in time. Pulsed EPR experiments can be subdivided in the time intervals τ_j, during which the spin system is

characterized by the corresponding Hamiltonian, and for each τ_j the evolution of the spin system can be described by solution of the Liouville von Neumann equation (eq. 3.2.2). Hence, the whole time evolution of the spin system can be expressed by a sequence of unitary transformations of the type:

$$\sigma_{\mathrm{det}} = \sigma(\tau_1 + \tau_2 + ... + \tau_n) = U(\tau_n)...U(\tau_2)U(\tau_1)\cdot\sigma(0)\cdot U'(\tau_1)U'(\tau_2)...U'(\tau_n) \tag{3.2.4}$$

The observed signal is then proportional to the trace of a product of the matrix of the density operator σ_{det} and the detection operators $\hat{S}_x$ or $\hat{S}_y$:

$$M_x(\tau_{\mathrm{det}}) \propto g\beta\cdot Tr\left\{\hat{S}_x\sigma_{\mathrm{det}}\right\}, \quad M_y(\tau_{\mathrm{det}}) \propto g\beta\cdot Tr\left\{\hat{S}_y\sigma_{\mathrm{det}}\right\} \tag{3.2.5}$$

This approach is called *density matrix formalism*.[67] When the density matrix is expressed in terms of explicit matrices, the unitary transformation operates the matrices with dimension of $2^N \times 2^N$ for N elementary spin of 1/2. In the eigenbasis of the unperturbed Hamiltonian, the elements of the density matrix have a defined physical meaning. Thus, the diagonal elements σ_{jj} represent the population of the j spin sublevel, whereas off-diagonal elements σ_{ij} represent coherences belonging to the transition $i \rightarrow j$. As the propagator $\exp\left(-i\hat{\mathcal{H}}_{EZ}\tau\right)$ is represented by a diagonal matrix, free precession of electron or nuclear spins can be readily described in $\hat{\mathcal{H}}_{EZ}$ eigenbasis, while the matrix elements of the pulse operators can cause complicated mixing of the density matrix elements. Therefore, explicit matrix representation of the time evolutions (eq. 3.2.2) – (eq. 3.2.4) of the coupled spin systems can be cumbersome in pulsed EPR experiments and for performing the evaluations, the density operator σ is often decomposed as a linear combination of the basis operators B_S:

$$\sigma(t) = \sum_S b_S B_S \tag{3.2.6}$$

There exist several different basis-sets. The spin operators $\left\{\hat{S}_x, \hat{S}_y, \hat{S}_z\right\}$ as well as spherical tensor operators $T_{l,m}(\boldsymbol{S})$, introduced in sections 3.1.1 and 3.1.2, respectively, can be chosen. But to provide physical insights and computational convenience, it is beneficial to use the *product operators* for linear decomposition of the density matrix (eq. 3.2.6), defined as:[86]

$$B_S = 2^{q-1}\prod_{k=1}^{N}\left(S_\nu^k\right)^{a_{sk}} \tag{3.2.7}$$

where N is the total number of S = 1/2 spins in the system, k index corresponding to the spins (for consistency with section 3.1.3 the indexing is performed by signs A and B for a dipolar coupled system). ν = x, y or z, q is a number of single-spin operators in the product, a_{sk} = 1 for

q spins and a_{sk} = 0 for rest $N - q$ spins. The orthogonal normalization of the product operators for spin 1/2 is given as:

$$Tr\{B_i, B_j\} = \delta_{i,j} 2^{N-2} \tag{3.2.8}$$

The complete basis set $\{B_S\}$ for a system with N spin 1/2 consists of 4^N product operators B_S. As an example, for $q = 0$, the product operator is unity operator $\left\{\frac{1}{2}\hat{\mathbf{1}}\right\}$. For one-spin systems $q = 0, 1$ and the complete product operator basis set is $\left\{\frac{1}{2}\hat{\mathbf{1}}, \hat{S}_x^A, \hat{S}_y^A, \hat{S}_z^A\right\}$ and $\left\{\frac{1}{2}\hat{\mathbf{1}}, \hat{S}_x^B, \hat{S}_y^B, \hat{S}_z^B\right\}$ for spins A and B, respectively. For a dipolar-coupled two spin system the complete basis-set (eq. 3.2.7) can formally be presented as a product:

$$\{B_1, B_2, \ldots, B_{16}\} = \left\{\frac{1}{2}\hat{\mathbf{1}}, \hat{S}_x^A, \hat{S}_y^A, \hat{S}_z^A\right\} \otimes \left\{\frac{1}{2}\hat{\mathbf{1}}, \hat{S}_x^B, \hat{S}_y^B, \hat{S}_z^B\right\} \tag{3.2.9}$$

and after the normalization the basis-set (eq. 3.2.8) takes form:

$$\begin{aligned}\{B_1, B_2, \ldots, B_{16}\} = \Big\{&\frac{1}{2}\hat{\mathbf{1}}, \hat{S}_x^A, \hat{S}_y^A, \hat{S}_z^A, \hat{S}_x^B, \hat{S}_y^B, \hat{S}_z^B, 2\hat{S}_x^A\hat{S}_x^B, 2\hat{S}_x^A\hat{S}_y^B, 2\hat{S}_x^A\hat{S}_z^B, 2\hat{S}_y^A\hat{S}_x^B, \\ &2\hat{S}_y^A\hat{S}_y^B, 2\hat{S}_y^A\hat{S}_z^B, 2\hat{S}_z^A\hat{S}_x^B, 2\hat{S}_z^A\hat{S}_y^B, 2\hat{S}_z^A\hat{S}_z^B \Big\}\end{aligned} \tag{3.2.10}$$

Any arbitrary density operator can be expressed as a linear combination of such set of the basis operators. Although the variety of the terms in the basis-set (eq. 3.2.10) seems to be complicated, this choice greatly simplifies calculations of pulsed EPR experiments of weakly dipolar and/or hyperfine coupled systems, because a density of the individual operator terms can be followed throughout the experiment and can be associated with a clear physical meaning. This is especially useful for description of such complicated EPR experiments, like DQC and SIFTER (given in sections 3.3.2 and 3.3.3, respectively).

Thus, the *one-spin product operators* $\hat{S}_z^A$ and $\hat{S}_z^B$ have a physical meaning of the electron spin polarization of spins A and B (longitudinal magnetization) $\hat{S}_x^A$, $\hat{S}_x^B$, $\hat{S}_y^A$ and $\hat{S}_y^B$ are allowed single quantum electron coherences (in-phase x and y - magnetizations of spins A and B). The *two-spin product operators* $2\hat{S}_x^A\hat{S}_z^B$, $2\hat{S}_y^A\hat{S}_z^B$ have a physical meaning of the electron spin coherence in anti-phase (antiphase x and y - magnetization of spin A, or more specifically x- and y - magnetization of spin A antiphase with respect to spin B); the product operators $2\hat{S}_x^A\hat{S}_x^B$, $2\hat{S}_y^A\hat{S}_y^B$, $2\hat{S}_x^A\hat{S}_y^B$ and $2\hat{S}_y^A\hat{S}_x^B$ are two-spin coherences of spins A and B and

$2\hat{S}_z^A\hat{S}_z^B$ is longitudinal two-spin order of spins *A* and *B*. Antiphase magnetization represents the doublets with individual components that have opposite phases. For example, $2\hat{S}_x^A\hat{S}_z^B$ corresponds to *A*-spin doublet with magnetization components along the $+x$ and $-x$ axis of the rotating frame, depending on the spin state $\left|m_S^B\right\rangle$ of the "passive" spin *B*. The antiphase doublets have zero integrated intensity. Two-spin coherence represents a superposition of zero and double quantum coherence and is discussed in section 3.3.2, in which DQC EPR experiment is described.

Evolution of the product operator B_i under the influence of another product operator B_j, leading to linear combination of product operators (referred as *C*), is given as:

$$e^{-i\varphi B_j}B_i e^{i\varphi B_j} = C \tag{3.2.11}$$

in which φB_j takes form of $(\Delta\omega_j\tau)S_z^j$ for evolution under Zeeman term in the rotating frame, where $\Delta\omega_j = \omega_{larmor}^j - \omega_{MW}$ is the Larmor frequency of a *j*-spin in the rotating frame; $(\pi\omega_{dd}\tau)2S_z^jS_z^k$ for evolution under weak dipolar coupling and $(\omega_1\tau)S_x^j$ for evolution under the acting of a pulse with a *flip angle* of $\omega_1\tau$ and applied along *x*-axis.

The operator evolution given by (eq. 3.2.11) can be simplified to the form:

$$e^{-i\varphi B_j}B_i e^{i\varphi B_j} \equiv B_i \xrightarrow{\varphi B_j} = B_i\cos\varphi - i\left[B_j, B_i\right]\sin\varphi \tag{3.2.12}$$

For one-spin product operators standard commutation relationship exists:

$$\left[\ \hat{S}_\alpha, \hat{S}_\beta\ \right] = i\hat{S}_\gamma \tag{3.2.13}$$

where (α,β,γ) is a cyclic permutation of (x,y,z). Commutators between one-spin and two-spin or two-spin and two-spin product operators are given.

With use of operator evolution (eq. 3.2.12) and commutation relationship (eq. 3.2.13) we will consider the influence of a microwave pulse with a given flip angle to a single spin system in equilibrium (magnetization has only longitudinal component). Thus, a microwave pulse with a flip angle of $\pi/2$ ($\pi/2$-pulse) with a phase *x* acts to a spin system in equilibrium as:

$$\sigma_0 = -\hat{S}_z \xrightarrow{\pi/2\ \ \hat{S}_x} \hat{S}_y \tag{3.2.14}$$

And a π pulse inverts the phase of a product operator:

$$\hat{S}_y \xrightarrow{\pi\ \ \hat{S}_x} -\hat{S}_y \tag{3.2.15}$$

This example brought us to an elementary experiment in pulsed EPR, Hahn echo[87] (Figure 15), which consists of two microwave pulses with the flip angles of $\pi/2$ and π. The equilibrium

macroscopic magnetization is flipped by the $\pi/2$ pulse to the transversal plane (eq. 3.2.14). In the transversal plane the spin sub-ensembles start to precess with the individual frequencies $\Delta\omega_j$ that leads to defocussing of the macroscopic transversal magnetization. The frequencies have a Gaussian distribution due to inhomogeneous line broadening. Thus, after the time of d_1 each of the spin sub-ensemble gains the phase of $\varphi_j = \Delta\omega_j d_1$ in the transversal plane. The macroscopic magnetization can be consequently refocused by application of the π pulse (eq. 3.2.15), after which the phases of the given sub-ensemble are expressed as $\varphi_j(\pi) = \Delta\omega_j d_1 + \pi$. After the time d_1 each of the spin sub-ensemble is refocused (eq. 3.2.15), leading to the signal in the form of the Hahn echo (Figure 15). Note, that no influence of the transversal relaxation is assumed, which is equivalent to $d_1 << T_2$.

3.3 EPR techniques for distance determinations

3.3.1 PELDOR/DEER

Pulsed electron-electron double resonance (PELDOR[20] or also called DEER[88,89]) is the most frequently used dipolar EPR technique for structural biology studies. The roots of this method originates from 1960, where pulsed double resonance technique has been applied for detection of the weak interaction between nuclear spins in solids.[90] For detection of the weak interactions between electron spins, which required significant technical advances, the analogues method has been firstly applied in 1981.[20] This pulsed EPR experiment comprised of the Hahn echo sequence complimented with an additional pulse applied at a different frequency. The 3-pulse sequence has a major disadvantage of having non-zero dead time, during which important experimental information is lost. The 3-pulse sequence has been extended to the 4 pulse sequence in 1998,[89] that overcomes an issue of non-zero dead time. Up to date this pulse sequence has been most commonly used for EPR-based distance measurements (the pulse sequence is given in Figure 15).

For the 4-pulse PELDOR experiment, two different microwave frequencies are required: probe and pump frequencies. In the probe sequence, in which the frequency of the pulses are resonant with spin *A*, first, a Hahn echo sequence is applied (Hahn echo is an initial point of the time evolution of the dipolar coupling). After the time interval, which is called *dipolar evolution window* (d_2 in Figure 15), the second π pulse is applied. It refocuses the Hahn echo at the time $2d_2$ after the primary Hahn echo. During evolution of the spin system during the time interval d_2 additional π pulse is applied at another microwave frequency (resonant with spin *B*). It inverts the spin *B* in the pair but, ideally, does not affect the detected spin *A*. The

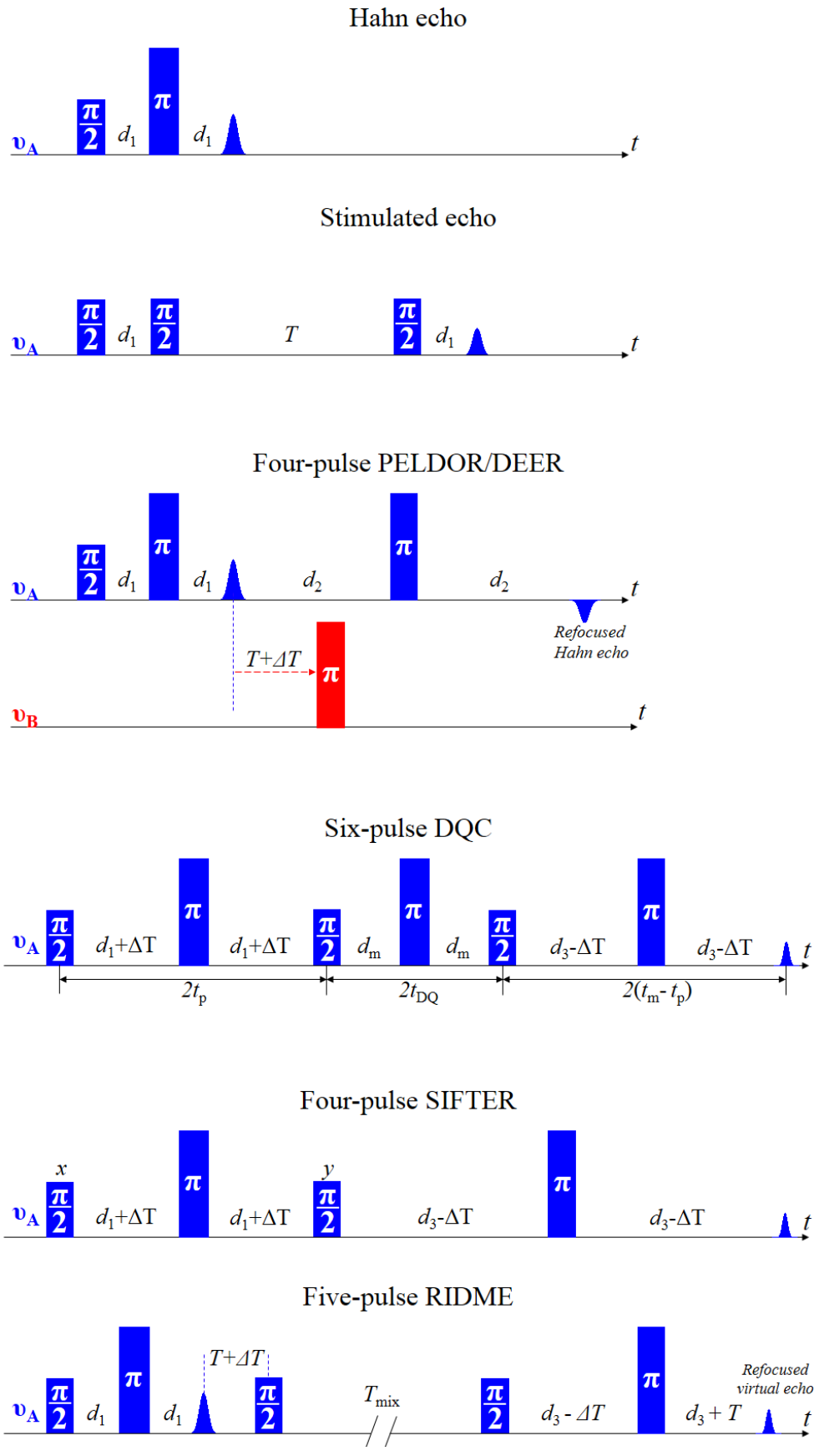

Figure 15. Hahn and stimulated echoes and dipolar spectroscopy pulse sequences.

dipolar coupled spin system is characterized by the Hamiltonian (eq. 3.1.50). However, for the spin *A* we keep only the terms that are relevant for the detection of PELDOR signal. Thus, in the rotating frame this spin Hamiltonian is given as:

$$\hat{\mathcal{H}}_{PELDOR} = \Delta\omega_A \cdot \hat{S}_z^A + \omega_{dd}\hat{S}_z^A\hat{S}_z^B = \left(\Delta\omega_A + \omega_{dd}\hat{S}_z^B\right)\hat{S}_z^A \tag{3.3.1}$$

Note, that week coupling approximation is assumed to be fulfilled and exchange interaction is neglected. Application of the π pump pulse on the spin *B* changes the resonance frequency of the spin *A* by $\pm\omega_{dd}$, depending on the initial state of the spin *B*. As the populations of the states of the spin *B* are almost identical in high temperature approximation, the number of spins *A* for which the resonance frequency changed by $\pm\omega_{dd}$ is almost the same to that changed by $-\omega_{dd}$. Thus, the sub-ensembles of the spins gain the phases either of $\varphi_j^A = \Delta\omega_j^A T + \omega_{dd}T$ or $\varphi_{j'}^A = \Delta\omega_j^A T - \omega_{dd}T$, where time *T* is counted from the position of the primary Hahn echo (Figure 15). At the time d_2 after the second detection π pulse, the inhomogeneous line broadening is completely refocused, but the additional phases of $\pm\omega_{dd}T$ lead to imperfect refocussing of the Hahn-echo signal:

$$S(T) = S_0 \cdot \frac{1}{2}\left(e^{i\omega_{dd}T} + e^{-i\omega_{dd}T}\right) = S_0\cos\left(\omega_{dd}T\right) \tag{3.3.2}$$

Thus, by changing the position of the pump pulse, the amplitude of the probe spins *A* refocused echo signal oscillates with the dipolar coupling frequency. The distance between two spins can be determined from the oscillation frequency.

In amorphous samples, averaging of the dipolar coupling frequency should be performed, as introduced in section 3.1.3. Thus, the PELDOR signal (eq. 3.3.2) takes form:

$$\begin{aligned} S(T) &= S_0\int_0^{\pi/2}\cos\left(\omega_{dd}T\right)\sin\theta d\theta = S_0\int_0^{\pi/2}\cos\left[D_{dip}\left(3\cos^2\theta - 1\right)T\right]\sin\theta d\theta = \\ &= S_0\int_0^1\cos\left[D_{dip}\left(3x^2 - 1\right)T\right]dx \end{aligned} \tag{3.3.3}$$

PELDOR signals (eq. 3.3.3), being a function of the inter-spin distance, are given in Figure 16. The real part of a Fourier transform (in the following the term real part is omitted for the sake of simplicity) of the signal give then the dipolar spectrum, which has a shape of a Pake doublet (section 3.1.3). It is worth noting, that due to invariance of the real part of the Fourier transform with respect to changing the sign of dipolar coupling frequency, the width of the corresponding Pake pattern is twice broader than of that obtained directly from CW EPR experiments (Figure 14).

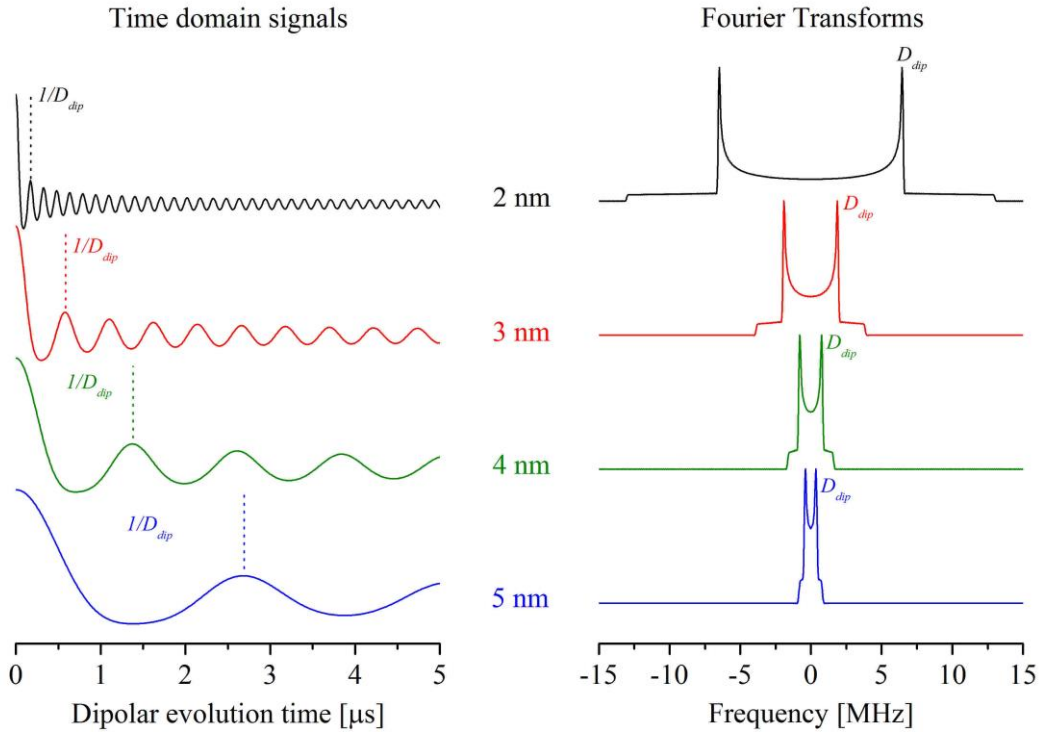

Figure 16. Calculated PELDOR signals as a function of interspin distance (left) and corresponding normalized Fourier transforms (right). Fixed interspin distance is assumed.

For the PELDOR signal described in (eq. 3.3.3) and the signals shown in Figure 16 it is assumed that inter-spin distance has a fixed value. However, due to conformational flexibility of molecules, distances are distributed rather than have fixed values. Thus, additional averaging over the distances has to be performed to describe PELDOR signals correctly:

$$S_{norm}(T) = \int_{R\min}^{R\max 1}\int_{0}^{1}\cos\left[\frac{52.04}{R^3}\left(3x^2-1\right)T\right]P(R)dxdR = \int_{R\min}^{R\max}K(T,R)P(R)dR = \tag{3.3.4}$$

$$= \boldsymbol{K(T,R)\cdot P(R)}$$

As can be seen the PELDOR signal is described by a *Fredholm integral equation of the first kind*, where *P(R)* is the *distance probability density* (for simplicity in the following referred as *distance distribution*) and *K(T,R)* is the *integral kernel function*. The PELDOR signals and the Fourier transforms, corresponding to Gaussian distance distributions with a fixed most probable distance of 4 nm and variable widths, are shown in Figure 17. Thus, with increased width of distance distribution the dipolar oscillation dampens quicker, the characteristic features of the Pake patterns are less defined and at some point it is not possible to obtain reliable most probable distance directly from the PELDOR signals. In such cases Tikhonov regularization analysis has to be performed (see section 3.3.5).

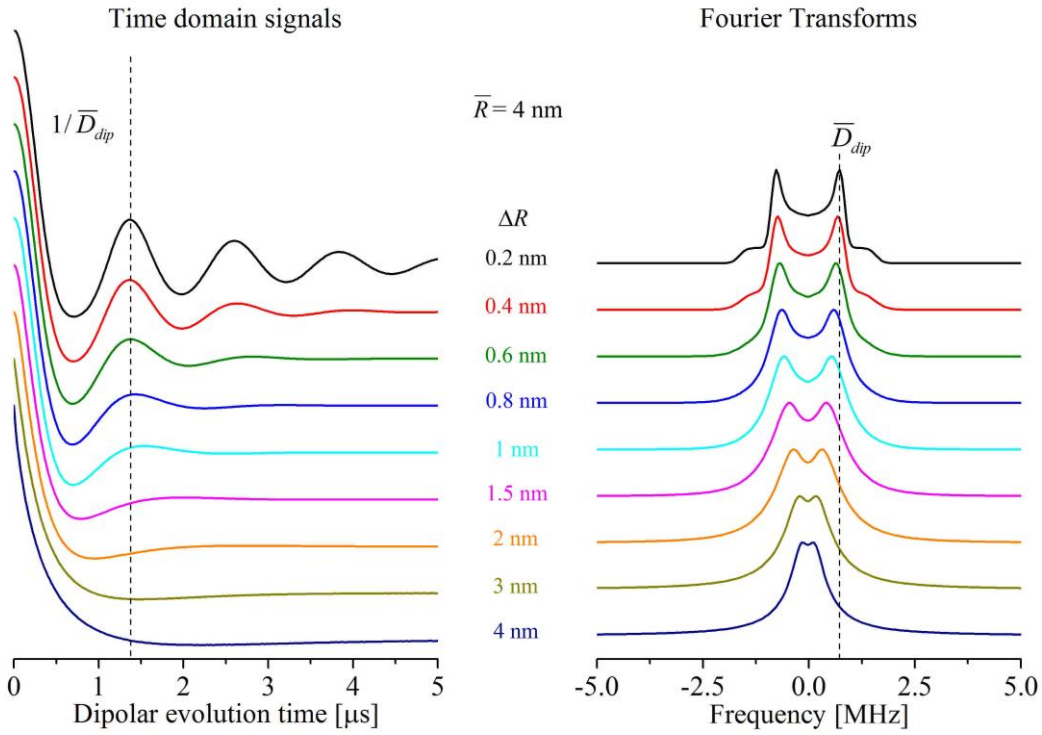

Figure 17. Calculated PELDOR signals corresponding to distance distributions defined as Gaussian functions with varied widths (left) and corresponding Fourier transforms (right). The most probable distance is fixed to 4 nm and full-width at half maximum is varied from 0.2 till 4 nm (the values are given in figure).

For nitroxide radicals and metal complexes, widths of the EPR spectra are often significantly broader than the *excitation bandwidth* of the applied pulses, which is proportional to a pulse amplitude of $\omega_1 = g\beta B_1 / \hbar$. Therefore, an *amplitude of the dipolar oscillations* λ (*dipolar modulation depth*) deviates from 100%, as assumed in (eq. 3.3.3) and (eq. 3.3.4). Thus, λ as a function of a pump π pulse amplitude ω_1, its duration t_p and the EPR line shape $F(\Delta\omega)$ function is defined as:[91]

$$\lambda = \int_{-\infty}^{\infty} \sin^2\left(\frac{\Omega}{2} t_p\right) \frac{\omega_1^2}{\Omega^2} F(\Delta\omega) d(\Delta\omega)$$
$$\Omega = \sqrt{\omega_1^2 + \Delta\omega^2} \qquad (3.3.5)$$

where Ω is the effective nutation frequency and the frequency offset $\Delta\omega$ is counted with respect to the pump pulse frequency. More simply, λ is the probability, that *B* spin is excited by the pump pulse. Thus, the PELDOR signal (eq. 3.3.4) is modified as given:

$$S_{norm}(T) = 1 - \lambda + \lambda \cdot \boldsymbol{K(T, R)} \cdot \boldsymbol{P(R)} \qquad (3.3.6)$$

It is important to note, that the signals (eq. 3.3.4) - (eq. 3.3.6) correspond to the case, where there is no orientational correlation between the anisotropic $\overline{\boldsymbol{g}}$ - and/or $\overline{\boldsymbol{A}}$ -tensors of both spins (for nitroxide radicals) or ZFS tensor (for high-spin systems) and the dipolar coupling

tensor (so called *orientation-selection free condition*). For biological systems labelled with commonly used MTSL tag this condition is fulfilled to a large extent, since conformational flexibilities of biomolecules and labels by themselves effectively average such correlations, especially at lower fields (X- and Q-bands), where $\bar{\boldsymbol{g}}$-tensor resolution is weak. For dipolar coupled high-spin metal ions this condition is usually fulfilled independently of magnetic field, as this correlation is effectively averaged by broad statistical distribution of ZFS parameters and excitation of the multiple transitions with microwave pulses. However, if rigid nitroxide spin labels are used (*C*-spin), and/or high fields are applied, the orientation-selection free condition is no longer valid, and modulation depth depends not only on ω_1, t_p and $F(\Delta\omega)$ but also on the angle θ, *i. e* a spectral position at which the PELDOR time trace is obtained. In this case the signals (eq. 3.3.4) and (eq. 3.3.6) are modified as:[92]

$$S_{norm}(T) = 1 - \int_{R\min}^{R\max} \int_{0}^{1} \lambda(\arccos x)\left(1 - \cos\left[\frac{52.04}{R^3}\left(3x^2 - 1\right)T\right]\right)P(R)dxdR \qquad (3.3.7)$$

where $x = \cos\theta$. Thus, PELDOR signals at a given spectral position is defined by geometry and conformational flexibility of labelled molecules. Therefore, analysis of the orientation selective PELDOR time traces (eq. 3.3.7), obtained at multiple spectral positions[a] can reveal additional structural information.

An important aspect influencing PELDOR signals is inter-molecular dipolar couplings. The spin *A* interacts not only with the spin *B* within the same molecule but also with spins *B* of other molecules. Upon application of the pump pulse, dipolar couplings with these spins lead to additional defocussing of the *A* spins echo signal and additional decay of PELDOR signals. For homogeneous spatial distribution of paramagnetic molecules, a PELDOR signal due to inter-molecular dipolar couplings can be accurately approximated with mono-exponential function as given:[20,91]

$$S_{inter-molecular}(T) = e^{-kC\lambda T}$$
$$k = \frac{2\pi\mu_0\beta_e^2 g_A g_B}{9\sqrt{3}\hbar} \qquad (3.3.8)$$

where *C* is the volume concentration of the paramagnetic molecules. Thus, the measured PEDLOR signal is a product of the signals due to intra- (eq. 3.3.6), (eq. 3.3.7) and inter-molecular couplings (eq. 3.3.8):

[a] In some cases multiple frequency bands are required.

$$S_{PELDOR}(T) = e^{-kC\lambda T} \cdot S_{norm}(T) \tag{3.3.9}$$

By choosing concentration of studied molecules, a compromise between the signal intensity and steepness of the signal decay due to inter-molecular couplings, both proportional to the concentration, is needed.

Inter-molecular dipolar signal (background) is an important issue in PELDOR and other pulsed dipolar spectroscopy experiments, since it is not usually trivial to divide it from the PELDOR signal. This is especially problematic for flexible molecules, a common case for biomolecules. As can be seen in Figure 17, dipolar oscillations dampen very quickly for flexible systems, requiring a PELDOR time trace to be recorded long enough[a] in order to be able to unambiguously fit a background function and consequently divided it out.

To summarize this section, from an experimental point of view PELDOR requires two different microwave frequencies, relatively high microwave powers and large spectrometer bandwidth, that requires certain technical advances. From a theoretical point of view, this experiment is significantly less complicated and more robust to different kind of imperfections (*e.g.* nuclear hyperfine couplings, not ideal pulses and not perfect set pulse phases) compared to other pulsed dipolar techniques. Thus, this dipolar spectroscopy technique is very efficient, robust and, therefore, the most widely used method for distance determination with EPR.

For some specific paramagnetic tags, *e.g.* with very narrow or very broad EPR spectra, the performance of PELDOR experiment is not optimal in terms of sensitivity and robustness. Therefore, the use of alternative dipolar spectroscopy techniques, like DQC and SIFTER for tags with very narrow EPR spectra and RIDME for tags with very broad EPR spectra is often necessary.

3.3.2 DQC

Multiple-quantum coherence (*MQC*) based filtering is well known tool in NMR spectroscopy since the beginning of 1980s.[93,94] By applying these filters it is possible to suppress the signals from undesired features and to focus only on relevant peaks, which significantly simplifies the analysis and enhances the performance of multiple-dimension correlation experiments. In pulsed EPR it has been a considerable challenge to generate MQC. Development of Fourier transform EPR techniques has encouraged an adaption of a powerful NMR approach for EPR spectroscopy. A particular useful application for EPR-based structural biology studies has been the *double quantum coherence* (*DQC*) filtering technique.[95,96] It selects

[a] This is often a challenging task due to limitations of transverse relaxation time.

the electron two-spin coherences (section 3.2), allowing the determination of weak dipolar couplings. This method requires excitation of the whole EPR spectrum that is not trivial for commonly used nitroxide radicals. But this limitation has been overcome by using of very short and powerful pulses in the laboratory of J. Freed.[96] This required considerable technical advances. On the other hand, paramagnetic tags with very narrow EPR spectra, like trityl radicals, would be of interest, since standard microwave pulses can be used for optimal performance of DQC experiments. Taking into consideration all the advantages of the tag and a fact that PELDOR is not optimal in this case, DQC forms useful complementary tool for structural biology.

The electron two spin coherences, a central phenomenon for DQC experiment, can be represented by the raising and lowering operators (introduced in section 3.1.1) as given by (eq. 3.3.10):

$$\begin{aligned} 2\hat{S}_x^A\hat{S}_x^B &= \frac{1}{2}\left(\hat{S}_+^A\hat{S}_+^B + \hat{S}_+^A\hat{S}_-^B + \hat{S}_-^A\hat{S}_+^B + \hat{S}_-^A\hat{S}_-^B\right) \\ 2\hat{S}_y^A\hat{S}_y^B &= -\frac{1}{2}\left(\hat{S}_+^A\hat{S}_+^B - \hat{S}_+^A\hat{S}_-^B - \hat{S}_-^A\hat{S}_+^B + \hat{S}_-^A\hat{S}_-^B\right) \\ 2\hat{S}_x^A\hat{S}_y^B &= \frac{1}{2i}\left(\hat{S}_+^A\hat{S}_+^B - \hat{S}_+^A\hat{S}_-^B + \hat{S}_-^A\hat{S}_+^B - \hat{S}_-^A\hat{S}_-^B\right) \\ 2\hat{S}_y^A\hat{S}_x^B &= \frac{1}{2i}\left(\hat{S}_+^A\hat{S}_+^B + \hat{S}_+^A\hat{S}_-^B - \hat{S}_-^A\hat{S}_+^B - \hat{S}_-^A\hat{S}_-^B\right) \end{aligned} \tag{3.3.10}$$

where all four product operators contain both double and zero quantum coherences (concerted and opposite spin-flips respectively). The two linear combinations given as:

$$\frac{1}{2}\left(2\hat{S}_x^A\hat{S}_x^B - 2\hat{S}_y^A\hat{S}_y^B\right) = \frac{1}{2}\left(\hat{S}_+^A\hat{S}_+^B + 2\hat{S}_-^A\hat{S}_-^B\right) = \{2QT\}_x \tag{3.3.11}$$

and

$$\frac{1}{2}\left(2\hat{S}_x^A\hat{S}_y^B + 2\hat{S}_y^A\hat{S}_x^B\right) = \frac{1}{2i}\left(\hat{S}_+^A\hat{S}_+^B - 2\hat{S}_-^A\hat{S}_-^B\right) = \{2QT\}_y \tag{3.3.12}$$

represent *pure double quantum coherence*. Similarly, *pure zero quantum coherence* is given by another linear combinations:

$$\frac{1}{2}\left(2\hat{S}_x^A\hat{S}_x^B + 2\hat{S}_y^A\hat{S}_y^B\right) = \frac{1}{2}\left(\hat{S}_+^A\hat{S}_-^B + 2\hat{S}_-^A\hat{S}_+^B\right) = \{ZQT\}_x \tag{3.3.13}$$

and

$$\frac{1}{2}\left(2\hat{S}_y^A\hat{S}_x^B - \hat{S}_x^A\hat{S}_y^B\right) = \frac{1}{2i}\left(\hat{S}_+^A\hat{S}_-^B - 2\hat{S}_-^A\hat{S}_+^B\right) = \{ZQT\}_y \tag{3.3.14}$$

The graphical representation of pure zero and double quantum coherences on the spin sublevel diagram (similar two-spin 1/2 diagram is given in Figure 13) is given in Figure 18.

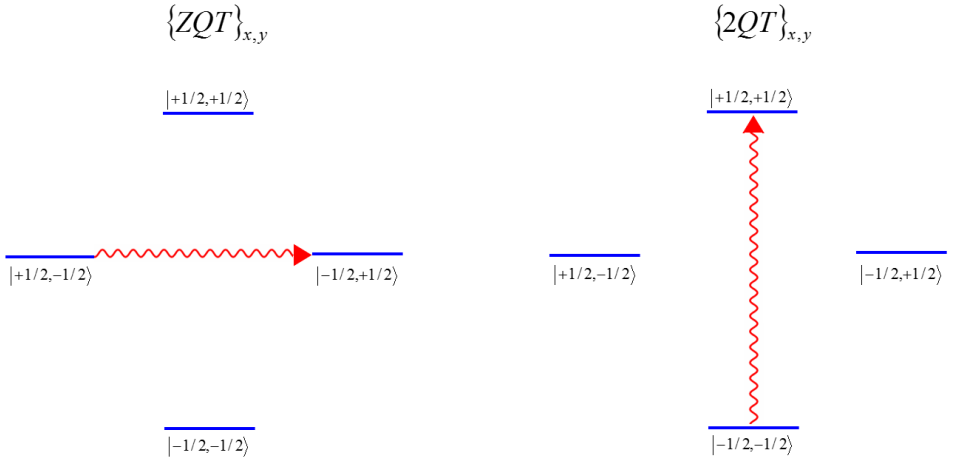

Figure 18. Graphical representation of the pure zero and double quantum coherences in a two-spin system with an elementary spin of 1/2. The wavy lines represent the corresponding coherences.

Experimentally, DQC and ZQC can be obtained by the pulse sequence shown in Figure 19, which is standard sequence for *preparation of MQC* in NMR spectroscopy.[93]

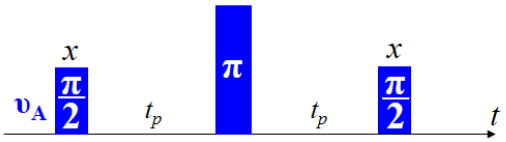

Figure 19. Pulse sequence for preparation of multiple-quantum coherence. The pulse propagators generate even coherence orders, i.e. 0 and 2 for two-spin system. If the last pulse applied along the y-axis, odd coherence order is produced.

We consider only weakly coupled two-spin system (coherence orders not higher than 2), for which spin Hamiltonian in the rotating frame is given as:

$$\hat{\mathcal{H}}_{DQC} = \hat{\mathcal{H}}'_{EZ} + \hat{\mathcal{H}}_{dd} = \Delta\omega_A \cdot \hat{S}_z^A + \Delta\omega_B \cdot \hat{S}_z^B + \omega_{dd} \hat{S}_z^A \hat{S}_z^B \qquad (3.3.15)$$

In weak coupling regime only secular part of the dipolar coupling Hamiltonian is conserved that allows the treatment of propagators $U_{EZ} = e^{-i\hat{\mathcal{H}}'_{EZ}t_p}$ and $U_{dd} = e^{-i\hat{\mathcal{H}}_{dd}t_p}$ independently. Thus, the first $(\pi/2)_x$ pulse of the sequence produces the in-phase single quantum (SQ) coherence $\hat{S}_y^A + \hat{S}_y^B$. This coherence evolves under the combination of the propagators U_{EZ} and U_{dd} during a time interval t_p (see Figure 15) then the π pulse propagator and again the same (U_{EZ} and U_{dd}) propagators during a second t_p interval into sums of in-phase $\hat{S}_y^A + \hat{S}_y^B$ and anti-phase $\hat{S}_x^A \hat{S}_z^B + \hat{S}_x^B \hat{S}_z^A$ SQ coherences:[97]

$$\hat{S}_y^A + \hat{S}_y^B \xrightarrow{\hat{\mathcal{H}}_{dd} t_p} \xrightarrow{\hat{\mathcal{H}}'_{EZ} t_p} \xrightarrow{(\pi)_x} \xrightarrow{\hat{\mathcal{H}}_{dd} t_p} \xrightarrow{\hat{\mathcal{H}}'_{EZ} t_p} \left(\hat{S}_y^A + \hat{S}_y^B\right)\cos\left(\omega_{dd} t_p\right) + \\ + 2\left(\hat{S}_x^A \hat{S}_z^B + \hat{S}_x^B \hat{S}_z^A\right)\sin\left(\omega_{dd} t_p\right) \tag{3.3.16}$$

The $(\pi)_x$ in the preparation sequence (Figure 19) removes the terms oscillating with the offset frequencies $\Delta\omega_A$ and $\Delta\omega_B$. From this expression it can be seen that the detectable in-phase coherence appears $\left(\hat{S}_y^A + \hat{S}_y^B\right)\cos\left(\omega_{dd} t_p\right)$. The coherence causes a Hahn echo signal at the time position $2t_p$, whose amplitude is modulated with dipolar coupling frequency. The last $(\pi/2)_x$ pulse in the preparation sequence converts the anti-phase SQ coherence into $\{2QT\}_y$ coherence (eq. 3.3.12):

$$2\left(\hat{S}_x^A \hat{S}_z^B + \hat{S}_x^B \hat{S}_z^A\right)\sin\left(\omega_{dd} t_p\right) \xrightarrow{(\pi/2)_x} 2\left(\hat{S}_x^A \hat{S}_y^B + \hat{S}_y^B \hat{S}_x^A\right)\sin\left(\omega_{dd} t_p\right) = \{2QT\}_y \sin\left(\omega_{dd} t_p\right) \tag{3.3.17}$$

After preparation, the $\{2QT\}_y$ (Figure 19 and the first three pulses of 6-pulse DQC sequence in Figure 15) is evolved under the propagator $U_{EZ} = e^{-i\hat{\mathcal{H}}'_{EZ} t_p}$ (the evolution of multiple quantum coherence is not affected by couplings). Thus:

$$\{2QT\}_y \xrightarrow{\hat{\mathcal{H}}'_{EZ} t} \{2QT\}_y \cos\left[\left(\Delta\omega_1 + \Delta\omega_2\right)t\right] - \{2QT\}_x \sin\left[\left(\Delta\omega_1 + \Delta\omega_2\right)t\right] \tag{3.3.18}$$

In the case of EPR spectroscopy, signals are detected in the forms of echoes, since free-induction decay signals decay too quick for the detection. Therefore the DQC should be refocused, that is accomplished by the $(\pi)_x$ pulse:

$$\{2QT\}_y \xrightarrow{(\pi)_x} -\{2QT\}_y, \quad \{2QT\}_x \xrightarrow{(\pi)_x} \{2QT\}_x \tag{3.3.19}$$

Afterwards, the $\{2QT\}_y$ is evolved again under the propagator $U_{EZ} = e^{-i\hat{\mathcal{H}}'_{EZ} t_p}$. Thus, after the preparation period, DQC evolves under the propagation formed by a combination of $U_{EZ} = e^{-i\hat{\mathcal{H}}'_{EZ} t_p}$, $U_{(\pi)_x} = e^{-i\pi\hat{S}_x}$ and again $U_{EZ} = e^{-i\hat{\mathcal{H}}'_{EZ} t_p}$, which forms *evolution of DQC*.

After being prepared and evolved, DQC is converted back to anti-phase SQ coherence, which then evolves under propagators corresponding to Hamiltonian (eq. 3.3.15) to the observable in-phase coherence. This forms *mixing and detection period*. Thus, the $\{2QT\}_y$ is converted by the $(\pi/2)_x$ pulse into anti-phase SQ coherence:

$$\begin{aligned}
&\{2QT\}_y \sin(\omega_{dd} t_p) = \frac{1}{2i}\left(\hat{S}_+^A \hat{S}_+^B - 2\hat{S}_-^A \hat{S}_-^B\right)\sin(\omega_{dd} t_p) \xrightarrow{(\pi/2)_x} \\
&\xrightarrow{(\pi/2)_x} -\left(\hat{S}_+^A \hat{S}_z^B + \hat{S}_+^B \hat{S}_z^A + \hat{S}_-^A \hat{S}_z^B + \hat{S}_-^B \hat{S}_z^A\right)\sin(\omega_{dd} t_p) = \\
&= 2\left(\hat{S}_x^A \hat{S}_z^B + \hat{S}_x^B \hat{S}_z^A\right)\sin(\omega_{dd} t_p)
\end{aligned} \tag{3.3.20}$$

which resembles the signal in (eq. 3.3.16). The anti-phase SQ coherence then evolves during the mixing time into in-phase SQ coherence, which is subsequently detected:

$$\begin{aligned}
&2\left(\hat{S}_x^A \hat{S}_z^B + \hat{S}_x^B \hat{S}_z^A\right)\sin(\omega_{dd} t_p) \xrightarrow{\hat{\mathcal{H}}_{dd} t_2} \xrightarrow{\hat{\mathcal{H}}'_{zz} t_2} \xrightarrow{(\pi)_x} \xrightarrow{\hat{\mathcal{H}}_{dd} t} \xrightarrow{\hat{\mathcal{H}}'_{zz} t} \\
&-\frac{1}{2i}\left(\hat{S}_+^A e^{-i\Delta\omega_1(t_2-t)} + \hat{S}_+^B e^{-i\Delta\omega_2(t_2-t)} - \hat{S}_-^A e^{i\Delta\omega_1(t_2-t)} - \hat{S}_-^B e^{i\Delta\omega_2(t_2-t)}\right)\sin(\omega_{dd} t_p)\times \\
&\times \sin\left(\omega_{dd}\left(t + \frac{(t_2 - t)}{2}\right)\right)
\end{aligned} \tag{3.3.21}$$

where $t = t_m - t_p$. The SQ coherence is refocused by $(\pi)_x$ pulse at $t_2 = t$ and the observed echo-signal is then defined as given by (eq. 3.2.5).

It is important to note, that not only DQC but also ZQC is filtered by the DQ filter. Furthermore, other SQ coherences are produced by different combination of pulses (e.g. Hahn echo from last two pulses in the sequence that is superimposed with DQ filtered signal). The proper DQ signal is selected by appropriated phase cycle. The real part of the signal (eq. 3.3.21) is defined as:

$$M(t_2) \propto \left[\cos(\Delta\omega_1(t_2 - t)) + \cos(\Delta\omega_2(t_2 - t))\right]\sin(\omega_{dd} t_p)\sin\left(\omega_{dd}\left(t + \frac{(t_2 - t)}{2}\right)\right) \tag{3.3.22}$$

After averaging over all resonance offsets, the terms in the square brackets yield the echo signal, with the maximum at $t_2 = t$. At this time position, the signal amplitude is modulated by $\sin(\omega_{dd} t_p)\sin(\omega_{dd} t)$ and, thus, by $\cos(\omega_{dd}(t_p - t))$. In this experiments the first two inter-pulse delays t_p ($d_1 + \Delta T$ in Figure 15) are incremented and two last delays are correspondingly decremented $t = t_m - t_p$ ($d_3 - \Delta T$), such that the detected echo signal is static and does not decay due to the transversal relaxation directly. The 6-pulse DQC sequence, shown in Figure 15, is essentially dead-time free and most used DQC EPR sequence.

After dipolar coupling averaging, the DQC signal takes the form given in (eq. 3.3.6), in which $T = 2t_p - t_m$ and $\lambda = 1$, with the assumption that the whole EPR spectrum is excited with all pulses of the sequence.

To summarize this section, we analyzed the DQC experiment with the product operator formalism and saw that the DQ filter only passes the signal due to the dipolar coupling of the two spins. The described pulse sequence is not limited to DQ filtering. Thus, for three and more coupled spin system, the triple and higher order quantum coherences can be filtered from all other coherences by using appropriate phase cycle, that is potentially useful for studying oligomeric states of large macromolecules. Based on the analysis given in this section, much higher complexity of DQC with respect to PELDOR can be appreciated. The use of DQC experiment for studying macromolecules labelled with standard nitroxide labels is not optimal due to broad EPR spectrum of this tag. However, the paramagnetic tags based on trityl radical are well suited for this experiment.

The method, which can alternatively be utilized in combination with paramagnetic tags with narrow EPR spectrum, is SIFTER. This method is significantly less complicated in terms of involved spin dynamics and setting up of the experiment.

3.3.3 SIFTER

Single-frequency technique for refocussing dipolar couplings (SIFTER),[98] based on *solid-echo* sequence, is a valuable EPR dipolar spectroscopy tool. The solid echo experiment consisting of two orthogonally phased $\pi/2$ pulses is a well-known method of dipolar NMR spectroscopy in solids that originated in 1963.[99] For purposes of EPR dipolar spectroscopy this method was adapted only in 2000.[98] Original NMR sequence cannot be applied in EPR as it does not completely refocus relatively large inhomogeneities due to distribution of g and hyperfine coupling values, typical in EPR for amorphous samples. This problem was solved by introducing two more refocussing π pulses (sequence is shown in Figure 15). In this experiment, two first inter-pulse delays (d_1 in Figure 15) are incremented and two following delays (d_3) are correspondingly decremented, that yields an oscillation of the refocused solid echo as a function of time $t = d_3 - d_1$.

The theoretical treatment of the solid-echo SIFTER experiment is performed again using the product operator formalism, introduced in section 3.2 and extensively used for the treatment of the DQC experiment. We consider weak-coupling regime and full excitation of the EPR spectrum by each pulse. The Hamiltonian given in (eq. 3.3.15) is also relevant for this experiment. The result of the $(\pi/2)_x$ and $(\pi)_x$ pulses and corresponding evolution after each pulse during both time intervals d_1 under Zeeman and dipolar coupling propagators were already

obtained for DQC experiment (eq. 3.3.16). The $(\pi/2)_y$ pulse[a] inverts the sign of the anti-phase coherence term, which under evolution during the time interval d_3 followed by another $(\pi)_x$ and again evolution during d_3, gives the density matrix (detection position):

$$\sigma_{\text{det}} = \cos[\omega_{dd}(d_3 - d_1)](\hat{S}_y^A + \hat{S}_y^B) - \sin[\omega_{dd}(d_3 - d_1)](2\hat{S}_z^A\hat{S}_x^B + 2\hat{S}_x^A\hat{S}_z^B) \qquad (3.3.23)$$

The first, in-phase SQ coherence term, gives a signal in a form of solid echo with an amplitude modulated by the dipolar coupling frequency, while the second, anti-phase SQ coherence term, is not detectable at this time position.

Thus, after dipolar coupling averaging, the detected signal takes form given in (eq. 3.3.6), with $\lambda = 1$, with the assumption that the whole EPR spectrum is excited.

As can be seen from this section SIFTER experiment is significantly easier than DQC. It also requires less extensive phase-cycle to cancel all SQ coherences, produced by different pulses. As SIFTER requires full excitation of the EPR spectrum, the use of this experiment with conventional nitroxide radicals has been rare. But with the development of fast in the EPR timescale *arbitrary wave form generators* (AWG), the forming of broadband shaped microwave pulses has become feasible (in NMR it has been successfully used since 1985[100]). Thus, the use of SIFTER technique with broad pulses has gained interest.[101,102] On the other hand, the use of this dipolar spectroscopy experiment with narrow EPR line trityl radical does not require shaped pulses and high-power pulses. Thus, trityl-based SIFTER is useful and less complicated alternative to corresponding DQC experiment.

3.3.4 RIDME

In this section we consider another dipolar spectroscopy experiment, which is useful for tags with very broad EPR spectra. *Relaxation-induced dipolar modulation enhancement* (*RIDME*)[103,104] is a dipolar spectroscopy technique, in which longitudinal relaxation is exploited to change the state of the spin *B*, rather than coherent excitation with a microwave pulse as in PELDOR experiment. RIDME is based on a *stimulated echo* experiment (sequence is shown in Figure 15), which has been first observed on protons in water by E. Hahn in 1950.[87] In 1996 the stimulated echo sequence has been applied to measure the dipolar coupling between two hetero nuclei, which are characterized by significantly different relaxation times.[105] Five years later this sequence has been utilized to determine dipolar couplings between two electron spins.[103] Similar to 3-pulse PELDOR, this sequence has a major disadvantage of non-zero dead time. To overcome this issue, two additional refocussing π pulses have been added to the

[a] Note that this pulse with a phase of *x* would transfer anti-phase SQ coherence into DQ coherence.

stimulated echo sequence that yielded dead time free 5-pulse RIDME sequence (Figure 15).[104] This sequence can be compared with 4-pulse PELDOR in a sense, that π pump pulse is replaced by a block of two $\pi/2$ pulses, applied at the same frequency as the detection pulses. But in contrast to PELDOR, RIDME is a stimulated echo-based experiment. Therefore, the description of RIDME effect is given on the basis of the three pulse stimulated echo sequence (Figure 15).

The first two pulses of this sequence $\pi/2$-d_1-$\pi/2$ create a polarization grating, which is characterized by a frequency of $2\pi/d_1$. The polarization grating is consequently stored during the time T (further referred as *store time*), and the density operator after the time T takes form:

$$\sigma(d_1+T) = -\cos(\Delta\omega d_1)\hat{S}_y \tag{3.3.24}$$

After the time T the third $\pi/2$ - pulse is applied. It transfers the stored polarization grating to the transverse plain, and the density operator at arbitrary time t after the third pulse is given as:

$$\begin{aligned}\sigma(d_1+T+t) = &-\frac{1}{2}\left[\cos(\Delta\omega(t-d_1))+\cos(\Delta\omega(t+d_1))\right]\hat{S}_y + \\ &+\frac{1}{2}\left[\sin(\Delta\omega(t-d_1))+\sin(\Delta\omega(t+d_1))\right]\hat{S}_x\end{aligned} \tag{3.3.25}$$

The density operator terms $\cos(\Delta\omega(t-d_1))\hat{S}_y$ and $\sin(\Delta\omega(t-d_1))\hat{S}_x$ result in a stimulated echo signal at time $t = d_1$, since to the both terms become independent from the individual resonance frequency offsets. The two remaining terms are not refocused into the signal, but become independent from $\Delta\omega$ during the negative time $t = -d_1$. They represent so-called *virtual stimulated echo*.[106] Although this echo does not give rise to the signal, it can be consequently refocused by application of additional π pulse after the last $\pi/2$ pulse. This, in turns, results in the detectable signal, called *refocused virtual stimulated echo* (for simplicity referred to as *refocused virtual echo* in the following).

The created polarization grating can be attenuated during the store time due to longitudinal relaxation T_1^A or sudden change of the resonance frequency of the detected spins. This results in decrease of the stimulated echo amplitude. In a dipolar-coupled spin system sudden changes of the resonance frequency of the detected spins A can be induced by a flip of the spin B due to its T_1^B - relaxation. Minima of the stimulated echo amplitude are achieved at d_1 time positions when spins A gain the phase φ_{B-flip} that corresponds to their jump from a maximum of a polarization grating to a minimum, $\varphi_{B-flip} = \omega_{dd}\cdot d_1 = (2n+1)\pi$, where n is integer. Thus, upon incrementing the time interval d_1, the amplitude of the stimulated echo oscillates

with dipolar coupling frequency. A dipolar modulation depth is determined by the choice of the store time and the longitudinal relaxation time of spin *B*:[104]

$$\lambda = \frac{1}{2}\left(1 - \exp\left(-\frac{T}{T_1^B}\right)\right) \tag{3.3.26}$$

Thus, the RIDME signal for dipolar coupled spin 1/2 systems in amorphous samples is described by (eq. 3.3.6) with modulation depth defined in (eq. 3.3.26).

As mentioned above, the original three pulse RIDME sequence (the stimulated echo sequence where d_1 is incremented an T is kept constant)[103] has non-zero dead time. Additionally, the detected signal attenuates with incrementing d_1 time due to transverse relaxation of spins *A*. Thus, the 5-pulse version has been developed in which instead of stimulated echo, the refocused stimulated or refocused virtual echoes is detected (the latter does not have additional decay of the signal due to transverse relaxation).[104]

RIDME is the most efficient when two spins in a pair have significantly different longitudinal relaxation times $T_1^B << T_1^A$, as initially proposed in analogues NMR experiment.[105] This is often the case when two different paramagnetic tags are used, nitroxide - trityl radical or metal ion - organic radical. However, high efficient RIDME experiments have also been obtained by using two identical high-spin systems.[83,107] For a high-spin system the longitudinal relaxation behavior is more complex. It can change the magnetic quantum number of spin *B* not only by $\Delta m_S^B = \pm 1$, as for elementary spin 1/2, but also effectively by $\Delta m_S^B = \pm 2$, $\Delta m_S^B = \pm 3$ and higher. This induces the changes of the resonance frequency of spin *A* by $\pm 2\omega_{dd}$, $\pm 3\omega_{dd}$, …, $\pm 2S\omega_{dd}$, additionally to the ω_{dd}.[83,107] Thus, a RIDME signal, obtained on a dipolar coupled system, in which spin *B* has a high spin multiplicity, contains multiple harmonics of the dipolar coupling frequency. This complicates data analysis and following interpretation, since weights of different harmonics depend on a sample and experimental conditions. PELDOR experiment with high spin systems is not affected by multiple harmonics of the dipolar coupling frequency. This is due to the change of the *B* spin state is driven by a microwave pulse, which is able to generate only SQ electron spin coherence, that benefits PELDOR over RIDME in terms of data interpretation. However, sensitivity of RIDME experiment with high-spin tags is significantly greater than that of PELDOR. This is due to very broad EPR spectrum of such spin tags, leading to only small fraction of spins being excited by the pump pulse that significantly reduces λ (eq. 3.3.5), as demonstrated for Gd^{3+} spin tags.[49]

To sum up this section, RIDME, that exploits longitudinal relaxation to drive transition of spin *B*, is valuable complementary tool for PELDOR. This method is best suited for distance

measurements between two paramagnetic tags, which have different T_1 relaxation times (*e.g.* metal ion - organic radicals, or in some cases trityl - nitroxide radicals). For high-spin systems RIDME can provide significantly larger modulation depth than PELDOR, however, being complicated by multiple harmonics of the dipolar coupling.

3.3.5 Conversion of dipolar couplings to distances

After considering dipolar spectroscopy techniques we approach data analysis section. Signals in dipolar spectroscopy experiments are described by the Fredholm integral equation of the first kind (eq. 3.3.6). In order to determine the unknown distance distribution $P(R)$ from the experimental signal $S(T)$, an *inverse problem* has to be solved. From the experimental point of view, it is a problem that consists of using the result of measurements to evaluate the parameters that caused this result. In many cases the inverse problem is not *well-posed*, meaning that one of the three following criteria is not fulfilled (Hadamard definition):

(1) Solution to the problem exists – *existence.*

(2) Only one solution exists – *uniqueness.*

(3) Solution depends continuously on the experimental results (*e.g.* changes on initial conditions) – *stability*.

A problem which is not well-posed is called *ill-posed*. In application to EPR-based distance measurements, violation of the criterion (3) plays an important role, meaning that small errors in experimental signals (noise, experimental instabilities or not proper averaged nuclear modulations) might lead to considerable error in found distance distributions.

One of the most powerful approaches that stabilizes the solution of ill-posed problems is *regularization*. Thus, an additional *regularization parameter* is introduced and that is responsible for the quality of the result given by a regularization method. One of the most commonly used regularization method is *Tikhonov regularization*.[108] The result obtained with this kind of regularization is defined as the function $P(R)$, which minimizes the quantity:[109,110]

$$G_P = \left\| \boldsymbol{S(T)} - \boldsymbol{K}(\boldsymbol{T},\boldsymbol{R})\boldsymbol{P}(\boldsymbol{R}) \right\|^2 + \alpha \left\| \boldsymbol{L}\boldsymbol{P}(\boldsymbol{R}) \right\|^2 \qquad (3.3.27)$$

In this minimization the constraints on $P(R) \geq 0$ must be considered.[110,111] In the functional α is a regularization parameter, $\boldsymbol{L}$ is an operator, for which the identity or the second derivative is frequently used, and a norm $\| \ \|$ is the Euclidian norm of a vector. For simplicity, we represent functional (eq. 3.3.27) in a shorter form of $G_P = \left\| \boldsymbol{S} - \boldsymbol{K}\boldsymbol{P} \right\|^2 + \alpha \left\| \boldsymbol{L}\boldsymbol{P} \right\|^2$. Thus, with an appropriate value for the regularization parameter α, the first term in the functional forces the solution to be

compatible with the experimental data, while the second term is a smooth estimate of this solution. The function $P(R)$, given by the minimum of the quantity (eq. 3.3.21), can be written explicitly as:[109]

$$\begin{aligned} \boldsymbol{P}_\alpha &= \boldsymbol{K}^{-1}\boldsymbol{S}\,, \\ \boldsymbol{K}^{-1} &= \left(\boldsymbol{K}^T\boldsymbol{K} + \alpha\boldsymbol{L}^T\boldsymbol{L}\right)^{-1}\boldsymbol{K}^T \end{aligned} \tag{3.3.28}$$

where $\boldsymbol{K}^T$ is the transpose of matrix $\boldsymbol{K}$ and in the parenthesis inverse matrix is presented. For dipolar spectroscopy applications, for the operator $\boldsymbol{L}$ the second derivative operator has been chosen. The expression (eq. 3.3.28), that is Tikhonov regularization functional (eq. 3.3.27) minimizer, is readily solved by using *singular value decomposition* (SVD), that is implemented in linear algebra routines (*e.g.* introduced in MATLAB or as *LAPACK* package for Fortran).

After getting the explicit solution, the next question is how to choose an appropriate value for the regularization parameter? Introduction of regularization parameter has a great influence on the result, obtained by a regularization method. If the chosen parameter is too small, the $P(R)$ will show artificial peaks, while if this parameter is too large, the $P(R)$ will be over-smoothed. Typically, small α is required for rigid systems, and large α is suitable for flexible systems. However, this information is not known in advance and therefore a reliable procedure for the determination of the regularization parameter is required. There are several different ways for defining an optimum parameter and one of the most reliable is the *L curve criterion*.[111,112] The L curve is a plot of $\log(\eta_\alpha)$ versus $\log(\rho_\alpha)$, where:

$$\rho_\alpha = \left\|\boldsymbol{S} - \boldsymbol{K}\boldsymbol{P}_\alpha\right\|^2 \tag{3.3.29}$$

quantifies the compatibility of the solution with experimental data (mean square error) and

$$\eta_\alpha = \left\|\boldsymbol{L}\boldsymbol{P}_\alpha\right\|^2 \tag{3.3.30}$$

quantifies the smoothness, as illustrated in Figure 20 (two calculated time traces with different widths of distance distribution and a *signal-to-noise ratio* of 50 are shown).

In the range of small regularization parameters (left corner of L-curve: Figure 20, middle raw), indicating under-smoothing, the slop is very steep as α increases, thus the second derivative (eq. 3.3.30) strongly decreases without affecting the mean square error (eq. 3.3.29). In contrast, for right corner of L-curve (over-smoothing), the mean square error increases strongly with increasing α, indicating poor compatibility of the found solution, whereas the second derivative decreases gradually, indicating that noise- or artefact-related peaks in the distance distribution are already smoothed. In the L curve, the optimal regularization parameter is located on the cross-point between the two lines, which are characterized by steep (linear fit

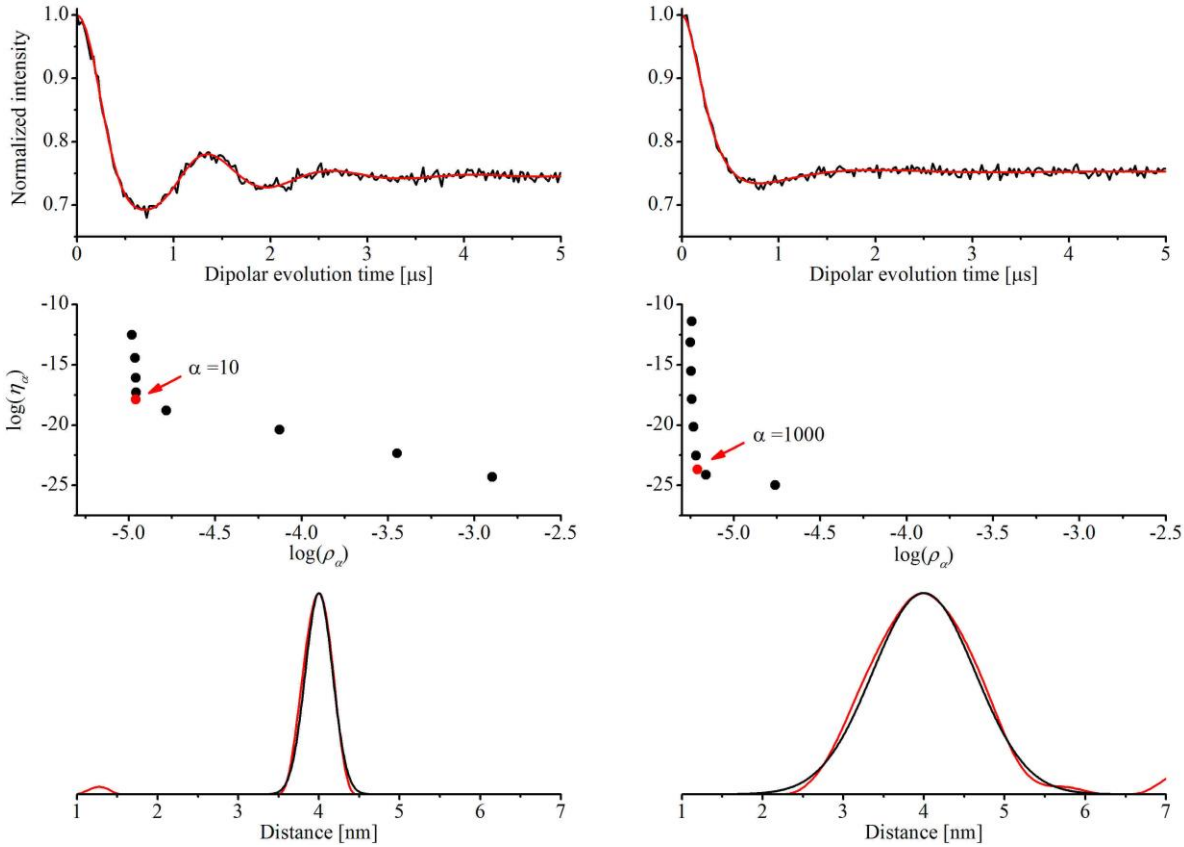

Figure 20. Top: Dipolar evolution time traces with modulation depth of 0.25 calculated from the Gaussian distance distribution (black curves) with full-width at half maximum of 0.4 nm (left) and 1.5 (right). Signal-to-noise ratio is chosen 50 for relevancy with experiments. Back-calculated time traces based on Tikhonov regularization (2.3.46) is represented by red curves. Middle: Corresponding L-curves. By red point an optimal regularization parameter is shown. Bottom: Corresponding distance distributions. Gaussian distance distribution used for calculation of the time traces (black) and obtained by Tikhononov regularization (red).

of the points in the under-smoothing region) and gentle-steep slopes (linear fit of the points in over-smoothing region), as demonstrated in Figure 20. It is worth noting, however, that the cross-point of the L-curve is not always well pronounced, as demonstrated for these two examples. For example, in case of broader or more complex distance distributions it can be non-trivial to find the optimal parameter. In such cases, additional inspection of the dipolar evolution time traces and distance distributions for all α parameters is required.

Tikhonov regularization analysis is the most commonly used approach for obtaining distances from dipolar spectroscopy experiments, due to its reliability and relatively high robustness. This regularization analysis is implemented in *DeerAnalysis toolbox*[111] optimized for MATLAB, and has been developed by G. Jeschke. For more general cases of Tikhonov regularization for Fredholm integral equation of the first kind, *FTIKREG* program, that has been developed by J. Weese for Fortran, is very useful.[109]

Alternatively to Tikhonov, *maximum entropy* regularization analysis can be used to obtain reliable distances.[113]

As shown above, an ill-posed problem can be mathematically stabilized by introduction of additional regularization parameter α that is the most general approach. Another way of mathematical stabilization of such kind of problems is introducing an assumption about the shape of distance distribution function $P(R)$. Thus, a solution of $P(R)$ with an assumption of one or two Gaussian peaks, that requires introduction of only few parameters, also stabilizes the ill-posed problem.[111] In cases of poor signal-to-noise ratios, where Tikhonov regularization might fail, this analysis is useful. For example, by comparing the series of relevant samples, it can be used to quantify the general tendency of distance variations. However, such analysis is not model-free as Tikhonov regularization and should be used with care.

4. Distance determinations using novel paramagnetic tags

The experimental part of the thesis consists of three sections. Description of the EPR-based distance measurements with trityl paramagnetic tags is given in the first section. Subsequently the distance measurements with high-spin manganese centers are presented. The distance determinations between a Mn^{2+} center and a nitroxide radical as well as between two Mn^{2+} centers are described.

4.1 Trityl radical

All advantages and peculiarities of trityl radicals have been discussed in sections 2.1 and 1.2. Dipolar EPR spectroscopy studies were performed on trityl biradical model system,[114] shown in Figure 21A. At Q-band frequencies (34 GHz) the width of the EPR spectrum of this paramagnetic center is very narrow (30 MHz at the level of 5% of maximum of signal intensity), such that the standard microwave pulses of our Q-band EPR spectrometer are capable of exciting the whole spectrum. Thus, the optimal EPR dipolar spectroscopy experiments are DQC and SIFTER (discussed in detail in sections 3.3.2 and 3.3.3, respectively). Upon increasing the microwave excitation frequency up to G-band, the trityl EPR spectrum broadens (130 MHz at the level of 5% of maximum), due to greater impact of the axially symmetric $\bar{\boldsymbol{g}}$-tensor at this high frequency. As the excitation bandwidth of the standard microwave pulses of our G-band setup is significantly smaller than the width of the EPR spectrum, optimal dipolar spectroscopy experiment is PELDOR (detailed description is given in section 3.3.1).

Summary of the dipolar spectroscopy experimental data and analysis based on Tikhonov regularization is presented in Figure 21. EPR dipolar spectroscopy experiments revealed pronounced dipolar oscillations, indicating relatively rigid structure of the trityl biradical (background-corrected time traces are shown in Figure 21B). The dipolar modulation depth varied for different dipolar spectroscopy experiment. Thus, after subtraction of the exponential background from Q-band DQC time trace, the modulation depth was 1, which was in agreement with DQ filtering, which should only pass the dipolar coupling signal. For SIFTER experiment the background function was obtained by performing the experiment on a trityl monoradical and resembled a Gaussian function, as has been shown in initial SIFTER study by G. Jeschke.[98] The background-corrected SIFTER time trace (Figure 21B) was obtained by division of the raw experimental time trace and the Gaussian shape background, corresponded for trityl monoradical SIFTER data. As the background function of SIFTER time trace was obtained

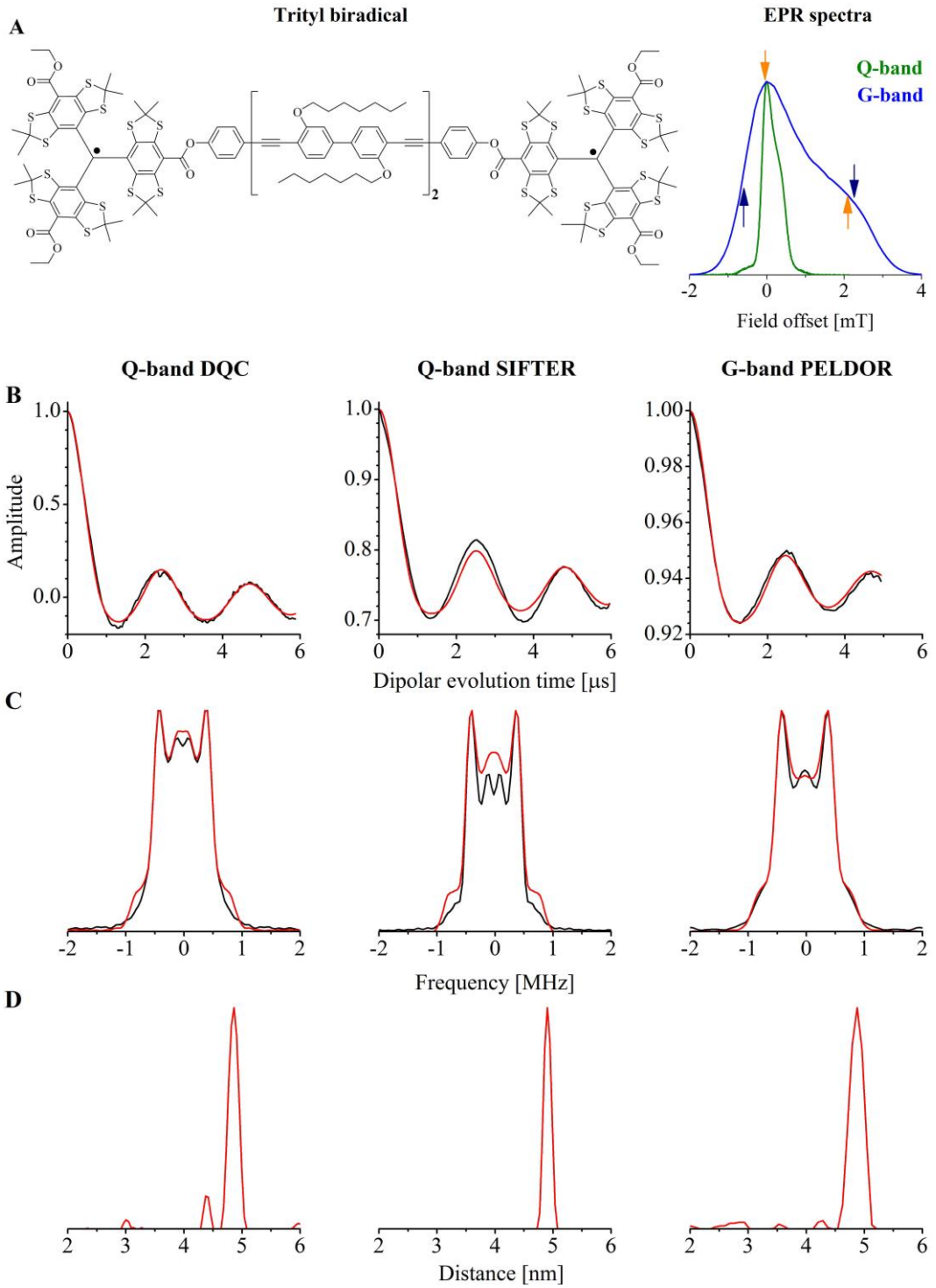

Figure 21. A: Chemical structure of trityl biradical (left) and corresponding EPR spectra (right). EPR spectra at Q- (green) and G- (blue) band frequencies were obtained at sample temperature of 50 and 25 K, respectively. Axis of abscissas represents the field offset from the maximum absorption position. Color coded up-down sets of arrows on G-band EPR spectrum represent two probe-pump resonance positions for PELDOR experiments. B: Background-corrected dipolar spectroscopy time traces (black) and back-calculated time traces based on Tikhonov regularization analysis (red). Q-band DQC (left) and SIFTER (middle) time traces were obtained at 50 K and G-band PELDOR (right) was obtained at 25 K. Frequency of pulses in DQC and SIFTER experiments was set on resonance with the maximum absorption position in the spectrum (0 mT offset). G-band PELDOR time trace is a sum of two time traces obtained at resonance positions shown in the spectrum. C: Corresponding Fourier transforms of experimental (black) and back-calculated (red) time traces. D: Corresponding distance distributions yielded by Tikhonov regularization analysis of the time traces.

differently compared to DQC one, the modulation depths seen in Figure 21B, cannot be compared with each other directly. It is important to notice, that up to now no theoretical description of background functions for single frequency dipolar spectroscopy experiments (DQC, SIFTER and RIDME) exists and background-correction procedure has more empiric character. Imperfections in obtaining the backgrounds also resulted in slight deviations of Fourier transforms of the corresponding time traces and distance distributions, obtained by Tikhonov regularization analysis (section 3.3.5). The most probable distances obtained from both experiments was 4.9 nm, consistent with literature data.[114,115] For our results, the advantages of SIFTER over DQC are higher sensitivity (about a factor of 4 larger signal-to-noise-ratio) and less complicated procedure for setting up the experiment in terms of shorter phase cycle for the microwave pulses.

G-band PELDOR experiments were obtained at two different resonance positions in the EPR spectrum, as shown in Figure 21A. The reason for obtaining multiple time traces was weak spectral anisotropy (orientation selection effects), arising from relatively rigid geometry of the trityl biradical and resolved axial $\bar{\boldsymbol{g}}$-tensor anisotropy, leading to more selective excitation of different molecular orientations with respect to Q-band. This weak orientation selection can be further reduced by addition of several PELDOR time traces that provides in effect more uniform excitation of all distance vector orientations with respect to the external magnetic field. As orientation selection was weak, addition of only two time traces, obtained at the spectral positions as shown in Figure 21A, was sufficient. This is indicated by the Fourier transform of the summed time trace (Figure 21C - right), resembling the complete Pake pattern and being consistent with Q-band DQC and SIFTER experiments. The most probable distance, yielded by Tikhonov regularization analysis of the summed G-band time trace, was 4.9 nm which was in agreement with the results of Q-band dipolar spectroscopy experiments.

These measurements demonstrate that the choice of the dipolar spectroscopy technique is dependent on the EPR-spectroscopic properties at a given microwave frequency. If excitation of the whole EPR spectrum of identical paramagnetic tags with microwave pulses is possible, the use of DQC and SIFTER dipolar spectroscopy experiments is beneficial in terms of higher sensitivity. SIFTER experiment appears to give even higher sensitivity than DQC and requires less demanding phase cycle and, therefore, easier set up of the experiment. The drawback of these single frequency techniques is that theoretical description of background functions is absent, that might lead to uncertainties and errors in the data analysis, especially in flexible systems, for which dipolar oscillation dampens very quickly. Upon increasing the microwave frequency, the width of EPR spectrum is far beyond the excitation bandwidth of available

microwave pulses, leading to PELDOR being the experiment of choice. Sensitivity of this experiment with trityl radical is higher than with conventional nitroxide radical.

In conclusion of this section, the results showed the high potential for utility of this kind of paramagnetic tag in dipolar spectroscopy applied for structural biology studies. Of particular interest is the relatively high chemical stability of trityls in cells, enabling studies of biomacromolecules in their native environment. Such studies has been challenging task for common structural biology methods, like X-ray crystallography and cryo-EM. On the other hand, trityl in combination with nitroxide radical, which are referred to as orthogonal tags, can be useful for determining inter- and intramolecular interactions in multi-subunit macromolecular complexes, such as membrane protein-ligand complexes. Thus, by labelling different subunits with orthogonal labels (*e.g.* larger molecule (membrane protein) labelled with two trityl radicals and smaller ligand/cofactor with nitroxide), inter- and intra-subunit distances can be concurrently determined with only one sample.

A third orthogonal paramagnetic tag to a pair of trityl and nitroxide organic radicals is a metal ion. Among numerous paramagnetic metal ions, manganese is of growing interest, as it is endogenous in biological systems and can readily replace magnesium ion,[116] an essential cofactor in many biomolecules. Mn^{2+} ion forms very complex spin system, having an electron and nuclear spins of 5/2 (for more details reader is refereed to section 3.1.2), that prevented it from use for dipolar spectroscopy applications, even despite the biological importance.

4.2 Manganese centers

4.2.1 Manganese center and nitroxide radical

To assess dipolar spectroscopy experiments with high-spin Mn^{2+} ions, as a first step a model compound, containing a Mn^{2+} ion coordinated by bis-terpyridine ligand was synthesized by J. Plackmeyer in our laboratories. Detailed description of EPR properties of Mn^{2+} is given in section 3.1.2. As an orthogonal spin, a conventional nitroxide radical was chosen (chemical structure of the system is shown in Figure 22A). This Mn^{2+} complex had relatively large ZFS with parameter D of about -1.5 GHz,[117] resulting in a very broad Q-band EPR spectrum (Figure 22C) with unresolved sextet of hyperfine structure lines of the central transition. The line broadening of the central transition can be roughly estimated by using second-order perturbation theory, as discussed previously (eq. 3.1.41). Nitroxide Q-band EPR spectrum of this model compound was relatively narrow and more intense and superimposed on the featureless Mn^{2+} spectrum (Figure 22C). At a higher microwave frequency, G-band, the

situation was different. The central transition of the Mn^{2+} ion EPR spectrum narrowed, while the nitroxide spectrum broadened. This difference is due to the spectral shape of Mn^{2+} being dominated by ZFS, while the major contribution to the nitroxide spectrum starting from Q-band frequency is $\bar{\boldsymbol{g}}$-tensor anisotropy. Mn^{2+} ion, being a high spin system, has larger transition moment with respect to nitroxide (eq. 3.1.39), resulting in shorter optimal lengths of the microwave pulses. Furthermore, these spins have different relaxation characteristics. Thus, exploiting differences of EPR properties of Mn^{2+} and nitroxide tags, corresponding EPR spectra can be sampled independently by changing only the pulse settings, as demonstrated in Figure 22D, and as has been reported for a Gd^{3+} system coupled to a nitroxide.[118]

Distance measurements on the Mn^{2+}-nitroxide system were performed by PELDOR technique. The background-corrected PELDOR time traces, obtained at Q-band frequencies, are depicted in Figure 22 B. The time traces were recorded by probing Mn^{2+} and pumping nitroxide spins (Figure 22B left) and vice versa (Figure 22B right) with a frequency offset between probe and pump pulses of ± 90 MHz. Both PELDOR time traces revealed pronounced dipolar oscillation, indicating a relatively rigid geometry of the model system. Tikhonov regularization analysis (Figure 22C right) revealed most probable distance of 2.65 nm that was in good agreement with predictions, based on analysis of the crystal structures of similar compounds.[119–121] Significantly more intense EPR spectrum (Figure 22C left) and higher transversal relaxation time of nitroxide spins with respect to spins of Mn^{2+}-bis-terpyridine system made it beneficial to obtain PELDOR by probing the nitroxide spins, despite their longer longitudinal relaxation time (Figure 22B). Furthermore, when probing Mn^{2+} spins, slight distortion in the time traces was observed, that resulted in the small intense artificial peak at about 2.1 nm in the distance distribution. One of the possible explanations for this peak is the occurrence of oscillation due to nuclear spin couplings. Averaging of this kind of oscillation requires stepping of a d_1 time interval for a period of nuclear Larmor frequency (PELDOR sequence given in Figure 15) and has been shown to be efficient for relatively long transversal relaxation times, however this was not the case for Mn^{2+} spins. Another possible explanation is imperfect fulfillment of the high-field approximation for ZFS of Mn^{2+}-bis-terpyridine complex that might lead to non-zero contributions to the secular term of the dipolar coupling Hamiltonian. Similar effects have been observed in PELDOR experiments on the orthogonal pair, consisting of a Gd^{3+} ion and a nitroxide radical[118] and has been studied for Gd^{3+} spins in detail elsewhere.[81,122] As can be seen from the distance distributions shown in Figure 22C, occurrence of distortions in the PELDOR signal, did not influence the main distance peak at 2.65 nm.

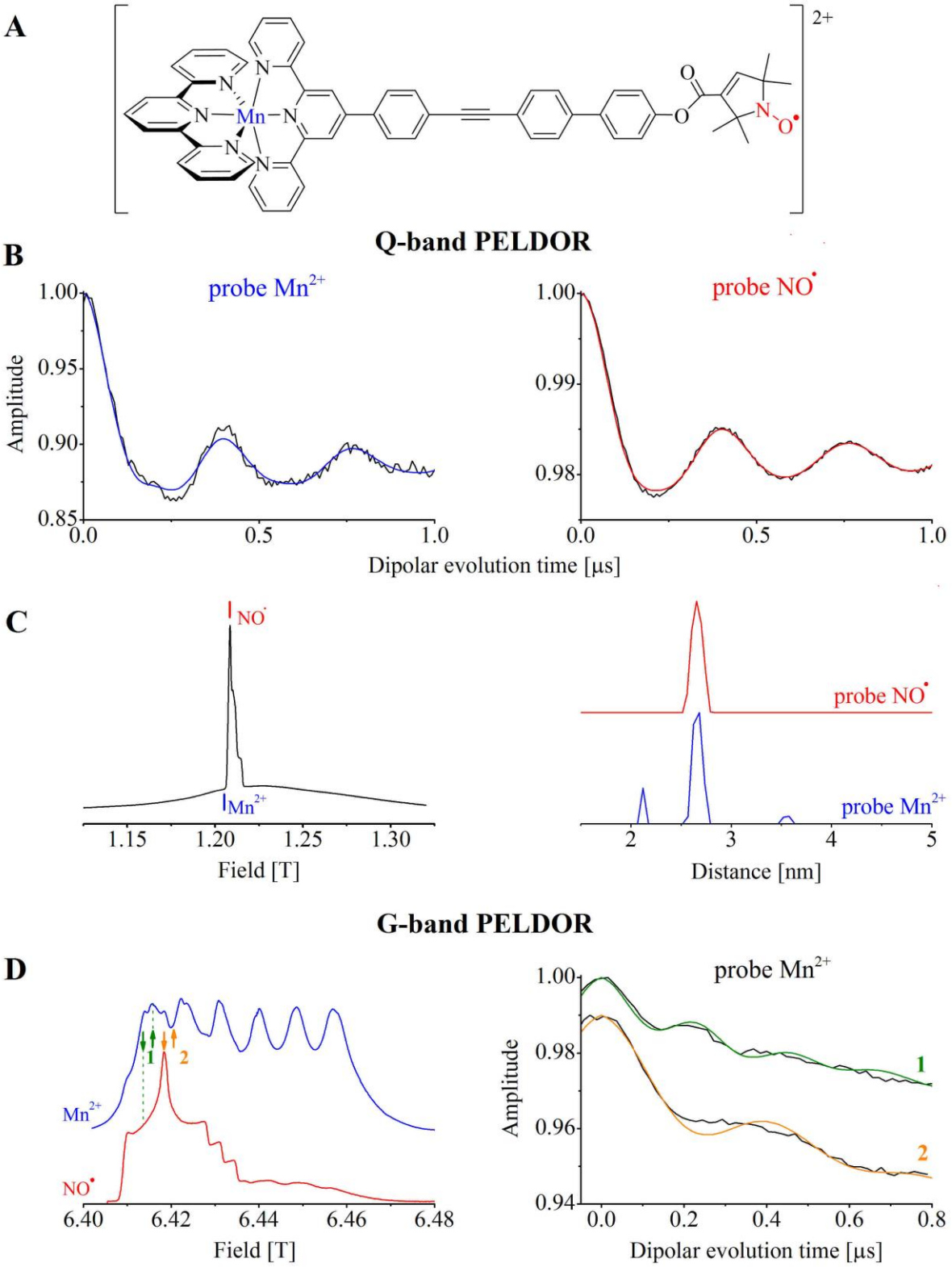

Figure 22. A: Chemical structure of Mn^{2+} - nitroxide complex. B: Background-divided Q-band PELDOR time trace obtained by probing Mn^{2+} (left) and nitroxide (right) spins at sample temperature of 5 K. C: Hahn-echo detected Q-band EPR spectrum obtained with pulse settings optimized for Mn^{2+} spins (left). Pump-probe spectral position for PELDOR experiments are shown by vertical bars (pump probe offset is ±90 MHz). Distance distributions obtained by Tikhonov regularization analysis of corresponding time traces (right). D: G-band Hahn-echo detected EPR spectrum recorded with pulse setting optimized for Mn^{2+} and nitroxide spins and obtained at sample temperature of 10 K (left) and PELDOR time traces (10 K) obtained at spectral positions 1 and 2 (right).

Dipolar modulation depth is larger when pumping the nitroxide spins, that is attributed to its significantly narrower EPR spectrum and, therefore, higher pumping efficiency (eq. 3.3.5). However, reduced modulation depth in PELDOR experiment, obtained when probing the nitroxide spins, is compensated by significantly larger signal intensity and longer transverse relaxation time of these spins. Taking this fact into account and due to observation of no distortions when probing the nitroxide spins, we conclude that for a given complex it is beneficial to perform PELDOR experiments upon probing this spin system. The situation can be completely different in EPR-based distance measurements when using a Mn^{2+} complex with smaller ZFS parameters. For further dipolar spectroscopy studies with Mn^{2+} spins, such observations have been taken into consideration, and a Mn^{2+}-DOTA complex, revealing significantly smaller ZFS parameters, has been chosen as a paramagnetic tag.

To conclude this part, our experiments demonstrate, that with Q-band, the most widely used frequencies in modern EPR spectroscopy, highly accurate distance measurements can be measured by exploiting Mn^{2+} centers in combination with orthogonal nitroxide radical.

To test the performance of PELDOR experiments at higher frequencies, we carried out G-band measurements. As mentioned above, at these high frequencies each line of the hyperfine structure sextet of Mn^{2+} central transition narrows and becomes more intense. This might lead to higher sensitivity upon probing these spins in PELDOR experiments at G-band frequencies, compared to corresponding experiment performed at Q-band frequencies. Conversely, with applications of high frequencies nitroxide EPR spectrum broadens due to significantly higher resolution of the $\bar{\boldsymbol{g}}$ -tensor anisotropy. This might result in the occurrence of spectral anisotropy of PELDOR signals. Thus, in order to test these effects, PELDOR experiments, obtained by pumping the nitroxide spins, were performed at two spectral positions, as marked by 1 and 2 in G-band spectrum (Figure 22D left).

The experimental time traces, shown in Figure 22D (right), yielded frequency of dipolar oscillation that was dependent on the spectral position of the pump pulse, indicating indeed the presence of orientation selection effects. Such observation is of interest, because orientation selective PELDOR signals can yield additional information about geometry of studied molecules, as has been demonstrated in studies of nucleic acid molecules, labelled with rigid nitroxide tags.[123,124] On the other hand, it requires sampling of multiple resonance positions throughout the EPR spectrum and significantly complicates data analysis. As PELDOR time traces were obtained only at two different spectral positions, and taking into account that orientation selection effect originates only from one spin in the pair, it was not possible to obtain distance and angular information with such small amount of the experimental data

unambiguously. Therefore, we performed simulation of the PELDOR signals only to follow changes to the dipolar coupling frequency as a function of the resonance position of pump pulse. The crystal structures of similar compounds[119–121] were used in our simulations. As these structures represent a static picture, we included Gaussian distribution for a mean distance of the width of 0.15 nm, as determined from Q-band PELDOR experiments. It is important to note, that the linker of the model compound (Figure 22A) allows rotation of the nitroxide moiety around its mean axis that, however, this was not introduced into the model. The two calculated G-band time traces are shown in Figure 22D (right). The period of dipolar oscillation as a function of the spectral position was in agreement with that yielded by the experimental PELDOR signals. However, dipolar oscillation of the experimental time traces dampened quicker than in simulated ones which might have been due to the absence of rotation of the nitroxide moiety in the model.

Another important issue is that dipolar modulation depths from our simulation were both about a factor of 2.8 larger than those revealed by the experiments. These reduced experimental values were also consistent with the corresponding Q-band PELDOR time trace, where a modulation depth of 0.11 was also smaller compared to expected value of 0.25[a]. Similar observations at both microwave frequencies led us to conclusion that for part of the molecules Mn^{2+} spins were not coupled to nitroxide spins, indicating partial decomposition of the compound in solution. This assumption is supported by a mass spectrum, in which peaks, corresponding not only to the model compound, as shown in Figure 22A, but also for Mn^{2+}-bis-terpyridine complex alone were observed.

In conclusion, our measurements demonstrate, that accurate distance measurements between a Mn^{2+} ion and a nitroxide radical can be performed at standard Q-band frequencies. Distances can be determined from PELDOR time traces using standard Tikhonov regularization analysis. Upon application of higher frequencies orientation selection effect, arising from $\bar{\boldsymbol{g}}$-tensor anisotropy of a nitroxide radical, significantly contributes to the PELDOR signals, that is potentially interesting, as such experimental observation can be exploited to extract additional information about structure of a molecule of interest. We believe, that these experimental results have the potential for biological applications, for example for studying nucleotide binding domains in proteins and locating metal binding sites in nucleic acids, especially in cases where conventional methods such as X-ray crystallography could not be used.

[a] The value of 0.25 is routinely achieved with our Q-band setup (20 ns pump pulse length) on 100% dipolar coupled nitroxide system.

4.2.2 Two manganese centers

After describing distance measurements on orthogonal pair of Mn^{2+}-nitroxide spins we approach distance measurements between two Mn^{2+} ions, which is a more complex spin system. Dipolar spectroscopy studies on a dipolar-coupled manganese system is performed with Mn^{2+}-DOTA centers. This center has advantages over Mn^{2+}-bis-terpyridine in terms of a significantly smaller ZFS and higher chemical stability. The ZFS parameter *D* of 280 MHz, as determined elsewhere,[125] should result in significantly higher sensitivity with respect to Mn^{2+}-bis-terpyridine center. In order to study peculiarities of distance measurements between two Mn^{2+}-DOTA centers with respect to standard nitroxide radical, two molecules were synthesized: one being doubly-labelled with nitroxides, while another with MnDOTA centers, based on the same rod-like linker (chemical structure is given in Figure 23A).

Nitroxide-based distance measurements were performed with Q-band PELDOR technique. The Hahn-echo detected Q-band EPR spectrum is shown in Figure 23B (left). The PELDOR time traces were obtained across the whole EPR spectrum (background-divided time traces are depicted in Figure 23B middle). The frequency offset between probe and pump pulses was kept at 50 MHz, except for a time trace shown in magenta, where the frequency offset was -50 MHz. The time traces revealed modulation depth of up to 0.24 and different oscillation frequencies, indicating orientation selectivity. The orientation selection effects can be qualitatively rationalized in terms of geometry of the molecule and maps of molecular orientations (Figure 4 - middle spectrum) excited by the microwave pulses at respective resonance positions. For the PELDOR time traces, depicted in orange and green, the detection pulses were resonant with the lower field edge of the EPR spectrum, in which the g_{xx} component of the $\bar{\boldsymbol{g}}$-tensor had a relatively large contribution to the excited orientations (Figure 4). The pump pulse for these two experiments also excited considerable amount of these orientations. As the *x* axes of the $\bar{\boldsymbol{g}}$-tensor of the nitroxide moieties were aligned along to mean linker axis of the molecule (Figure 23A), the molecules with $\boldsymbol{R}$ vector orientations, aligned parallel to the magnetic field vector $\boldsymbol{B_0}$, gave significant contribution to these two PELDOR signals (Figure 23B). This resulted in the oscillation with doubled dipolar coupling frequency having considerable contribution to the overall signal. For the green time trace, increased contribution from other molecular orientations (g_{yy} and g_{zz} that corresponds to perpendicular orientations of $\boldsymbol{R}$ vector) gave rise to a component, oscillating with single dipolar coupling frequency, which had the weight larger than in PELDOR time trace depicted by orange. For all other time traces,

the g_{xx} component only had a minor contribution to the signal, which resulted in time traces that lacked the parallel orientation of the dipolar coupling tensor.

Orientation selection effects were decreased by summation of the time traces that in effect provides more uniform excitation of all vector ***R*** orientations. Fourier transform of the summed PELDOR time trace (shown by black in Figure 23B - middle) resembled complete Pake pattern. This time trace was consequently analyzed by conventional Tikhonov regularization analysis that yielded the most probable distance of 3 nm (Figure 23B - right). This distance was in agreement with the crystal structure. The small distance peak at about 2.4 nm was a result of not perfect averaging of the orientation selection effects by the procedure described above. The width of distance distribution at half maximum of 0.1 nm was attributed to the bending flexibility of the molecular linker (Figure 23A - left) and rotation of the single bonds of the molecule.

To summarize this part, strong orientation selection was observed in Q-band PELDOR experiments on bisnitroxide molecule with a rigid structure. Dipolar modulation depth was up to 0.24, leading to relatively high sensitivity of these measurements. The most probable distance of 3 nm, obtained by means of Tikhonov regularization of summed PELDOR time trace, was in perfect agreement with crystal structure.

The EPR experiments performed on the corresponding molecule, doubly-labelled with MnDOTA centers, are depicted in Figure 23C. These experiments were performed at W-band frequencies due to initial higher sensitivity of these frequencies compared to Q-band. The Hahn-echo detected EPR spectrum is characterized by six very narrow lines of the central transition of MnDOTA complex, each separated by 252 MHz corresponding to the ^{55}Mn hyperfine coupling constant. Such a narrow width of the lines is due to very small ZFS of this complex that is advantageous in terms of increased sensitivity. Orientation selection effects are expected to be negligible with respect to corresponding nitroxide case, due to broad distribution of ZFS parameters of Mn^{2+}, and therefore, significant overlapping of multiple orientations and m_S, m_I states that have the same resonance conditions. The PELDOR time traces were obtained with pump-probe pulses set at three different resonance positions in the EPR spectrum, as depicted in Figure 23C (left). The modulation depth for these experiments (up to 0.017) was approximately an order of magnitude smaller than for nitroxide measurements (up to 0.24) at Q-band frequencies. This was attributed to significantly larger width of the EPR spectrum of Mn^{2+} centers, as discussed in previous section. Similar modulation depth for dipolar- coupled Mn^{2+} centers have been reported elsewhere.[57,125–127] The modulation depth for the time trace, obtained by pump and probe two neighboring hyperfine lines (red arrows in the EPR spectrum

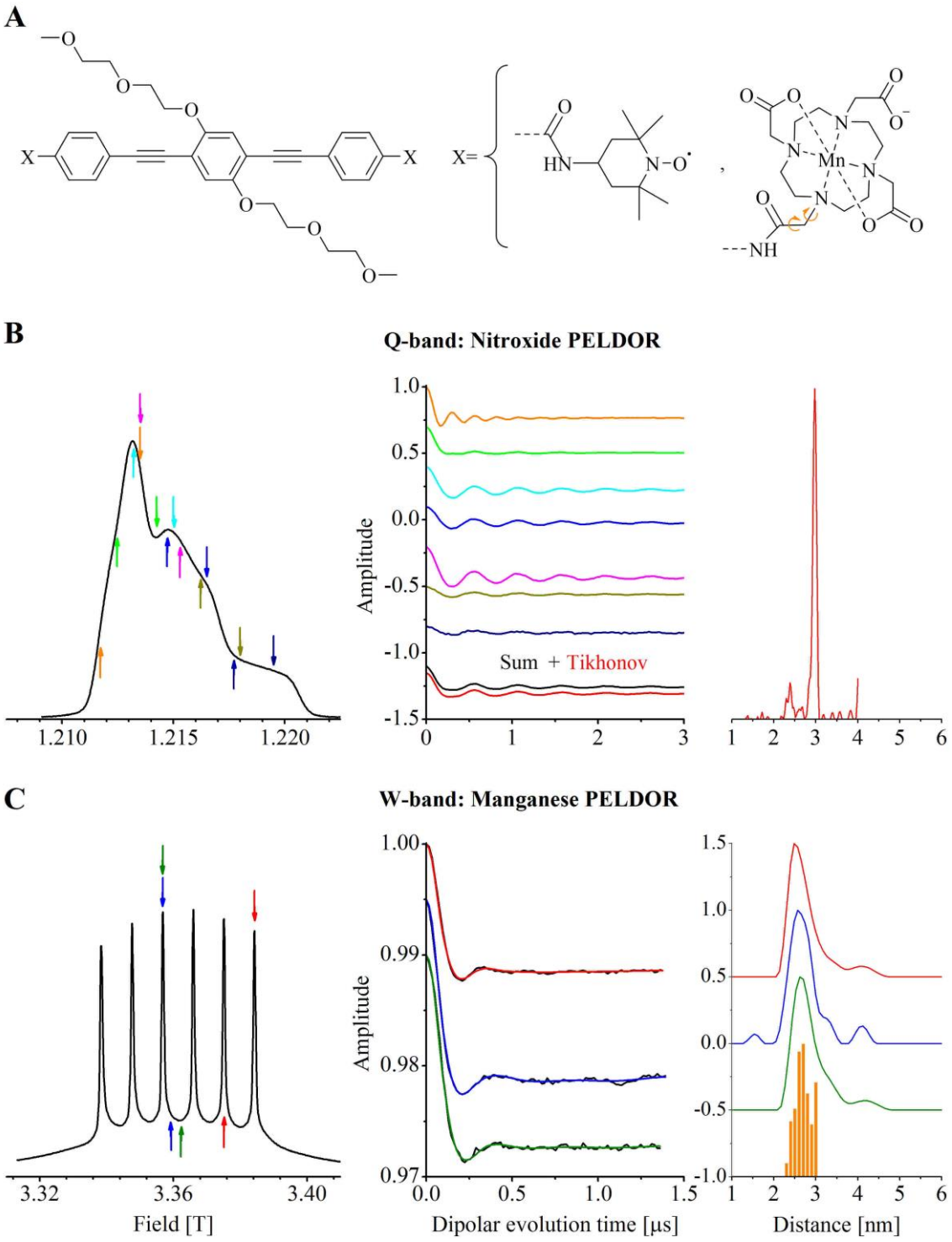

Figure 23. A: Chemical structure of nitroxide and Mn2+ model compounds.B: Hahn-echo detected EPR spectrum of nitroxide compound at Q-band frequencies with pump (down-arrows) and probe (up-arrows) pulse positions for PELDOR experiment (left); the same color of down/up arrows represents one PELDOR experiment. Corresponding background-divided PELDOR time traces (middle); summed PELDOR time trace and back-calculation, based on Tikhonov regularization, are depicted in black and red, respectively. Distance distribution based on Tikhonov regularization of summed PELDOR time trace (right). Experiments performed at 50 K. C: Hahn-echo detected EPR spectrum of Mn^{2+} compound at W-band frequencies (left). The background-divided PELDOR time traces (black) with back-calculations based on Tikhonov regularization (middle) with colors, corresponding to the spectral positions (arrows in the spectrum). Distance distributions, obtained by Tikhonov regularization of the experimental time traces and rotamer analysis, shown as histograms (right). T = 6K.

Figure 23C), was smaller (0.012) compared to other two time traces (0.016-0.017). This is due to increased length of the pump pulse, associated with larger resonator over-coupling that was needed for the frequency offset which corresponded to the hyperfine coupling constant of 252 MHz. The reduced value of modulation depth, however, did not lead to lower sensitivity for this PELDOR time trace, but in contrast, this measurement (252 MHz offset) revealed the highest sensitivity (see Table 1, where the signal-to-noise ratios per square root of the total accumulation time are given). This was achieved due the probe pulses being set on resonance with the 5th hyperfine component line of the central transition, resulting in significantly larger echo signal intensity that improves the sensitivity.

The dipolar oscillation of the Mn^{2+} PELDOR time traces dampens quicker than for corresponding nitroxide time traces, indicating broader manganese interspin distance distribution. Tikhonov regularization analysis revealed the most probable distance of about 2.5 - 2.6 nm with a full width at half maximum of about 0.6 nm. The broader distance distribution was attributed to the internal flexibility of the Mn^{2+} spin tags. The arm, tethering MnDOTA center to the linker, allows for rotation around two single bonds, as indicated by orange arrows in Figure 23A (right side). Thus, the rotamer analysis, in which the distances between two Mn^{2+} were examined upon rotation of these single bonds of both tethering arms, revealed the distance distribution (Figure 23C - right, orange histogram), resembling that obtained by Tikhonov regularization analysis of the PELDOR time traces. Thus, the Mn^{2+}-DOTA centers based distance measurements reveal additional broadening due to internal flexibility of the tethering arm that will consequently lead to decreased accuracy of distance determination.

It is worth noting, that for high spin systems influence of the pseudo-secular term of the dipolar coupling Hamiltonian (see section 3.1.3) is stronger when compared to spin 1/2 systems, as has been shown for dipolar-coupled Gd^{3+} spin system.[81,82,128] For the cases where the difference between the resonance frequencies of two spins in the pair is not significantly larger than dipolar coupling frequency, enhanced contribution from the pseudo-secular term leads to dampening of the dipolar oscillation in PELDOR signals that is not associated with the flexibility of the molecule. It has been demonstrated for Gd^{3+} systems, that such contribution is dependent on the ZFS and its distribution as well as on the pump-probe frequency offset for a given distance.[82,128] For short distances the Gd^{3+} complexes with larger ZFS and/or large offsets in PELDOR experiments are required to avoid additional dampening of dipolar oscillation. Alternatively, use of RIDME experiment can be beneficial as it intrinsically provides large differences of resonance frequencies of two spins.[83] For dipolar-coupled Mn^{2+} spin system contribution from the pseudo-secular term is expected to be reduced, as discussed in section

3.1.3. To show this experimentally, PELDOR time traces were obtained with three different frequency offsets for pump and probe pulses with absolute values of 70, 150 and 252 MHz. The offset of 252 MHz provides excitation of two different hyperfine components of the central transition of manganese spins. No considerable changes of PELDOR time traces and corresponding distance distributions were observed. Moreover, the widths of distance distributions were consistent with predictions, based on rotamer analysis (Figure 23C - right). Thus, these experimental observations suggested only insignificant contribution from the pseudo-secular term of the dipolar coupling Hamiltonian for dipolar-coupled Mn^{2+}-DOTA centers with a given distance.

To summarize, PELDOR measurements with two Mn^{2+} centers yielded the distance of 2.5 - 2.6 nm and the width of distance distribution of 0.6 nm, that is consistent with the predictions, based on rotamer analysis. Relatively high sensitivity can be achieved by performing the measurements by probing and pumping two neighboring hyperfine component lines of the central transition. Consistency of the experimental distance distributions with prediction indicated the insignificant contribution from the pseudo-secular term of the dipolar coupling Hamiltonian. This observation together with absence of spectral anisotropy led the conventional approach for analysis of PELDOR measurements, based on Tikhonov regularization as implemented in DeerAnalysis toolbox, to be also applicable for high-spin Mn^{2+} centers.

An important parameter that governs sensitivity of dipolar spectroscopy measurements is the dipolar modulation depth. For Mn^{2+}-based PELDOR measurements it is typically an order of magnitude smaller compared to measurements performed with nitroxide radical, leading to lower sensitivity. Attempt to increase sensitivity of metal-based PELDOR measurements have been performed on Gd^{3+} ions. Thus, significant improvement has been achieved by using double-mode resonator structures[128,129] as well as shaped broadband pump pulses[130] and spin sublevel pre-polarization techniques.[131] Another interesting approach has been the use of RIDME, which is significantly less experimentally demanding as aforementioned PELDOR experiments. Thus, this approach was also chosen in the thesis.

Theoretical basics of RIDME experiment is given in section 3.3.4. RIDME-based distance measurements were performed at two microwave frequencies: W - (94 GHz) and J - (263 GHz) bands. The experimental RIDME time traces on Mn^{2+} compound (Figure 23A) in protonated and deuterated solvents are shown in Figure 24A by magenta and black curves, respectively. In this figure also the reference W-band RIDME measurements, obtained on mono-Mn^{2+}-DOTA complex, are depicted (Figure 24A, middle). RIDME experiments on bis-

Mn^{2+} model compound, in which the store times were chosen accordingly to T_{1e} for a given frequency, yielded dipolar modulation depth of up to 0.55 (Figure 23A). This value was approximately a factor of 30 larger than that, achieved in PELDOR experiments, constituting a significant gain in sensitivity with RIDME. Another noticeable observation with this dipolar spectroscopy experiment was a strong dependence of the signal decay on the deuteration of the solvent (Figure 24A). Thus, the RIDME signals decay considerably quicker for the case of protonated solvent (time traces depicted in magenta in Figure 24A), such that almost no signals were observed at dipolar evolution time of 1.5 µs. The reason for such observation is that the background function in RIDME experiment is more complex than in PELDOR, including not only inter-molecular dipolar couplings, but also transverse relaxation-related component. In the case of protonated solvent, electron-nuclear spin diffusion is considerably stronger, resulting in shorter T_{2e} and, thus, a significantly faster decay of the RIDME signals. Due to this peculiarity, further RIDME experiments were performed on compound in deuterated solvent.

The raw experimental W - (94 GHz) and J - (263 GHz) band RIDME time traces with background functions and background-divided time traces are shown in Figure 24B and 24C, respectively. The W-band time traces were obtained with two different store times: 20 µs corresponding roughly to 3 times T_{2e} (left column Figure 24B and 24C) and 80 µs corresponding approximately to the T_{1e} relaxation time at 94 GHz (middle column Figure 24B and 24C). For the shorter store time, the dipolar modulation depth was about 0.3 (Figure 24C - left) and for the longer store time it was about 0.55 (Figure 24C - middle). These modulation depths were larger compared to the predicted ones of 0.1 and 0.3 for the shorter and longer store time, respectively. The predicted values are given with an assumption of coupled spin 1/2 system (eq. 3.3.26). Deviation in the modulation depths was also observed in J-band RIDME measurements (Figure 24C - right), obtained with store time of 30 µs, which corresponds approximately to the T_{1e} relaxation time at respective frequency. Thus, experimental modulation depths was 0.37, while the predicted value was 0.3. The larger experimental values might indicate the influence of high electron spin of the Mn^{2+} spin system, and therefore, more complex relaxation behavior.

Analysis of the background-divided RIDME time traces was performed with Tikhonov regularization. Distance distributions and back-calculated RIDME time traces are shown in Figure 24D and 24C, respectively, in red. All distance distributions showed two resolved maxima rather than the one found by PELDOR (Figure 23C). Similar complex distance distributions have been observed in RIDME experiments with two Gd^{3+} ions and with Mn^{2+} - bis-nitroxide system.[83,107,132] Such observations have been attributed to harmonics of the dipolar coupling frequency, arising from multi-quantum relaxation in high-spin system.

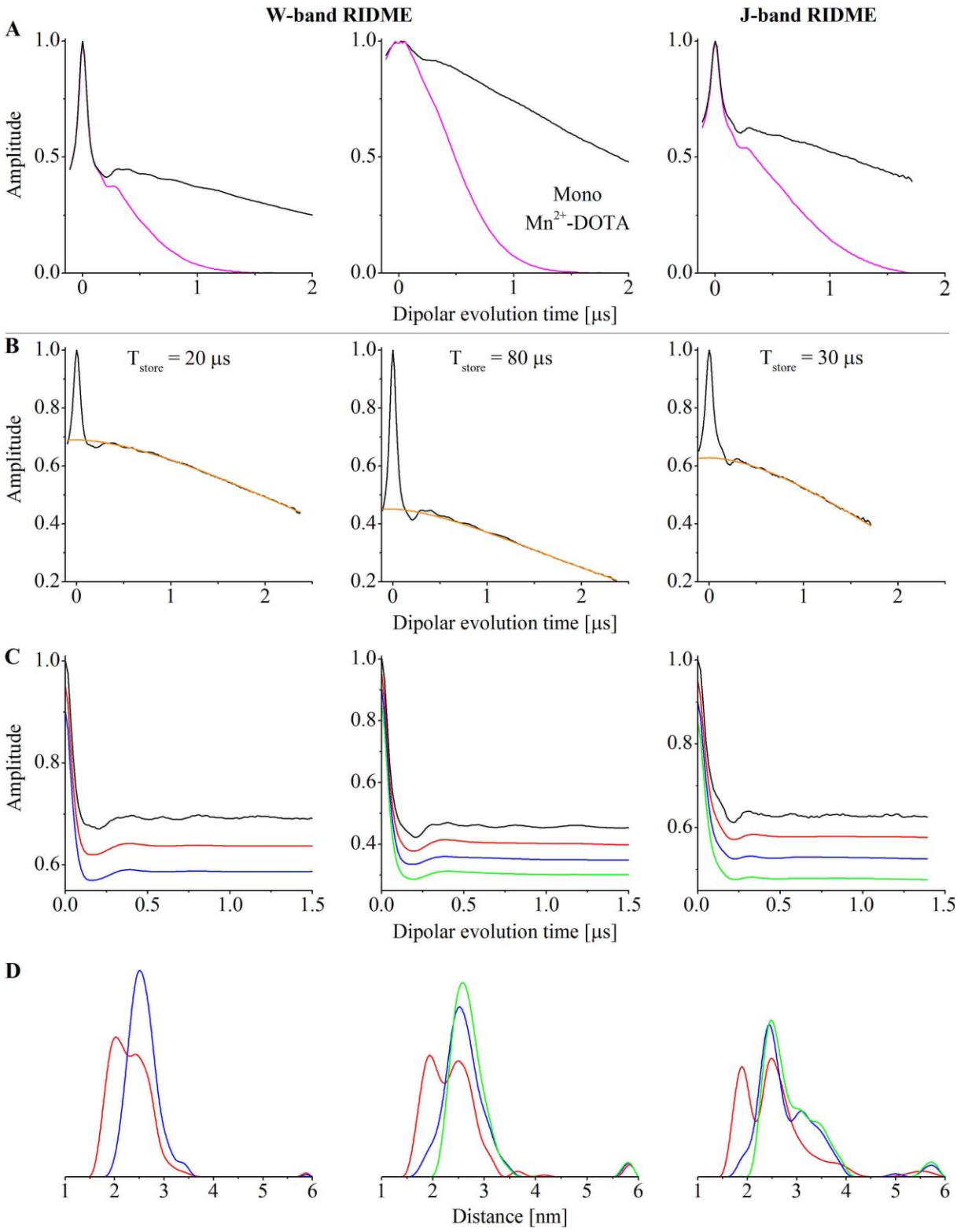

Figure 24. A: Raw experimental RIDME time traces on bis-Mn2+-DOTA complex with store times, corresponding to T1e, obtained at W - (left) and J - band (right) frequencies; reference W-band RIDME measurements on mono- Mn2+-DOTA complex (middle). Measurements are performed in deuterated (black) and protonated (magenta) solvents. B: Raw experimental RIDME time traces in deuterated solvent (black) with stretched-exponential background functions (orange). Measurements are obtained at W-band with store time of 20 µs (left) and 80 µs (T_{1e}) (middle) and at J-band with store time of 30 µs (T_{1e}) (right). C: Corresponding background-divided RIDME time traces (black) with back-calculations based on standard Tikhonov regularization analysis (red) and Tikhonov regularization with kernel (4.2.1) (blue) and (4.2.2) (green). D: Corresponding distance distributions.

The W-band RIDME time trace, obtained with 20 µs store time, and Tikhonov regularization analysis are depicted in Figures 24C and 24D (left). The distance peak at about 2.5 nm (see Figure 24D in red) was consistent with PELDOR measurements, while the peak at about 2.0 nm corresponded to the second harmonic of the dipolar coupling frequency. In order to test this assumption, this harmonic was explicitly added to the kernel function of the Fredholm equation for the Tikhonov regularization:

$$K(T,R)=\int_0^1\left(\frac{1}{2}\cos\left[\frac{52.04}{R^3}\left(3x^2-1\right)T\right]+\frac{1}{2}\cos\left[2\cdot\frac{52.04}{R^3}\left(3x^2-1\right)T\right]\right)dx \qquad (4.2.1)$$

Thus, the use of the regularization analysis with a modified kernel (eq. 4.2.1) led to the disappearance of the 2 nm peak, leaving the position of the 2.5 nm peak unchanged (Figure 24D left, distance distribution is depicted in blue). It was found that a weight of 0.5 for both components lead to the distance distribution similar to the ones found using PELDOR experiment and consistent with the rotamer analysis (Figure 23C, right).

The W-band RIDME time trace with 80 µs store time and the analysis based on Tikhonov regularization is shown in Figure 24C and 24D (middle). As in the case described above, the expected 2.5 nm distance is found by conventional Tikhonov regularization analysis (Figure 24D middle, distance distribution depicted in red). Assuming that the first and second harmonics of the dipolar coupling frequency were equally weighted, as in the short store time RIDME measurement, the distance peak at 2 nm again disappeared when the modified kernel function (eq. 4.2.1) was used in Tikhonov regularization (Figure 24D middle, distance distribution depicted in blue). However, unlike for the measurement with shorter store time, there was an additional small shoulder at about 1.8 nm in this distance distribution. To test whether this feature was due to the buildup of a triple quantum relaxation component, a kernel function having an explicit third harmonic contribution given by

$$K(T,R)=\int_0^1\left(0.425\cdot\cos\left[\frac{52.04}{R^3}\left(3x^2-1\right)T\right]+0.425\cdot\cos\left[2\cdot\frac{52.04}{R^3}\left(3x^2-1\right)T\right]+\right.$$
$$\left.+0.15\cdot\cos\left[3\cdot\frac{52.04}{R^3}\left(3x^2-1\right)T\right]\right)dx \qquad (4.2.2)$$

was used. The resulting distance distribution is shown in Figure 24D (middle) in green. When the weight of the third harmonic component in the kernel function was set to 0.15 and those of the first and second harmonics to 0.425, the 1.8 nm peak disappeared and the shape of the distance distribution more closely resembled that of the 20 µs store time RIDME and PELDOR measurements.

Reduced transverse relaxation time of Mn^{2+} spins at J-band with respect to W-band frequencies led to decrease in sensitivity of RIDME experiments. The distance distribution from the 30 μs store time J-band RIDME measurements, using conventional Tikhonov regularization analysis and that with modified kernels (eq. 4.2.1) and (eq. 4.2.2) are shown in Figure 24D (right). They were similar to the one obtained from 80 μs store time W-band measurements, with the most probable distance being consistent with expectations. However, conventional Tikhonov regularization analysis gave a wing in distance distribution that extended from 3 to 4 nm (red curve in Figure 24D - right), which was not present in neither of the W-band RIDME measurements. Tikhonov analysis with the modified kernels enhanced the intensity of this wing (blue and green curves in Figure 24D right). A possible cause for this observation might have been incomplete cancellation of the moving Hahn echo from the last two pulses (see RIDME pulse sequence in Figure 15) and refocused stimulated echo due to imperfect phases of the microwave pulses in the 8-step phase cycle. When such imperfections were accounted for, the corresponding distance distributions were comparable with that, obtained from W-band measurements.

It is worth noting, that all three RIDME time traces had small amplitude oscillations (Fourier transform of the difference between experimental RIDME time traces and back-calculations revealed multiple features in the frequency domain) with the amplitude not more than 3% of the amplitude of the dipolar oscillations. They can be partially seen in Figures 24C. These oscillations remain when the long store time W-band RIDME time trace was divided by the short store time one, that indicated a buildup of the amplitude of these oscillations with increasing the store time. Reference measurements on mono-Mn^{2+}-DOTA complex (Figure 24A - middle) also had a small amplitude oscillation but with a distinct single frequency of about 1.7 MHz. This frequency corresponded to the ^{14}N hyperfine coupling and likely arose from non-coherent ESEEM effects.[133] Importantly, the oscillations seen in RIDME measurements (Figure 24C) were so small in amplitude that they did not affect the Tikhonov analysis in any substantive way.

The results of PELDOR and RIDME experiments on bis-Mn^{2+}-complex are summarized in Table 1.

Table 1. Results of PELDOR and RIDME measurements on bis-Mn^{2+} system

Experiment	Parameter	R_{max} [nm]	ΔR ($FWHM$) [nm]	λ	$SNR/\sqrt{t}$ [$h^{-0.5}$]
PELDOR	70 MHz	2.6	0.6	0.016	60
	150 MHz	2.6	0.6	0.017	50
	-252 MHz	2.5	0.6	0.012	70
RIDME	W-band, 20μs	2.5[a]	0.6[a]	0.308	210
	W-band, 80μs	2.6[b]	0.6[b]	0.547	150
	J-band	2.5[b]	0.6[b]	0.373	50

High-frequency RIDME experiments, presented in this thesis, demonstrate that efficient distance measurements between two Mn^{2+} centers are possible. This experiments were up to 3 times more sensitive than the most sensitive PELDOR measurement (with -252 MHz pump-probe frequency offset), as indicated in last column of Table 1. However, Mn^{2+}-based RIDME experiments have some disadvantages compared to the most widely used dipolar spectroscopy technique. Thus, the background function of RIDME is more complex, having several contributions. Although it can be adequately modeled with a stretched exponential function, as has been previously demonstrated,[83,104,107] the full theoretical description is not yet present. One can also see that RIDME background strongly depends on whether the solvent protonated or deuterated (see Figure 24A), suggesting the dependence on the transverse relaxation of Mn^{2+} spins. It was demonstrated that deuterating the solvent led to much slower decay of the signal that is an important consideration for relatively long distances. A more detailed theoretical understanding of how to accurately model the RIDME background functions would be useful in terms of minimization of errors in the background-correction procedure.

As has been discussed in section 3.3.4, RIDME exploits longitudinal relaxation to change the magnetic quantum number of one of the spins in the pair. For high spins systems relaxation can change the magnetic quantum number not only by ±1, but also by ±2 units and even higher, that creates the dipolar coupling frequency harmonics in the RIDME time traces and correspondingly in the distance distributions. For relatively rigid molecules the distances can still be accurately extracted from conventional Tikhonov regularization, as presented in this thesis and elsewhere.[83,107,132] However, for more flexible systems, a common case for biomolecules, harmonics of dipolar coupling frequencies cannot be easily distinguished and the conventional Tikhonov analysis can lead to the distance distribution that deviates from the real one, even assuming that the background function has been determined correctly. But this

[a] The results obtained by Tikhonov regularization with kernel given by (eq. 4.2.1)
[b] Tikhonov regularization with kernel given by (eq. 4.2.2)

analysis can still be used to make an adequate estimation of the distance, since for flexible systems the distance is initially not well defined. For more accurate distance determination the Tikhonov regularization with the modified kernel function can be of interest. As shown in Figure 24D, with this approach the unwanted contributions from the harmonics of the dipolar coupling frequency can be removed from the distance distributions. However, the weights of the different components vary, depending on the sample and experimental conditions leading to additional parameters that must be accounted for in the data analysis. Moreover, the more complex background function of RIDME can complicate analysis of contributions from dipolar coupling frequency harmonics, as has been shown in RIDME on a protein labelled with Gd^{3+} centers.[83] These observations suggest, that accurate RIDME-based distance determination can be challenging task for flexible molecules, while for relatively rigid molecules RIDME measurements can be accurately interpreted and are efficient, yielding higher sensitivity compared to PELDOR.

Such peculiarities of dipolar spectroscopy experiments with high-spin Mn^{2+} lead us to conclusion that by using PELDOR technique, distances between two manganese centers can be determined accurately, as demonstrated for Mn^{2+}-DOTA centers. However, sensitivity of these PELDOR experiments is lower compared to that, achieved with standard nitroxide radicals due to typically lower dipolar modulation depths. Considerable gain in sensitivity of Mn^{2+} based distance measurements can be achieved by applying another dipolar spectroscopy technique, RIDME. But large sensitivity gain comes together with more complicated data analysis. Complexity of RIDME with high-spin systems can lead to less accurate distance determination compared to PELDOR, when flexible molecules are studied. This suggests, that in general case Mn^{2+}-based RIDME measurements are best suited, when accurate distances are not required, for example for determining the quaternary structures of proteins or for optimizing labelling conditions. Such applications can be performed quickly due to higher sensitivity and relative simplicity of setting up the RIDME experiment. For the cases, where more accurate distances are required, RIDME can be complemented with PELDOR, which would require longer measurement time. PELDOR experiment, performed with pump and probe pulses set on resonance with two neighboring hyperfine component lines of the central transition, has higher sensitivity with respect to other pump/probe resonance frequency settings. Therefore, it can be efficiently used to refine the RIDME measurements.

The more detailed theoretical understanding of RIDME background function and more quantitative description for the weights of dipolar coupling frequency harmonics would help to address an issue of reduced accuracy of distance determination even for flexible biomolecules.

This would make RIDME with high-spin Mn^{2+} systems very efficient and stand-alone EPR dipolar spectroscopy method that is valuable in studying catalytic active centers and long range structural rearrangements in enzymes and ribozymes during their catalytic function and for other applications.

5. Summary and outlook

Nanometric distance determinations were performed using EPR dipolar spectroscopy with novel paramagnetic tags: trityl radical and high-spin Mn^{2+} ion. The trityl radical is more stable in reducing environments, has larger relaxation times at room temperature and significantly narrower EPR spectrum compared to commonly used nitroxide radicals. Such unique properties make it a valuable alternative paramagnetic tag that is well suited for performing distance measurements on biomolecules in their native environment at physiological conditions. The Mn^{2+} ion can naturally occur in enzymes as a cofactor. Additionally it can replace Mg^{2+}, an essential cofactor in many enzymes, nucleic acids and nucleotide binding domain of membrane and G - proteins. Although these novel paramagnetic tags have unique properties and are of significant interest for structural biology applications, distance measurements using Mn^{2+} have been underexplored. Thus, this thesis is focused on studying dipolar spectroscopy experiments using these novel tags. Distance measurements were obtained on the three model systems: one containing two trityl tags, another with a high-spin Mn^{2+} ion and a nitroxide radical, and a third with two Mn^{2+} ions.

A bis-trityl model system was synthesized in the group of S. Sigurdsson (University of Iceland). Dipolar spectroscopy experiments were performed at two different microwave frequencies (34 and 180 GHz). It was demonstrated that the choice of dipolar spectroscopy technique is dependent on the properties of the paramagnetic tag at a given microwave frequency. At 34 GHz, the width of the trityl EPR spectrum is sufficiently narrow, such that standard microwave pulses are able to excite the whole spectrum. In such a case, the single-frequency dipolar spectroscopy techniques, DQC and SIFTER are optimally suited. Both experiments yielded a distance of 4.9 nm that was in excellent agreement with literature data. It was found that SIFTER measurements provided considerable gain in sensitivity with respect to DQC with a signal-to-noise ratio approximately 4 times larger. Furthermore, SIFTER is experimentally less demanding, as it requires only a short phase cycle for the microwave pulses. At high microwave frequency (180 GHz) the trityl EPR spectrum broadens due to a larger impact of the $\boldsymbol{g}$-tensor anisotropy that does not allow full excitation of the spectrum with standard microwave pulses. Therefore, the use of double frequency dipolar spectroscopy technique, PELDOR, is favorable. Due to the width of the trityl EPR spectrum being still considerably narrower than that of standard nitroxide radicals, sensitivity of PELDOR measurements with trityl was better. The high-frequency trityl-based PELDOR measurements yielded weak spectral anisotropy that was minimized by averaging the time traces. Tikhonov

regularization analysis of the resultant time trace yielded a distance of 4.9 nm, which was consistent with low-frequency measurements.

The results demonstrate that trityl paramagnetic tags can be used for highly sensitive and accurate EPR-based distance measurements. Alternatively, trityl can be used together with standard nitroxide radical. Due to significant differences in EPR properties, these paramagnetic tags are often referred as orthogonal. The notion of orthogonal spin-labelling has emerged in dipolar spectroscopy in the last decade and have great potential for studying inter- and intra-subunit interactions in large macromolecular complexes. For example, for determining the distances in a protein-ligand system, the use of two orthogonal paramagnetic tags is often sufficient, and a trityl - nitroxide radical pair can be a suitable combination. For larger complexes, consisting of three and more subunits, more orthogonal tags might be required. A third possible orthogonal label is a Mn^{2+} center, which can occur endogenously in biological systems.

To study the influence of the high-spin multiplicity of Mn^{2+} on the performance of distance measurements, two model systems were synthesized. A molecule including a Mn^{2+} and a nitroxide radical was synthesized in our laboratories by J. Plackmeyer, while another molecule with two Mn^{2+} ions was synthesized in the group of C. Policar (ENS Paris).

PELDOR experiments on Mn^{2+}-nitroxide system were performed at two microwave frequencies (34 and 180 GHz). The 34 GHz PELDOR measurements, obtained upon probing either nitroxide or Mn^{2+} spins, yielded a distance of 2.65 nm, which is in agreement with predictions, based on analysis of crystal structures of similar compounds. Probing the nitroxide spins yielded better sensitivity despite considerably lower modulation depth of the EPR signal. Besides the signal intensity, the modulation depth is an important parameter that governs sensitivity of distance measurements. Measurements obtained by probing the Mn^{2+} spins revealed distortions in the PELDOR time traces, which however did not significantly affect the results of Tikhonov regularization. Such observations can be partially attributed to relatively large Zero-field Splitting (ZFS) with parameter D of about 1.5 GHz of the Mn^{2+}-bis-terpyridine center. The high-frequency (180 GHz) PELDOR measurements, obtained upon pumping the nitroxide spins, yielded strong spectral anisotropy. Each frequency of dipolar oscillation was qualitatively rationalized by taking into account orientations of the molecules, excited by the pump pulse, and molecular geometry. Spectral anisotropy of PELDOR time traces is an interesting observation since not only the distances but also orientation of the nitroxide radical with respect to the interspin vector can be determined. If the nitroxide is rigidly attached to the

biomolecule, this could be potentially used as additional information for structure determination.

Further dipolar spectroscopy experiments on bis-Mn^{2+} systems were performed with Mn^{2+}-DOTA centers. The DOTA ligand provides a very small ZFS of Mn^{2+} spins with parameter *D* of about 280 MHz, resulting in higher sensitivity in dipolar spectroscopy experiments. The PELDOR measurements, obtained at 94 GHz, yielded a distance between Mn^{2+} centers of 2.5 -2.6 nm that was in agreement with predictions based on a rotamer analysis. The measurements gave dipolar modulation depth from 1.2% up to 1.7%, which is about an order of magnitude smaller than that achieved routinely with standard nitroxide radicals (up to 24%). To test the influence of the pseudo-secular term of the dipolar coupling Hamiltonian, PELDOR measurements were obtained with three different frequency offsets between the pump and probe pulses ranging from 70 to 252 MHz. With biggest offset, excitation of two hyperfine lines of the central transition with pump and probe pulses was possible, resulting in higher sensitivity. No significant differences were observed in the PELDOR time traces and in the corresponding distance distributions upon changing the frequency offset, suggesting only minor contribution from the pseudo-secular term. This observation in combination with the absence of spectral anisotropy made it possible to extract the distances from PELDOR measurements by conventional Tikhonov regularization analysis.

The dipolar modulation depths, that are typically observed in Mn^{2+}-based PELDOR, are significantly smaller than in experiments with conventional nitroxide tags. High-spin paramagnetic tags have a relatively broad EPR spectrum. This results in low excitation efficiency of the pump pulse that consequently decreases sensitivity of the measurements. The sensitivity issue can be addressed by the use of another dipolar spectroscopy technique, RIDME. Thus, RIDME measurements were performed at the microwave frequencies of 94 and 263 GHz. The dipolar modulation depths were up to 55 %, leading to a free-fold higher sensitivity than the most sensitive PELDOR measurements (252 MHz frequency offset). The RIDME measurements featured a more complex background function, including not only intermolecular dipolar couplings but also contribution from transverse relaxation that led to a quick decay of the signal when protonated solvent was used. Furthermore, the signals contained harmonics of the dipolar coupling frequency, originating from more complex relaxation of high-spin systems, that is able to change the magnetic quantum number of a spin in the pair not only by 1, but 2 units and higher. These features can lead to reduced accuracy of the distance determination in cases where flexible molecules are studied. The multiple-contribution background function can be adequately modelled with a stretched-exponential function, while

harmonic contributions can be accounted for by using a modified kernel of the Fredholm integral equation for Tikhonov regularization analysis. Although analysis with the modified kernel yielded the distance distributions that are in good agreement with PELDOR measurements, interpretation of RIDME measurements is more complex and prone for errors since additional parameters must be accounted for.

Based on this observations we concluded that the RIDME technique is best suited for quantitative analysis of relatively rigid systems or cases where accurate distances are less important and sensitivity is of highest priority. For obtaining more accurate distances in cases of flexible systems, RIDME can be refined with PELDOR measurements.

The PELDOR and RIDME studies demonstrate that accurate distances can be determined by dipolar EPR spectroscopy on high-spin Mn^{2+} ions, thus extending the family of biologically relevant paramagnetic tags. The use of Mn^{2+} tags alone or in combination with orthogonal labelling by nitroxide and/or trityl radicals provides a powerful experimental toolkit for functional studies of biological systems.

The results of this thesis form the basis for further studies using novel paramagnetic tags for determining inter- and intramolecular interactions and conformational changes in macromolecular complexes, such as membrane protein-ligand complexes in their native environment. The experimental results obtained with high-spin Mn^{2+} ions are important for structural characterization of the nucleotide-binding domains of membrane transporter complexes and G-proteins or the metal centers in enzymes and ribozymes.

6. Deutsche Zusammenfassung

Gepulste dipolare EPR-Spektroskopie ist eine wertvolle Methode, um Abstände von 1.5 bis 10 nm zwischen zwei Spinmarkern zu messen. Diese Information kann für Strukturbestimmungen hilfreich sein, wo traditionelle Methoden wie Kristallstrukturanalyse und NMR nicht angewendet werden können. Zusätzlich ist es möglich, Änderungen in Konformation und Flexibilität zu verfolgen. Für diese Studien haben sich stabile Nitroxidradikale als Spinmarker etabliert. Diese werden spezifisch durch die *site-directed spin labelling* Methode (SDSL) kovalent an das zu untersuchende Biomolekül gebunden. In den letzten Jahren wurden weitere Spinmarker für Abstandsbestimmungen mittels EPR-Spektroskopie entwickelt. Besonders interessant sind Triarylmethylradikale (im Folgenden abgekürzt als Trityl) und paramagnetische Metallzentren.

Im Vergleich zu Nitroxidradikalen hat das Tritylradikal einige Vorteile: Eine höhere Stabilität in einer reduzierenden Umgebung wie im Inneren von Zellen, längere Elektronenspin-Relaxationszeiten bei Raumtemperatur und ein schmaleres EPR-Spektrum. Deswegen ist dieses organische Radikal ein alternativer Spinmarker, der besonders gut für die Forschung von Biomolekülen in einer nativen Umgebung unter physiologischen Bedingungen geeignet ist. Auch paramagnetische Metallzentren sind weniger reduktionsempfindlich als Nitroxidradikale. Zusätzlich sind diese Spinmarker interessant in biologischen Fragestellungen. Zum Beispiel besitzen zahlreiche Enzyme paramagnetische Manganzentren als Cofaktoren. Zudem kann Magnesium, ein wesentlicher Cofaktor in Enzymen, Nukleinsäuren und Nukleotid-Bindungsdomänen der G- und Membranproteine, oft durch das paramagnetische Mangan ersetzt werden. Um Abstandsmessungen an Biomolekülen, die nur ein Metallzentrum besitzen, durchzuführen, können zusätzliche Spinmarker in Form eines Nitroxid-, Tritylradikals oder eines anderen paramagnetischen Metallkomplexes mithilfe der SDSL-Methode kovalent gebunden werden.

Nitroxidradikale, Tritylradikale und Metallzentren haben deutlich unterschiedliche EPR-spektroskopische Eigenschaften, welche oft als orthogonale Spinmarker bezeichnet werden. Solche Spinmarker sind nützlich für die Untersuchung von verschiedenen Untereinheiten bei makromolekularen Komplexen. Somit können die intramolekularen Abstände innerhalb einer Untereinheit sowie intermolekularen Abstände zwischen den unterschiedlichen Untereinheiten mit nur einer einzigen Probe bestimmt werden. Zusätzlich können die orthogonalen Marker sehr effektiv genutzt werden, um Metallzentren in Biomolekülen mithilfe der Trilateration-Strategie genau zu lokalisieren.

Die hier vorliegende Doktorarbeit beschäftigt sich mit der Nutzung dieser neuen Spinmarker für Abstandsmessungen. Solche Spinmarker sind noch kaum erforscht, obwohl sie für biologische Anwendungen eine große Rolle spielen könnten.

Das erste Ziel dieser Doktorarbeit war eine Studie über Tritylradikale mithilfe der dipolaren EPR-Spektroskopie. Zu diesem Zweck wurden sowohl *double quantum coherence* (DQC) und *single frequency technique for refocussing dipolar couplings* (SIFTER) Experimente als auch Hochfrequenz *pulsed electron electron double resonance* (PELDOR) Experimente mit einem Trityl-Modellsystem durchgeführt. Dabei wurden die Besonderheiten der unterschiedlichen dipolaren Spektroskopiemethoden mit diesem Spinmarker untersucht, um die Empfindlichkeit und Robustheit für die Abstandsmessungen zu optimieren.

Das zweite Ziel war eine Studie über den Einfluss der Hochspin-Multiplizität des Mangans auf die Abstandsbestimmungen. Für diesen Zweck wurde zuerst ein Modellsystem mit einem orthogonalen Mn^{2+} Ion und Nitroxidradikal mithilfe der PELDOR-Spektroskopie untersucht. Anschließend wurde ein weiteres Modellsystem mit zwei Mn^{2+}-Ionen untersucht, um PELDOR und *relaxation-induced dipolar modulation enhancement* (RIDME) Experimente bezüglich ihrer Empfindlichkeit und Robustheit sowie Genauigkeit der Datenanalyse zu optimieren.

Das Trityl-Modellsystem wurde in der Arbeitsgruppe von Prof. Sigurdsson synthetisiert. Die EPR Messungen wurden bei zwei verschiedenen Mikrowellenfrequenzen (34 und 180 GHz) durchgeführt. Es wurde gezeigt, dass die Auswahl der optimalen Methode von den EPR-spektroskopischen Eigenschaften des Systems bei den jeweiligen Mikrowellenfrequenzen abhängig ist. Das EPR-Spektrum des Trityls ist bei 34 GHz so schmal, dass das ganze Spektrum von einem üblichen Mikrowellenpuls angeregt werden kann. In diesem Fall sind die DQC und SIFTER Experimente am besten geeignet. Der mit diesen Methoden bestimmte Abstand von 4.9 nm ist in guter Übereinstimmung mit Werten aus der Literatur. Es wurde festgestellt, dass die SIFTER Messung eine höhere Empfindlichkeit als DQC besitzt, da das Signal-zu-Rausch Verhältnis um den Faktor vier größer ist. Außerdem ist die SIFTER-Methode experimentell weniger anspruchsvoll, da ein deutlich kürzerer Phasenzyklus für die Mikrowellenpulse benötigt wird.

Bei einer höheren Mikrowellenfrequenz von 180 GHz verbreitert sich das Trityl EPR-Spektrum aufgrund der besseren Auflösung der $\boldsymbol{g}$ - Tensor-Anisotropie, daher kann ein üblicher Mikrowellenpuls das EPR-Spektrum nicht mehr vollständig anregen. Deshalb ist in diesem Fall die PELDOR-Methode besser geeignet. Aufgrund des relativ schmalen EPR- Spektrums des Tritylradikals ist die Empfindlichkeit der PELDOR-Experimente mit diesem Spinmarker

größer als unter Verwendung der üblichen Nitroxidradikale. Die 180 GHz PELDOR-Messungen zeigten eine schwache spektrale Anisotropie, die durch die Mittelung der PELDOR-Zeitspuren minimiert werden konnte. Es konnte hier ein Abstand bestimmt werden, welcher im Einklang mit den Messungen bei kleineren Mikrowellenfrequenzen ist.

Die Ergebnisse zeigen, dass der Trityl-Spinmarker für hoch empfindliche Abstandsbestimmungen verwendet werden kann. Alternativ kann das Tritylradikal zusammen mit Nitroxidradikalen benutzt werden. Wie bereits erwähnt, sind diese Marker dann orthogonal. Ein dritter möglicher orthogonaler Spinmarker ist ein Mn^{2+}-Zentrum, welches zudem in biologischen Systemen endogen ist.

Um den Einfluss der Hochspin-Multiplizität von Mn^{2+}-Zentren auf die EPR-Abstandsbestimmung zu untersuchen, wurden zwei Modellsysteme synthetisiert. Das System mit einem Mn^{2+}-Zentrum und einem Nitroxidradikal wurde in unserer Arbeitsgruppe von Dr. Plackmeyer synthetisiert. Das System mit zwei identischen Mn^{2+}-Zentren wurde in der Arbeitsgruppe von Prof. Policar synthetisiert.

Die PELDOR-Experimente mit den orthogonalen Spinmarker wurden ebenfalls bei 34 und 180 GHz durchgeführt. Die 34 GHz PELDOR Messungen, bei denen entweder die Nitroxid- oder Mn^{2+}-Zentrum-Spins detektiert wurden, lieferten einen Abstand von 2.65 nm, welcher gut mit der Vorhersage aus Kristallstrukturen ähnlicher Verbindungen übereinstimmt. Die Detektion der Nitroxid-Spins zeigte eine erhöhte Empfindlichkeit trotz deutlich kleinerer dipolaren Modulationstiefe des EPR-Signals. Die Modulationstiefe ist neben der Signalintensität ein wichtiger Parameter für die Empfindlichkeit der Experimente. Ein anderes Experiment, welches durch die Detektion der Metallzentrumspins durchgeführt wurde, lieferte eine Verzerrung in der PELDOR-Zeitspur, die allerdings die Analyse nur unwesentlich beeinflusste. Teilweise können solche Beobachtungen der großen Nullfeldaufspaltung des Mn^{2+}-Bis(terpyridin)-Zentrums mit der Konstante D von ca. 1.5 GHz zugesprochen werden. Die Hochfrequenz (180 GHz) PELDOR-Messungen, welche durch Pumpen der Nitroxid-Spins aufgenommen wurden, zeigten eine starke spektrale Anisotropie. Die Frequenzen der dipolaren Oszillation konnten in Bezug auf die angeregten Molekülorientierungen und der Molekülgeometrie qualitativ bestimmt werden. Aufgrund der starken spektralen Anisotropie kann nicht nur der Abstand sondern auch die Orientierung des Nitroxidradikals zum Interspinvektor bestimmt werden. Sofern das Nitroxidradikal starr mit dem Molekül verbunden ist, kann dies als zusätzliche Information für die Strukturbestimmung benutzt werden.

Weitere dipolare Spektroskopie Experimente mit dem Bis-Mn^{2+}-System wurden mit dem Mn^{2+}-DOTA-Zentrum durchgeführt. Der DOTA Ligand liefert eine kleine Nullfeldaufspaltung

des Manganspins mit der Konstante *D* von ca. 280 MHz, die zu einer höheren Empfindlichkeit der Messungen führt. Die 94 GHz PELDOR Messungen ergaben einen Abstand von 2.5 - 2.6 nm zwischen den Mn^{2+}- Zentren, der in guter Übereinstimmung mit den auf Rotameranalyse basierenden Vorhersagen ist. Diese Messungen zeigten dipolare Modulationstiefen von 1.2% bis zu 1.7%, die ungefähr eine Größenordnung kleiner als die entsprechende Modulationstiefen für die Nitroxidradikale (bis zu 24%) sind. Die PELDOR-Zeitspuren wurden mit drei unterschiedlichen Frequenzoffsets zwischen den Pump- und Detektionspulsen aufgenommen (im Bereich von 70 bis 252 MHz). Dadurch wurde der Einfluss des pseudo-säkularen Anteils des dipolaren Hamiltonoperators zur Abstandmessung untersucht. Beim maximalen Offset konnten zwei benachbarte Hyperfeinlinien des zentralen Elektronenspinübergangs von den Pump- und Detektionspulsen angeregt werden, was zu einer höheren Empfindlichkeit des PELDOR-Experiments führte. Da sich die PELDOR-Zeitspuren und die entsprechenden Abstandsverteilungen nicht signifikant bei der Variation des Frequenzoffsets änderten, kann auf einen geringen Beitrag des pseudo-säkularen Anteils des dipolaren Hamiltonoperators geschlossen werden. Außerdem liegt keine spektrale Anisotropie vor. Folglich ist es möglich, die Mn^{2+}-PELDOR-Experimente mit der klassischen Tikhonov-Regularisierung zur Berechnung der Abstandverteilung zu analysieren.

Die dipolaren Modulationstiefen, die in den PELDOR-Experimenten mit Mn^{2+}-Zentren üblicherweise beobachtet wurden, sind deutlich kleiner als für die entsprechenden Experimente mit Nitroxidradikalen. Die Hochspin-Metallkomplexe haben sehr breite EPR-Spektren. Deswegen hat der Pump-Puls eine geringe Anregungseffizienz, welche zu einer Abnahme der Empfindlichkeit für diese Experimente führt. Allerdings kann die RIDME-Spektroskopie dieses Problem beheben. Daher wurden RIDME-Experimente mit Mn^{2+}-Zentren bei 94 und 263 GHz durchgeführt. Die dipolaren Modulationstiefen in den RIDME-Zeitspuren waren bis zu 55%. Das Signal-zu-Rausch-Verhältnis wurde näherungsweise bestimmt, um die relative Effizienz von Mn^{2+} - PELDOR und RIDME Experimenten vergleichen zu können. Dabei zeigte sich, dass die RIDME Messungen bis zu einem Faktor drei empfindlicher sind als die empfindlichste PELDOR-Messung (252 MHz Frequenzoffset). Allerdings besitzt RIDME eine kompliziertere Hintergrundfunktion, die nicht nur die intermolekulare dipolare Kopplung, sondern auch den Beitrag der transversalen Relaxation der Mn^{2+}-Spins enthält. Dies führt zu einem deutlich schnelleren Abklingen des RIDME-Signals, sofern ein protoniertes Lösungsmittel benutzt wird. Außerdem besitzen die RIDME-Zeitspuren das Vielfache der dipolaren Kopplungsfrequenz, die von der komplexen Relaxation des Hochspin-System stammen. Aufgrund dieser Relaxation kann sich die magnetische Quantenzahl der Mn^{2+}-Spins

um mehr als eins ändern. Diese Besonderheiten des RIDME Experiments mit Mn^{2+}-Zentren könnten zu einer geringeren Genauigkeit der Abstandsbestimmung führen, wenn flexible Moleküle untersucht werden. Die komplexe Hintergrundfunktion wurde mit einer gestreckten Exponentialfunktion gefittet, während das Vielfache der dipolaren Kopplungsfrequenz durch einen modifizierten Integralkern der Fredholmschen Integralgleichung für die Tikhonov-Regularisierung beschrieben werden konnte. Die Analyse der RIDME-Zeitspuren mit diesem modifizierten Ansatz lieferte Abstandsverteilungen, die in guter Übereinstimmung mit den PELDOR Ergebnissen sind. Allerdings ist die Interpretation der RIDME Experimente komplex, da zusätzliche Parameter in der modifizierten Analyse betrachtet werden müssen.

Aufgrund dessen ist die RIDME-Methode für die quantitative Analyse von relativ rigiden Systemen oder für die Fälle, in denen genaue Abstände weniger wichtig sind und Empfindlichkeit als höchste Priorität angesehen wird, am besten geeignet. Für flexible Systeme kann das RIDME Experiment durch zusätzliche PELDOR Experimente ergänzt werden, um genauere Abstände zu bestimmen.

Unsere Ergebnisse zeigen, dass genaue Abstände mithilfe der dipolaren Spektroskopie mit Hochspin-Mn^{2+}-Zentren bestimmt werden können, welches die Familie der biologisch relevanten Spinmarker erweitert. Die Nutzung von Mn^{2+}-Marker allein oder zusammen mit den Nitroxid- und Tritylradikalen liefert ein wirkungsvolles Werkzeug für funktionale Studien von biologischen Systemen.

Die in dieser Arbeit erhaltenen Ergebnisse bilden die Grundlage für weitere Forschungsarbeiten mit diesen neuen Spinmarkern für die Untersuchung der Wechselwirkungen und Konformationsänderungen in makromolekularen Komplexen, wie zum Beispiel Membranprotein-Ligand Komplexe in einer nativen Umgebung. Für die Strukturcharakterisierung der Nukleotidbindungsdomänen von Membrantransporter-Komplexen und G-Proteinen oder von Metallzentren in Enzyme und Ribozyme sind die hier erzielten Forschungsresultate mit Manganionen wichtig.

7. Bibliography

1. Carter, J. C. W. & Sweet, R. M. *Macromolecular crystallography*. *Methods in Enzymology* (Academic Press, New York, USA, 1997).
2. Feigin, L. A. & Svergun, D. I. *Structure Analysis by Small-Angle X-Ray and Neutron Scattering*. (Plenum Press, New York, USA, 1987).
3. Mertens, H. D. T. & Svergun, D. I. Structural characterization of proteins and complexes using small-angle X-ray solution scattering. *J. Struct. Biol.* **172,** 128–141 (2010).
4. Kühlbrandt, W. Beam-induced motion correction for sub-megadalton cryo-EM particles. *Elife* **3,** e03678 (2014).
5. Callaway, E. The Revolution Will Not Be Crystallized. *Nature* **525,** 172–174 (2015).
6. Bartesaghi, A. *et al.* 2.2 Å resolution cryo-EM structure of β-galactosidase in complex with a cell-permeant inhibitor. *Science (80-.).* **348,** 1147–1151 (2015).
7. Glaeser, R. M. How good can cryo-EM become? *Nat Methods* **13,** 28–32 (2016).
8. Wühtrich, K. *NMR of Proteins and Nucleic Acids*. (Wiley, New York, 1986).
9. Ernst, R. R. Nuclear Magnetic Resonance Fourier Transform Spectroscopy (Nobel Lecture). *Angew. Chem. Int. Ed.* **31,** 805–823 (1992).
10. Bax, A. Multidimensional nuclear magnetic resonance methods for protein studies. *Curr. Opin. Struct. Biol.* **4,** 738–744 (1994).
11. Marion, D. *et al.* Overcoming the overlap problem in the assignment of 1H NMR spectra of larger proteins by use of three-dimensional heteronuclear 1H-15N Hartmann-Hahn-multiple quantum coherence and nuclear Overhauser-multiple quantum coherence spectroscopy: application to . *Biochemistry* **28,** 6150–6156 (1989).
12. Aue, W. P., Bartholdi, E. & Ernst, R. R. Two-dimensional spectroscopy. Application to nuclear magnetic resonance. *J. Chem. Phys.* **64,** 2229 (1976).
13. Bonvin, A. M. J. J., Boelens, R. & Kaptein, R. NMR analysis of protein interactions. *Curr. Opin. Chem. Biol.* **9,** 501–508 (2005).
14. Hong, M. & Schmidt-Rohr, K. Magic-angle-spinning NMR techniques for measuring long-range distances in biological macromolecules. *Acc. Chem. Res.* **46,** 2154–2163 (2013).
15. Overhauser, A. W. Polarization of nuclei in metals. *Phys. Rev.* **92,** 411–415 (1953).
16. Song, C., Hu, K.-N., Joo, C.-G., Swager, T. M. & Griffin, R. G. TOTAPOL: A Biradical Polarizing Agent for Dynamic Nuclear Polarization Experiments in Aqueous Media. *J. Am. Chem. Soc.* **128,** 11385–11390 (2006).
17. Lakowicz, J. R. *Principles of Fluorescence Spectroscopy*. (Springer, New York, USA, 2006).
18. Roy, R., Hohng, S. & Ha, T. A practical guide to single-molecule FRET. *Nat. Methods* **5,** 507–516 (2008).
19. Giepmans, B. N., Adams, S. R., Ellisman, M. H. & Tsien, R. Y. The Fluorescent Toolbox for Assessing Protein Location and Function. *Science (80-.).* **312,** 217–224 (2006).
20. Milov, A. D., Salikhov, K. M. & Shchirov, M. D. Use of the double resonance in electron spin echo method for the study of paramagnetic center spatial distribution in solids. *Sov. Phys. Solid State* **23,** 975–982 (1981).

21. Pannier, M., Veit, S., Godt, A., Jeschke, G. & Spiess, H. W. Dead-Time Free Measurement of Dipole–Dipole Interactions between Electron Spins. *J. Magn. Reson.* **142,** 331–340 (2000).

22. Berliner, L. J., Grunwald, J., Hankovszky, H. O. & Hideg, K. A novel reversible thiol-specific spin label: Papain active site labeling and inhibition. *Anal. Biochem.* **119,** 450–455 (1982).

23. Hubbell, W. L., Gross, A., Langen, R. & Lietzow, M. A. Recent advances in site-directed spin labeling of proteins. *Curr. Opin. Struct. Biol.* **8,** 649–656 (1998).

24. Reddy, T. J., Iwama, T., Halpern, H. J. & Rawal, V. H. General Synthesis of Persistent Trityl Radicals for EPR Imaging of Biological Systems. *J. Org. Chem.* **67,** 4635–4639 (2002).

25. Hubbell, W. L., López, C. J., Altenbach, C. & Yang, Z. Technological advances in site-directed spin labeling of proteins. *Curr. Opin. Struct. Biol.* **23,** 725–733 (2013).

26. Jeschke, G. & Polyhach, Y. Distance measurements on spin-labelled biomacromolecules by pulsed electron paramagnetic resonance. *Phys. Chem. Chem. Phys.* **9,** 1895–1910 (2007).

27. Sale, K., Song, L., Liu, Y. S., Perozo, E. & Fajer, P. Explicit treatment of spin labels in modeling of distance constraints from dipolar EPR and DEER. *J. Am. Chem. Soc.* **127,** 9334–9335 (2005).

28. Fleissner, M. R. *et al.* Site-directed spin labeling of a genetically encoded unnatural amino acid. *Proc. Natl. Acad. Sci. U. S. A.* **106,** 21637–21642 (2009).

29. Cekan, P., Smith, A. L., Barhate, N., Robinson, B. H. & Sigurdsson, S. T. Rigid spin-labeled nucleoside C: A nonperturbing EPR probe of nucleic acid conformation. *Nucleic Acids Res.* **36,** 5946–5954 (2008).

30. Ramos, A. & Varani, G. A New Method To Detect Long-Range Protein - RNA Contacts: NMR Detection of Electron - Proton Relaxation Induced by Nitroxide Spin-Labeled RNA. *J. Am. Chem. Soc.* **120,** 10992–10993 (1998).

31. Nguyen, P. & Qin, P. Z. RNA dynamics: Perspectives from spin labels. *Wiley Interdiscip. Rev. RNA* **3,** 62–72 (2012).

32. Shelke, S. A. & Sigurdsson, S. T. Site-directed spin labelling of nucleic acids. *Eur. J. Org. Chem.* 2291–2301 (2012).

33. Schiemann, O. *et al.* Spin labeling of oligonucleotides with the nitroxide TPA and use of PELDOR, a pulse EPR method, to measure intramolecular distances. *Nat. Protoc.* **2,** 904–923 (2007).

34. Barhate, N., Cekan, P., Massey, A. P. & Sigurdsson, S. T. A nucleoside that contains a rigid nitroxide spin label: A fluorophore in disguise. *Angew. Chem. Int. Ed.* **46,** 2655–2658 (2007).

35. Rajca, A. *et al.* A spirocyclohexyl nitroxide amino acid spin label for pulsed EPR spectroscopy distance measurements. *Chem. Eur. J.* **16,** 5778–5782 (2010).

36. Meyer, V. *et al.* Room-temperature distance measurements of immobilized Spin-labeled Protein by DEER/PELDOR. *Biophys. J.* **108,** 1213–1219 (2015).

37. Owenius, R., Eaton, G. R. & Eaton, S. S. Frequency (250 MHz to 9.2 GHz) and viscosity dependence of electron spin relaxation of triarylmethyl radicals at room temperature. *J. Magn. Reson.* **172,** 168–175 (2005).

38. Kuzhelev, A. A. *et al.* Room-Temperature Electron Spin Relaxation of Triarylmethyl Radicals at the X- and Q- Bands. *J. Phys. Chem. B* **119,** 13630–13640 (2015).

39. Ardenkjaer-Larsen, J. H. *et al.* EPR and DNP Properties of Certain Novel Single Electron Contrast Agents Intended for Oximetric Imaging. *J. Magn. Reson.* **133,** 1–12 (1998).

40. Shevelev, G. Y. *et al.* Physiological-Temperature Distance Measurement in Nucleic Acid using Triarylmethyl-Based Spin Labels and Pulsed Dipolar EPR Spectroscopy. *J. Am. Chem. Soc.* **136,** 9874–9877 (2014).

41. Yang, Z. *et al.* Pulsed ESR Dipolar Spectroscopy for Distance Measurements in Immobilized Spin Labeled Proteins in Liquid Solution. *J. Am. Chem. Soc.* **134,** 9950–9952 (2012).

42. Yang, Z. *et al.* A triarylmethyl spin label for long-range distance measurement at physiological temperatures using T1 relaxation enhancement. *J. Magn. Reson.* **269,** 50–54 (2016).

43. Denysenkov, V. P., Prisner, T. F., Stubbe, J. & Bennati, M. High-field pulsed electron-electron double resonance spectroscopy to determine the orientation of the tyrosyl radicals in ribonucleotide reductase. *Proc. Natl. Acad. Sci. U. S. A.* **103,** 13386–13390 (2006).

44. Cunningham, T. F., Putterman, M. R., Desai, A., Horne, W. S. & Saxena, S. The double-histidine Cu2+-binding motif: A highly rigid, site-specific spin probe for electron spin resonance distance measurements. *Angew. Chem. Int. Ed.* **54,** 6330–6334 (2015).

45. Cunningham, T. F. *et al.* Cysteine-specific Cu2+ chelating tags used as paramagnetic probes in double electron electron resonance. *J. Phys. Chem. B* **119,** 2839–2843 (2015).

46. Coremans, J. W. A. *et al.* A W-Band Electron Paramagnetic Resonance Study of a Single Crystal of Azurin. *J. Am. Chem. Soc.* **116,** 3097–3101 (1994).

47. Raitsimring, A. M. *et al.* Gd3+ complexes as potential spin labels for high field pulsed EPR distance measurements. *J. Am. Chem. Soc.* **129,** 14138–14139 (2007).

48. Reed, G. H. & Markham, G. D. in *Biological Magnetic Resonance* (eds. Berliner, L. & Reuben, J.) 73–142 (Plenum Press, New York, USA, 1984).

49. Goldfarb, D. Gd3+ spin labeling for distance measurements by pulse EPR spectroscopy. *Phys. Chem. Chem. Phys.* **16,** 9685–9699 (2014).

50. Gordon-Grossman, M., Kaminker, I., Gofman, Y., Shai, Y. & Goldfarb, D. W-Band pulse EPR distance measurements in peptides using Gd3+ –dipicolinic acid derivatives as spin labels. *Phys. Chem. Chem. Phys.* **13,** 10771–10780 (2011).

51. Yagi, H. *et al.* Gadolinium tagging for high-precision measurements of 6 nm distances in protein assemblies by EPR. *J. Am. Chem. Soc.* **133,** 10418–10421 (2011).

52. Matalon, E. *et al.* Gadolinium(III) spin labels for high-sensitivity distance measurements in transmembrane helices. *Angew. Chem. Int. Ed.* **52,** 11831–11834 (2013).

53. Song, Y. *et al.* Pulsed dipolar spectroscopy distance measurements in biomacromolecules labeled with Gd(III) markers. *J. Magn. Reson.* **210,** 59–68 (2011).

54. Martorana, A. *et al.* Probing protein conformation in cells by EPR distance measurements using Gd3+ spin labeling. *J. Am. Chem. Soc.* **136,** 13458–13465 (2014).

55. Qi, M., Groß, A., Jeschke, G., Godt, A. & Drescher, M. Gd(III)-PyMTA label is suitable for in-cell EPR. *J. Am. Chem. Soc.* **136,** 15366–15378 (2014).

56. Mascali, F. C., Ching, H. Y. V., Rasia, R. M., Un, S. & Tabares, L. C. Using Genetically Encodable Self-Assembling GdIII Spin Labels to Make In-cell Nanometric Distance Measurements. *Angew. Chem. Int. Ed.* **55,** 11041–11043 (2016).

57. Banerjee, D., Yagi, H., Huber, T., Otting, G. & Goldfarb, D. Nanometer-Range Distance Measurement in a Protein Using Mn2+ Tags. *J. Phys. Chem. Lett.* **3,** 157−160 (2012).

58. Abragam, A. & Price, M. Theory of the Nuclear Hyperfine Structure of Paramagnetic Resonance Spectra in Crystals. *Proc. R. Soc. London. Ser. A.* **205,** 135–153 (1951).

59. Abragam, A. & Bleaney, B. *Electron Paramagnetic Resonance of Transition Ions*. (Oxford University Press, Oxford, England, 1970).

60. Altshuler, S. & Kozyrev, B. *Electron Paramagnetic Resonance*. (John Wiley & Sons, New York, USA, 1974).

61. Hu, K. N., Bajaj, V. S., Rosay, M. & Griffin, R. G. High-frequency dynamic nuclear polarization using mixtures of TEMPO and trityl radicals. *J. Chem. Phys.* **126,** 044512 (2007).

62. Grinberg, O. Y., Dubinskii, A. A. & Lebedev, Y. S. Electron Paramagnetic Resonance of free Radicals at 2 mm wavelength (in russian). *Usp. Khim.* **52,** 1490–1513 (1983).

63. Sakurai, J. J. *Modern Quantum Mechanics*. (Addison-Wesley, USA, 1994).

64. Abragam, A. *The Principles of Nuclear Magnetism*. (Clarendon Press, Oxford, England, 1961).

65. Orbach, R. On the Theory of Spin-Lattice Relaxation in Paramagnetic Salts. *Proc. Phys. Soc.* **77,** 821–826 (1961).

66. Eaton, G. R., Eaton, S. S., Barr, B. R. & Weber, R. T. *Quantitative EPR*. (Springer-Verlag, Wien, Austria, 2010).

67. Schweiger, A. & Jeschke, G. *Principles of pulse electron paramagnetic resonance*. (Oxford University Press, Oxford, England, 2001).

68. Kneubühl, F. K. Line Shapes of Electron Paramagnetic Resonance Signals Produced by Powders, Glasses, and Viscous Liquids. *J. Chem. Phys.* **33,** 1074–1078 (1960).

69. Sands, R. H. Paramagnetic Resonance Absorption in Glass. *Phys. Rev.* **99,** 1222–1226 (1955).

70. Stoll, S. & Schweiger, A. EasySpin, a comprehensive software package for spectral simulation and analysis in EPR. *J. Magn. Reson.* **178,** 42–55 (2006).

71. Racah, G. Theory of complex spectra. II. *Phys. Rev.* **62,** 438–462 (1942).

72. Buckmaster, H. A., Chatterjee, R. & Shing, Y. H. The application of tensor operators in the analysis of EPR and ENDOR spectra. *Phys. Stat. Sol.(a)* **13,** 9–50 (1972).

73. Bacquet, G., Dugas, J., Escribe, C., Gaite, J. M. & Michoulier, J. Comparative electron paramagnetic resonance study of Fe3+ and Gd3+ ions in monoclinic zirconia. *J. Phys. C Solid State Phys.* **7,** 1551–1563 (1974).

74. McGavin, D. G., Tennant, W. C. & Weil, J. A. High-spin Zeeman terms in the spin Hamiltonian. *J. Magn. Reson.* **87,** 92–109 (1990).

75. Eden, M. Computer simulations in solid-state NMR. I. Spin dynamics theory. *Concepts Magn. Reson.* **17A,** 117–154 (2003).

76. Markham, G. D., Nageswara Rao, B. D. & Reed, G. H. Analysis of EPR powder pattern lineshapes for Mn(II) including third-order perturbation corrections. Applications to Mn(II) complexes with enzymes. *J. Magn. Reson.* **33,** 595–602 (1979).

77. Meirovitch, E. & Poupko, R. Line shape studies of the electron spin resonance spectra of manganese protein complexes. *J. Phys. Chem.* **82,** 1920–1925 (1978).

78. Bir, G. L. Intensity of allowed and forbidden electron paramaegnetic resonance lines. *Sov. Phys. Solid State* **5,** 1628–1635 (1964).

79. Raitsimring, A. M., Astashkin, A. V., Poluektov, O. G. & Caravan, P. High-field pulsed EPR and ENDOR of Gd3+ complexes in glassy solutions. *Appl. Magn. Reson.* **28,** 281–295 (2005).

80. Slichter, C. P. *Principles of Magnetic Resonance*. (Springer-Verlag Berlin Heidelberg, Germany, 1990).

81. Potapov, A. *et al.* Distance measurements in model bis-Gd(III) complexes with flexible 'bridge'. Emulation of biological molecules having flexible structure with Gd(III) labels attached. *J. Magn. Reson.* **205,** 38–49 (2010).

82. Dalaloyan, A. *et al.* Gd(III)-Gd(III) EPR distance measurements – the range of accessible distances and the impact of zero field splitting. *Phys. Chem. Chem. Phys.* **17,** 18464–18476 (2015).

83. Collauto, A. *et al.* RIDME distance measurements using Gd(III) tags with a narrow central transition. *Phys. Chem. Chem. Phys.* **18,** 19037–19049 (2016).

84. Pake, G. E. Nuclear Resonance Absorption in Hydrated Crystals: Fine Structure of the Proton Line. *J. Chem. Phys.* **16,** 327–336 (1948).

85. Anderson, P. in *Solid State Physics* (eds. Seitz, F. & Turnbull, D.) 99–214 (Academic Press, New York, USA, 1963).

86. Sørensen, O., Eich, G., Levitt, M., Bodenhausen, G. & Ernst, R. Product operator formalism for the description of NMR pulse experiments. *Prog. Nucl. Magn. Reson. Spectrosc.* **16,** 163–192 (1983).

87. Hahn, E. L. Spin Echoes. *Phys. Rev.* **80,** 580–594 (1950).

88. Larsen, R. G. & Singel, D. J. Double electron-electron measurement of electron disordered solids resonance spin-echo spin pair separations modulation : Spectroscopic in orientationally disordered solids. *J. Chem. Phys.* **98,** 5134–5146 (1993).

89. Martin, R. E. *et al.* Determination of End-to-End Distances in a Series of TEMPO Diradicals of up to 2.8 nm Length with a New Four-Pulse Double Electron Electron Resonance Experiment. *Angew. Chemie Int. Ed.* **37,** 2833–2837 (1998).

90. Emshwiller, M., Hahn, E. L. & Kaplan, D. Pulsed Nuclear Resonance Spectroscopy. *Phys. Rev.* **118,** 414–424 (1960).

91. Salikhov, K. M., Dzuba, S. A. & Raitsimring, A. M. The theory of electron spin-echo signal decay resulting from dipole-dipole interactions between paramagnetic centers in solids. *J. Magn. Reson.* **42,** 255–276 (1981).

92. Marko, A. *et al.* Analytical method to determine the orientation of rigid spin labels in DNA. *Phys. Rev. E* **81,** 021911 (2010).

93. Piantini, U., Sorensen, O. W. & Ernst, R. R. Multiple quantum filters for elucidating NMR coupling networks. *J. Am. Chem. Soc.* **104,** 6800–6801 (1982).

94. Rance, M. *et al.* Improved spectral resolution in COSY 1H NMR spectra of proteins via double quantum filtering. **117,** 479–485 (1983).

95. Saxena, S. & Freed, J. H. Double quantum two-dimensional Fourier transform electron spin resonance : distance measurements. **251,** 102–110 (1996).

96. Borbat, P. P. & Freed, J. H. Multiple-quantum ESR and distance measurements. *Chem. Phys. Lett.* **313,** 145–154 (1999).

97. Borbat, P. P. & Freed, J. H. in *Structure and Bonding* (eds. Timmel, C. R. & Harmer, J. R.) **152,** 1–82 (Springer-Verlag Berlin Heidelberg, Germany, 2013).

98. Jeschke, G., Pannier, M., Godt, A. & Spiess, H. W. Dipolar spectroscopy and spin alignment in electron paramagnetic resonance. *Chem. Phys. Lett.* **331,** 243–252 (2000).

99. Powels, J. G. & Mansfield, P. Double-pulse Nuclear-resonance transients in solids. *Phys. Lett.* **2,** 58–59 (1962).

100. Baum, J., Tycko, R. & Pines, A. Broadband and adiabatic inversion of a two-level system by phase-modulated pulses. *Phys. Rev. A* **32,** 3435–3447 (1985).

101. Schöps, P., Spindler, P. E., Marko, A. & Prisner, T. F. Broadband spin echoes and broadband SIFTER in EPR. *J. Magn. Reson.* **250,** 55–62 (2015).

102. Doll, A. & Jeschke, G. EPR-correlated dipolar spectroscopy by Q-band chirp SIFTER. *Phys. Chem. Chem. Phys.* **18,** 23111–23120 (2016).

103. Kulik, L. V., Dzuba, S. A., Grigoryev, I. A. & Tsvetkov, Y. D. Electron dipole-dipole interaction in ESEEM of nitroxide biradicals. *Chem. Phys. Lett.* **343,** 315–324 (2001).

104. Milikisyants, S., Scarpelli, F., Finiguerra, M. G., Ubbink, M. & Huber, M. A pulsed EPR method to determine distances between paramagnetic centers with strong spectral anisotropy and radicals: The dead-time free RIDME sequence. *J. Magn. Reson.* **201,** 48–56 (2009).

105. Sachleben, J. R., Frydman, V. & Frydman, L. Dipolar determinations in solids by relaxation-assisted NMR recoupling. *J. Am. Chem. Soc.* **118,** 9786–9787 (1996).

106. Balibanu, F., Hailu, K., Eymael, R., Demco, D. E. & Blümich, B. Nuclear magnetic resonance in inhomogeneous magnetic fields. *J. Magn. Reson.* **145,** 246–258 (2000).

107. Razzaghi, S. *et al.* RIDME Spectroscopy with Gd(III) Centers. *J. Phys. Chem. Lett.* **5,** 3970–3975 (2014).

108. Tikhonov, A. N. & Arsenin, V. Y. *Solution of Ill-Posed Problems*. (Wiley, New York, USA, 1977).

109. Weese, J. A reliable and fast method for the solution of Fredhol integral equations of the first kind based on Tikhonov regularization. *Comput. Phys. Commun.* **69,** 99–111 (1992).

110. Jeschke, G., Panek, G., Godt, A., Bender, A. & Paulsen, H. Data Analysis Procedures for Pulse ELDOR Measurements of Broad Distance Distributions. *Appl. Magn. Reson* **26,** 223–244 (2004).

111. Jeschke, G. *et al.* DeerAnalysis2006 - a comprehensive software package for analyzing pulsed ELDOR data. *Appl. Magn. Reson.* **30,** 473–498 (2006).

112. Chiang, Y.-W., Borbat, P. P. & Freed, J. H. The determination of pair distance distributions by pulsed ESR using Tikhonov regularization. *J. Magn. Reson.* **172,** 279–295 (2005).

113. Chiang, Y. W., Borbat, P. P. & Freed, J. H. Maximum entropy: A complement to Tikhonov regularization for determination of pair distance distributions by pulsed ESR. *J. Magn. Reson.* **177,** 184–196 (2005).

114. Reginsson, G. W., Kunjir, N. C., Sigurdsson, S. T. & Schiemann, O. Trityl Radicals: Spin Labels for Nanometer-Distance Measurements. *Chem. Eur. J.* **18,** 13580–13584 (2012).

115. Kunjir, N. C., Reginsson, G. W., Schiemann, O. & Sigurdsson, S. T. Measurements of short distances between trityl spin labels with CW EPR, DQC and PELDOR. *Phys. Chem. Chem. Phys.* **15,** 19673–19685 (2013).

116. Bock, C. W., Katz, A. K., Markham, G. D. & Glusker, J. P. Manganese as a replacement for magnesium and zinc: Functional comparison of the divalent ions. *J. Am. Chem. Soc.* **121,** 7360–7372 (1999).

117. Gätjens, J., Sjödin, M., Pecoraro, V. L. & Un, S. The relationship between the Manganese(II) Zero-Field Interaction and Mn(II)/Mn(III) Redox Potential of Mn(4′-X-terpy)2 Complexes. *J. Am. Chem. Soc.* **129,** 13825–13827 (2007).

118. Lueders, P., Jeschke, G. & Yulikov, M. Double electron-electron resonance measured between Gd3+ ions and nitroxide radicals. *J. Phys. Chem. Lett.* **2,** 604–609 (2011).

119. Rompel, A., Bond, A. D. & McKenzie, C. J. Bis(2,2′:6′,2″-terpyridyl-κ3 N) manganese(II) dinitrate dihydrate. *Acta Cryst.* **E60,** m1759–m1760 (2004).

120. Liu, H.-G., Qiu, Y.-C. & Wu, J.-Z. Bis[4′-(4-methylphenyl)-2,2′:6′,2″-terpyridine-κ 3 N, N ′, N ″]manganese(II) bis(perchlorate). *Acta Cryst.* **E63,** m2393–m2394 (2007).

121. Margraf, D., Schuetz, D., Prisner, T. F. & Bats, J. W. Biphenyl-4,4′-diyl bis(2,2,5,5-tetramethyl-1-oxyl-3-pyrroline-3-carboxylate). *Acta Cryst.* **E65,** o1784–o1784 (2009).

122. Yulikov, M., Lueders, P., Warsi, M. F., Chechik, V. & Jeschke, G. Distance measurements in Au nanoparticles functionalized with nitroxide radicals and Gd3+–DTPA chelate complexes. *Phys. Chem. Chem. Phys.* **14,** 10732–10746 (2012).

123. Schiemann, O., Cekan, P., Margraf, D., Prisner, T. F. & Sigurdsson, S. T. Relative orientation of rigid nitroxides by peldor: Beyond distance measurements in nucleic acids. *Angew. Chem. Int. Ed.* **48,** 3292–3295 (2009).

124. Marko, A. *et al.* Conformational flexibility of DNA. *J. Am. Chem. Soc.* **133,** 13375–13379 (2011).

125. Vincent Ching, H. Y. *et al.* Nanometric distance measurements between Mn(II) DOTA centers. *Phys. Chem. Chem. Phys.* **17,** 23368–23377 (2015).

126. Martorana, A. *et al.* Mn(II) tags for DEER distance measurements in proteins via C-S attachment. *Dalt. Trans.* **44,** 20812–20816 (2015).

127. Ching, H. Y. V. *et al.* The Use of Mn(II) Bound to His-tags as Genetically Encodable Spin-Label for Nanometric Distance Determination in Proteins. *J. Phys. Chem. Lett.* **7,** 1072–1076 (2016).

128. Ramirez-Cohen, M. *et al.* Overcoming artificial broadening in Gd3+-Gd3+ distance distributions arising from dipolar pseudo-secular terms in DEER experiments. *Phys. Chem. Chem. Phys.* **18,** 12847–12859 (2016).

129. Kaminker, I. *et al.* W-band orientation selective DEER measurements on a Gd3+/nitroxide mixed-labeled protein dimer with a dual mode cavity. *J. Magn. Reson.* **227,** 66–71 (2013).

130. Doll, A. *et al.* Gd(III)-Gd(III) distance measurements with chirp pump pulses. *J. Magn. Reson.* **259,** 153–162 (2015).

131. Doll, A. *et al.* Sensitivity enhancement by population transfer in Gd(III) spin labels. *Phys. Chem. Chem. Phys.* **17,** 7334–7344 (2015).

132. Meyer, A. & Schiemann, O. PELDOR and RIDME Measurements on a High-Spin Manganese(II) Bisnitroxide Model Complex. *J. Phys. Chem. A* **120,** 3463–3472 (2016).

133. Kulik, L. V., Salnikov, E. S. & Dzuba, S. A. Nuclear Spin Relaxation in Free Radicals as Revealed in a Stimulated Electron Spin Echo Experiment. **11,** 1–11 (2005).

8. Curriculum Vitae

Contact Address

Dmitry Akhmetzyanov
Goethe University Frankfurt am Main
Institute of Physical and Theoretical Chemistry
Max-von-Laue-Str. 7
60438 Frankfurt
Germany
Telephone: +49 (0) 69-798-29-183

Personal Data

Date of birth	03.02.1989
Place of birth	Zelenodolsk, Russia
Current address	Huegelstr 83, 60433 Frankfurt am Main, Germany
Telephone	+49-176-846-15-649
E-mail	dmitry@epr.uni-frankfurt.de

Education and Academic Career

2012 – 2016 **Doctoral study under the supervision of Prof. Thomas Prisner**
Goethe University Frankfurt am Main
Institute of Physical and Theoretical Chemistry

2010 – 2012 **Studies of physics (Master of Physics)**
Kazan (Volga Region) Federal University
Institute of Physics
Quantum Electronics and Radiospectroscopy department

2006 – 2010 **Studies of radiophysics (Bachelor of Radiophysics)**
Kazan (Volga Region) Federal University
Institute of Physics
Quantum Electronics and Radiospectroscopy department

1996 – 2006 **School studies**
Gymnasium №3 of the city of Zelenodolsk, Russia

Professional and teaching experience

2012 – present time **Assistant in the Physical Chemistry practical course**
Institute of Physical and Theoretical Chemistry, Goethe University

2010 – 2012 **Engineer in the Laboratory of Radiospectroscopy of Dielectrics**
under the supervision of Prof. Valery Tarasov
Zavoisky Physical-Technical Institute of the Kazan Scientific Center of the Russian Academy of Sciences

Language skills

Russian – native speaker
English – fluent
German – advanced
French – beginner

Awards

Runner-up of the JEOL student lecture prize on the 49th Annual International Meeting of the ESR Spectroscopy Group of the Royal Society of Chemistry, 3-7 April 2016, Colchester, England.

Publications

1. M. A. Geiger, M. Orwick-Rydmark, K. Märker, W. T. Franks, **D. Akhmetzyanov**, D. Stöppler, M. Zinke, E. Specker, M. Nazaré, A. Diehl, B. J. van Rossum, F. Aussenac, T. Prisner, Ü. Akbey, H. Oschkinat. Temperature dependence of cross-effect dynamic nuclear polarization in rotating solids: advantages of elevated temperatures. *Phys. Chem. Chem. Phys*., 2016, **18**, 30696.

2. **D. Akhmetzyanov**, H. Y. Vincent Ching, V. P. Denysenkov, P. Demay-Drouhard, H. C. Bertrand, L. C. Tabares, C. Policar, T. F. Prisner, S. Un. RIDME Spectroscopy on High-Spin Mn^{2+} Centers. *Phys. Chem. Chem. Phys*., 2016, **18**, 30857.

3. B. Joseph, V. M. Tormyshev, O. Yu. Rogozhnikova, **D. Akhmetzyanov**, E. G. Bagryanskaya, T. F. Prisner. Selective High-Resolution Detection of Membrane Protein-Ligand Interaction in Native Membranes using Trityl-Nitroxide PELDOR. *Angew. Chem*., 2016, **128**, 11710.

4. P. Demay-Drouhard, H. Y. V. Ching, **D. Akhmetzyanov**, R. Guillot, L. C. Tabares, H. C. Bertrand, C. Policar. A bis-MnII-DOTA complex for pulsed dipolar spectroscopy. *Chem. Phys. Chem*., 2016, **17**, 2066.

5. C. Sauvée, G. Casano, S. Abel, A. Rockenbauer, **D. Akhmetzyanov**, H. Karoui, D. Siri, F. Aussenac, W. Maas, R. T. Weber, Th. Prisner, M. Rosay, O. Ouari, P. Tordo. Tailoring of polarizing agents in the bTurea series for Cross Effect Dynamic Nuclear Polarization in aqueous media. *Chem. Eur. J*., 2016, **22**, 5598.

6. **D. Akhmetzyanov**, P. Schöps, A. Marko, N. Kunjir, S. Th. Sigurdsson, T. F. Prisner. Pulsed EPR Dipolar Spectroscopy at Q- and G-band on a Trityl Biradical. *Phys. Chem. Chem. Phys*., 2015, **17**, 24446.

7. **D. Akhmetzyanov**, J. Plackmeyer, B. Endeward, V. Denysenkov, T. F. Prisner. Pulsed electron–electron double resonance spectroscopy between a high-spin Mn^{2+} ion and a nitroxide spin label. *Phys. Chem. Chem. Phys*., 2015, **17**, 6760.

8. J. Mao, **D. Akhmetzyanov**, O. Ouari, V. Denysenkov, B. Corzilius, J. Plackmeyer, P. Tordo, T. F. Prisner. C. Glaubitz. Host-Guest Complexes as Water-Soluble High-Perfomance DNP Polarizing Agents. *J. Am. Chem. Soc*., 2013, **135**, 19275.

9. **D. Akhmetzyanov**, V. Dudnikova, E. Zharikov, E. Zhiteitsev, A. Konovalov, V. Tarasov. EPR study of the effect of ionizing radiation on chromium centers in Mg2SiO4: Cr,Li laser crystals. *Phys. Solid State*, 2013, **55**, 1892.

10. **D. Akhmetzyanov**, V. Dudnikova, E. Zharikov, E. Zhiteitsev, O. Zaitseva, A. Konovalov, V. Tarasov. EPR study of the effect of partial pressure of oxygen in the growth atmosphere on concentration of chromium centers in synthetic forsterite. *Phys. Solid State*, 2013, **55**, 520.

Participation at International conferences

1. **talk+poster:** D. Akhmetzyanov, H. Y. Vincent Ching, P. Demay-Drouhard, L. C. Tabares, H. C. Bertrand, C. Policar, T. F. Prisner, S. Un. Pulse EPR Dipolar Spectroscopy with High-Spin Mn^{2+} Ions. The 49th Annual International Meeting of the ESR Spectroscopy Group of the Royal Society of Chemistry, 3-7 April 2016, Colchester, England.

2. **poster:** D. Akhmetzyanov, P. Schöps, A. Marko, N. Kunjir, S. Th. Sigurdsson, T. F. Prisner. Pulsed EPR Dipolar Spectroscopy at Q- and G-band on a Trityl Biradical. 37th Discussion Meeting of the GDCh-Division of "Magnetic Resonance" (FGMR), 7-10 September 2015, Darmstadt, Germany.

3. **poster:** D. Akhmetzyanov, H.Y. Vincent Ching, B. Endeward, P. Demay-Drouhard, J. Plackmeyer, V. Denysenkov, S. Un, L. Tabares, H. C. Bertrand, C. Policar, T. F. Prisner. Pulsed EPR Dipolar Spectroscopy with High-Spin Mn^{2+} Ions. 37th Discussion Meeting of the GDCh-Division of "Magnetic Resonance" (FGMR), 7-10 September 2015, Darmstadt, Germany.

4. **poster:** D. Akhmetzyanov, P. Schöps, A. Marko, N. Kunjir, S. Th. Sigurdsson, T. F. Prisner. Pulsed EPR Dipolar Spectroscopy at Q- and G-band on a Trityl Biradical. European congress on Magnetic Resonance (EUROMAR), 5-10 July 2015, Prague, Czech Republic

5. **talk+poster:** D. Akhmetzyanov, J. Plackmeyer, B. Endeward, V. Denysenkov and T. F. Prisner. Pulsed Electron-Electron Double Resonance Spectroscopy on a High-Spin Mn^{2+} Ion coupled with a nitroxide radical. 36th Discussion Meeting of the GDCh-Division of "Magnetic Resonance" (FGMR), 29 September - 4 October 2014, Berlin, Germany.

6. **talk:** D. Akhmetzyanov, J. Plackmeyer, B. Endeward, V. Denysenkov and T. F. Prisner. Pulsed Electron-Electron Double Resonance Spectroscopy on a High-Spin Mn^{2+} Ion non-covalently attached to a Nitroxide Radical. Modern Development of Magnetic Resonance (MDMR), 23-27 September 2014, Kazan, Russia

7. **talk**: D. Akhmetzyanov, J. Plackmeyer, B. Endeward, V. Denysenkov and T. F. Prisner. Pulsed Electron-Electron Double Resonance Spectroscopy on a High-Spin Mn^{2+} Ion non-covalently attached to a Nitroxide Radical. Rocky Mountain EPR Symposium, 13 - 17 July 2014, Copper Mountain, Colorado, USA

PCCP

PAPER

View Article Online
View Journal | View Issue

Cite this: *Phys. Chem. Chem. Phys.*, 2016, **18**, 30857

RIDME spectroscopy on high-spin Mn^{2+} centers†

D. Akhmetzyanov,‡[a] H. Y. V. Ching,‡[b] V. Denysenkov,[a] P. Demay-Drouhard,[cd] H. C. Bertrand,[cd] L. C. Tabares,[b] C. Policar,[cd] T. F. Prisner*[a] and S. Un*[b]

Received 28th July 2016,
Accepted 5th October 2016

DOI: 10.1039/c6cp05239h

www.rsc.org/pccp

Pulsed EPR dipolar spectroscopy is a powerful tool for determining the structure and conformational dynamics of biological macromolecules, as it allows precise measurements of distances in the range of 1.5–10 nm. Utilization of high-spin Mn^{2+} species as spin probes for distance measurements is of significant interest, because they are biologically compatible and endogenous in numerous biological systems. However, to date dipolar spectroscopy experiments with this kind of species have been underexplored. Here we present pulsed electron electron double resonance (PELDOR also called DEER) and relaxation-induced dipolar modulation enhancement (RIDME) experiments, which have been performed at W-band (94 GHz) and J-band frequencies (263 GHz) on a bis-MnDOTA (DOTA = 1,4,7,10-tetraazacyclododecane-1,4,7,10-tetraacetate) model system. The distances obtained from these experiments are in good agreement with predictions. RIDME experiments reveal a significantly higher modulation depth compared to PELDOR, which is an important consideration for biological samples. These experiments also feature higher harmonics of the dipolar coupling frequency due to effective multiple-quantum relaxation of high-spin Mn^{2+} as well as the multiple-component background function. Harmonics of the dipolar coupling frequency were taken into account by including additional terms in the kernel function of Tikhonov regularization analysis.

Introduction

Pulsed electron paramagnetic resonance (EPR) dipolar spectroscopy, which can precisely measure distances in the range of 1.5–10 nm, has become a valuable tool for structural biology by providing important information about tertiary structures, conformational flexibilities and intermolecular interactions of biomacromolecules.[1–3] Pulsed electron–electron double resonance (PELDOR,[4] also called DEER[5,6]) is the most commonly used of such EPR techniques, where the distances are measured by determining the magnitude of the magnetic dipolar coupling (ω_{dd}) between pairs of spin probes, which in the weak coupling regime is given by the formula (1)[6]:

$$\omega_{dd} = \frac{\mu_B{}^2 g_A g_B}{\hbar} \frac{1}{R^3}\left(3\cos^2(\theta) - 1\right) = \frac{D_{dd}}{R^3}\left(3\cos^2(\theta) - 1\right) \quad (1)$$

where μ_B is the Bohr magneton, $\hbar$ is the Planck constant divided by 2π, g_A and g_B are the effective values of the g-tensor, corresponding to the excited A and B spins, R is the electron–electron distance and θ is the angle between the vector $\boldsymbol{R}$ and the external magnetic field $\boldsymbol{B}_0$. Typically such measurements are done using nitroxide radicals, which have been site-specifically attached to proteins or nucleic acid molecules.[7–11] In the last decade, paramagnetic Gd^{3+} and Mn^{2+} chelate complexes have been introduced as alternative spin probes for PELDOR spectroscopy.[12,13] Due to their high-spin multiplicities, Gd^{3+} and Mn^{2+} PELDOR measurements benefit from the use of high microwave excitation frequencies and corresponding high magnetic fields. Using high magnetic fields provides higher sensitivity, which is an important consideration for biological applications where often only a small quantity of the sample is available and spin-labelling efficiency is not 100%. Although Gd^{3+} spin-labels have been widely used for biological PELDOR applications, Mn^{2+} remains underexplored.[13–16] From the perspective of biological applications, Mn^{2+} is interesting, because many enzymes contain Mn^{2+} at their catalytic active site,[17,18] it can also readily replace diamagnetic Mg^{2+} in biological constructs[19] due to their identical charge and similarity in ionic radii.[20] These properties make EPR-based distance measurements using Mn^{2+} a potentially powerful experimental toolkit for structural biology.

Compared to nitroxide and other organic radicals, Mn^{2+} is a more complicated spin system with an electron spin of $S = 5/2$. Thus, the EPR spectrum of Mn^{2+} complexes with non-zero

[a] *Goethe-University Frankfurt am Main, Institute of Physical and Theoretical Chemistry and Center for Biomolecular Magnetic Resonance, Max von Laue Str. 7, 60438 Frankfurt am Main, Germany. E-mail: prisner@chemie.uni-frankfurt.de*
[b] *Institute for Integrative Biology of the Cell (I2BC), Department of Biochemistry, Biophysics and Structural Biology, Université Paris-Saclay, CEA, CNRS UMR 9198, Gif-sur-Yvette, F-91198, France. E-mail: sun.un@cea.fr*
[c] *Département de Chimie, Ecole Normale Supérieure, PSL Research University, UPMC Univ Paris 06, CNRS, Laboratoire des Biomolécules (LBM), 24 rue Lhomond, 75005 Paris, France*
[d] *Sorbonne Universités, UPMC Univ Paris 06, Ecole Normale Supérieure, CNRS, Laboratoire des Biomolécules (LBM), 24 rue Lhomond, 75005 Paris, France*
† Electronic supplementary information (ESI) available. See DOI: 10.1039/c6cp05239h
‡ Authors contributed equally to the work.

quadrupole Zero-Field Splitting (ZFS) parameters reveals a fine structure, consisting of five resonance lines $|m_S\rangle \rightarrow |m_S \pm 1\rangle$, where m_S is the projection of the electron spin vector to the magnetic field vector. Each of these is further split into a sextet of hyperfine lines, arising from the ^{55}Mn nuclear spin (I = 5/2, 100% abundant). In disordered samples, the total width of the EPR spectrum is defined to a large extent by the ZFS and ^{55}Mn hyperfine coupling.[21,22] The individual widths of the six hyperfine lines corresponding to the central $|-1/2,m_I\rangle \rightarrow |1/2,m_I\rangle$ transition, where m_I is the projection of the ^{55}Mn nuclear spin vector to the magnetic field vector, do not depend on ZFS in first order perturbation theory and hence these lines are very sharp. The other electron spin transitions have a first order ZFS dependency and are typically broad and featureless.

One of the important properties that governs the sensitivity of PELDOR experiments is the dipolar modulation depth. It is defined by the fraction of spins (referred to as B spins in the following) that are inverted by the applied pump pulse at the second microwave frequency, ν_B (see Fig. 1). The fraction of spins that are detected (referred to as A spins that are in resonance with the pulses at the microwave frequency of ν_A) is also an important parameter for sensitivity, since it contributes to the echo amplitude. For Mn^{2+} centers only a part of one of the six hyperfine lines of the central $|-1/2,m_I\rangle \rightarrow |1/2,m_I\rangle$ transition can be excited by the pump pulse, leading to low modulation depths of about 0.5 to 2%.[13–15,23]

As has been shown for Gd^{3+} complexes,[24,25] one way to improve on this low modulation depth condition is to use the relaxation-induced dipolar modulation enhancement (RIDME)[26,27] experiment instead of PELDOR. Unlike PELDOR, where the single-quantum electron spin transition of the B spin is driven coherently by a microwave pulse, in RIDME the B spin transition is driven incoherently by electron spin longitudinal relaxation, which is characterized by the time constant T_{1e}. Experimentally it is achieved by replacing the pump pulse at the second microwave frequency ν_B by a mixing block, composed of two $\pi/2$ pulses, applied at the detection frequency ν_A (Fig. 1).[27] In this case, the dipolar modulation depth is defined by the formula (2):

$$\lambda(T_{mix}) = \frac{1}{2}\left(1 - \exp\left(-\frac{T_{mix}}{T_{1e}}\right)\right) \quad (2)$$

where T_{mix} is the time between the two $\pi/2$ pulses in the mixing block, during which the B spin flips due to longitudinal relaxation.[27] For a dipolar-coupled spin 1/2 system the highest theoretically achievable value for the modulation depth is 50%,[27] however, as has been observed for Gd^{3+} systems, high-spin systems can achieve a larger value, due to the possibility of multiple-quantum relaxation ($\Delta m_S > 1$) of the B spin.[24] Longitudinal relaxation can drive not only single quantum transition $\Delta m_S = \pm 1$, as is the case for the spin 1/2 system, but also effectively double ($\Delta m_S = \pm 2$) and higher-quantum transitions of the B spin leading to the presence of the corresponding harmonic frequencies ($n\omega_{dd}$) in the RIDME experiments. Thus, the dipolar coupling harmonics have been observed in RIDME experiments with Gd^{3+} (ref. 24 and 25) and Mn^{2+} bis-nitroxide model compound[28] and have been attributed to the high electron spin multiplicity of the metal ion.

In the current work we describe the RIDME experiments on the bis-Mn^{2+} complex[23] shown in Fig. 2 at W-band (94 GHz, 3.3 T) and J-band (263 GHz, 9.4 T) microwave frequencies. We examined how the multiple quantum components affect the RIDME measurements and compared the performance of these experiments with PELDOR.

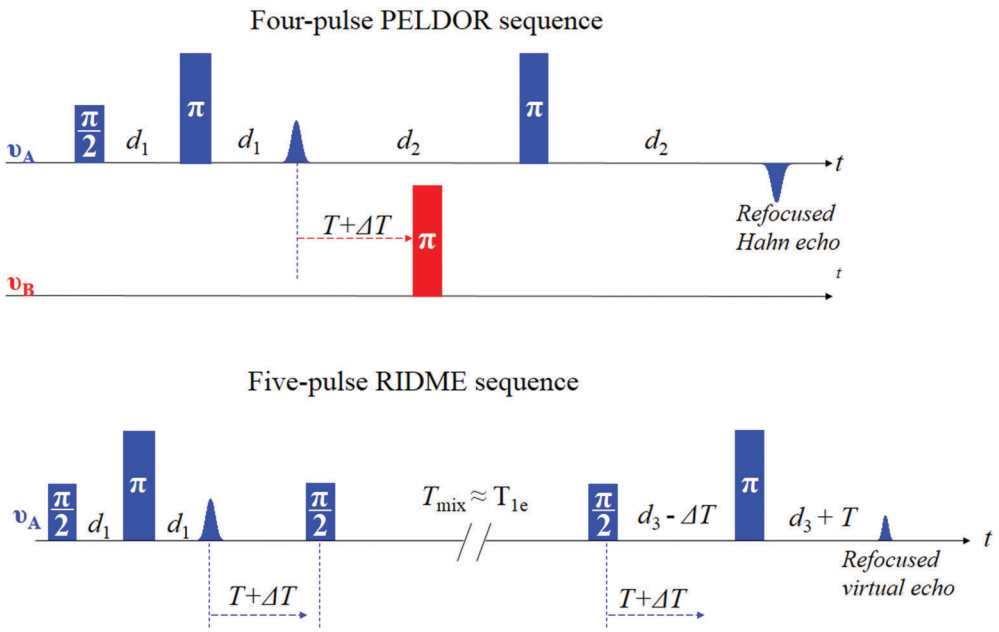

Fig. 1 Pulse schemes for the four-pulse PELDOR and five-pulse RIDME experiments.

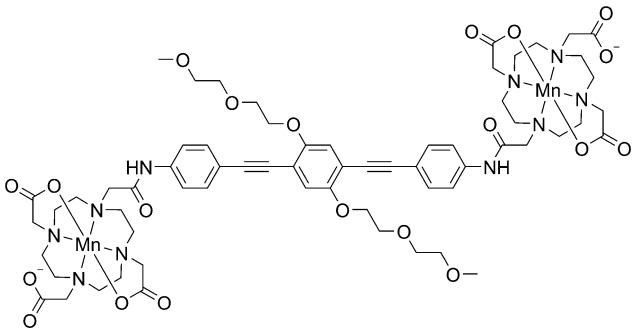

Fig. 2 The schematic chemical structure of compound **1** used in this study.

Experimental results and discussion

Pulsed EPR spectroscopy

Hahn echo-detected field-swept EPR spectrum

The field-swept Hahn echo-detected EPR spectrum of complex **1** obtained at W-band (94 GHz) frequencies is depicted in Fig. 3. It is characterized by six very narrow lines of the central $|-1/2,m_I\rangle \rightarrow |1/2,m_I\rangle$ transition of the MnDOTA complex, each separated by 252 MHz corresponding to the ^{55}Mn hyperfine coupling constant.[14] The sharpness of the lines is due to small ZFS of MnDOTA (D = 280 MHz and E = 0, each with a Gaussian distribution of 150 MHz).[14] Thus, the major contribution to the linewidth is the second and third-order perturbation terms of ZFS as well as unresolved hyperfine couplings with nitrogen and proton nuclei of the first Mn^{2+} coordination sphere. Upon increasing the microwave frequency up to the J-band (263 GHz), small narrowing of the linewidths was observed. For example, the width of the 4th hyperfine line of the central transition went from 7.7 G at 95 GHz to 6.5 G at 263 GHz. By comparison, the corresponding linewidths for molecule with a single spin-label (Fig. S1, ESI†) were 5.9 and 5.2 G. This increase in linewidth with double labelling (3.5 to 5 MHz) was due to dipolar coupling.

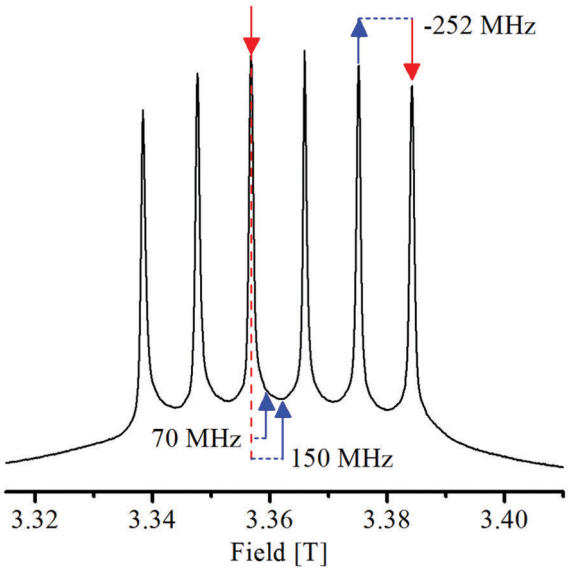

Fig. 3 The 25 K W-band field-swept Hahn echo-detected EPR spectrum of complex **1** in a deuterated solvent. The arrows indicate the resonance field positions used in the PELDOR experiments, with the red down-arrows and the blue up-arrows indicating the pump and probe positions, respectively. The pump–probe frequency offsets ($\nu_{pump} - \nu_{probe}$) are also given.

W-band (94 GHz) PELDOR experiments

W-band (94 GHz) PELDOR experiments performed on complex **1** in a deuterated solvent are shown in Fig. 4. The time traces were obtained with pump–probe pulses set at three different resonance positions in the EPR spectrum, which are shown in Fig. 3. Dipolar modulation depth of the time trace recorded with a pump–probe frequency offset of −252 MHz, corresponding to the ^{55}Mn hyperfine coupling, was smaller (1.2%) compared to the other two time traces (1.6–1.7%) due to the increased length of the pump pulse. Similar modulation depths on dipolar-coupled Mn^{2+} centers have been reported in other studies.[14,15,23] Although the modulation depth for the first case (−252 MHz offset) was about 40% smaller compared to the other two time traces, a greater sensitivity was achieved for this time trace (see Table 1, where signal-to-noise ratios (SNR) per square root of the total accumulation time are given). This is due to the fact that this PELDOR time trace was detected in resonance with the 5th hyperfine line of the central transition (see Fig. 3). As a result, the echo intensity is significantly larger, which improves the sensitivity. A further improvement of the sensitivity of such a type of PELDOR experiment can be achieved using resonators with a larger bandwidth or double-mode structures. Both have been successfully used for Gd^{3+}-based PELDOR experiments.[29,30] Another approach for increasing the sensitivity has been the use of shaped broadband pump pulses.[31–35]

The distance distributions obtained by Tikhonov regularization analysis by the DeerAnalysis[36] toolbox are shown in Fig. 4C. The most probable distances were about 2.5–2.6 nm with a full width at half maximum of about 0.6 nm for each PELDOR time trace. The distance distributions were in agreement with the structural predictions.[23]

W-(94 GHz) and J-band (263 GHz) RIDME experiments

Experimental RIDME time traces obtained at W-(94 GHz) and J-band (263 GHz) frequencies on complex **1** in protonated and deuterated solvents are shown in Fig. 5. The mixing times corresponded approximately to the T_{1e} relaxation time at 25 K for the respective frequencies. As the microwave frequency increased, the T_{1e} value shortened by a factor that was roughly equal to the ratio of microwave frequencies. Similarly, the phase memory time T_{me} also shortened upon increasing the frequency (for more details, see Sections 6 and 10 of the ESI†). Whereas no significant change to T_{1e} was found upon using a deuterated solvent, the T_{me} value lengthened, and changes to the slope of the echo decay as a function of interpulse delay were observed (see Fig. S7, S8, S31 and S32, ESI†). Thus, the mixing time at W-band frequencies was equal to 80 μs for both solvents, while at J-band frequencies the mixing times were 30 μs for the deuterated and 25 μs for the protonated solvent samples. As can be seen from Fig. 5, deuterating the solvent

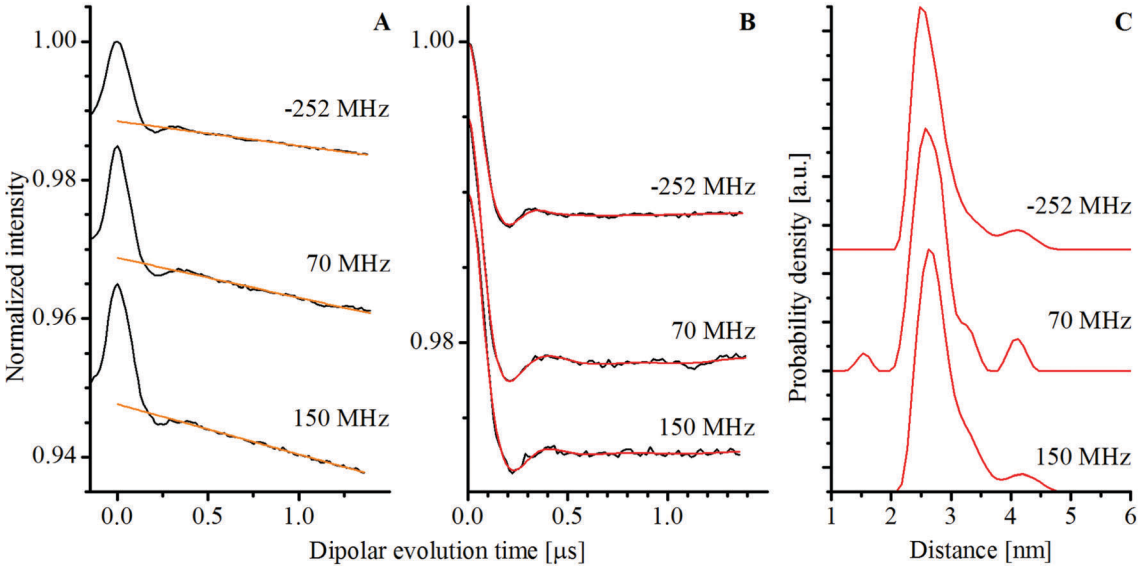

Fig. 4 The 6 K, W-band PELDOR experiments of complex **1** in a deuterated solvent, recorded at different pump–probe frequency offsets and resonance positions in the EPR spectrum (see Fig. 3). (A) The experimental time traces (black) with corresponding mono-exponential background-functions (orange). (B) The background-divided time traces (black) with corresponding fits (red) based on Tikhonov regularization analysis using a regularization parameter of 10. (C) The distance distributions obtained using Tikhonov regularization in the DeerAnalysis[36] toolbox. For better visualization, the PELDOR time traces (A and B) and distance distributions (C) have been vertically offset.

Table 1 Results of PELDOR and RIDME measurements on complex **1**

Experiment	Parameter	R_{max} [nm]	ΔR (fwhm) [nm]	λ	SNR/$\sqrt{t}$ [$h^{-0.5}$]
PELDOR	70 MHz	2.6	0.6	0.016	60
	150 MHz	2.6	0.6	0.017	50
	−252 MHz	2.5	0.6	0.012	70
RIDME	W-band, 20 μs	2.5[a]	0.6[a]	0.308	210
	W-band, 80 μs	2.6[b]	0.6[b]	0.547	150
	J-band	2.5[b]	0.6[b]	0.373	50

[a] Obtained by Tikhonov regularization with kernel function (eqn (4)). [b] Obtained by Tikhonov regularization with kernel function (eqn (5)).

influences significantly the background functions. This is related to the multiple components which contribute to the background function of RIDME. Unlike PELDOR background signals that are dominated by inter-molecular dipolar couplings, RIDME background signals additionally contain a contribution related to the transversal relaxation. In the case of a protonated solvent, the electron-nuclear spin diffusion is considerably stronger, resulting in a significantly faster decay of the RIDME signals (Fig. 5, RIDME time traces in red).

The experimental W- and J-band RIDME time traces of complex **1** in a deuterated solvent with corresponding fitted background functions (analytic functions are given in Table S1, ESI†) as well as background-divided time traces are shown in Fig. 6. The W-band time traces were obtained with two different mixing times: 20 μs corresponding roughly to 3 times T_{me} (left column, Fig. 6) and 80 μs corresponding approximately to the T_{1e} relaxation time at 94 GHz (middle column, Fig. 6). For a shorter mixing time, the dipolar modulation depth was about 30% (Fig. 6D) and for a longer mixing time it was about 55% (Fig. 6E). The experimental modulation depths were larger than the theoretical values (about 10 and 30%, respectively) obtained using eqn (2).[27] The higher experimental modulation depths might indicate the influence of the high electron spin of the Mn^{2+} ion. By comparison, the modulation depth at the J-band was about 37%, while the calculated value was about 30% (with T_{1e} of 30 μs at this frequency).

Analysis of the background-divided RIDME time traces was performed with Tikhonov regularization (see the Experimental section). The distance distributions and back-calculated dipolar evolution functions, based on the Tikhonov analysis with the conventional kernel function (identical to that used in the DeerAnalysis toolbox), given as:

$$K(T,R) = \int_0^1 \cos\left(\frac{D_{dd}}{R^3}(3x^2-1)\cdot T\right)\mathrm{d}x \qquad (3)$$

are depicted in red in Fig. 6.

The distance distributions obtained from the RIDME measurements all showed two resolved maxima rather than the one found by PELDOR. Similar complex distance distributions have been reported for RIDME experiments with Gd^{3+} ions ($S = 7/2$)[24,25] and

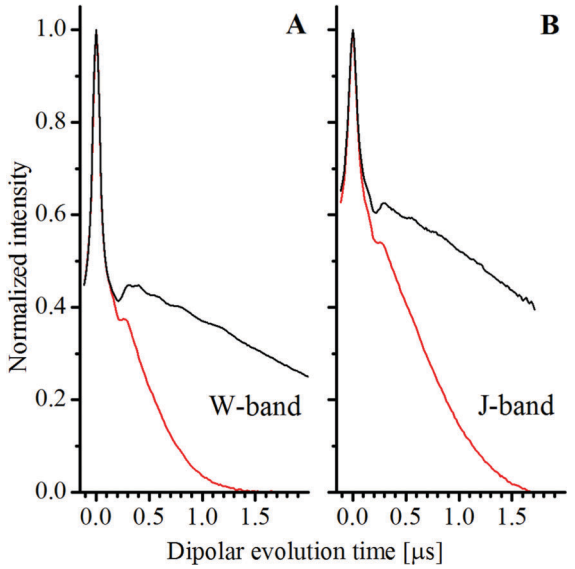

Fig. 5 The experimental RIDME time traces obtained at 25 K. (A) The traces recorded at W-band frequencies in deuterated (black) and protonated (red) solvents. (B) The traces recorded at the J-band. The mixing times were set approximately equal to the T_{1e} relaxation time of Mn^{2+} spins in the samples at the given frequency and temperature.

for the Mn^{2+} – bis-nitroxide complex.[28] This apparent increase in the complexity of the distance distributions has been attributed to multi-quantum longitudinal relaxation of high-spin systems.

The W-band RIDME time trace with a 20 μs mixing time and its analysis are depicted in Fig. 6A, D and G. The peak at about 2.5 nm obtained from Tikhonov regularization analysis with the conventional kernel function (eqn (3)) corresponded to the expected interspin distance.[23] The 2.0 nm peak corresponded to the contribution from the second harmonic of the dipolar coupling frequency. In order to test this, the second harmonic of the dipolar coupling frequency was explicitly added to the kernel function for the Tikhonov regularization:

$$K(T,R)=\int_0^1\left[\frac{1}{2}\cos\left(\frac{D_{dd}}{R^3}(3x^2-1)\cdot T\right)+\frac{1}{2}\cos\left(2\cdot\frac{D_{dd}}{R^3}(3x^2-1)\cdot T\right)\right]dx \quad (4)$$

This led to the disappearance of the 2.0 nm feature (Fig. 6G), leaving the position of the 2.5 nm peak unchanged. It was found that a weight of 0.5 for both components led to a single peak similar to the one found using PELDOR and in agreement with predictions[23] (for more detailed analysis of the dependence of the distance distributions on the weight of the $2\omega_{dd}$ component see Section 7.1 of the ESI† and Fig. S9).

The W-band RIDME time trace with a 80 μs mixing time (approximately T_{1e} at this frequency) and the analysis based on Tikhonov regularization are shown in Fig. 6B, E and H. As above, the expected 2.5 nm distance is found by Tikhonov analysis with the conventional kernel function (Fig. 6H). Assuming that the first and second harmonics of dipolar coupling frequency are equally weighted, as was the case for the experiment with a 20 μs mixing time, the peak at 2.0 nm again disappeared from the distance distribution when the modified kernel function (eqn (4)) was used (Fig. 6E and H in blue). However unlike for the measurement with a shorter mixing time, there was an additional small shoulder at about 1.8 nm in the distance distribution. To test whether this feature was due to the buildup of a triple quantum relaxation component, a kernel function having an explicit third harmonic contribution given by

$$K(T,R)=\int_0^1\left[0.425\cos\left(\frac{D_{dd}}{R^3}(3x^2-1)\cdot T\right)+0.425\cos\left(2\cdot\frac{D_{dd}}{R^3}(3x^2-1)\cdot T\right)+0.15\cos\left(3\cdot\frac{D_{dd}}{R^3}(3x^2-1)\cdot T\right)\right]dx \quad (5)$$

was used and the resulting distance distributions are shown in Fig. 6E and H in green. When the weight of the third harmonic component in the kernel function was set to 0.15 and those of the first and second harmonics to 0.425, the 1.8 nm peak disappeared (Fig. 6H and Fig. S17, ESI†) and the shape of the distance distribution more closely resembled that of the 20 μs mixing time RIDME measurements (for more detailed analysis of the dependence of the distance distribution on the weight of $2\omega_{dd}$ and $3\omega_{dd}$ components see Section 7.2 of the ESI†).

Reduced phase memory time at the J-band with respect to W-band frequencies led to a decrease in sensitivity for RIDME experiments on compound **1**. The distance distribution from the 30 μs mixing time J-band RIDME measurements using the conventional (eqn (3)) and modified kernels (eqn (4) and (5)) is shown in Fig. 6F and I (for more detailed analysis of the dependence of the distance distribution on the weight of $2\omega_{dd}$ and $3\omega_{dd}$ components see Section 7.3 of the ESI†). They were similar to the one obtained from 80 μs mixing time W-band measurements, with the most probable distance being consistent with expectations. However, Tikhonov regularization analysis using the conventional kernel function gave a wing that extended from 3 to 4 nm (red curve in Fig. 6I), which was not present in neither of the W-band RIDME measurements. Tikhonov analysis with the modified kernels (eqn (4) and (5)) enhanced the intensity of this wing (blue and green curves in Fig. 6I). A possible cause of this peak might have been the incomplete cancellation of the moving Hahn echo arising from the last two pulses (see the RIDME pulse sequence in Fig. 1) and the refocused stimulated echo due to imperfect phases of the microwave pulses in the 8-step phase cycle. The correction procedure of the J-band time trace is given in Section 8 of the ESI,† the corrected time trace and the Tikhonov regularization analysis are presented in Fig. S29 (ESI†). As can be seen from this figure, when imperfect phases are accounted for, the wing in the distance distribution was nearly completely suppressed.

It is worth noting that all three RIDME time traces had small amplitude oscillations (see Fig. 6D–F). The Fourier transforms

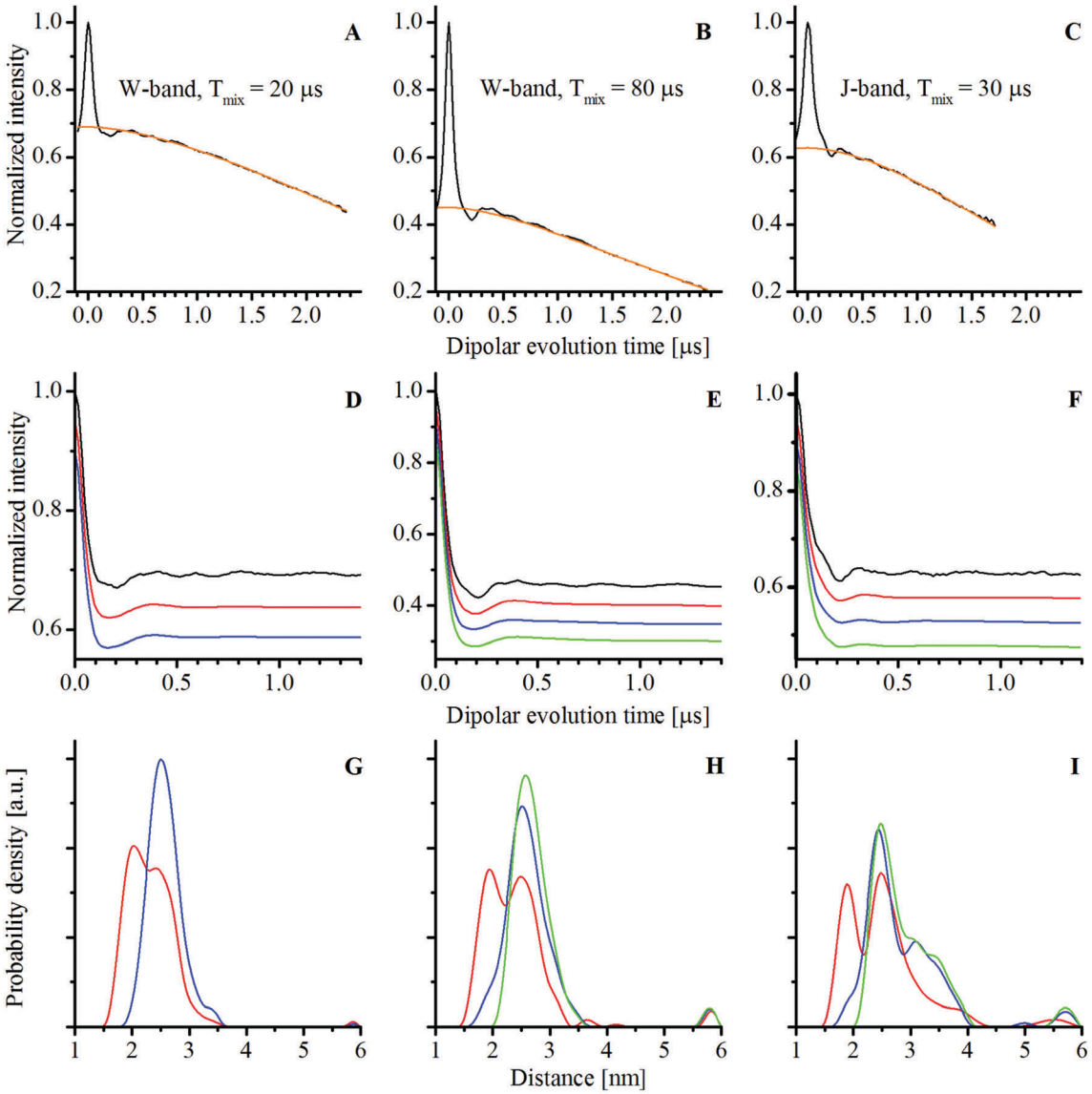

Fig. 6 The RIDME experiments in a deuterated solvent at different microwave frequencies and mixing times obtained at 25 K. (A, D and G) The experiment at W-band frequency with 20 µs mixing time. (B, E and H) The experiment at W-band frequency with 80 µs mixing time. (C, F and I) The experiment at J-band frequency with 30 µs mixing time. Detection of the RIDME signal was performed on the refocused virtual echo. (A–C) The experimental time traces (black) with corresponding stretched-exponential background functions (orange). (D–F) The background-divided experimental RIDME time traces with corresponding fits based on Tikhonov regularization analysis with standard single-frequency component kernel function (red); equally-weighted single- and double-frequency components (0.5 each) modified kernel function (blue); and equally-weighted single- and double-frequency components (0.425 each) with additional triple-frequency component (0.15) modified kernel function (green). Tikhonov regularization was performed using an in-house program with the regularization parameters set to 10 for all fitting procedures. For better visualization, the traces have been vertically offset. (G–I) The corresponding distance distributions obtained from the Tikhonov regularizations using the different kernel functions.

of the differences between the experimental RIDME time traces and back calculations revealed multiple peaks in the frequency domain (see Fig. S12, S16, S19, S24 and S27, ESI†). However, the amplitudes of these oscillations were not more than 3% of the amplitude of the dipolar oscillations. These oscillations remained when the long mixing-time W-band RIDME time trace was divided by the short mixing-time one (see Fig. S30, ESI†). This indicated that the amplitude of these oscillations built up with an increasing mixing time. A more detailed analysis of these oscillations is given in Section 7 of the ESI,† where differences in the background-divided RIDME time traces and back-calculations, based on Tikhonov analysis with different kernel functions, are shown (Fig. S11, S15, S18, S23 and S26, ESI†). Measurements on the mono-MnDOTA complex (chemical structure is shown in Fig. S1, ESI†) also had a small amplitude oscillation (see Section 5 of the ESI,† Fig. S6) but with a distinct single frequency of about 1.7 MHz. This frequency corresponded to the ^{14}N hyperfine coupling[14] and likely arose from non-coherent ESEEM effects.[37] Importantly, the oscillations seen in RIDME (Fig. 6D–F) were so small in

amplitude that they did not affect the Tikhonov analysis in any substantive way.

Comparison of PELDOR and RIDME experiments

The RIDME experiments yielded significantly larger dipolar modulation depths (up to 55%) than those obtained using PELDOR (up to 1.7%). This is a significant advantage in terms of sensitivity. The signal-to-noise ratio per square root of the total accumulation time of the RIDME and PELDOR measurements was determined in order to assess their relative efficiencies (Table 1 and see Section 15 of the ESI† for details). The RIDME measurements were up to 3 times more sensitive than the most sensitive PELDOR measurement (with −252 MHz pump–probe frequency offset), as indicated in Table 1.

However, RIDME measurements on Mn^{2+} centers have some disadvantages with respect to PELDOR. Determination of the background function for PELDOR experiments is already a non-trivial task, especially for flexible molecules, which have dipolar oscillations that dampen very quickly. But even in such cases, the PELDOR background functions have only a single component, namely inter-molecular dipolar couplings, which for randomly distributed molecules can be accurately approximated with a mono-exponential function.[4,6] By contrast, the background functions of RIDME measurements are more complex, having several different contributions which, as in previous studies,[24,25,27] appear to be adequately modeled with a stretched exponential function (analytical functions for the backgrounds are given in Table S1, ESI†). Comparisons of the RIDME and PELDOR background functions are shown in Fig. 6A–C and 4A. One can also see that the RIDME background functions strongly depend on whether the solvent is protonated or deuterated (see Fig. 4). This indicated a strong dependence on the transverse relaxation of the Mn^{2+} spin. Whereas the RIDME background definition is relatively robust in the case of a deuterated solvent (see Section 14 of the ESI† for the analysis of the influence of differently defined backgrounds on the modulation depth and the results of Tikhonov regularization analysis), a more detailed theoretical understanding of how to model the RIDME background function would be important to minimize the uncertainty in the background-correction procedure, especially for the cases where exchange of the solvent is not possible.

In contrast to PELDOR, RIDME exploits longitudinal relaxation to change the m_S state of one of the spins in the pair. In high-spin systems relaxation can effectively change m_S not only by ±1, but also by ±2 and higher. This creates additional harmonics of the dipolar coupling frequency in the experimental time trace that can be seen in the distance distribution. For model systems studied previously[24,25,28] and in this study (see Fig. 6G–I), the distance can still be precisely extracted from Tikhonov analysis with a conventional kernel function (eqn (3)). However, for more flexible systems, a not uncommon case for biomolecules, these peaks cannot be so easily distinguished. Thus, the Tikhonov analysis with the conventional kernel function can lead to the distance distribution that deviates from the real one, even assuming that the background function has been determined correctly (see Section 12 and Fig. S34 of the ESI,† where this situation is modelled). But this analysis can still be used to make an adequate estimation of the distance, since for flexible systems the distance is initially not well defined. For more precise determination of the distance the Tikhonov regularization with the modified kernel can be of interest. As can be seen from Fig. 6G–I, with this approach the unwanted contributions from the harmonics of the dipolar-coupling frequency can be removed from the distance distributions. However, the weights of the different components vary, depending on the sample and experimental conditions,[24–25,28] leading to additional parameters that must be accounted for in the data analysis. Moreover, the more complex background function of RIDME can complicate the analysis of the harmonics contributions of the dipolar coupling, as has been shown in RIDME on a protein labelled with Gd^{3+} centers.[25] Such peculiarities associated with the complex background function and harmonics of the dipolar coupling frequency in RIDME experiments with Mn^{2+} can make it difficult to obtain meaningful information particularly in flexible biological systems. However, for systems with a relatively rigid structure, where dipolar oscillations are easily seen, RIDME measurements can be quantitatively interpreted and have higher sensitivity compared to PELDOR.

These considerations suggest that Mn^{2+} – based RIDME measurements are best suited for cases where accurate distances are not required, for example for determining the quaternary structures of proteins or for optimizing labelling conditions. Such applications can be performed more quickly due to the higher sensitivity and relative simplicity of setting up the RIDME experiment. For the cases where accurate distances are needed, RIDME can be complemented with PELDOR, which requires longer measurement times.

Experimental

The concentration of compound **1** was 50 μM in D_2O : glycerol-d_8 or H_2O : glycerol, 4 : 1, v : v with 100 mM HEPES at pD or pH 8. The detailed synthesis of the compound and initial characterization are presented in another study.[23] RIDME and PELDOR experiments were performed in a deuterated solvent with the exception of some RIDME time traces shown in Fig. 4.

W-band pulsed EPR measurements

Pulsed EPR experiments at W-band frequencies were performed on a Bruker Elexsys E680 EPR spectrometer, equipped with a Bruker ''power upgrade 2'' and an Oxford Instruments CF935 flow cryostat. The Hahn echo-detected field-swept EPR spectrum was obtained with 10 and 20 ns pulses, an interpulse delay of 400 ns, 1 shot per point, a pulse repetition time of 11 ms, a sweep width of 0.1 T at a temperature of 25 K.

All RIDME experiments were performed with a deadtime-free five pulse sequence at a sample temperature of 25 K.[27]

The W-band RIDME experiment with a mixing time of 20 μs was conducted with 10 ns and 20 ns π/2 and π pulses, respectively. This short mixing time was about $3T_{me}$ time in order to eliminate the transversal component of the

magnetization. Hence, the unnecessary echo signals originating from the π/2 pulses of the mixing block and other pulses in the sequence, and, therefore, distortions in the RIDME time traces, are removed. Initial delay between pulses (d_1 in Fig. 1) was 400 ns. The initial time position for the mixing block (position of the first π/2 pulse in the block) was 300 ns after the first π pulse. The time delay between the second π/2 in the block and the last π pulse (d_3 in Fig. 1) was 2.5 μs. The sequence can be represented: 10 ns-400 ns-20 ns-(300 ns + ΔT)-10 ns-20μs-10 ns-(2.5 μs − ΔT)-20 ns-2.4 μs-echo. The time increment ΔT was 16 ns with 156 number of points. A shot repetition time was 1 ms and the number of shots per point was 100. The 8-step phase cycle protocol[27] for the π/2 pulses was used. 55 scans were taken corresponding to a total accumulation time of about 2 hours. For the RIDME experiments with a mixing time of 80 μs on compound **1** in a deuterated solvent, 371 scans were taken corresponding to a total accumulation time of about 14.23 hours. For analogous measurements in a protonated solvent, 507 scans were taken corresponding to a total accumulation time of about 16 hours. All W-band RIDME measurements were performed with the resonance position of the pulses set to the highest field hyperfine line of the central transition.

W-band PELDOR measurements were performed at 6 K using the standard four-pulse, deadtime-free PELDOR/DEER sequence,[1,6] with a four-step two-phase cycle.[38] The initial interpulse delay (between detection π/2 and π pulses) was 544 ns and the dipolar evolution window was 2226 ns. The initial time delay between the detection π pulse and the pump pulse was 364 ns which was incremented by 16 ns with 100 number of points. The shot repetition time was 800 μs with 100 shots per point. For measurements with a pump–probe frequency offset of 70 MHz, the pump pulse duration was 24 ns and the duration of the π/2 and π detection pulses was 12 and 24 ns. The number of scans was 256 resulting in a total accumulation time of about 2.34 hours. For measurements with a pump–probe frequency offset of 150 MHz, the pump pulse duration was 24 ns and the duration of the π/2 and π detection pulses was 36 and 72 ns. The number of scans was 363 resulting a total accumulation time of about 3.32 hours. For measurements with a pump–probe frequency offset of −252 MHz, the pump pulse duration was 58 ns and the duration of the π/2 and π detection pulses was 30 and 58 ns. The number of scans was 243 resulting in a total accumulation time of about 2.22 hours.

J-band pulsed EPR measurements

J-band RIDME experiments were performed on a 263 GHz Bruker Elexsys E780 pulsed EPR spectrometer. The system is equipped with a 9.4 T superconducting magnet, with a quasi-optical front-end with a microwave power of about 15 mW and an arbitrary waveform generator (AWG). The J-band RIDME experiment with a mixing time of 30 μs was conducted with 18 ns and 32 ns π/2 and π pulses, respectively. Initial delay between pulses (d_1 in Fig. 1) was 400 ns. The initial time position for the mixing block (the position of the first π/2 pulse in the block) was 300 ns after the first π pulse. The time delay between the second π/2 in the block and the last π pulse (d_3 in Fig. 1) was 2.0 μs. The sequence can be represented: 18 ns-400 ns-32 ns-(300 ns + ΔT)-18 ns-30 μs-18 ns-(2.0 μs − ΔT)-32 ns-1.9 μs-echo. The time increment ΔT was 16 ns with 115 number of points. The shot repetition time was 0.5 ms and the number of shots per point was 100. A 8-step phase cycle protocol[27] for the π/2 pulses was used. 930 scans were taken corresponding to a total accumulation time of about 12.95 hours.

The J-band RIDME time trace on compound **1** in a protonated solvent (Fig. 4) was obtained with 16 ns and 30 ns π/2 and π pulses, respectively, and a mixing time of 25 μs. All the other parameters were identical to those in the previous case. The number of scans was 1133 resulting to a total acquisition time of about 18 hours. All J-band RIDME time traces were obtained with the resonance position of the pulses set to the lowest field hyperfine line of the central transition. No change in the time traces upon changing the resonance position of the pulses to the highest field hyperfine line was observed.

Tikhonov regularization analysis

The Tikhonov program used in our analysis closely followed the one found in DeerAnalysis.[36] This implementation was faster and more flexible with regard to the use of non-conventional kernels. Our implementation was validated by comparing the results against those obtained using DeerAnalysis for a set of PELDOR measurements.

Our Fortran-90 program was an adaption of the program FTIKREG[39] which minimizes a functional:

$$G(P) = \|KP - F\|^2 + \lambda\|LP\|, \quad (6)$$

where

$$F(T) = K(T,R)P(R) \quad (7)$$

and for PELDOR measurements, as described previously,[36] $F(T)$ is the PELDOR form factor, $P(R)$ is the distance distribution and $K(T,R)$ is the kernel function. The conventional kernel function that was used was identical to that used in DeerAnalysis.[36,40] L was the second derivative operator. Although provided as an option in FTIKREG, $P(R)$ was always constrained to be positive in our implementation.[36] Low-level linear algebra routines (*e.g.* SVD) in the original FTIKREG were replaced with appropriate optimized operating system libraries. The ''self-consistency'' method of FTIKREG was not implemented since it has been shown previously that the L-curve graphical solution method was more appropriate.[36,41] Based on the visual inspection of the Tikhonov solutions and L-curves (see above), a regularization parameter of 10 was found to be appropriate for the reported measurements.

Conclusion

RIDME and PELDOR experiments were performed on a model compound, containing two dipolar-coupled Mn^{2+} ions. RIDME experiments were performed at W- and J-band microwave frequencies. For the studied system, where the ligand for Mn^{2+} ion is DOTA, it is advantageous to perform the experiments at W-band

frequency, due to a higher electron spin phase memory time at this frequency. A significant influence of the solvent deuteration on the background function was observed for RIDME experiments at both frequencies.

Both types of EPR dipolar spectroscopy experiments, RIDME and PELDOR, yielded a distance of 2.5–2.6 nm in good agreement with predictions. RIDME gave a significantly larger modulation depth (up to 55%) with respect to PELDOR (up to 1.7%) that led to a significant gain in sensitivity. In general, RIDME is instrumentationally less demanding than PELDOR, since it does not require a second microwave frequency and an associated increased spectrometer bandwidth. The complex background function and contributions from harmonics of the dipolar coupling frequency can reduce the accuracy of distances determined using RIDME especially in cases where systems are flexible. The harmonic contributions can be accounted for by using a kernel that includes such terms in the Tikhonov analysis, but at the price of increased complexity in interpretation. Based on this, we concluded that the RIDME technique is best suited for the quantitative analysis of relatively rigid systems or cases where accurate distances are less important and sensitivity is of highest priority.

Acknowledgements

This work was supported by a joint ANR/DFG project (MnHFPELDOR, ANR-DFG Chemistry 2011-INTB-1010-01) and DFG (PR 294/14-1), the French Infrastructure for Integrated Structural Biology (FRISBI, ANR-10-INSB-05-01), the CNRS "Interface PCB" program, the DFG Priority Program 1601 (New Frontiers in Sensitivity for EPR Spectroscopy). The W-band EPR spectrometer was funded by the Region Ile-de-France "Sesame" program, the CEA, and CNRS and the J-band EPR spectrometer by the Cluster of Excellence Frankfurt (CEF) Macromolecular Complexes.

References

1 M. Pannier, S. Veit, A. Godt, G. Jeschke and H. W. Spiess, *J. Magn. Reson.*, 2000, **142**, 331.
2 G. Jeschke, *Annu. Rev. Phys. Chem.*, 2012, **63**, 419.
3 O. Schiemann and T. F. Prisner, *Q. Rev. Biophys.*, 2007, **40**, 1.
4 A. D. Milov, K. M. Salikhov and M. D. Shchirov, *Phys. Solid State*, 1981, **23**, 565.
5 R. G. Larsen and D. J. Singel, *J. Chem. Phys.*, 1993, **98**, 5134.
6 R. E. Martin, M. Pannier, F. Diederich, V. Gramlich, M. Hubrich and H. W. Spiess, *Angew. Chem., Int. Ed.*, 1998, **37**, 2833.
7 W. L. Hubbell, A. Gross, R. Langen and M. Lietzow, *Curr. Opin. Struct. Biol.*, 1998, **8**, 649.
8 W. L. Hubbell, C. J. López, C. Altenbach and Z. Yang, *Curr. Opin. Struct. Biol.*, 2013, **23**, 725.
9 G. E. Fanucci and D. S. Cafiso, *Curr. Opin. Struct. Biol.*, 2006, **16**, 644.
10 I. Krstic, B. Endeward, D. Margraf, A. Marko and T. F. Prisner, *Top. Curr. Chem.*, 2012, **321**, 159.
11 S. A. Shelke and T. T. Sigurdsson, *Eur. J. Org. Chem.*, 2012, 2291.
12 A. Raitsimring, C. Gunanathan, A. Potapov, I. Efremenko, J. Martin, D. Milstein and D. Goldfarb, *J. Am. Chem. Soc.*, 2007, **129**, 14138.
13 D. Banerjee, H. Yagi, T. Huber, G. Otting and D. Goldfarb, *J. Phys. Chem. Lett.*, 2012, **3**, 157.
14 H. Y. V. Ching, P. Demay-Drouhard, H. C. Bertrand, C. Policar, L. C. Tabares and S. Un, *Phys. Chem. Chem. Phys.*, 2015, **17**, 23368.
15 A. Martorana, Y. Yang, Y. Zhao, Q.-F. Li, X.-C. Su and D. Goldfarb, *Dalton Trans.*, 2015, **44**, 20812.
16 H. Y. V. Ching, F. C. Mascali, H. C. Bertrand, E. M. Bruch, P. Demay-Drouhard, R. M. Rasia, C. Policar, L. C. Tabares and S. Un, *J. Phys. Chem. Lett.*, 2016, **7**, 1072.
17 K. Wieghardt, *Angew. Chem., Int. Ed.*, 1989, **28**, 1153.
18 G. Reed and G. Markham, in *Biological Magnetic Resonance*, ed. L. Berliner and J. Reuben, 1984, vol. 6, p. 73.
19 T. Schweins, K. Scheffzek, R. Aßheuer and A. Wittinghofer, *J. Mol. Biol.*, 1997, **266**, 847.
20 C. W. Bock, A. K. Katz, G. D. Markham and J. P. Glusker, *J. Am. Chem. Soc.*, 1999, **121**, 7360.
21 G. L. Bir and L. S. Sochava, *Phys. Solid State*, 1964, **5**, 2637.
22 G. L. Bir, *Phys. Solid State*, 1964, **5**, 1628.
23 P. Demay-Drouhard, H. Y. V. Ching, D. Akhmetzyanov, R. Guillot, L. C. Tabares, H. C. Bertrand and C. Policar, *ChemPhysChem*, 2016, **17**, 2066.
24 S. Razzaghi, M. Qi, A. I. Nalepa, A. Godt, G. Jeschke, A. Savitsky and M. Yulikov, *J. Phys. Chem. Lett.*, 2014, **5**, 3970.
25 A. Collauto, V. Frydman, M. D. Lee, E. H. Abdelkader, A. Feintuch, J. D. Swarbrick, B. Graham, G. Otting and D. Goldfarb, *Phys. Chem. Chem. Phys.*, 2016, **18**, 19037.
26 L. V. Kulik, S. Dzuba, I. Grigoryev and Y. D. Tsvetkov, *Chem. Phys. Lett.*, 2001, **343**, 315.
27 S. Milikisyants, F. Scarpelli, M. G. Finiguerra, M. Ubbink and M. Huber, *J. Magn. Reson.*, 2009, **201**, 48.
28 A. Meyer and O. Schiemann, *J. Phys. Chem. A*, 2016, **120**, 3463.
29 I. Kaminker, I. Tkach, N. Manukovsky, T. Huber, H. Yagi, G. Otting, M. Bennati and D. Goldfarb, *J. Magn. Reson.*, 2013, **227**, 66.
30 M. R. Cohen, V. Frydman, P. Milko, M. Iron, E. H. Abdelkader, M. D. Lee, J. D. Swarbrick, A. Raitsimring, G. Otting, B. Graham, A. Feintuch and D. Goldfarb, *Phys. Chem. Chem. Phys.*, 2016, **18**, 12847.
31 P. E. Spindler, S. J. Glaser, T. E. Skinner and T. F. Prisner, *Angew. Chem., Int. Ed.*, 2013, **52**, 3425.
32 A. Doll, S. Pribitzer, R. Tschaggelar and G. Jeschke, *J. Magn. Reson.*, 2013, **230**, 27.
33 A. Doll, M. Qi, N. Wili, S. Pribitzer, A. Godt and G. Jeschke, *J. Magn. Reson.*, 2015, **259**, 153.
34 A. Doll, M. Qi, S. Pribitzer, N. Wili, M. Yulikov, A. Godt and G. Jeschke, *Phys. Chem. Chem. Phys.*, 2015, **17**, 7334.
35 P. E. Spindler, I. Waclawska, B. Endeward, J. Plackmeyer, C. Ziegler and T. F. Prisner, *J. Phys. Chem. Lett.*, 2015, **6**, 4331.
36 G. Jeschke, V. Chechik, P. Ionita, A. Godt, H. Zimmermann, J. Banham, C. Timmel, D. Hilger and H. Jung, *Appl. Magn. Reson.*, 2006, **30**, 473.

37 L. V. Kulik, E. S. Salnikov and S. Dzuba, *Appl. Magn. Reson.*, 2005, **28**, 1.
38 E. Matalon, T. Huber, G. Hagelueken, B. Graham, V. Frydman, A. Feintuch, G. Otting and D. Goldfarb, *Angew. Chem., Int. Ed.*, 2013, **52**, 11831.
39 J. Weese, *Comput. Phys. Commun.*, 1992, **69**, 99.
40 G. Jeschke, G. Panek, A. Godt, A. Bender and H. Paulsen, *Appl. Magn. Reson.*, 2004, **26**, 223.
41 Y.-W. Chiang, P. P. Borbat and J. H. Freed, *J. Magn. Reson.*, 2005, **172**, 279.

Electronic Supplementary Material (ESI) for Physical Chemistry Chemical Physics.

RIDME Spectroscopy on High-Spin Mn^{2+} Centers

Supporting Information

D. Akhmetzyanov,‡[a] H. Y. V. Ching,‡[b] V. Denysenkov,[a] P. Demay-Drouhard,[c,d] H. C. Bertrand,[c,d] L. C. Tabares,[b] C. Policar,[c,d] T. F Prisner*[a] and S. Un*[b]

[a] Goethe-University Frankfurt am Main, Institute of Physical and Theoretical Chemistry and Center for Biomolecular Magnetic Resonance, Max von Laue Str. 7, 60438 Frankfurt am Main, Germany

[b] Institute for Integrative Biology of the Cell (I2BC), Department of Biochemistry, Biophysics and Structural Biology, Université Paris-Saclay, CEA, CNRS UMR 9198, Gif-sur-Yvette, F-91198, France.

[c] Département de Chimie, Ecole Normale Supérieure, PSL Research University, UPMC Univ Paris 06, CNRS, Laboratoire des Biomolécules (LBM), 24 rue Lhomond, 75005 Paris, France.

[d] Sorbonne Universités, UPMC Univ Paris 06, Ecole Normale Supérieure, CNRS, Laboratoire des Biomolécules (LBM), 24 rue Lhomond, 75005 Paris, France.

‡ Authors contributed equally to the work

* Corresponding authors

Table of contents

1. Chemical structure of mono-MnDOTA complex

Chemical structure of mono-MnDOTA (compound **2**) is depicted in Figure S1.

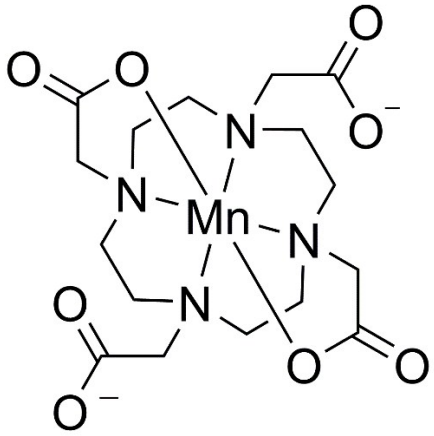

Figure S1. Chemical structure of compound **2**

2. W-band RIDME on compound **1** in deuterated solvent with different pulse lengths

W-band RIDME time traces on compound **1** in a deuterated solvent (D_2O:glycerol-d_8, 4:1, v:v, with 100 mM HEPES at pD 8) obtained with different pulses lengths 10/20 ns (hard pulses) and 40/80 ns (soft pulses) with analysis based on Tikhonov regularization in DeerAnalysis toolbox[1] are shown in Figure S2. The intensity of the second dipolar-coupling frequency harmonic, seen in the time traces and the corresponding distance distribution, is reduced for the case of long pulses. This can be attributed to significantly reduced excitation bandwidth of 80 ns π pulse with respect to 20 ns π pulse and as a result the multiple dipolar coupling frequency components are artificially supressed in the corresponding RIDME time trace.

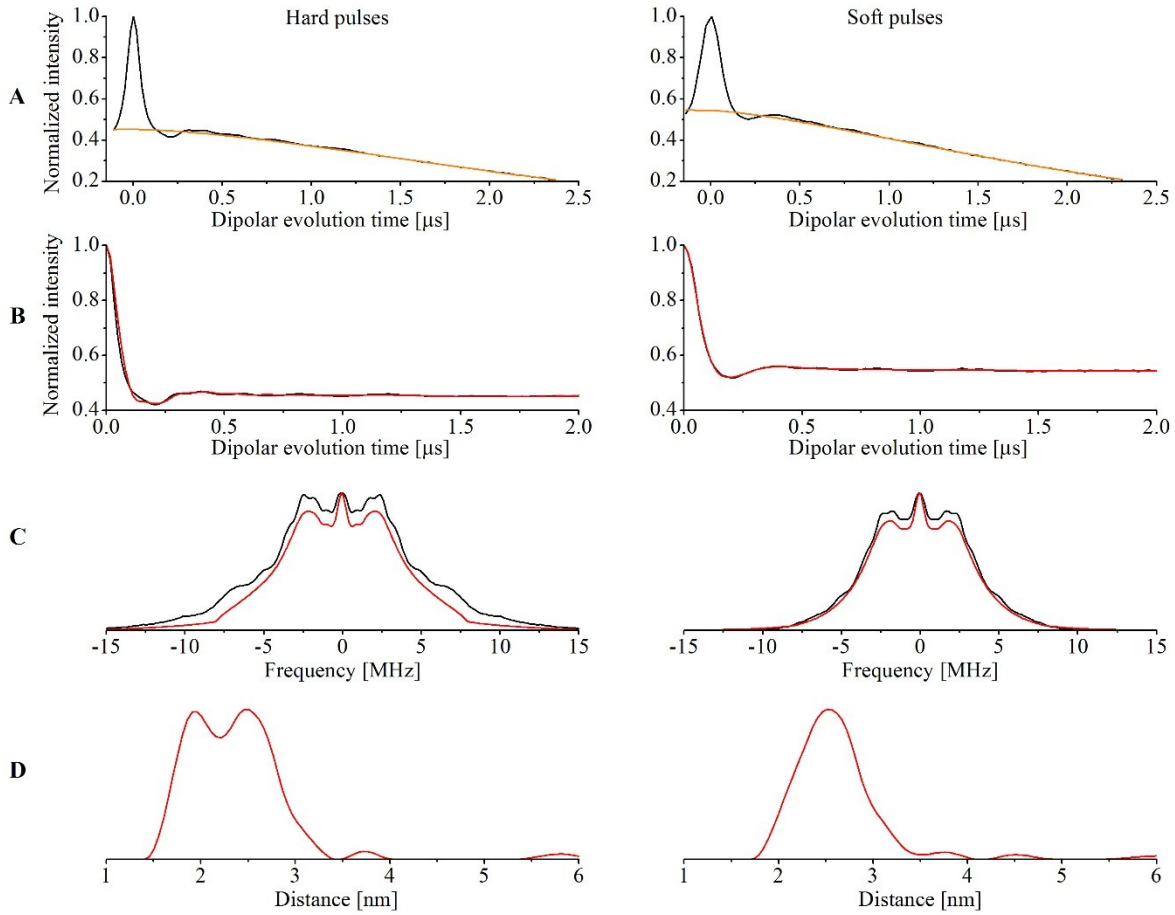

Figure S2. A. Experimental W-band RIDME time trace obtained on compound **1** at 25 K (black lines) in a deuterated solvent, with corresponding stretched-exponential background function (orange lines). Left side. RIDME time traces obtained with hard pulses (π-pulse length of 20 ns). Right side. RIDME time traces obtained with soft pulses (π-pulse length of 80 ns). The spectral position, where the time traces were obtained, corresponded to highest-field hyperfine coupling component (See Figure 3). RIDME time traces were obtained with mixing time of 80 µs.

B. Background-divided RIDME time traces (black lines) with corresponding fits based on Tikhonov regularization analysis (red lines) obtained in DeerAnalysis with a regularization parameter of 10.

C. Fourier transform of background-divided RIDME time traces (black lines) and of the Tikhonov regularization fits (red lines).

D. Distance distributions obtained with Tikhonov regularization analysis.

3. W-band RIDME on compound **1** in protonated solvent with different pulse lengths

W-band RIDME time traces on compound **1** in a protonated solvent (H_2O:glycerol, 4:1, v:v, with 100 mM HEPES at pH 8) obtained with different pulses lengths 10/20 ns (hard pulses) and 40/80 ns (soft pulses) with analysis based on Tikhonov regularization in DeerAnalysis toolbox are depicted in Figure S3. The background functions of these RIDME time traces decay significantly faster than the corresponding background functions of RIDME time traces obtained with a sample in a deuterated solvent (Figure S2). This effect is attributed to proton nuclear spin diffusion that leads to fast decay of the refocused virtual echo. This effect significantly complicates the background-correction procedure and further analysis of the dipolar evolution functions. Therefore, subsequent RIDME experiments were performed with a sample dissolved in a deuterated solvent.

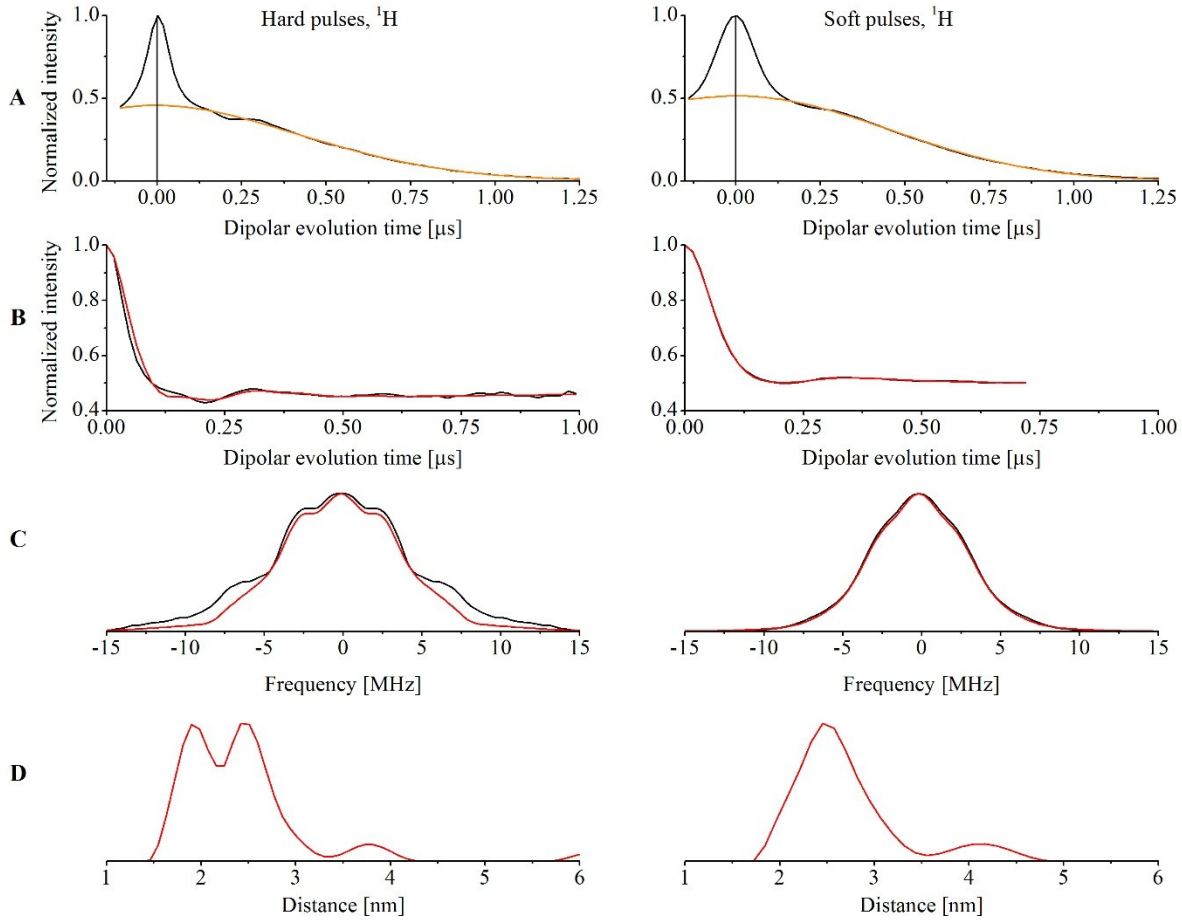

Figure S3. A. Experimental W-band RIDME time trace obtained on compound **1** at 25 K (black lines) in protonated solvent, with corresponding stretched-exponential background function (orange lines). Left side. RIDME time traces obtained with hard pulses (π-pulse length of 20 ns). Right side. RIDME time traces obtained with soft pulses (π-pulse length of 80 ns). The spectral position, where the time traces were obtained corresponded to the highest-field hyperfine coupling component (See Figure 3). RIDME time traces were obtained with mixing time of 80 µs.
B. Background-divided RIDME time traces (black lines) with corresponding fits based on Tikhonov regularization analysis (red lines) obtained in DeerAnalysis with a regularization parameter of 10.
C. Fourier transform of background-divided RIDME time traces (black lines) and of the Tikhonov regularization fits (red lines).
D. Distance distributions obtained with Tikhonov regularization analysis.

4. W-band RIDME on compound **1** in protonated solvent obtained at different spectral positions

W-band RIDME time traces on compound **1** in protonated solvent were obtained at three different position in the EPR spectrum. The first position was chosen to be on resonance with the highest field hyperfine line (the data are shown in Figure S3 - left). The second resonance field position was set 100 G larger than the position of the highest field hyperfine line and the third position was set in the middle between the 3rd and the 4th hyperfine lines. The background-divided RIDME time traces, corresponding Fourier transforms and distance distributions, obtained by Tikhonov regularization with conventional kernel function, are shown in Figure S4.

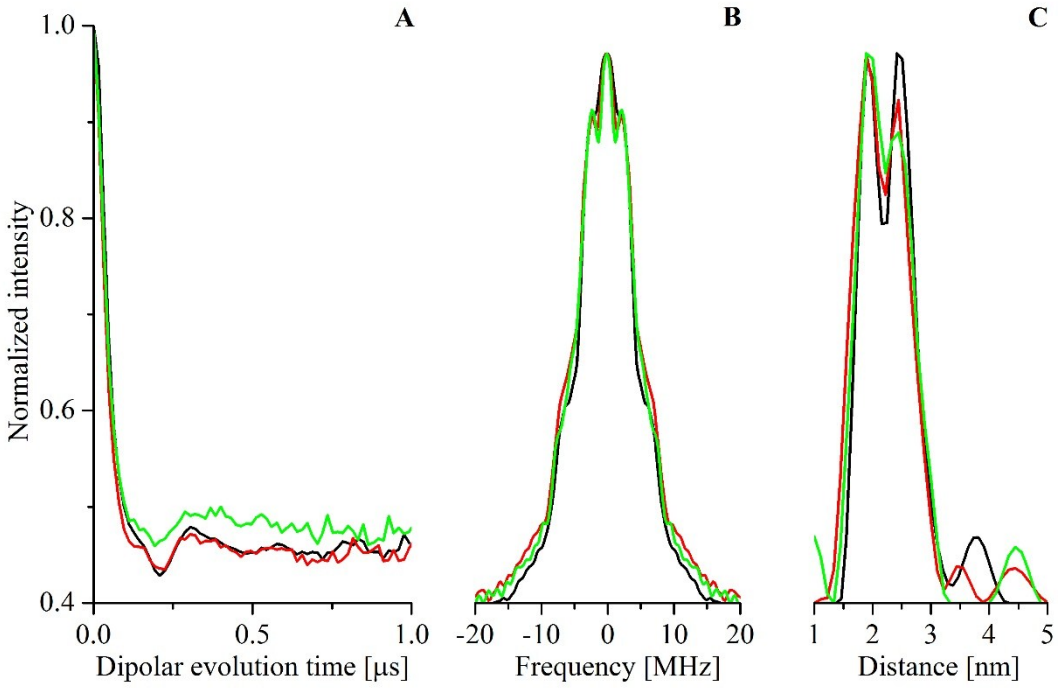

Figure S4. A. Background-divided W-band RIDME time trace obtained on compound **1** in protonated solvent at 25 K (hard pulses). The spectral positions, where the time traces were obtained, corresponded to the highest hyperfine coupling component (black), 100 G larger than the highest hyperfine coupling component (red) and the middle between 3rd and 4th hyperfine components (green). **B.** Corresponding Fourier transforms. **C.** Corresponding distance distributions, obtained by Tikhonov regularization with conventional kernel function in DeerAnalysis toolbox with a regularization parameter of 10.

Insignificant changes were observed in the RIDME time traces (and corresponding Fourier transforms and distance distributions) upon changing the resonance position. As the spectral position, corresponding to the highest hyperfine line, is the most sensitive, it was used for further RIDME studies.

5. RIDME on mono-MnDOTA complex in deuterated and protonated solvents obtained at W-band frequencies

W-band RIDME experimental time traces on mono-MnDOTA (compound **2**) obtained with hard and soft pulses are depicted in Figure S5. The measurements were performed with a sample in deuterated (D_2O:glycerol-d_8, 4:1, v:v, with 100 mM HEPES at pD 8) and protonated solvents (H_2O:glycerol, 4:1, v:v, with 100 mM HEPES at pH 8).

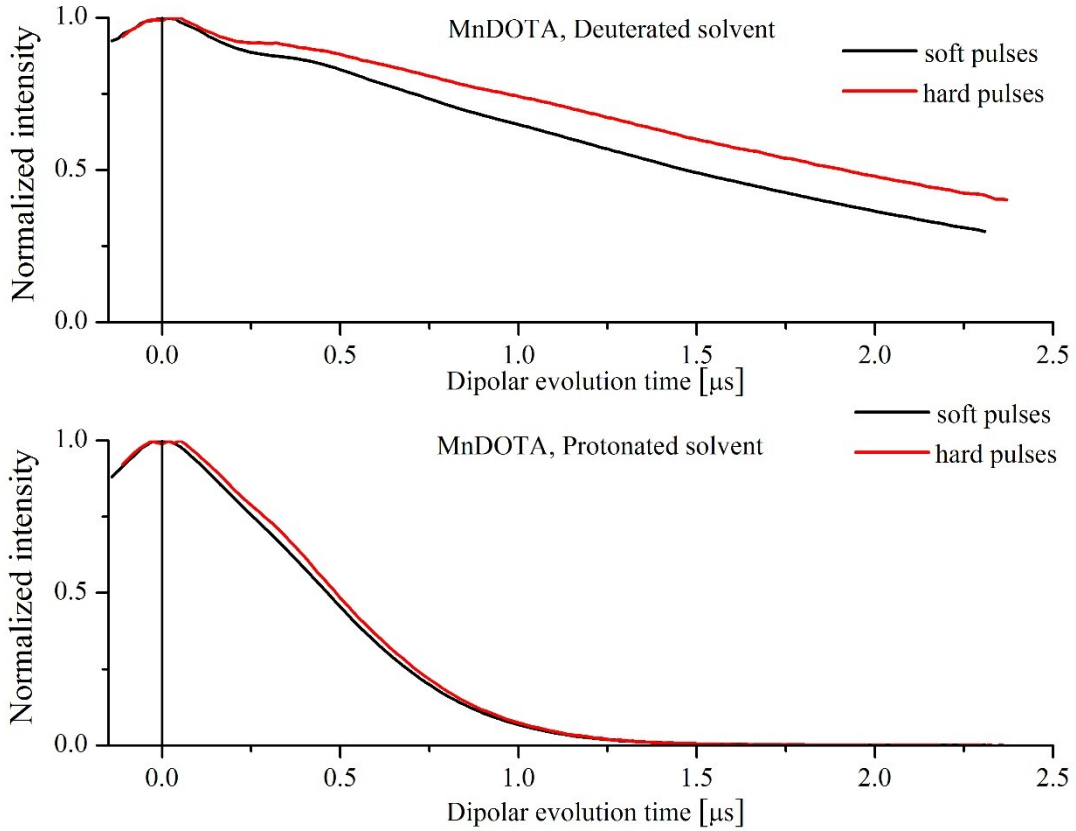

Figure S5. Top. RIDME experimental time traces on compound **2** in a deuterated solvent. The time traces are obtained with soft (black) and hard (red) pulses. Bottom. RIDME time traces on compound **2** in a protonated solvent. The time traces are obtained with soft (black) and hard (red) pulses. The mixing time for all experiments was 80 μs.

RIDME experimental time traces on mono-MnDOTA (compound **2**) with corresponding stretched exponential background function as well as background-divided time traces with corresponding Fourier transforms are depicted in Figure S6. The RIDME time traces, obtained with compound **2** in deuterated solvent, reveal an oscillation with a frequency of about 1.7 MHz. This value corresponded to isotropic hyperfine coupling of Mn^{2+} with 4 equivalent nitrogen nuclei belonging to the DOTA ring. This coupling has been determined by ELDOR detected NMR experiment on similar MnDOTA complex in another study.[2] It is worth noting that the frequency of the oscillation, revealed by RIDME experiment, corresponds purely to the ^{14}N hyperfine coupling, but not the combination of the hyperfine coupling frequency with the ^{14}N Larmor frequency (ν_L of about 10 MHz at W-band frequencies), as would be expected for coherent ESEEM effect. Thus, this oscillation, possibly appears due to incoherent ESEEM effect. This effect has been studied in detail on nitroxide radical in the temperature range of 130 K - 240 K at X-band frequencies and appeared due to the relaxation of protons from the methyl group.[3] Thus, upon fast reorientation of the methyl groups, the proton hyperfine coupling

fluctuates, which causes nuclear relaxation.[3] In our case, the effect is assumed to appear due to nitrogen nuclei relaxation. The longitudinal relaxation rate of the ^{14}N is enhanced due to the coupling to fast relaxing Mn^{2+} ions. The fact that the modulation depth of nuclear oscillations of about 3-4 % is an order of magnitude lower than the modulation depth of dipolar oscillation, indicates that ^{14}N longitudinal relaxation is significantly longer than that of electron spin (1 to 2 orders of magnitude). Note also that the presence of four equivalent ^{14}N nuclei significantly increases the probability of one of the ^{14}N nuclei undergoing an arbitrary spin flip.

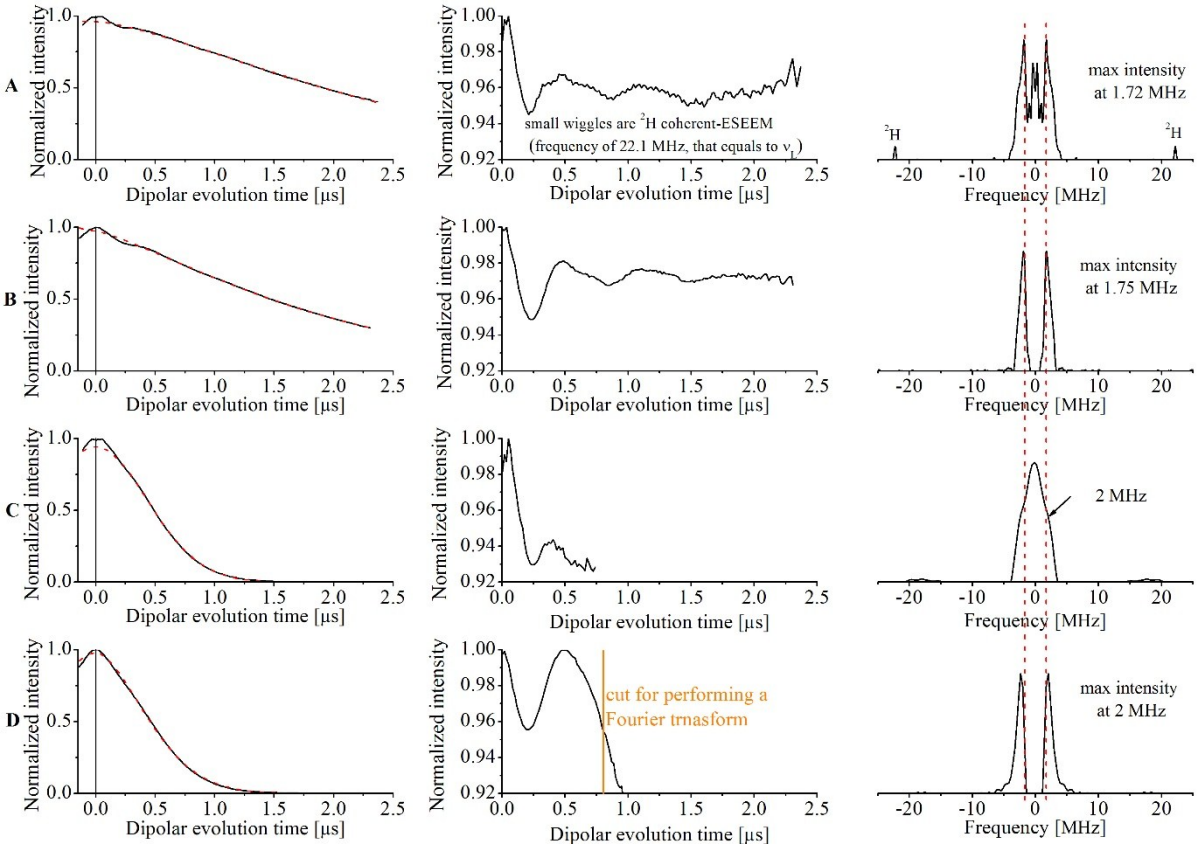

Figure S6. Experimental RIDME time trace, obtained on compound **2** with corresponding stretched exponential background function (left). The time traces were obtained with mixing time of 80 µs. Corresponding background-divided RIDME time trace (middle) and Fourier transform of background-divided time trace (right). **A** Sample in a deuterated solvent and RIDME time trace recorded with hard pulses. **B** Sample in a deuterated solvent and RIDME time trace recorded with soft pulses. **C** Sample in a protonated solvent and RIDME time trace recorded with hard pulses. **D** Sample in a protonated solvent and RIDME time trace recorded with soft pulses.

The RIDME time traces obtained on compound **2** in a protonated solvent decay considerably faster than those obtained in a deuterated solvent. Such a fast decaying backgrounds dampen all kind of oscillations. Therefore, the ambiguity in obtaining of the background function is significant and reliable analysis of the oscillation after background-correction procedure might be not possible. Thus, the background-divided time traces reveal some oscillations with a frequency of about 2 MHz. Due to the uncertainty of obtaining the background functions, this oscillations can correspond with an error of about 0.3 MHz to the ^{14}N, as was discussed above.

6. Relaxation measurements on mono- and bis-MnDOTA complexes at W-band frequencies

Phase memory time measurements (T_{me}) are given in Figure S7. The measurements are performed with standard two-pulse Hahn-echo sequence with hard pulses. Longitudinal electron relaxation time measurements (T_{1e}) are given in Figure S8. Measurements are performed with inversion recovery sequence with hard pulses. The values for T_{1e} are determined as τ_3 - τ_2, where τ_3 and τ_2 are the constants, after which echo decayed by a factor of e^3 and e^2, respectively. Longitudinal relaxation time defined in this way is less affected by spectral diffusion. Due to relatively high error, relaxation times are assumed to be the same for all cases.

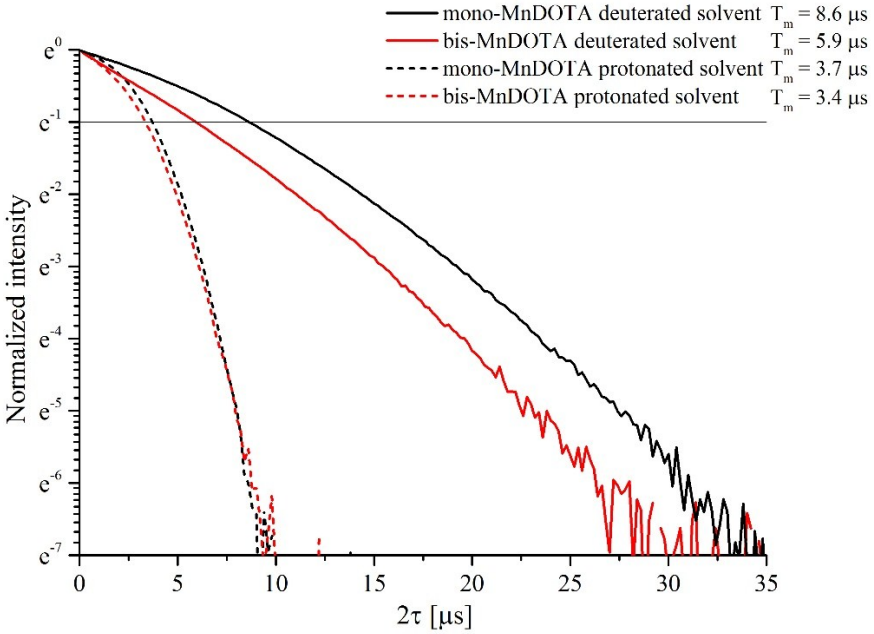

Figure S7. Phase memory time measurements at the spectral position used for RIDME experiments.

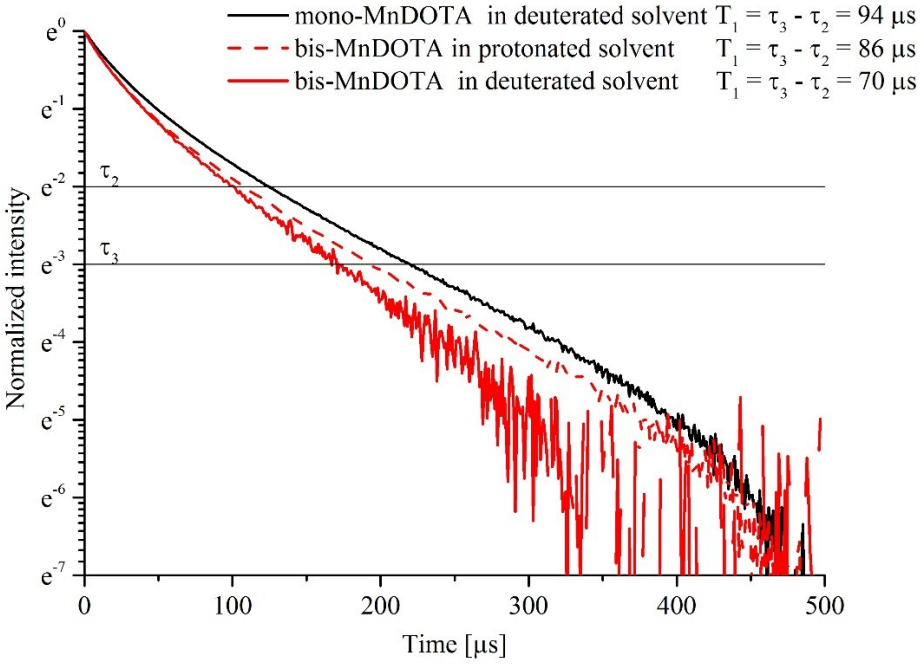

Figure S8. Longitudinal relaxation time measurements at the spectral position used for RIDME experiments.

7. Tikhonov regularization with modified kernel function: influence of the weights of multiple dipolar coupling frequency components

7.1 W-band RIDME with mixing time of 20 μs

Distance distributions obtained with the kernel function for the Tikhonov regularization, where the weight of the first and second harmonic of the dipolar-coupling frequency were varied (parameter β in equation S1) are depicted in Figure S9.

$$K(T,R)=\int_0^1\left[\beta\cos\left(\frac{D_{dd}}{R^3}\left(3x^2-1\right)T\right)+(1-\beta)\cos\left(2\cdot\frac{D_{dd}}{R^3}\left(3x^2-1\right)T\right)\right]dx \tag{S1}$$

Figure S9 shows how the intensity of the peak at 2.0 nm from the second dipolar coupling frequency harmonic, decreases with increasing weight (1 - β) in the kernel function. With the weight β = 0.5 the peak at 2.0 nm disappears and the peak corresponding to the expected distance (2.5 nm) achieves its maximum intensity. When β < 0.5, an additional peak with longer distance appears. This peak roughly corresponds to half the dipolar coupling frequency, as the Tikhonov regularization is now performed with the second term of equation S1 being dominant. The cases where the weight of the second harmonic of the dipolar-coupling frequency exceeds the weight of the first harmonic do not have physical meaning. Such analysis was performed only to observe a tendency in the distance distribution.

Adding the second dipolar coupling frequency harmonic component into the kernel function leads to an increase in the RMSD between the RIDME time trace and corresponding back-calculation. The RMSD map is given in Figure S10. The case where a single peak at the expected distance in the distance distribution was observed (β = 0.5) did not correspond to the minimal RMSD value, although it appeared to be a local minima. Mapping the differences between the background-divided RIDME time trace (also modulation depth scaled) and corresponding back-calculation (see Figure S11 and Fourier transform in Figure S12) showed small amplitude oscillations at all β values. The RMSD values shown in Figure S10 are influenced by these oscillations and cannot be used as a judgment of the fit with different weights of multiple dipolar-coupling frequency components. Such oscillations were not observed with mono-MnDOTA complex. In order to understand the origin of these effects more deeply, a more systematic study is needed.

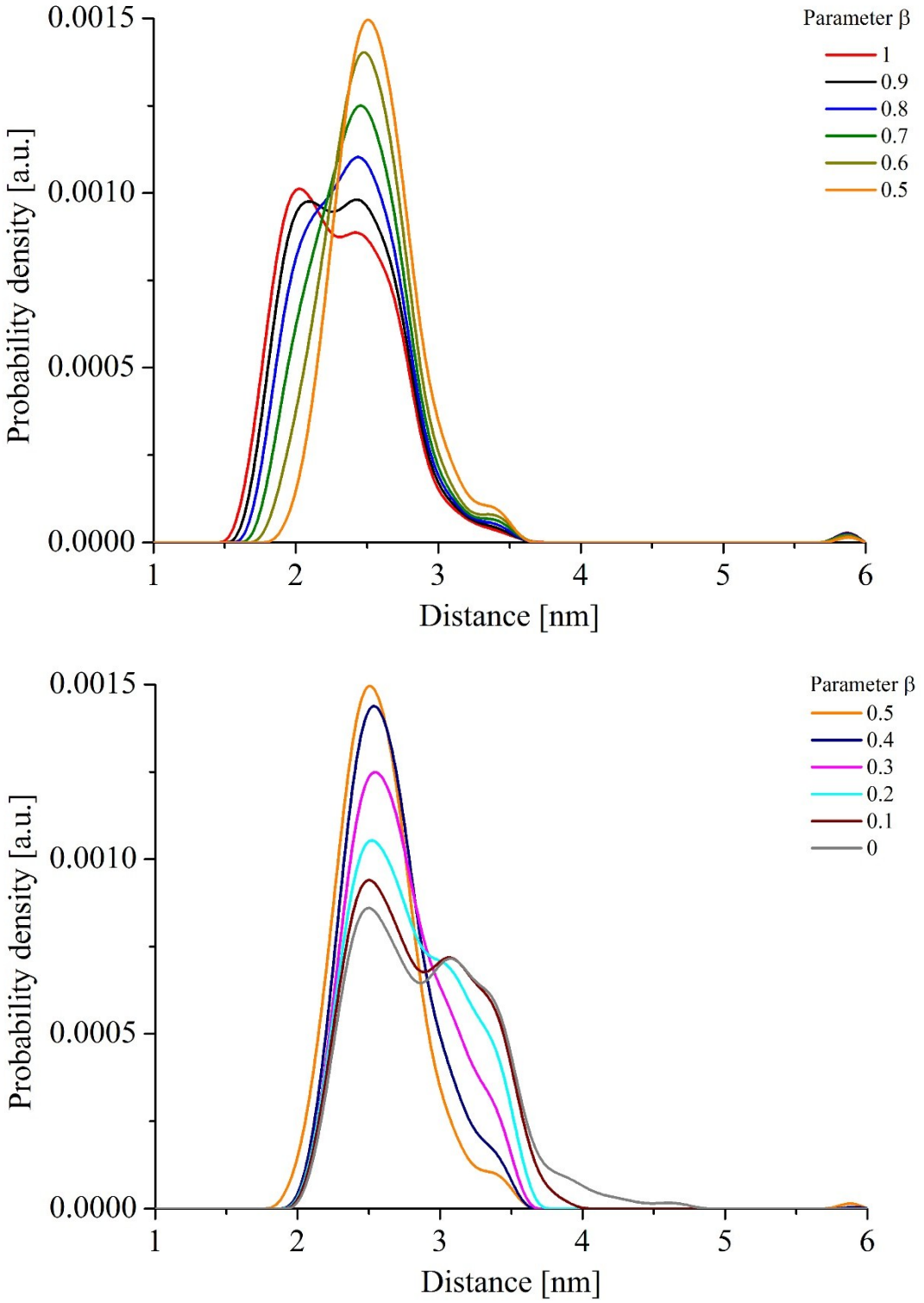

Figure S9. Distance distributions obtained by Tikhonov regularization analysis with the kernel function shown in equation S1 and regularization parameter is 10. Parameter β was varied with a step of 0.1. For better visual comparison the graphs were splitted in two layers. (Top) β is varied in the range [1, 0.5]. (Bottom) β is varied in the range [0.5, 0]. B of 0.5 is present in both layers as a referential data. Analysis is performed for the RIDME time trace with mixing time of 20 μs obtained on compound **1** in deuterated solvent.

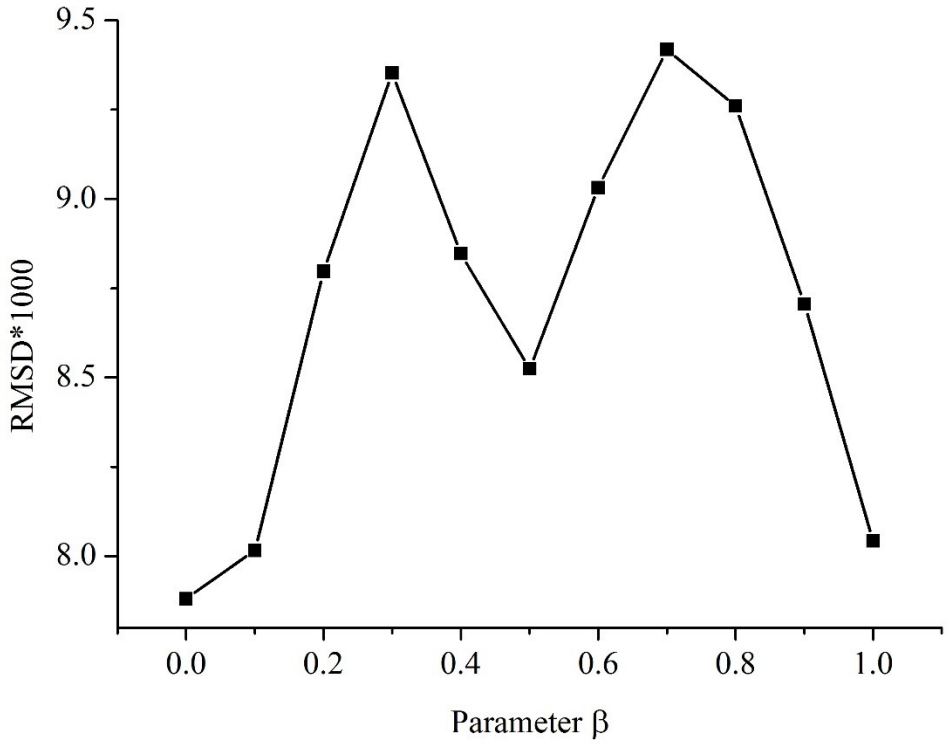

Figure S10. RMSD between modulation depth-scaled RIDME time trace (mixing time of 20 µs, compound **1** in deuterated solvent) and corresponding back-calculation based on Tikhonov regularization analysis with the kernel function shown in equation S1 and regularization parameter is 10.

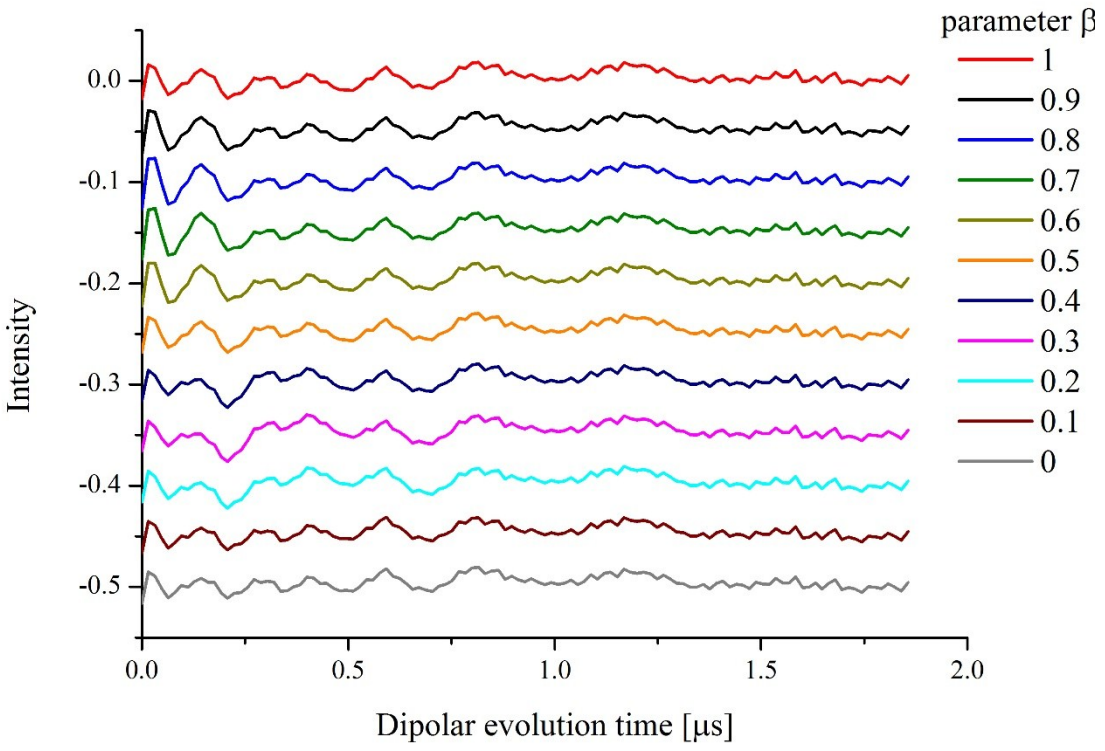

Figure S11. Difference between modulation depth-scaled RIDME time trace (mixing time of 20 µs, compound **1** in deuterated solvent) and corresponding back-calculation based on Tikhonov regularization analysis with the kernel function shown in equation S1 and regularization parameter is 10. All the differences have been vertically offset for better visualization.

The Fourier transforms of the differences (Figure S10) are shown in Figure S11. Several features can be observed in the Fourier transform, as shown in this figure.

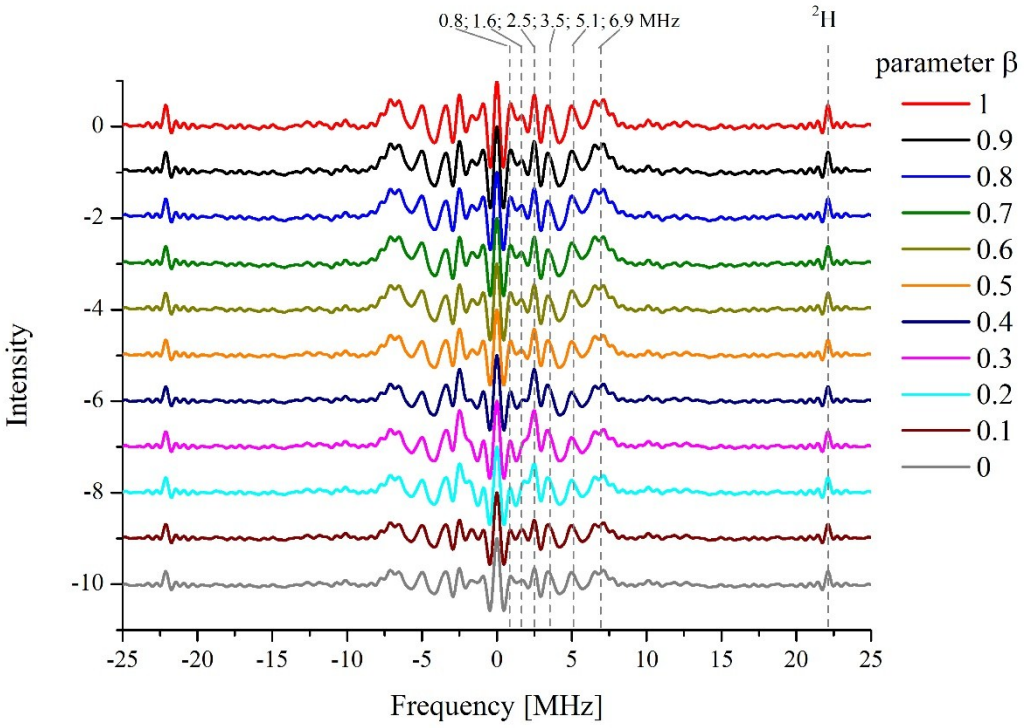

Figure S12. Fourier transform of the difference between modulation depth-scaled RIDME time trace (mixing time of 20 µs, compound **1** in deuterated solvent) and corresponding back-calculation based on Tikhonov regularization analysis with the kernel function shown in equation S1 and regularization parameter is 10. All the Fourier transforms have been vertically offset for better visualization.

7.2 W-band RIDME with mixing time of 80 μs

Distance distributions obtained with the kernel function for the Tikhonov regularization where the weight of the first and second harmonic of the dipolar coupling frequency were varied (parameter β in equation S1) for 80 μs mixing time is depicted in Figure S13. The situation is similar to the case of W-band RIDME time trace with 20 μs mixing time. The RMSD map (Figure S14) is also similar where the RMSD values increase upon adding additional components to the kernel function. The differences between this experimental time trace and back-calculations are depicted in Figure S15 (corresponding Fourier transforms are shown in Figure S16). The features are similar to the previous case, suggesting that the RMSD does not reflect the quality of analysis with different kernel function.

The distance distributions obtained with the kernel function where the weights of the first and second terms were the same, reveals some feature at short distance, which was not the case for 20 μs mixing time (Figure S9). One possible reason for these features could be higher quantum longitudinal relaxation. To account for this, the third harmonic of the dipolar coupling frequency was explicitly included into the kernel function (equation S2), and Tikhonov regularization analysis was performed. Parameter γ reflects the weight for this component. Parameters β' were kept the same and γ was varied from 0 till 0.333, with the step of 0.05 (except for the last case), such that the summed weight of 2β'+ γ equals 1.

$$K(T,R)=\int_0^1\left[\beta'\cos\left(\frac{D_{dd}}{R^3}\left(3x^2-1\right)T\right)+\beta'\cos\left(2\cdot\frac{D_{dd}}{R^3}\left(3x^2-1\right)T\right)+\gamma\cos\left(3\cdot\frac{D_{dd}}{R^3}\left(3x^2-1\right)T\right)\right]dx \quad \text{(S2)}$$

The distance distributions revealed by this analysis is shown in Figure S17 and the differences between experimental time trace (modulation-depth scaled) and corresponding back-calculations are shown in Figure S18 (corresponding Fourier transforms are shown in Figure S19). The RMSD values depending on γ is shown in Figure S20. Whereas the RMSD map contains the minimum at γ value of 0.15 (corresponding of 0.425), and distance distributions obtained with corresponding kernel function lacks the component at about 1.8 nm, this RMSD value is still larger than that revealed by Tikhonov analysis with the conventional kernel function.

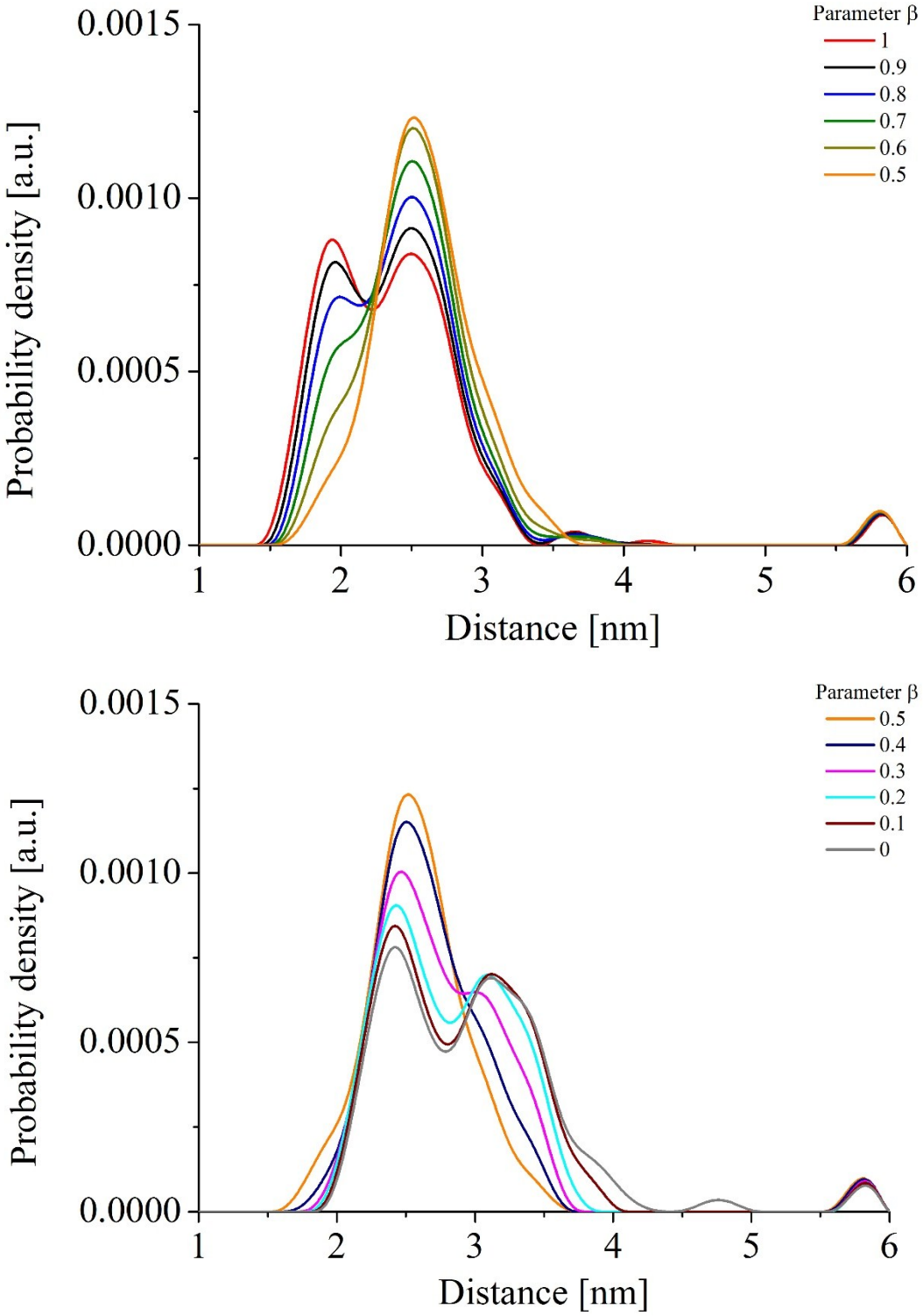

Figure S13. Distance distributions obtained by Tikhonov regularization analysis with the kernel function shown in equation S1 and regularization parameter is 10. Parameter β was varied with a step of 0.1. For better visual comparison the graphs were splitted in two layers. (Top) β is varied in the range [1, 0.5]. (Bottom) β is varied in the range [0.5, 0]. B of 0.5 is present in both layers as a referential data. Analysis is performed for the RIDME time trace with mixing time of 80 μs obtained on compound **1** in deuterated solvent.

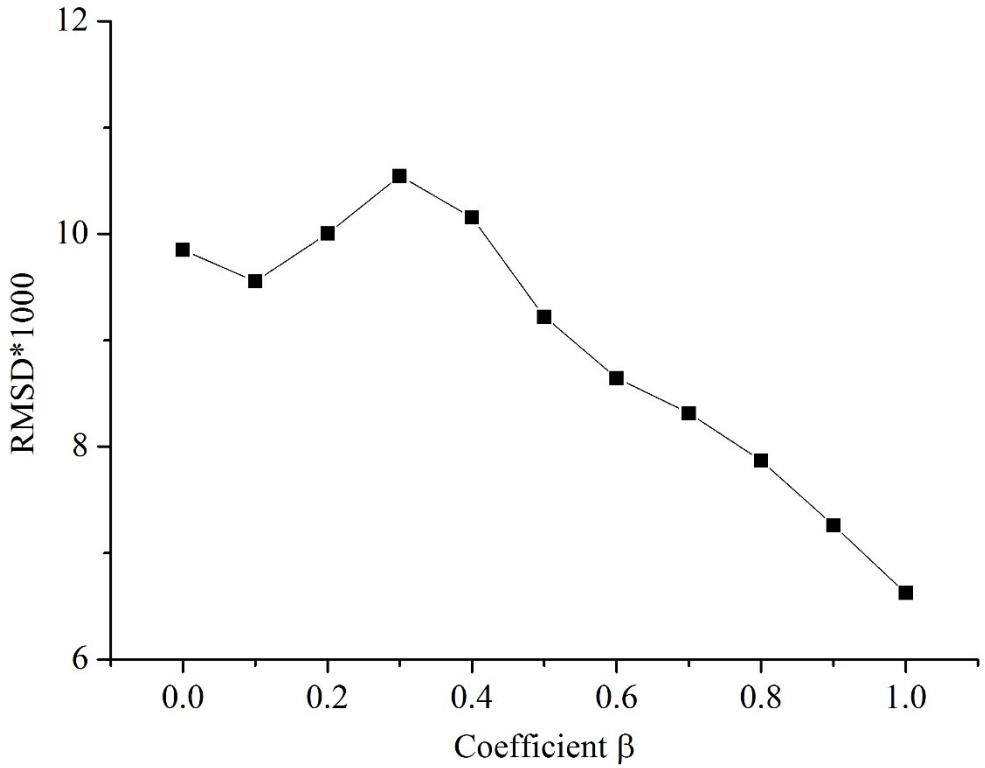

Figure S14. RMSD between modulation depth-scaled RIDME time trace (mixing time of 80 µs, compound **1** in deuterated solvent) and corresponding back-calculation based on Tikhonov regularization analysis with the kernel function shown in equation S1 and regularization parameter is 10.

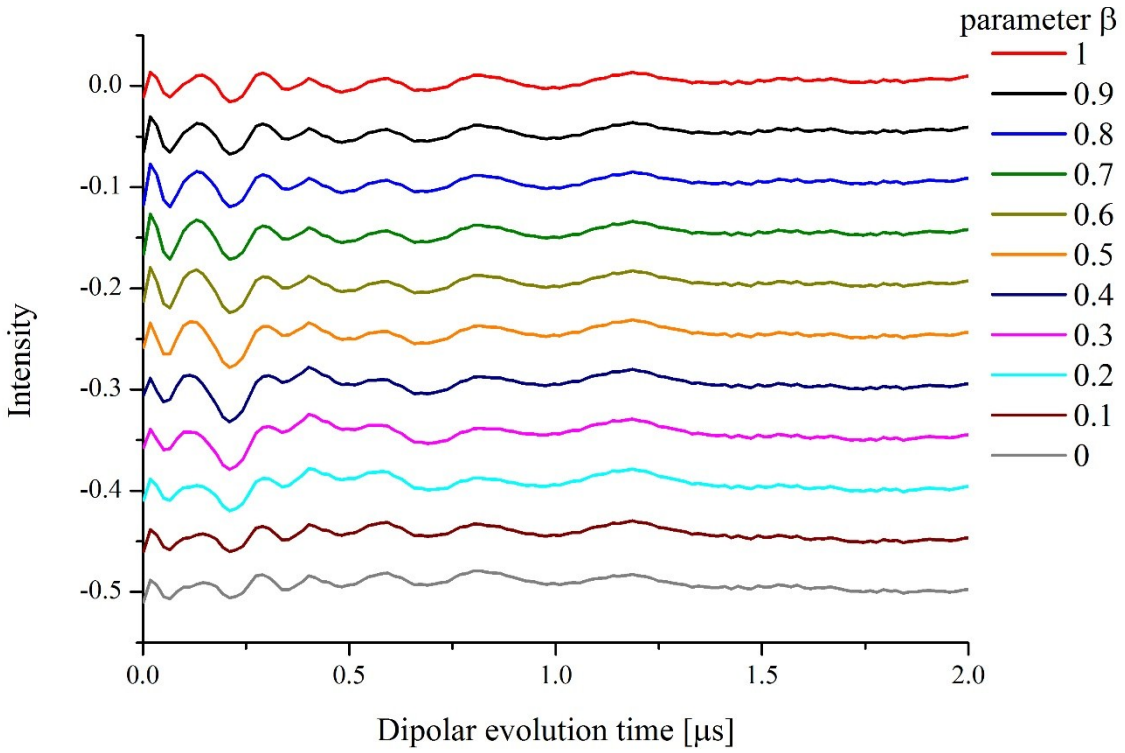

Figure S15. Difference between modulation depth-scaled RIDME time trace (mixing time of 80 µs, compound **1** in deuterated solvent) and corresponding back-calculation based on Tikhonov regularization analysis with the kernel function shown in equation S1 and regularization parameter is 10. All the differences have been vertically offset for better visualization.

The Fourier transforms of the differences, depicted in Figure S15, are shown in Figure S16. The features in the Fourier transform, observed in the previous case, can be also seen in this figure.

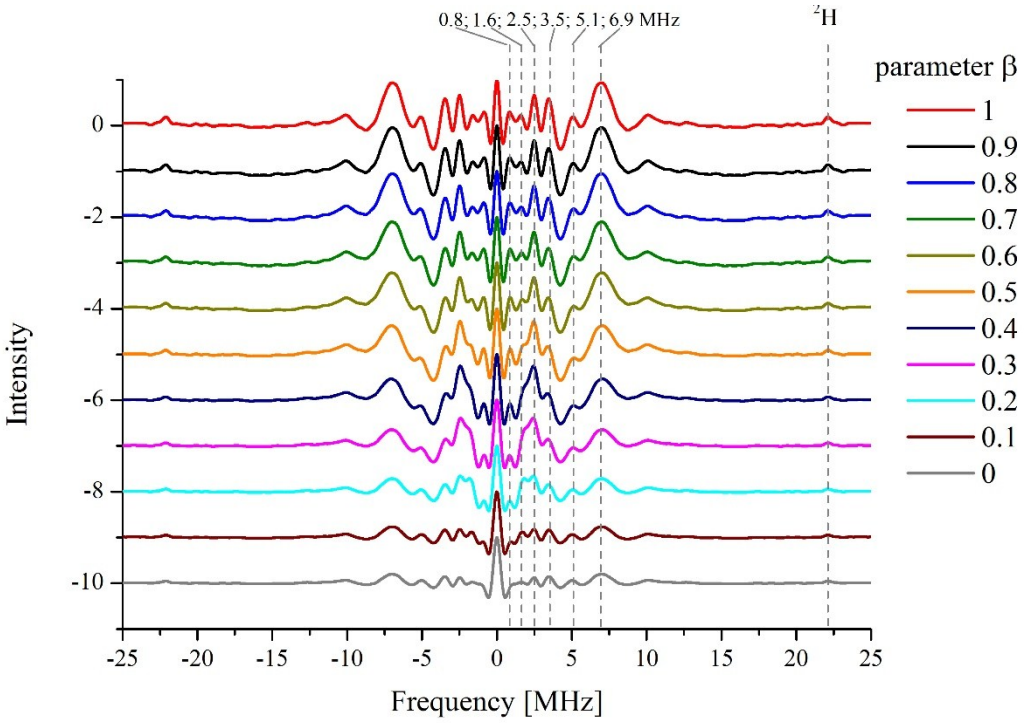

Figure S16. Fourier transform of the difference between modulation depth-scaled RIDME time trace (mixing time of 80 µs, compound **1** in deuterated solvent) and corresponding back-calculation based on Tikhonov regularization analysis with the kernel function shown in equation S1 and regularization parameter is 10. All the Fourier transforms have been vertically offset for better visualization.

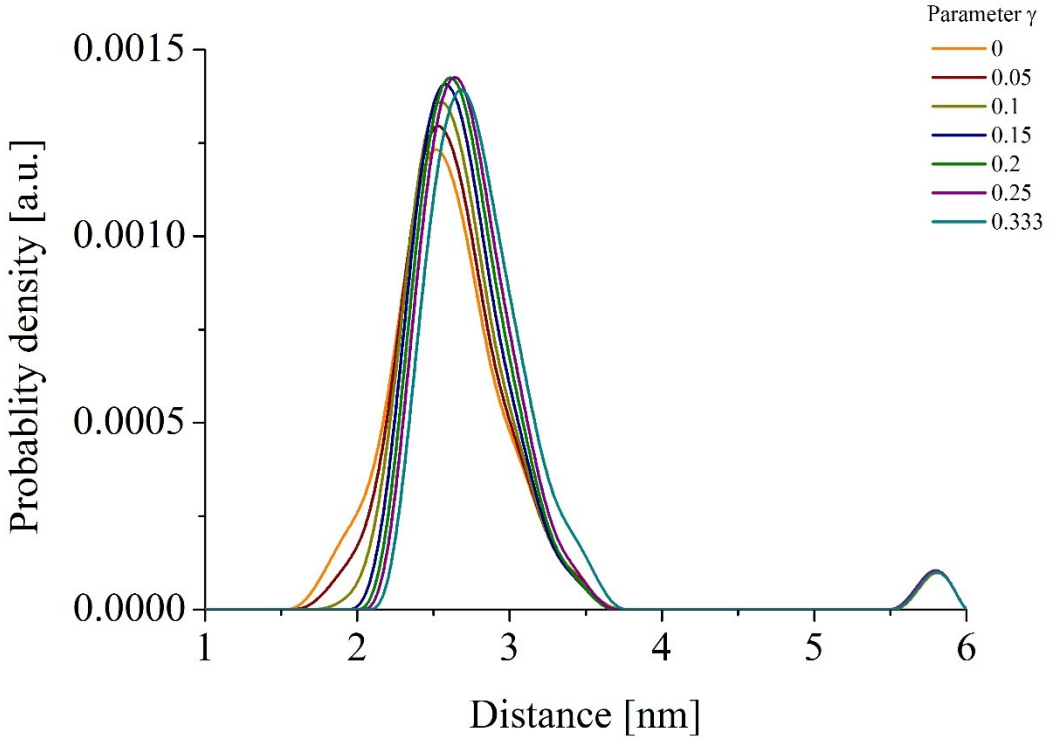

Figure S17. Distance distributions obtained by Tikhonov regularization analysis with the kernel function shown in equation S2 and regularization parameter is 10. Parameter γ was varied with a step of 0.05. Analysis is performed for the RIDME time trace with mixing time of 80 µs obtained on compound **1** in deuterated solvent.

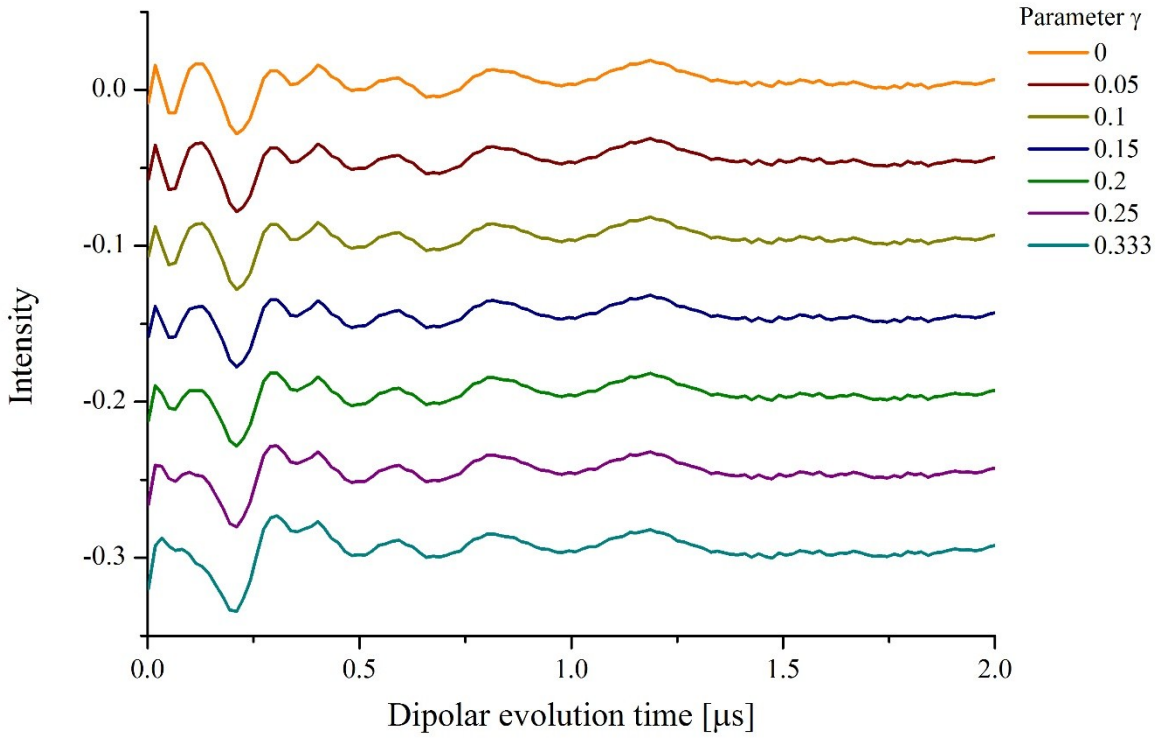

Figure S18. Difference between modulation depth-scaled RIDME time trace (mixing time of 80 μs, compound **1** in deuterated solvent) and corresponding back-calculation based on Tikhonov regularization analysis with the kernel function shown in equation S2 and regularization parameter is 10. All the differences have been vertically offset for better visualization.

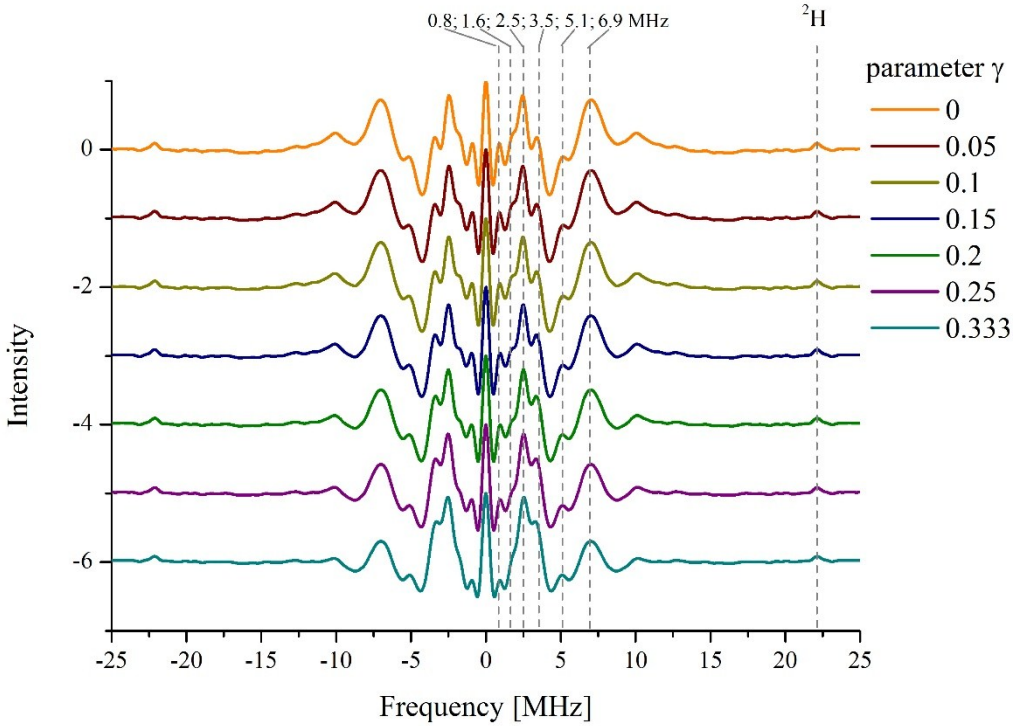

Figure S19. Fourier transform of the difference between modulation depth-scaled RIDME time trace (mixing time of 80 μs, compound **1** in deuterated solvent) and corresponding back-calculation based on Tikhonov regularization analysis with the kernel function shown in equation S2 and regularization parameter is 10. All the Fourier transforms have been vertically offset for better visualization.

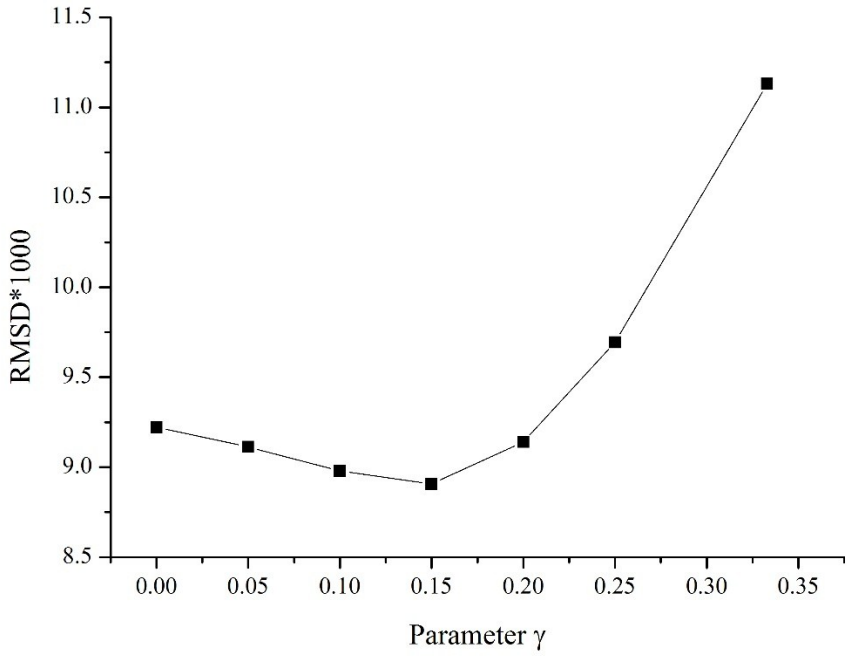

Figure S20. RMSD between modulation depth-scaled RIDME time trace (mixing time of 80 µs, obtained on compound **1** in deuterated solvent) and corresponding back-calculation based on Tikhonov regularization analysis with the kernel function shown in equation S2 and regularization parameter is 10.

7.3 J-band RIDME with mixing time of 30 μs

Distance distributions obtained with the kernel function for the Tikhonov regularization where the weight of the first and second harmonic of the dipolar coupling frequency were varied (parameter β in equation S1) for J-band RIDME time trace is depicted in Figure S21. The corresponding map of RMSD between J-band RIDME time trace (mixing time of 30 μs) and back-calculations is depicted in Figure S22. The differences between corresponding time traces are given in Figure S23 (corresponding Fourier transforms are shown in Figure S24). Again the RIDME maps featured oscillations that were every similar to the W-band data. Taking into account this and the fact that RIDME on mono-MnDOTA complex does not reveal these oscillations, might suggest that they are not experimental artefacts and are specific to the RIDME on compound **1**. However, the frequency for these oscillations do not correspond to the hyperfine couplings to ^{14}N or ^{1}H.

The possible origins of the wing from about 3 to 4 nm in the distance distributions is given in the next section. As is the case of W-band RIDME time traces with the mixing time of 80 μs, the J-band distance distributions obtained with kernel function with $\beta = 0.5$ shows small peaks at about 1.8 nm. Therefore, as in the case with the W-band RIDME time trace, the analysis is also performed using Tikhonov regularization with the kernel function, given in equation S2, where the third dipolar-coupling frequency harmonic is added. The distance distributions, differences between experimental time traces and back-calculations with corresponding Fourier transforms and the RMSD map is presented in Figures S25-S28, respectively. As in the W-band RIDME (80 μs mixing time) case, the small intensity peak disappears with increasing γ. And with the value 0.15 the minimum of RMSD was achieved, which is still, however, larger than that obtained with conventional kernel function.

We conclude that RMSD values between RIDME time traces and back-calculations for both frequencies are influenced to a significant extent by oscillations, the origin of those are not completely understood. Therefore, RMSD is not a good criteria for choosing proper weights of first-, second- and third dipolar-coupling frequency harmonics.

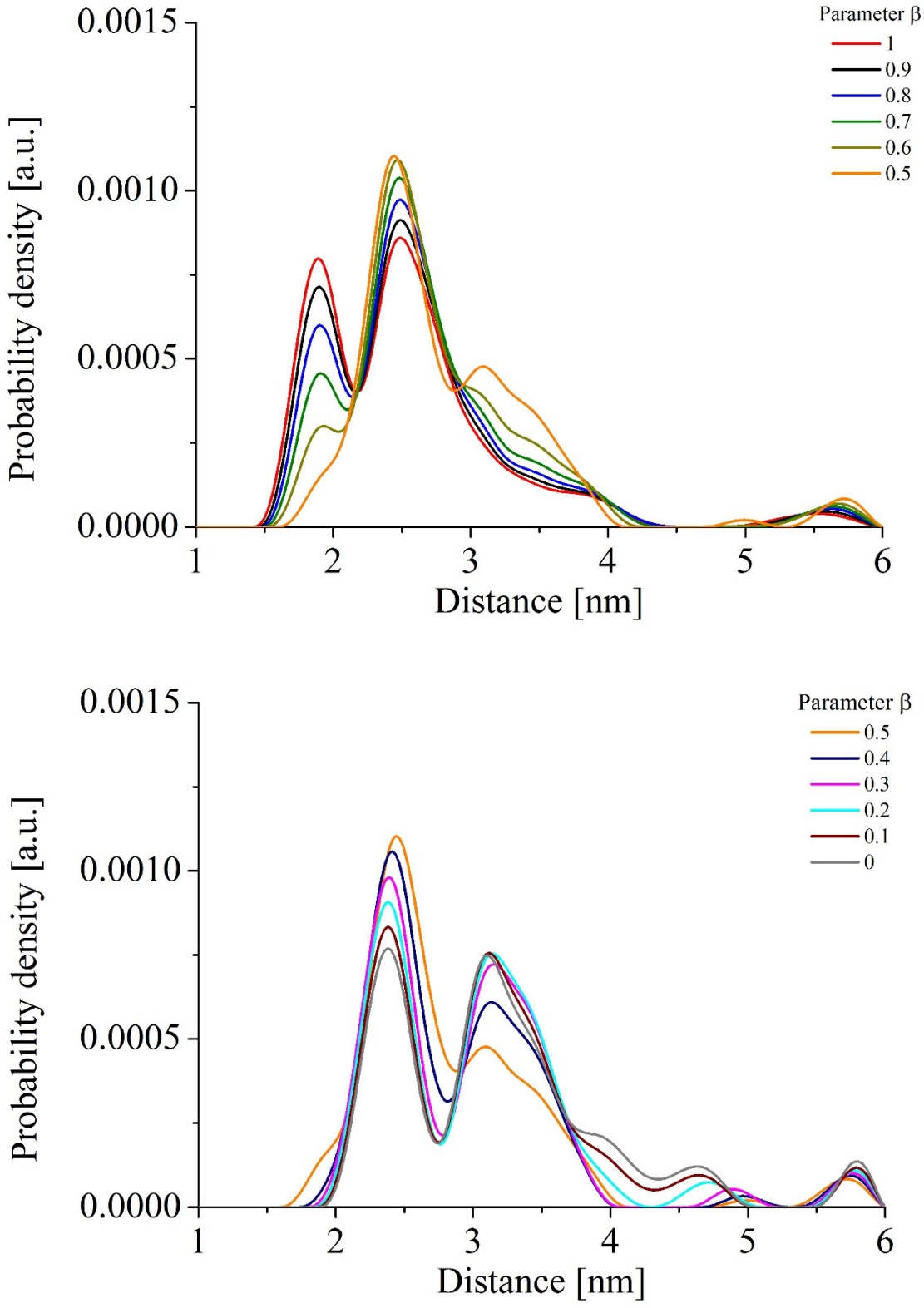

Figure S21. Distance distributions obtained by Tikhonov regularization analysis with the kernel function shown in equation S1 and regularization parameter is 10. Parameter β was varied with a step of 0.1. For better visual comparison the graphs were splitted in two layers. (Top) β is varied in the range [1, 0.5]. (Bottom) β is varied in the range [0.5, 0]. B of 0.5 is present in both layers as a referential data. Analysis is performed for the J-band RIDME time trace with mixing time of 30 μs obtained on compound **1** in deuterated solvent.

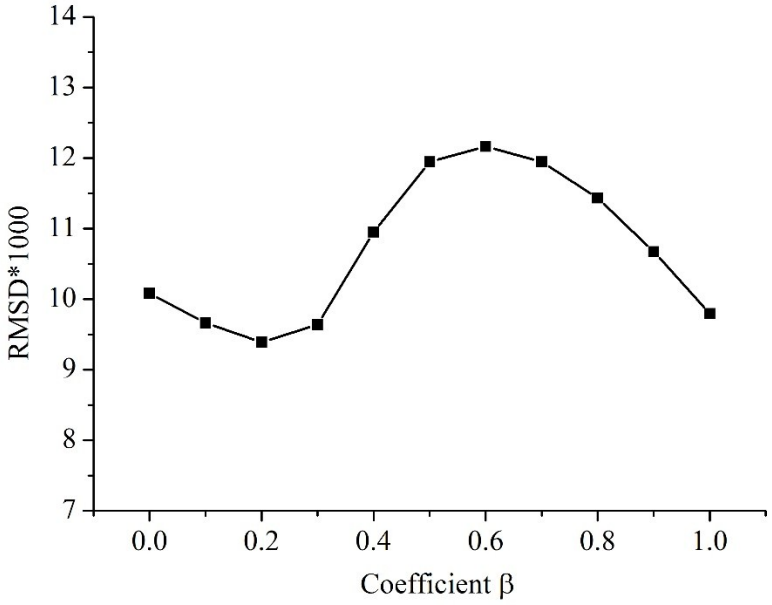

Figure S22. RMSD between modulation depth-scaled J-band RIDME time trace (mixing time of 30 µs, compound **1** in deuterated solvent) and corresponding back-calculation based on Tikhonov regularization analysis with the kernel function shown in equation S1 and regularization parameter is 10.

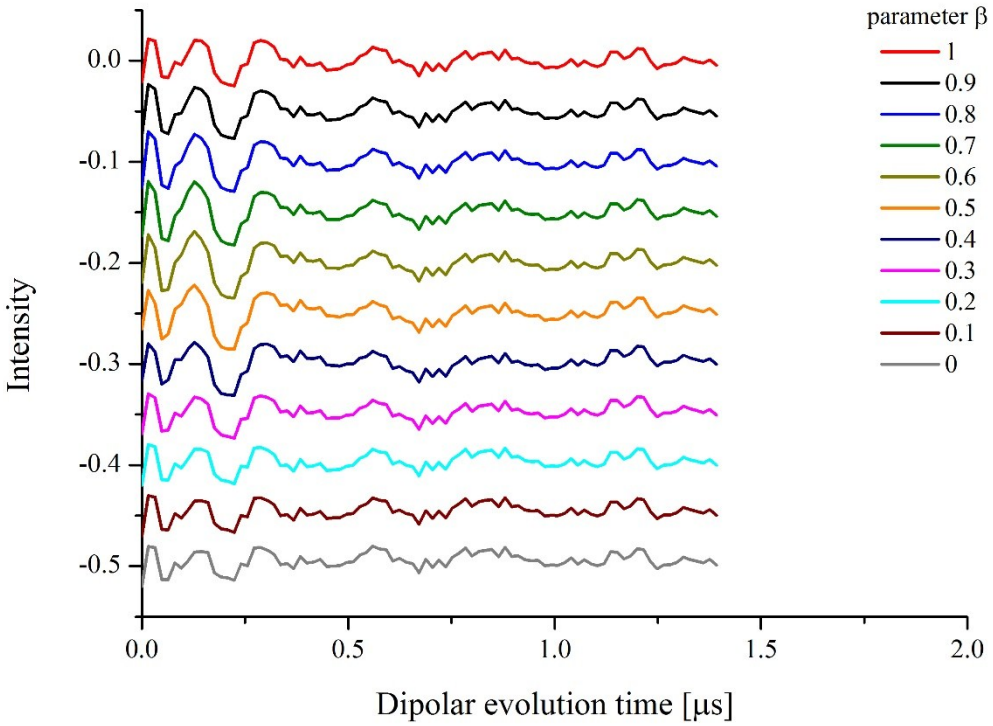

Figure S23. Difference between modulation depth-scaled J-band RIDME time trace (mixing time of 30 µs, compound **1** in deuterated solvent) and corresponding back-calculation based on Tikhonov regularization analysis with the kernel function shown in equation S1 and regularization parameter is 10. All the differences have been vertically offset for better visualization.

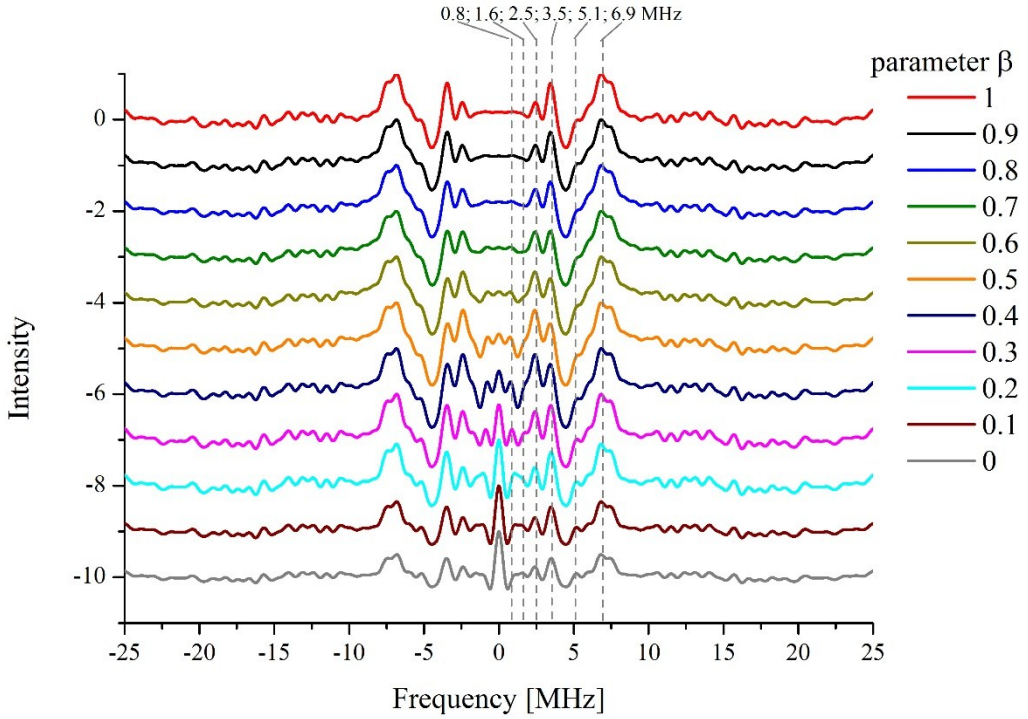

Figure S24. Fourier transform of the difference between modulation depth-scaled J-band RIDME time trace (mixing time of 30 µs, compound **1** in deuterated solvent) and corresponding back-calculation based on Tikhonov regularization analysis with the kernel function shown in equation S1 and regularization parameter is 10. All the Fourier transforms have been vertically offset for better visualization.

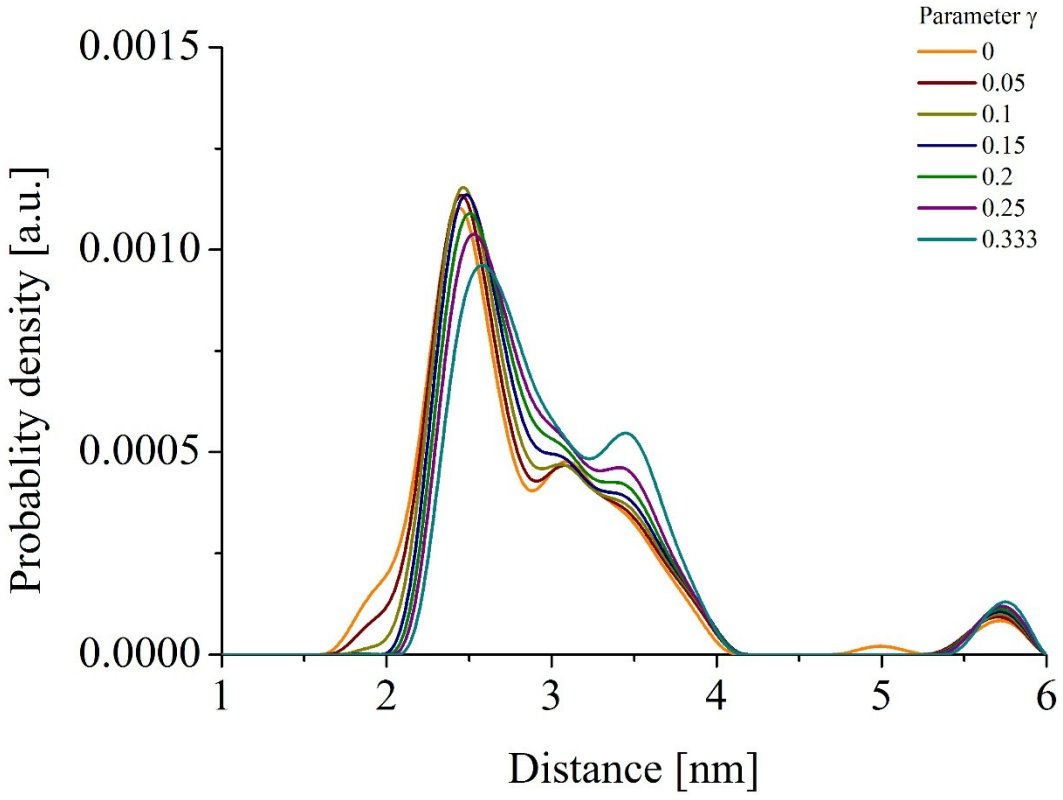

Figure S25. Distance distributions obtained by Tikhonov regularization analysis with the kernel function shown in equation S2 and regularization parameter is 10. Parameter γ was varied with a step of 0.05. Analysis is performed for the J-band RIDME time trace with mixing time of 30 µs obtained on compound **1** in deuterated solvent.

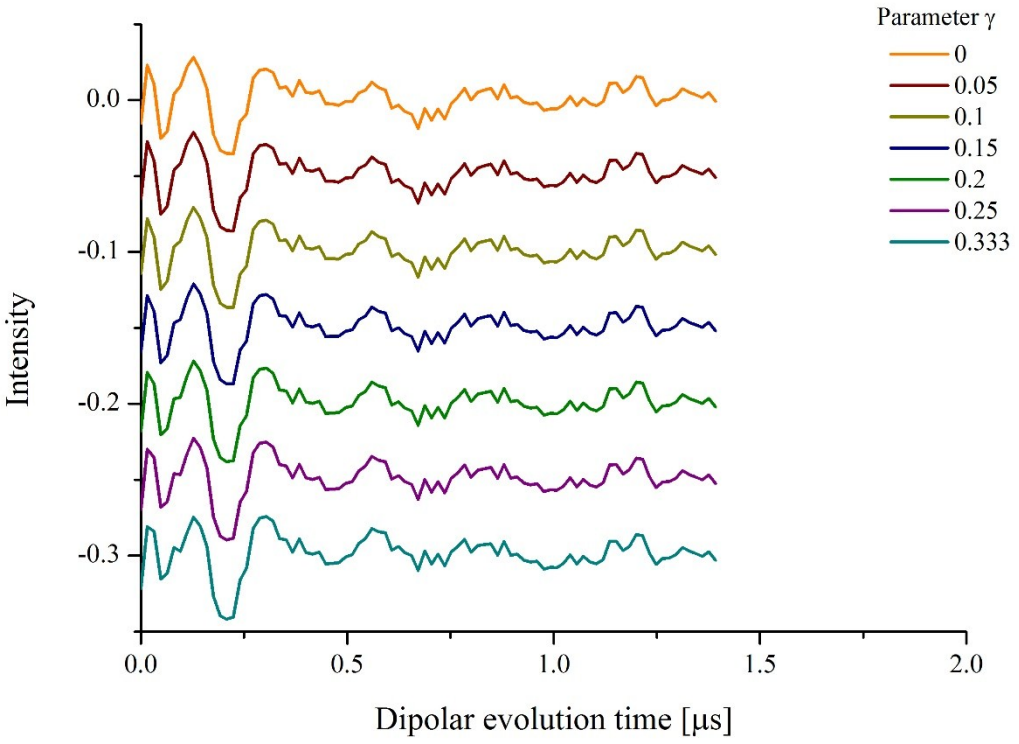

Figure S26. Difference between modulation depth-scaled J-band RIDME time trace (mixing time of 30 μs, compound **1** in deuterated solvent) and corresponding back-calculation based on Tikhonov regularization analysis with the kernel function shown in equation S2 and regularization parameter is 10. All the differences have been vertically offset for better visualization.

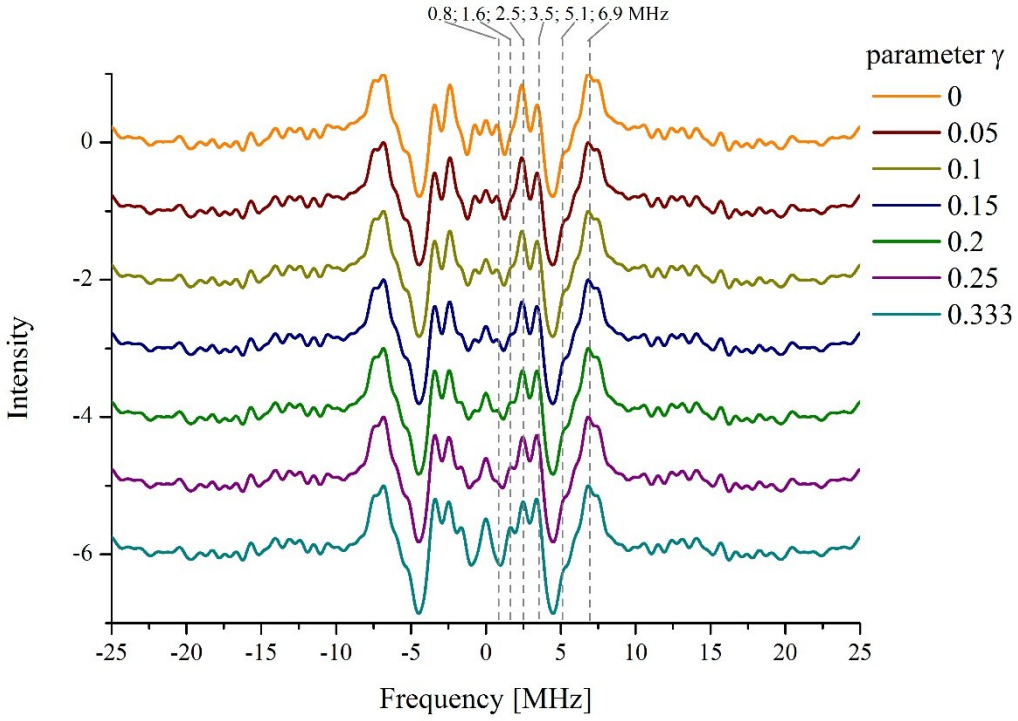

Figure S27. Fourier transform of the difference between modulation depth-scaled J-band RIDME time trace (mixing time of 30 μs, compound **1** in deuterated solvent) and corresponding back-calculation based on Tikhonov regularization analysis with the kernel function shown in equation S2 and regularization parameter is 10. All the Fourier transforms have been vertically offset for better visual representation.

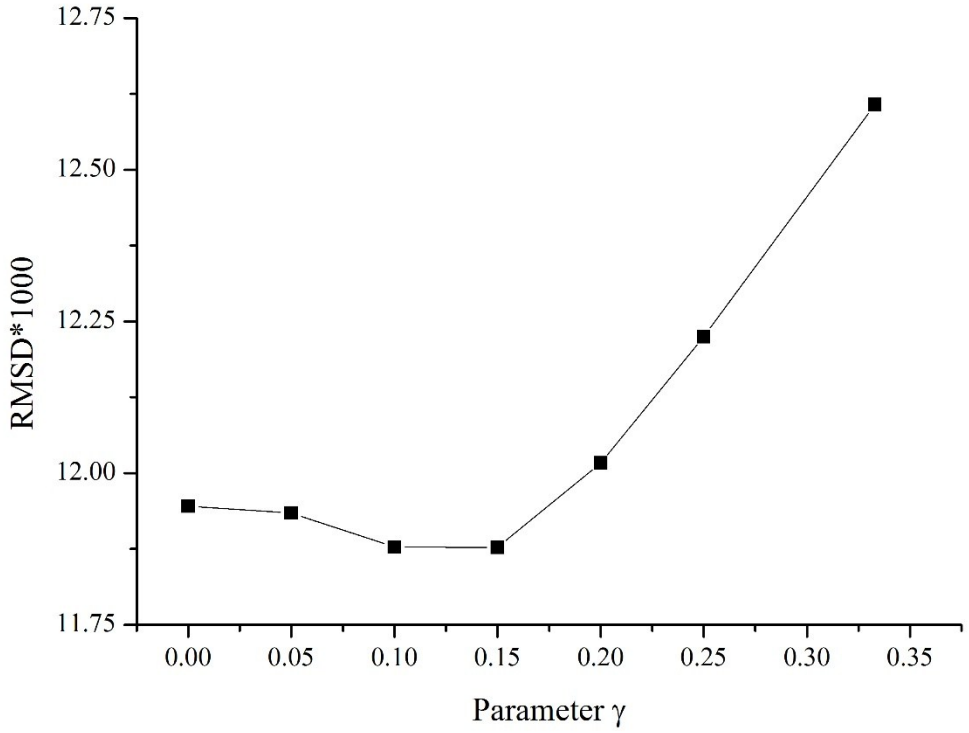

Figure S28. RMSD between modulation depth-scaled J-band RIDME time trace (mixing time of 30 µs, compound **1** in deuterated solvent) and corresponding back-calculation based on Tikhonov regularization analysis with the kernel function shown in equation S2 and regularization parameter is 10.

8. Wing from 3 to 4 nm in the distance distribution corresponded to J-band RIDME time trace

Five-pulse RIDME is a single frequency dipolar spectroscopy experiment. To record the undistorted initial part of the time trace, an 8-step phase-cycle is needed to cancel moving Hahn echo from the last two pulses and the refocused stimulated echo which originates from all five pulses.[4] W-band RIDME experiments were performed on the EPR spectrometer with 4-fixed and power/phase - calibrated microwave channels, whereas the phases in the J-band spectrometer were generated with an arbitrary waveform generator (AWG). If the phases are not set perfectly, the cancelling of both echo signals is not 100% efficient, which can distort the initial part of the RIDME time trace. Fourier transform of the background-divided J-band RIDME time trace (Figure S29 B) reveals an intense zero-frequency component, which was not observed for the W-band RIDME time traces (see Figure S30). Tikhonov regularization of this time trace reveals a wing from 3 to 4 nm in the distance distribution, which becomes significantly more intense upon modification of the kernel function (see Figure 6I). To test the effect of the intense zero-frequency component seen in the Fourier transform, additional stretched exponential function was subtracted from the background-divided J-band RIDME trace as a baseline (see Figure S29 A). This baseline function was fitted such that the zero-frequency component in the Fourier transform of the resulted time trace disappears. The resultant baseline function and the corrected RIDME time trace as well as the Fourier transforms of background-divided and additionally baseline corrected time traces are depicted in Figure S29 A and S29 B. Comparison of the Fourier transforms of both W-band RIDME time traces with the Fourier transform of the baseline corrected J-band time trace is given in Figure S30 B. Tikhonov regularization analysis of the baseline-corrected RIDME time trace with the conventional and modified kernel functions (see equations 4 and 5 in the main text) is given in Figure S29 C and S29 D. As can be seen from Figure S29 D, the distance distributions yielded by Tikhonov analysis with conventional kernel function does not contain such a prominent wing from 3 to 4 nm compared to analysis of the J-band RIDME time trace (Figure 6I).

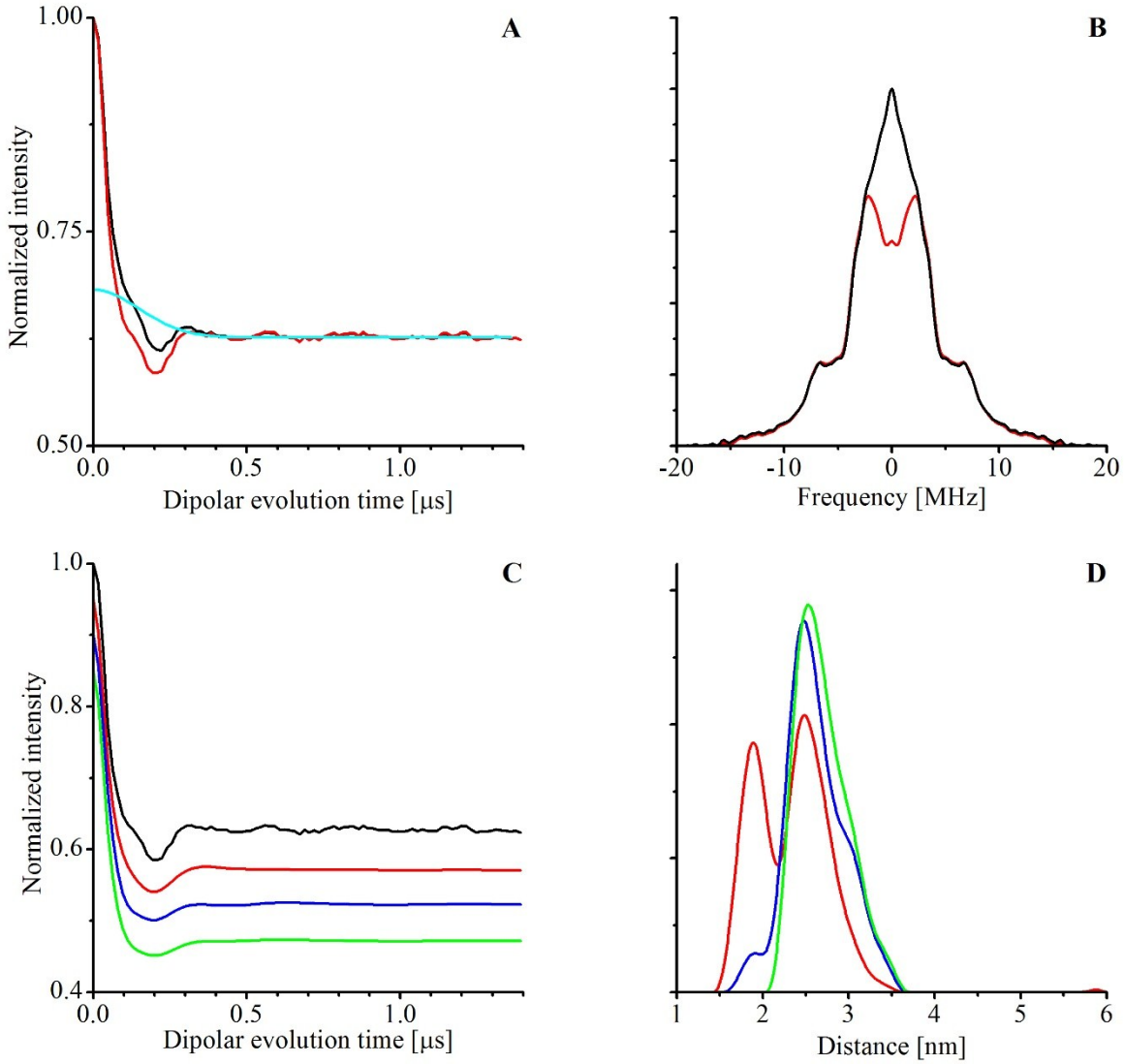

Figure S29. **(A)** The 25 K background-divided RIDME time trace on compound **1** in deuterated solvent obtained at J-band frequencies with mixing time of 30 µs (black, from Figure 6F), stretched-exponential baseline (cyan) and baseline-subtracted RIDME time trace (red). **(B)** Fourier transform of the J-band background-divided RIDME time trace (black, from Figure 6F) and of the baseline subtracted background-divided RIDME time trace (red). **(C)** The baseline-subtracted background-divided RIDME time trace (black) with corresponding fits based on Tikhonov regularization analysis with standard single-frequency component kernel function (red); equally-weighted single- and double-frequency components (0.5 each) modified kernel function (blue); and equally-weighted single- and double-frequency components (0.425 each) with additional triple-frequency component (0.15) modified kernel function (green). Tikhonov regularization was performed using an in-house program with the regularization parameters set to 10 for all fitting procedures. **(D)** The corresponding distance distributions obtained from the Tikhonov regularizations using the different kernel functions.

9. W-band RIDME time traces with 20 and 80 µs mixing times, the time traces obtained as a division, corresponding Fourier transforms and J-band time trace

The W-band RIDME time traces with corresponding Fourier transforms are depicted in Figure S30.

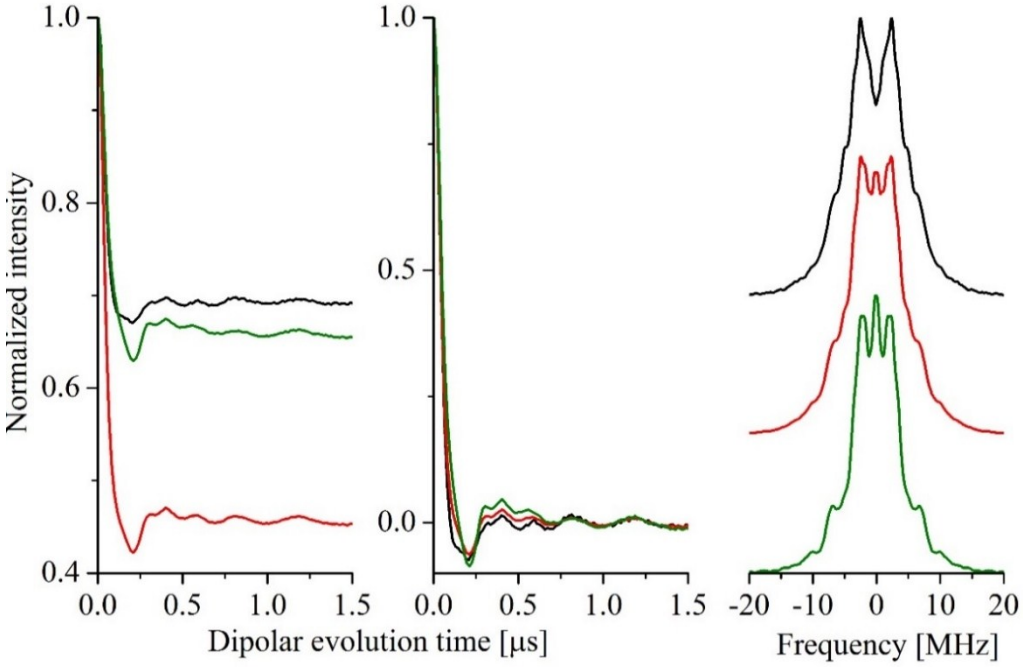

Figure S30 A. **Left**. W-band RIDME time traces on compound **1** in deuterated solvent obtained with 20 µs (black), 80 µs (red) mixing times and their divison (green). **Middle**. Modulation depth scaled RIDME time traces. **Right**. Corresponding Fourier transforms.

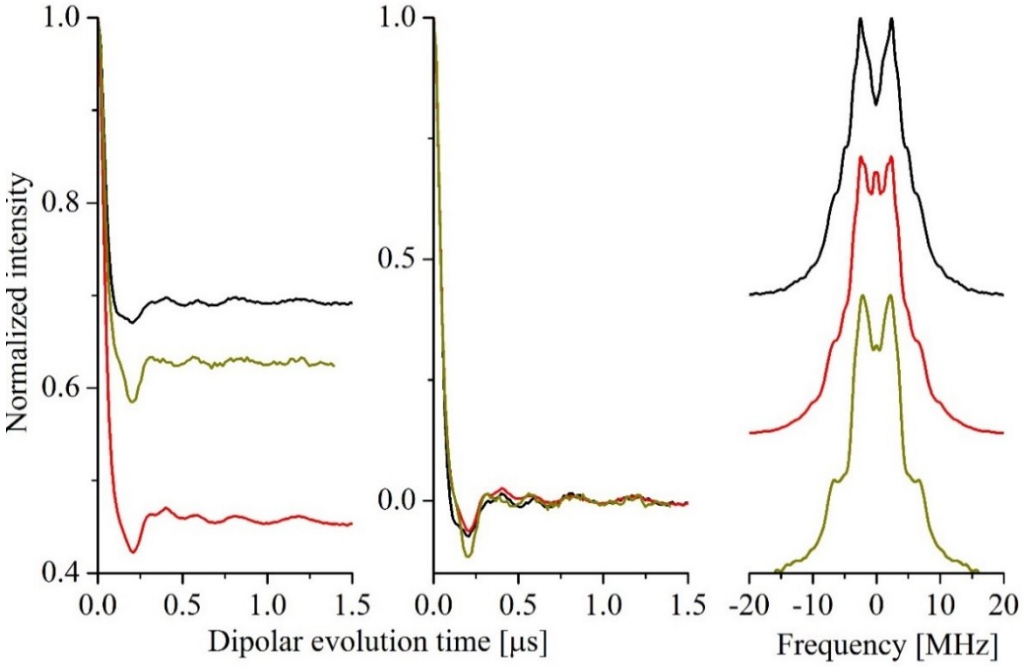

Figure S30 B. **Left**. W-band RIDME time traces on compound **1** in deuterated solvent obtained with 20 µs (black), 80 µs (red) mixing times and corrected J-band RIDME time trace with 30 µs mixing time (dark gold). **Middle**. Modulation depth scaled RIDME time traces. **Right**. Corresponding Fourier transforms.

10. Comparison of electron spin relaxation times at W- and J-band frequencies

Electron spin relaxation time measurements are given in Figures S31 (T_{1e}) and S32 (T_{me}).

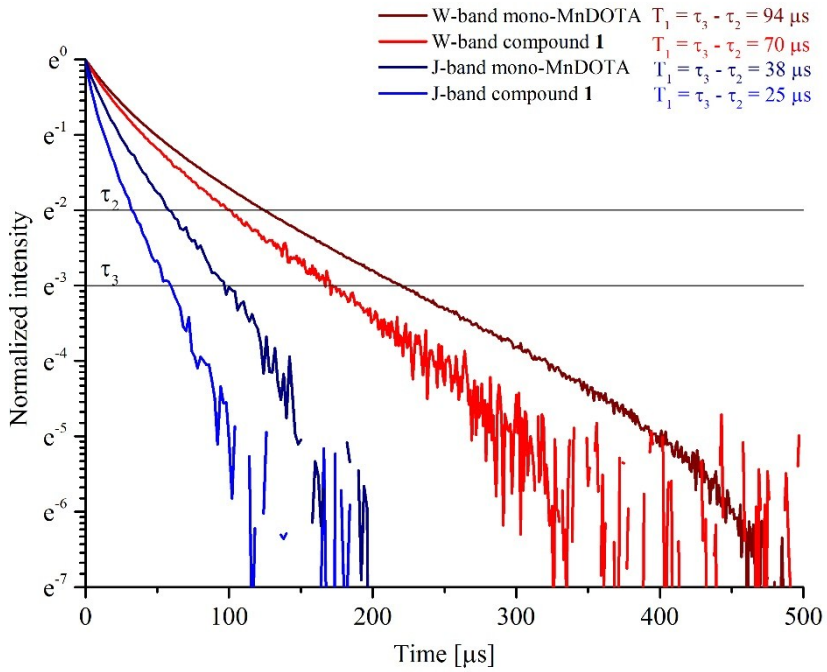

Figure S31. Longitudinal relaxation time measurements on compound **1** and mono-MnDOTA complexes in deuterated solvent at 25K at W- and J-band frequencies. At W- and J-band inversion and saturation recovery (1ms saturation pulse) sequences were used. Spectral position was the highest field hyperfine component.

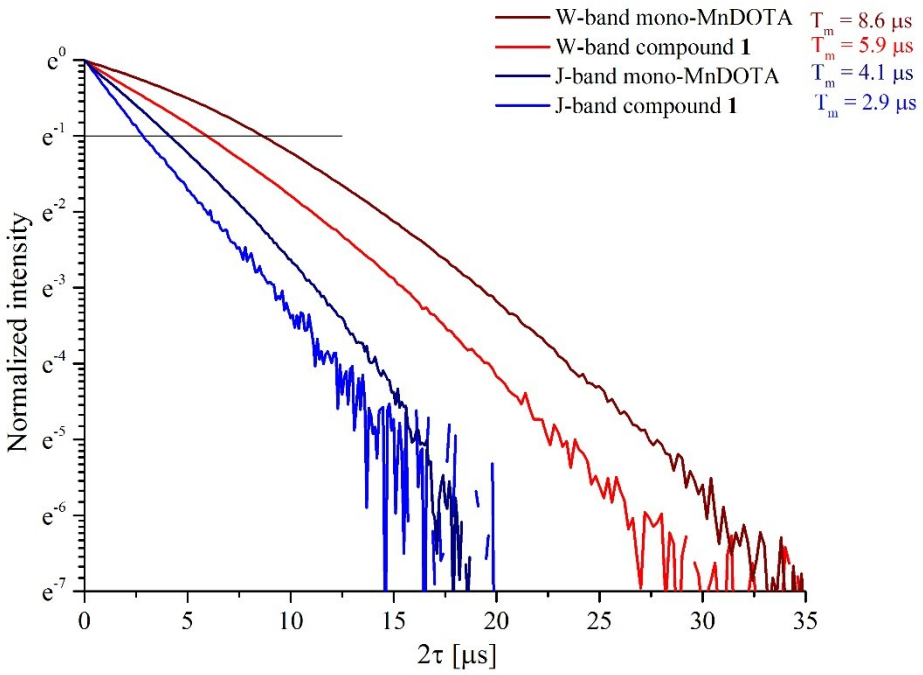

Figure S32. Phase memory time measurements on compound **1** and mono-MnDOTA complexes in deuterated solvent at 25K at W- and J-band frequencies. Hahn-echo sequence were used. Spectral position was the highest field hyperfine component.

11. Comparison of the distance distributions corresponding to different experiments

Distance distributions obtained by Tikhonov regularization analysis of different dipolar spectroscopy experiments are depicted in Figure S33.

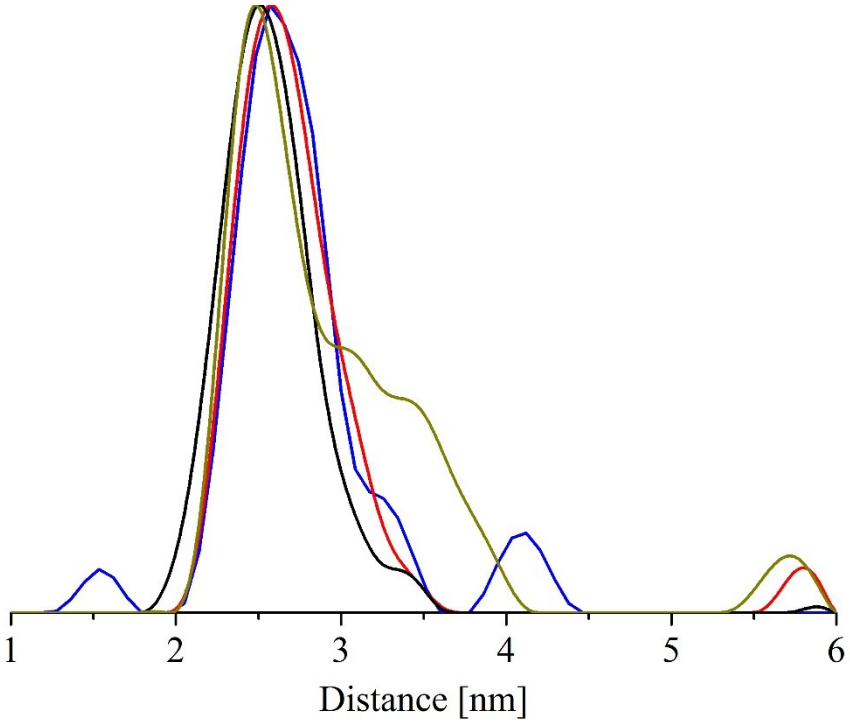

Figure S33. Distance distributions obtained with Tikhonov regularization of PELDOR time trace with 70 MHz pump-probe frequency offset (blue), W-band RIDME time trace obtained with a mixing time of 20 µs with the modified kernel function (equation 4 in the main text) (black), W-band RIDME time trace obtained with a mixing time of 80 µs with the modified kernel function (equation 5) (red), J-band RIDME time trace obtained with a mixing time of 30 µs with the modified kernel function (equation 5) (dark gold). All distance distributions correspond to compound **1** in deuterated solvent. Regularization parameter for all distance distributions was 10. Tikhonov analysis for PELDOR was performed with DeerAnalysis toolbox and for RIDME time traces with in-house program.

12. Broad distance distributions measured by RIDME

In order to model a situation in which RIDME experiments are performed on a relatively flexible system, such that Tikhonov regularization analysis with conventional kernel function would give a single peak, because the first and second harmonics of the dipolar coupling cannot be easily distinguished, the Gaussian distance distribution with the most probable distance of 4 nm and a full-width at half maximum of 1.5 nm was generated (Figure S34 C, black). Based on this distance distribution, the RIDME time trace, where single and double dipolar coupling frequency components have the equal weights of 0.5, was generated (Figure S34, A black). Tikhonov regularization analysis on this RIDME time trace was performed with different kernel functions. Analysis with the conventional kernel function reveals a peak in the distance distribution with a shifted most probable distance (15% shift with respect to the expected distance of 4 nm) (Figure S34 C, red). However, Tikhonov analysis with the modified kernel function (see equation 4 in the main text) reveals a distance distribution, which is almost exactly the same, as was used to generate the RIDME time trace (Figure S34 C, green). The back-calculated time traces and the differences between the generated RIDME time trace and the back-calculations are depicted in Figure S34 A and B, respectively.

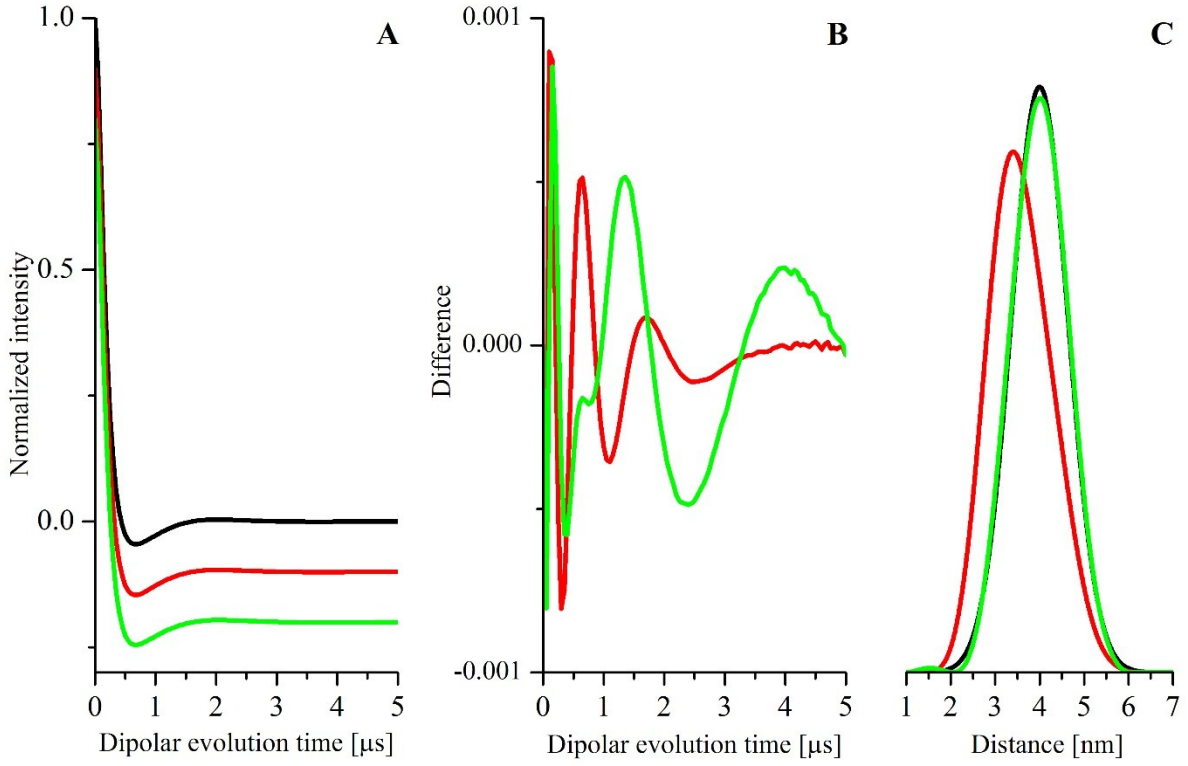

Figure S34. **(A)** Generated RIDME time trace (black) with back-calculated time traces, based on Tikhonov regularization analysis with the conventional kernel function (red) and the modified kernel function (equation 4 in the main text) (green). The time traces were vertically shifted for better visual comparison. Regularization parameter was 100. In-house written code was used for performing Tikhonov regularization. **(B)** Differences between calculated RIDME time trace and back-calculations, based on Tikhonov analysis with the conventional kernel (red) and the modified kernel function (equation 4) (green). **(C)** Distance distributions: input Gaussian distance distribution (black), distance distributions yielded by Tikhonov regularization with conventional kernel function (red) and kernel function (equation 4) (green).

13. Background functions in RIDME experiments

Background functions in the RIDME time traces were fitted by a stretched-exponential function: $y = A \cdot e^{-\left(\frac{t}{\tau}\right)^{\gamma}}$ with parameters given in Table S1.

Table S1. Parameters of the stretched-exponential functions for backgrounds in RIDME experiments

RIDME time trace	A	τ [μs]	γ
W-band, 20 μs mixing time, deuterated solvent	0.6903	3.8244	1.6782
W-band, 80 μs mixing time, deuterated solvent	0.4513	2.7676	1.6046
J-band, 30 μs mixing time, deuterated solvent	0.6280	2.6381	1.7725
W-band, 80 μs mixing, protonated solvent	0.4572	0.6116	1.8945
J-band, 25 μs mixing time, protonated solvent	0.5936	0.8386	1.9619

14. Assessment of ambiguity of background definition in RIDME and its influence on Tikhonov regularization analysis

The stretched exponential function is an adequate model for the background decay in RIDME experiment, but there is one source of ambiguity in its definition, the point in the time trace which is selected to be the starting point for the background fit. This is important since the initial part of the experimental time trace has a strong impact on the Tikhonov regularization analysis and poor background modelling can lead to distortions in distance distribution. Thus, in order to test how the initial point selected influenced the results of the Tikhonov regularization analysis, we incremented this point every 112 ns throughout the RIDME time traces and performed correspondingly the modified Tikhonov regularization analysis.

14.1 W-band RIDME with mixing time of 20 µs

The raw experimental RIDME time trace and the background functions, defined at multiple initial positions of the time trace, are shown in Figure S35 (left). The stretched exponential background functions were defined at 15 initial positions starting from 96 ns (position "start$_1$" in Figure S35) till 1664 ns (position "start$_{15}$") with a step of 112 ns. The correspondingly background-divided RIDME time traces are shown in Figure S35 (right). The figure shows that the background functions defined at initial points corresponding to 1552 ns and 1664 ns do not properly model the background decay. However, it is instructive to see, how such improperly modelling affects the Tikhonov regularization analysis.

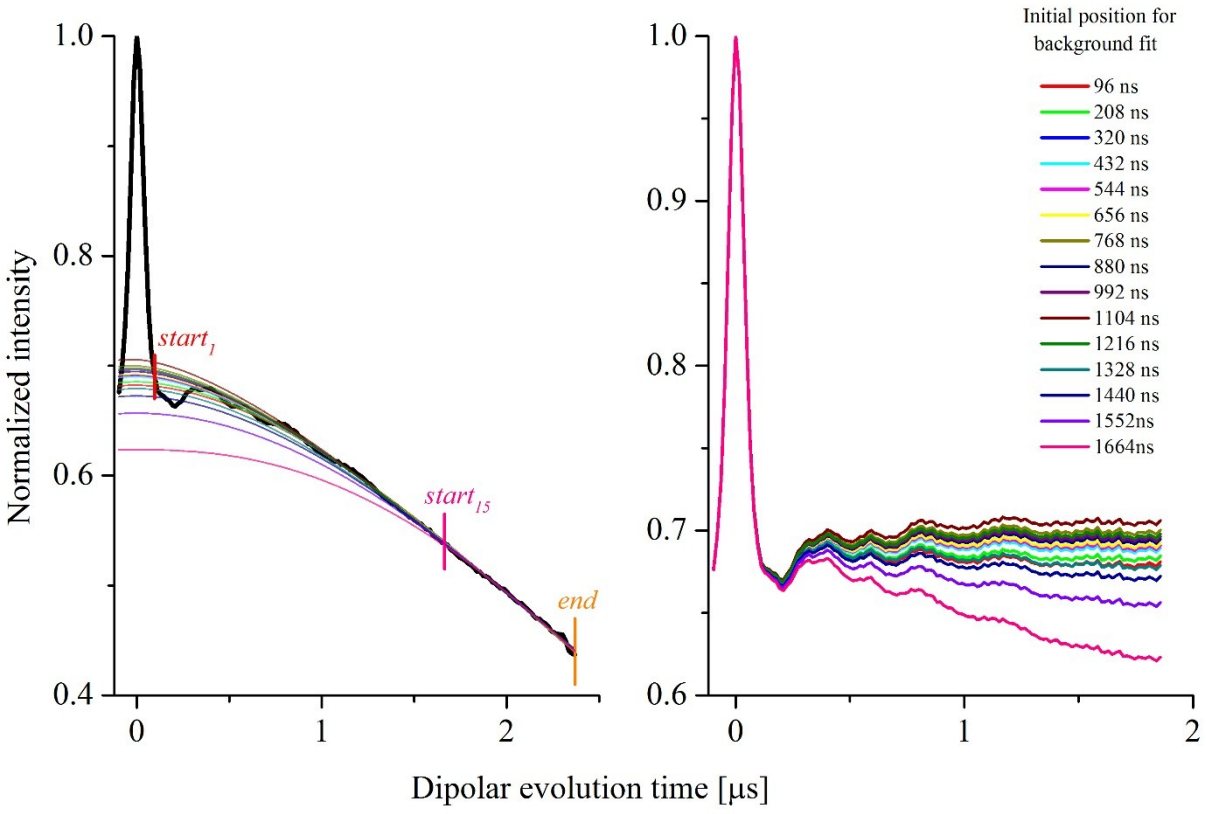

Figure S35. Left: Raw experimental RIDME time trace with 20 µs mixing time obtained on complex **1** in deuterated solvent (black) and background functions. Right: Background-divided RIDME time traces.

Results of Tikhonov regularization analysis, using kernel function (4), are shown in Figures S36 and S37.

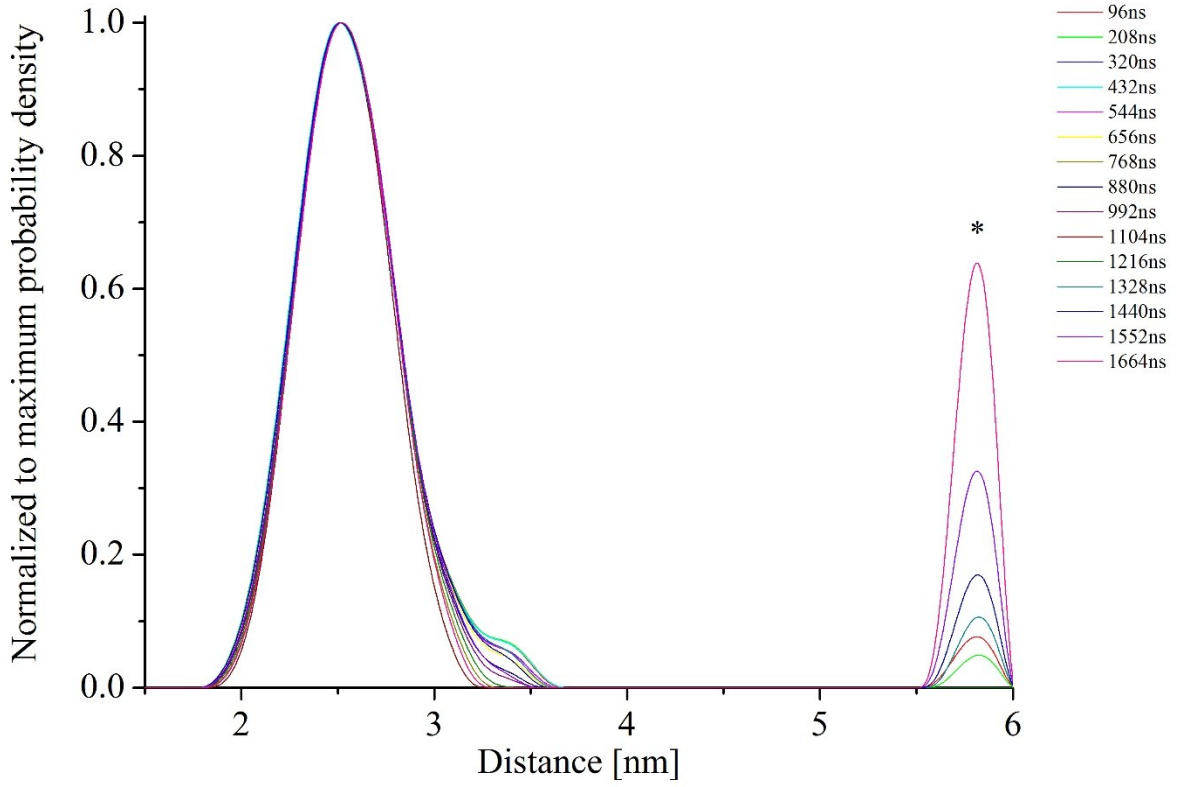

Figure S36. Distance distributions obtained by Tikhonov regularization analysis of the background-divided RIDME time traces (20 µs mixing time, deuterated solvent) shown in Figure S35. The distance distributions were normalized to the probability density of the most probable distance.

As can be seen from Figure S36, no significant effect on the main distance peak was observed, even when using 1552 ns and 1664 ns as initial points (Figure S35). However, additional distance peak at about 5.8 nm appeared, which was especially intense for the imperfectly defined background functions.

The background-divided RIDME time traces with correspondingly back-calculated time traces, based on Tikhonov regularization analysis with kernel function (4), are shown in Figure S37. For the background functions with defined initial points at 96 ns to 1440 ns, only insignificant changes of the dipolar modulation depths were observed (Figure S37). For the time traces corresponding to backgrounds, with defined initial points at 1552 ns and 1664 ns, deviation of modulation depths was stronger.

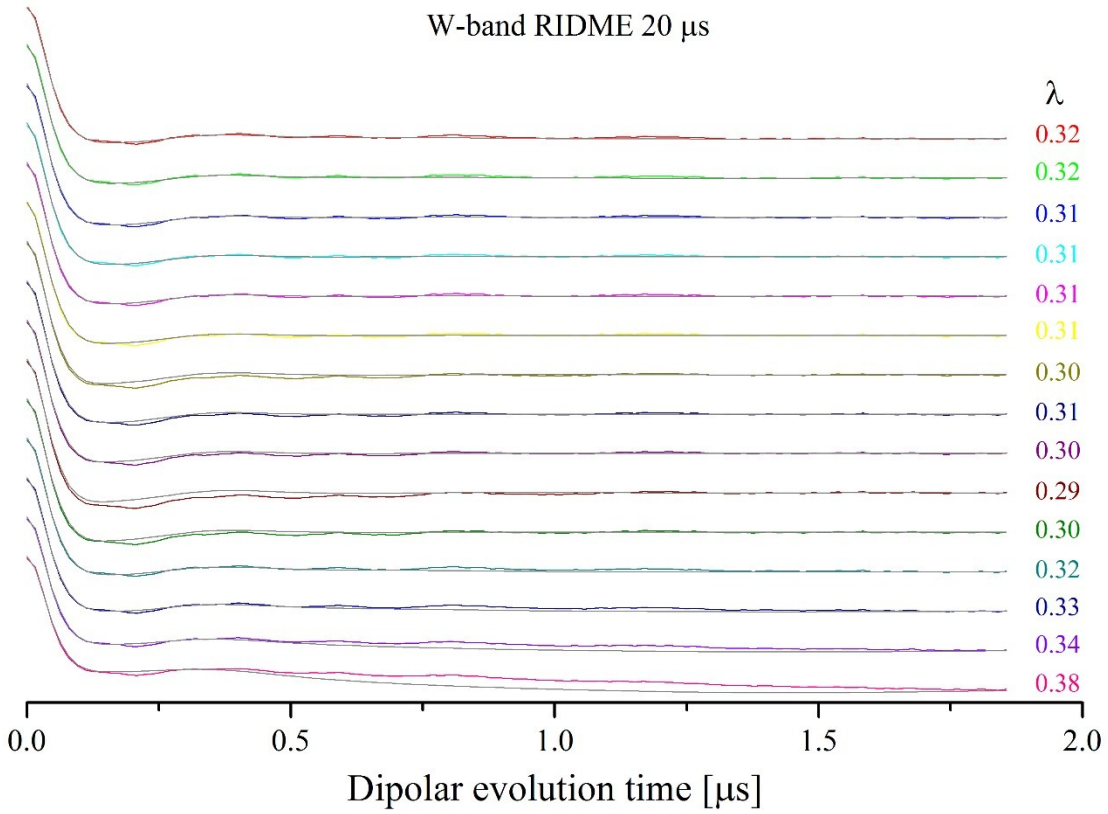

Figure S37. Background-divided RIDME time traces with 20 µs mixing time obtained on complex **1** in deuterated solvent (color-code is consistent with Figures S35 and S36) and back-calculations, based on Tikhonov regularization analysis (gray).

14.2 W-band RIDME with mixing time of 80 µs

The raw experimental time trace, corresponding background functions and background-divided RIDME time traces (80 µs mixing time) are shown in Figure S38.

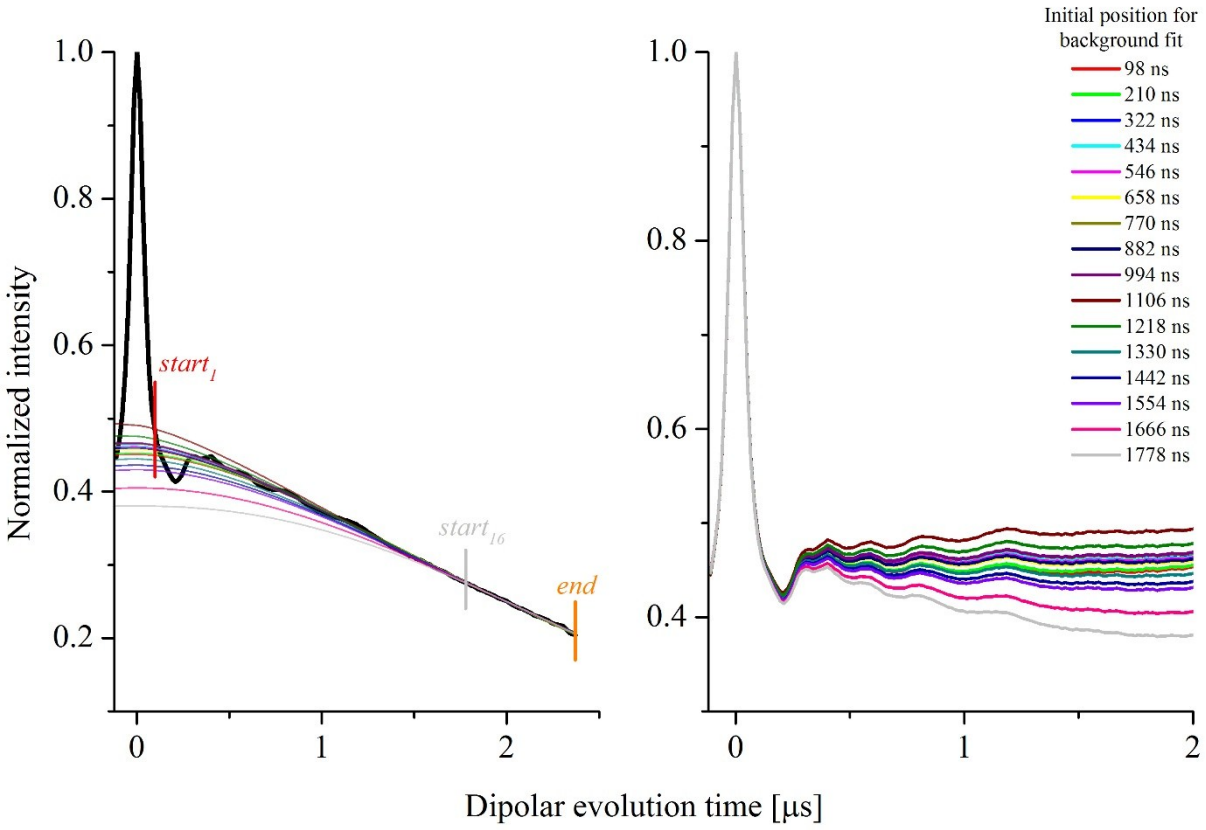

Figure S38. Left: Raw experimental RIDME time trace with 80 µs mixing time obtained on complex **1** in deuterated solvent (black) and background functions. Right: Background-divided RIDME time traces.

The corresponding distance distributions obtained by Tikhonov regularization analysis with kernel (5) and background-divided time traces overlaid with back-calculation are shown in Figures S39 and S40, correspondingly.

As with the W-band RIDME with 20 µs mixing time, we kept two imperfect background functions in order to study their influence on the Tikhonov regularization analysis. As can be seen in Figure S39, the main distance peak and the modulation depth did not strongly depend on the choice of the initial point used to model the background. However, increasingly poorer fits of background did lead to concomitant increase in the intensity of the distance peak at 5.8 nm and stronger deviation of the modulation depth.

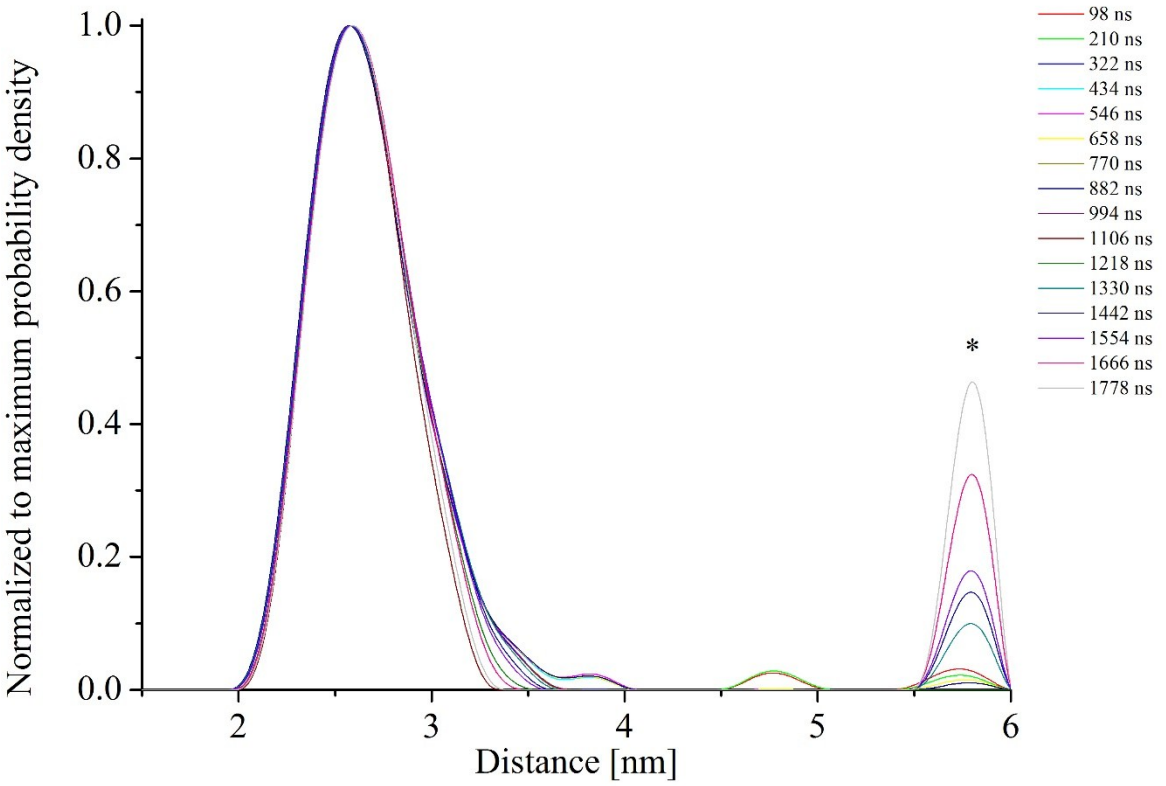

Figure S39. Distance distributions obtained by Tikhonov regularization analysis of the background-divided RIDME time traces (80 µs mixing time, deuterated solvent) shown in Figure S32. The distance distributions were normalized to the probability density of the most probable distance.

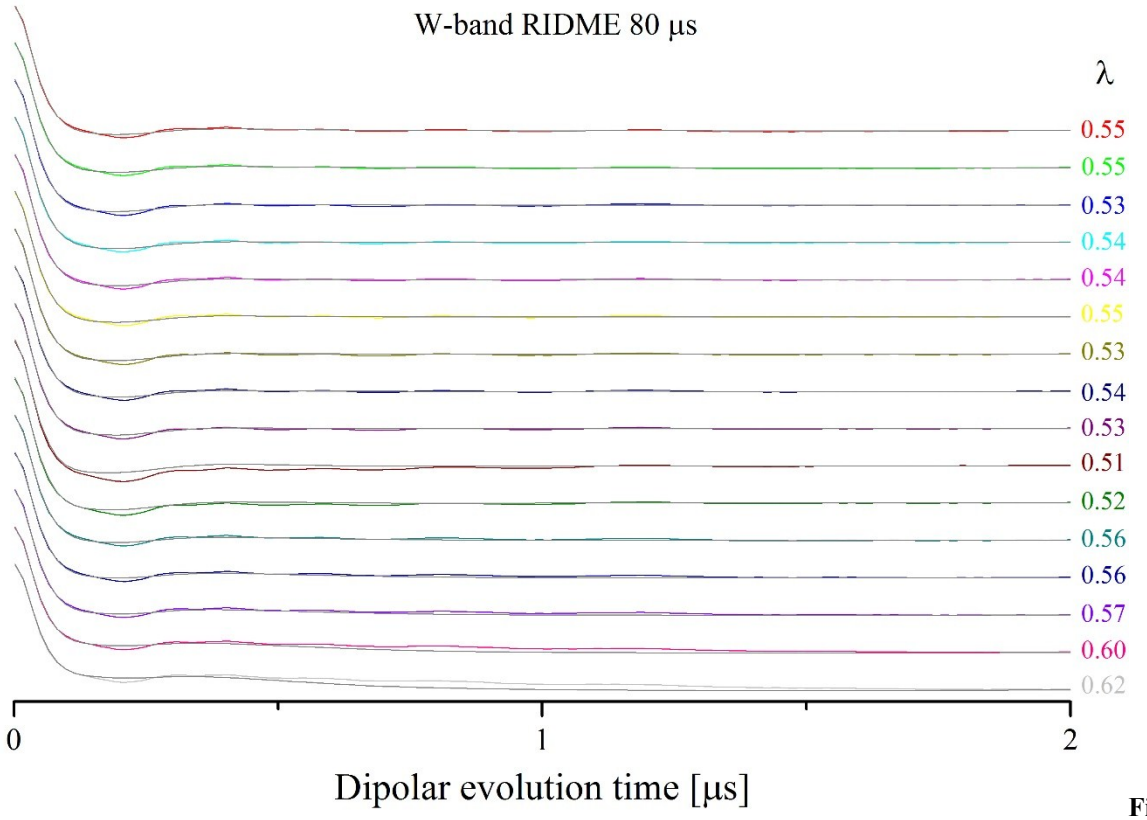

Figure S40. Background-divided RIDME time traces with 80 µs mixing time obtained on complex **1** in deuterated solvent (color-code is consistent with Figures S32 and S33) and back-calculations, based on Tikhonov regularization analysis (gray).

14.3 J-band RIDME with mixing time of 30 µs

The raw experimental J-band RIDME time trace, corresponding background functions and background-divided time traces are shown in Figure S41.

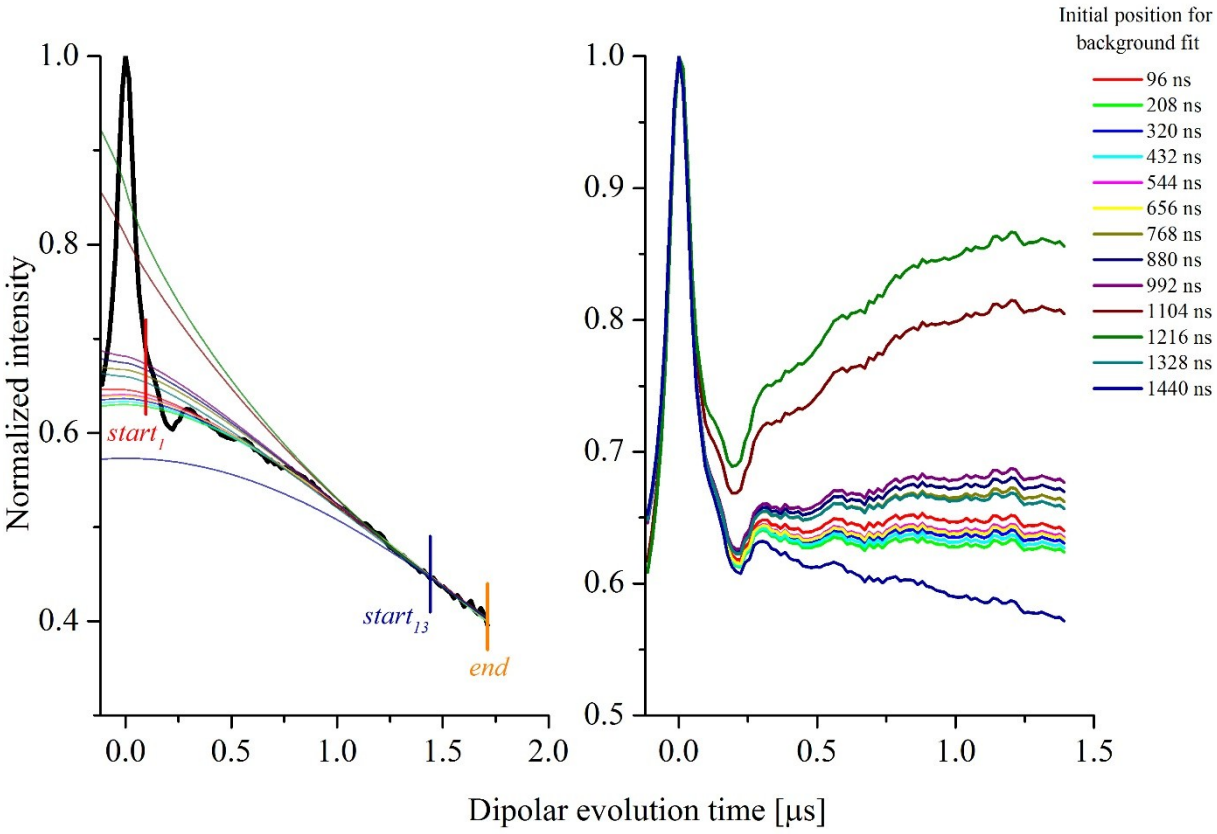

Figure S41. Left: Raw experimental J-band RIDME time trace with 30 µs mixing time obtained on complex **1** in deuterated solvent (black) and background functions. Right: Background-divided RIDME time traces.

As can be seen in Figure S41, two backgrounds (initial times of 1104 ns and 1216 ns) not only significantly deviated from the decay of the RIDME signal but qualitatively had different shapes. Therefore, such backgrounds and correspondingly background-divided time traces were excluded in further analysis.

The distance distributions obtained by Tikhonov regularization analysis with kernel (5) and background-divided time traces overlaid with back-calculation are shown in Figures S42 and S43, correspondingly.

As can be seen, differently defined background functions had greater impact on the shape of the main distance peak (Figure S42). We attribute such effect to the experimental imperfections of J-band RIDME time trace associated with the incomplete cancellation of the moving refocused stimulated and Hahn echoes (for more details see Section 8 and Figure S29).

In conclusion, the ambiguity of background definition of RIDME time traces on complex **1** in deuterated solvent had relatively small impact on Tikhonov regularization analysis and dipolar modulation depth.

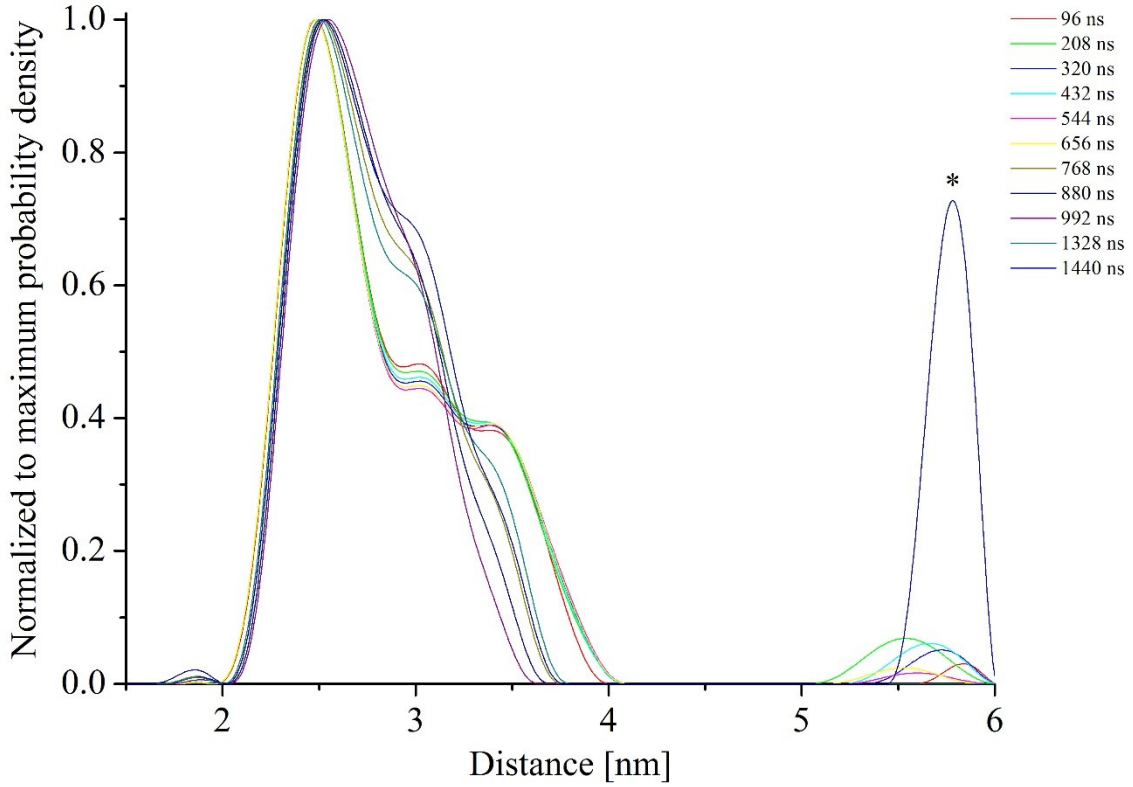

Figure S42. Distance distributions obtained by Tikhonov regularization analysis of the background-divided J-band RIDME time traces (30 µs mixing time, deuterated solvent) shown in Figure S35. The distance distributions were normalized to the probability density of the most probable distance.

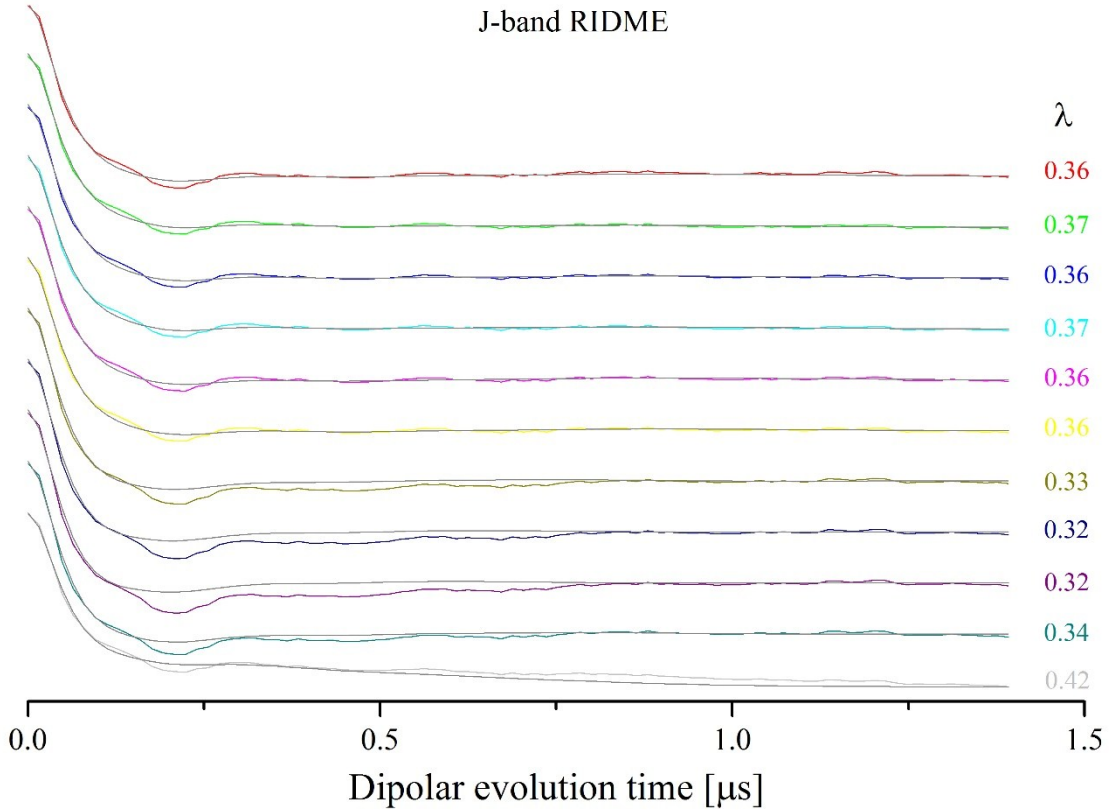

Figure S43. Background-divided J-band RIDME time traces obtained on complex **1** in deuterated solvent (color-code is consistent with Figures S35 and S36) and back-calculations, based on Tikhonov regularization analysis (gray).

15. Analysis of PELDOR and RIDME sensitivity

Relative sensitivity of PELDOR and RIDME measurements were estimated as signal-to-noise ratio (SNR) per square root of accumulation time:

$$sensitivity \propto \frac{SNR}{\sqrt{t_{acc}}} = \frac{\lambda}{rms \cdot \sqrt{t_{acc}}}, \qquad rms = \sqrt{\frac{\sum_{j=1}^{N}\left(F_{j+1} - F_j\right)^2}{N}} \tag{S3}$$

in which λ is the dipolar modulation depth of the corresponding measurement and *rms* is defined in the intervals with length, corresponding approximately to 10% of the whole length of the time trace, as defined in Figure S44. As the length of RDME time traces were longer than that of PELDOR, positions of the time intervals for RIDME were chosen consistently with PELDOR, as shown in this figure.

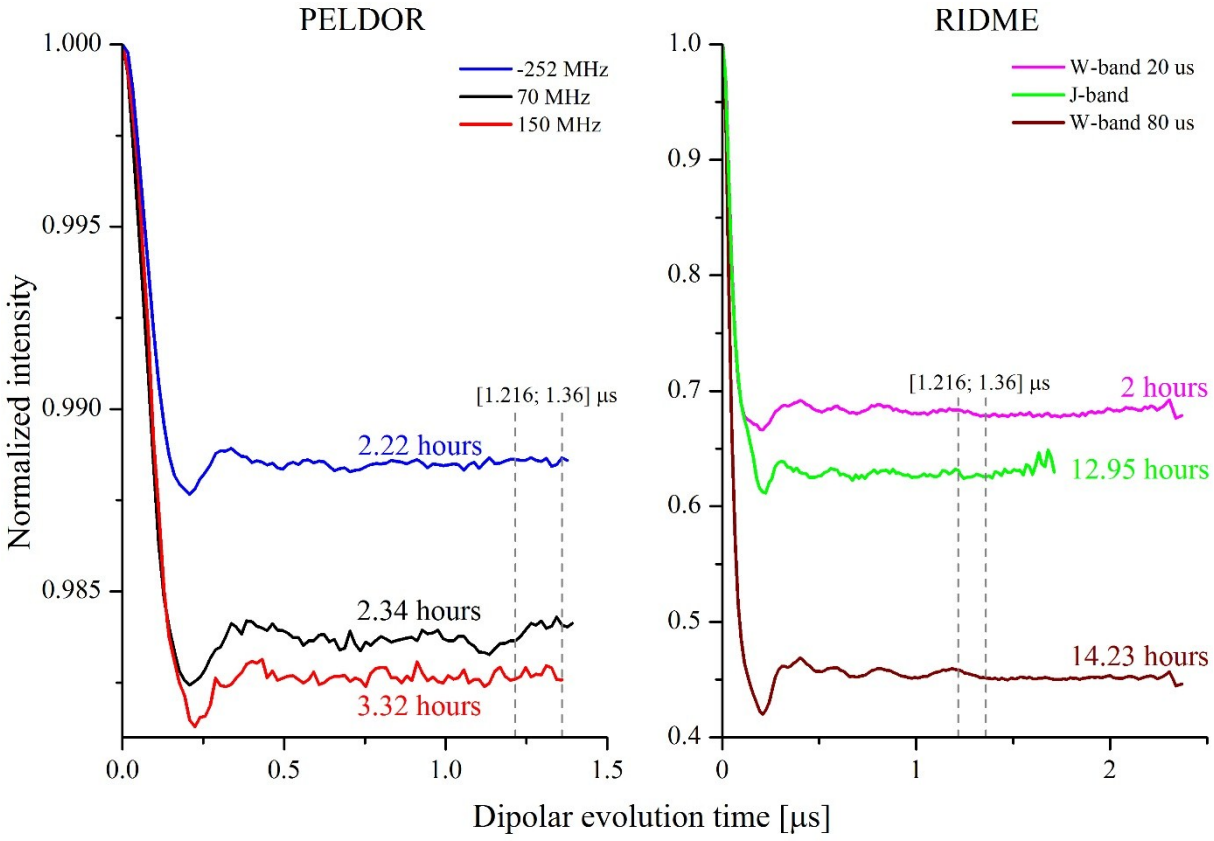

Figure S44. Background-divided PELDOR (left) and RIDME (right) time traces on compound **1** in deuterated solvent. Dashed vertical bars indicate time intervals, in which rms values are defined.

The values are summarized in Table 1 of the main text.

16. References

1. G. Jeschke, V. Chechik, P. Ionita, A. Godt, H. Zimmermann, J. Banham, C. Timmel, D. Hilger and H. Jung, *Appl. Magn. Reson*., 2006, **30**, 473.
2. H. Y. V. Ching, P. Demay-Drouhard, H. C. Bertrand, C. Policar, L. C. Tabares and S. Un, *Phys. Chem. Chem. Phys*., 2015, **17**, 23368.
3. L. V. Kulik, E. S. Salnikov and S. Dzuba, *Appl. Magn. Reson*., 2005, **28**, 1.
4. S. Milikisyants, F. Scarpelli, M. G. Finiguerra, M. Ubbink and M. Huber, *J. Magn. Reson*. 2009, **201**, 48.

ChemPubSoc Europe

DOI: 10.1002/cphc.201600234

CHEMPHYSCHEM Articles

A Bis-Manganese(II)–DOTA Complex for Pulsed Dipolar Spectroscopy**

Paul Demay-Drouhard,[a] H. Y. Vincent Ching,[b] Dmitry Akhmetzyanov,[c] Régis Guillot,[d] Leandro C. Tabares,[b] Hélène C. Bertrand,*[a] and Clotilde Policar*[a]

High-spin gadolinium(III) and manganese(II) complexes have emerged as alternatives to standard nitroxide radical spin labels for measuring nanometric distances by using pulsed electron–electron double resonance (PELDOR or DEER) at high fields/frequencies. For certain complexes, particularly those with relatively small zero-field splitting (ZFS) and short distances between the two metal centers, the pseudosecular term of the dipolar coupling Hamiltonian is non-negligible. However, in general, the contribution from this term during conventional data analysis is masked by the flexibility of the molecule of interest and/or the long tethers connecting them to the spin labels. The efficient synthesis of a model system consisting of two $[Mn(dota)]^{2-}$ (MnDOTA; $DOTA^{4-}$ = 1,4,7,10-tetraazacyclododecane-1,4,7,10-tetraacetate) directly connected to the ends of a central rodlike oligo(phenylene–ethynylene) (OPE) spacer is reported. The rigidity of the OPE is confirmed by Q-band PELDOR measurements on a bis-nitroxide analogue. The Mn^{II}–Mn^{II} distance distribution profile determined by W-band PELDOR is in reasonable agreement with one simulated by using a simple rotamer analysis. The small degree of flexibility arising from the linking MnDOTA arm appears to outweigh the contribution from the pseudosecular term at this interspin distance. This study illustrates the potential of MnDOTA-based spin labels for measuring fairly short nanometer distances, and also presents an interesting candidate for in-depth studies of pulsed dipolar spectroscopy methods on Mn^{II}–Mn^{II} systems.

1. Introduction

Measuring nanometer-scale distances in biomacromolecules, such as proteins or nucleic acids, is an efficient way to unravel useful information about their structure and dynamics.[1–6] One of the ways this can be achieved is by using pulsed electron paramagnetic resonance (EPR) techniques, through which distances can be measured by determining the magnitude of magnetic dipolar coupling between pairs of paramagnetic centers.[7–9] The most commonly used method is pulsed electron–electron double resonance (PELDOR, also known as DEER).[10–13] PELDOR measurements with nitroxide radicals ($S = 1/2$), which can be incorporated into biomacromolecules through site-directed mutagenesis and spin labeling,[14,15] have been extensively studied;[7–9] most measurements are performed at X (9.5 GHz) and Q-band (34 GHz) frequencies.[16,17] Theoretically, the sensitivity of the measurement can be further improved by using higher fields/frequencies. However, the spectral width for organic radicals increases with field as their g anisotropy becomes resolved, which potentially provides information on orientations,[18–20] but can also reduce the expected sensitivity gain and complicate data analysis.[21] Furthermore, commonly used nitroxide radicals, such as (*S*)-(1-oxyl-2,2,5,5-tetramethyl-2,5-dihydro-1*H*-pyrrol-3-yl)methyl methanesulfonothioate (MTSL) and (2,2,6,6-tetramethyl piperidin-1-yl)oxyl (TEMPO) derivatives, can be readily converted into EPR-silent *N*-hydroxylamines in the reducing environment of a cell;[22] this complicates PELDOR measurements in complex cellular environments.

In the last decade, high-spin gadolinium(III) ($S = 7/2$) and manganese(II) ($S = 5/2$) complexes have emerged as attractive alternatives.[23–28] At higher fields, the main feature in their EPR spectra is the $|-1/2> \rightarrow |+1/2>$ "central transition". The spectral width of this transition is proportional to D^2/ν_0, in which D is the size of the zero-field splitting (ZFS), assuming the asymmetry parameter E is equal to zero, and ν_0 is the spectrometer frequency. Consequently, unlike radicals, the spectral width of the Gd^{III} or Mn^{II} central transition becomes narrower and better resolved as the observation frequency increases. Furthermore,

[a] Dr. P. Demay-Drouhard, Dr. H. C. Bertrand, Prof. C. Policar
Ecole Normale Supérieure—PSL Research University
Département de Chimie, Sorbonne Universités—UPMC Univ Paris 06
CNRS UMR 7203 LBM, 24 rue Lhomond
75005 Paris (France)
E-mail: helene.bertrand@ens.fr
clotilde.policar@ens.fr

[b] Dr. H. Y. V. Ching, Dr. L. C. Tabares
Institute for Integrative Biology of the Cell (I2BC)
Department of Biochemistry, Biophysics and Structural Biology
Université Paris-Saclay, CEA, CNRS UMR 9198
Gif-sur-Yvette, F-91198 (France)

[c] D. Akhmetzyanov
Goethe-University Frankfurt am Main
Institute of Physical and Theoretical Chemistry and
Center for Biomolecular Magnetic Resonance
Max von Laue Str. 7, 60438 Frankfurt am Main (Germany)

[d] Dr. R. Guillot
Institut de Chimie Moléculaire et des Matériaux O'Orsay
Université Paris-Sud, UMR CNRS 8182, Université Paris-Saclay
91405 Orsay (France)

[**] $DOTA^{4-}$ = 1,4,7,10-tetraazacyclododecane-1,4,7,10-tetraacetate

Supporting Information for this article can be found under: http://dx.doi.org/10.1002/cphc.201600234.

these metal centers are generally stable within biological environments. Gd^{III}–Gd^{III} PELDOR distance measurements at Q (34 GHz) and W-band (95 GHz) frequencies have been performed in vitro on synthetic model compounds,[29–31] proteins,[32–35] peptides,[36,37] and DNA,[38] and also on proteins,[39] peptides,[40] and DNA[41] inside cells. Mn^{II} centers, which have received much less attention, are very promising in a biological context because Mn^{II} is endogenous in biological environments and present at the active site of numerous enzymes.[42] Mn^{II} can also replace Mg^{II} in other biomacromolecules due to similarities in size and charge.[43] Unlike Gd^{III}, the central transition of Mn^{II} centers is split into a sextet by the hyperfine interaction to the ^{55}Mn nucleus ($I = 5/2$), which reduces the sensitivity of Mn^{II}–Mn^{II} PELDOR measurements by a factor of six if D values are comparable.[26] However, this is partially compensated for by the lower spin multiplicity of Mn^{II} compared with that of Gd^{III}.[26] To date, only three Mn^{II}–Mn^{II} PELDOR studies have been reported and all were performed at the W-band frequency.[26–28] In the first instance, the distance between two $[Mn(edta)]^{2-}$ (MnEDTA; $EDTA^{4-}$ = ethylenediaminetetraacetate) derivatives, grafted through a disulfide tether onto cysteine residues of a protein fragment, was measured.[26] The dipolar modulation depth (λ), an important sensitivity parameter, was found to be low (0.4%), and this was attributed to the large D value ($D = 3000$ MHz) of MnEDTA. Recently, Martorana et al. reported the attachment of $[Mn(pedta)]^{-}$ derivatives (MnPEDTA; $PEDTA^{3-}$ = *N*-(pyrid-2-ylmethyl)ethylenediamine-*N*,*N*′,*N*′-triacetate) to cysteine residues of ubiquitin mutants through C–S conjugation.[28] For two of the derivatives, the D values were 1860(900) and 3060(600) MHz; the values in parentheses denote their distributions. As expected, in the corresponding Mn^{II}–Mn^{II} PELDOR measurements, λ values ($\approx$0.7–1%), which were comparable to or somewhat greater than that of MnEDTA, were observed. However, in contrast to MnEDTA, narrow distance distribution profiles, down to 0.6 nm full-width at half-height (fwhh), were observed in the MnPEDTA measurements; this was attributed to the short length and rigidity of the tether connecting the spin label to the protein.[28] Previously, we reported the grafting of two $[Mn(dota)]^{2-}$ (MnDOTA; $DOTA^{4-}$ = 1,4,7,10-tetraazacyclododecane-1,4,7,10-tetraacetate; $D = 280(150)$ MHz) derivatives through a flexible succinimidyl thioether tether onto a series on polyproline spacers.[27] The PELDOR measurements gave higher λ values (1.2 to 2%) and the Mn–Mn distance distributions were in good agreement with those obtained from molecular dynamics simulations. However, under certain acquisition conditions, additional features in the frequency-domain spectra became apparent and they were attributed to contributions from the pseudosecular term of the dipolar coupling Hamiltonian, which was found to be non-negligible for MnDOTA.[27] Similar observations have also been reported for Gd^{III}–Gd^{III} PELDOR measurements,[30] for which they were found to be more apparent for shorter interspin distances (< 3.4 nm). Thus, conventional application of Tikhonov regularization, as implemented in the DeerAnalysis toolbox,[44] which disregards the contribution from the pseudosecular term,[45] resulted in extra peaks in and/or broadening of the distance distribution profiles.[30] However, for MnDOTA, these effects were mostly obscured by the intrinsic flexibility of the macromolecules and/or the tether to the metal spin label.[27] In contrast, the pseudosecular term contributions were expected to be much smaller for MnEDTA and MnPEDTA due to their larger and more distributed D values.[28]

Taken together, it appears that a compromise between ZFS parameters, their distribution, and flexibility needs to be reached for Mn^{II} spin labels. However, despite the shortcomings of MnDOTA in specific cases, spin labels based on this motif are still very promising for biological Mn^{II} PELDOR and other pulsed dipolar EPR spectroscopic distance measurements because of sensitivity and stability[46] considerations. To assess the limitations of MnDOTA, in particular, at shorter and less flexible distances, we present herein the preparation and characterization of a water-soluble Mn^{II}–Mn^{II} complex with an expected Mn–Mn distance of around 2.5 nm, in which the chelating DOTA ligands have been directly attached to the backbone of a rigid oligo(phenylene–ethynylene) (OPE)[30,45,47–54] spacer through amide bonds. A bis-nitroxide analogue was also synthesized to evaluate the size and flexibility of the OPE spacer in the bis-Mn^{II} complex. PELDOR measurements performed on both systems are discussed.

2. Results

2.1. Synthesis of the Target Compounds

A convergent synthesis of symmetric OPE spacers containing alternate phenyl rings with and without small polyethyleneglycol (PEG) chains (diethyleneglycol methyl ether), which were introduced to improve water solubility, was devised by a double Sonogashira coupling between a *para*-substituted ethynylbenzene and a central diiodinated building block equipped with the PEG chains, which was synthesized in three steps. Compound **2**, prepared by tosylation of diethylene glycol monomethyl ether **1**,[55] was reacted with hydroquinone in a double Williamson reaction to afford the intermediate **3** in good yield.[56] Subsequent diiodination of **3** by using iodine in conjunction with KIO_3 in acetic acid afforded the diiodo building block **4** in satisfactory yield after recrystallization.[57] This protocol has been scaled up and provides an easy access to grams (30 g) of intermediate **4** (Scheme 1).

A double Sonogashira coupling between **4** and commercially available *p*-ethynylaniline (**5**), by using $[Pd(PPh_3)_2Cl_2]$ (0.1 equiv) and CuI (0.2 equiv) in a mixture of triethylamine/THF (1:1), afforded the dicoupled product **6** (OPE-diNH_2) in modest yield (52%; Scheme 2). To functionalize both extremities of this spacer with DOTA macrocycles, OPE-diNH_2 **6** was reacted with bromoacetyl bromide in the presence of K_2CO_3 to afford bromide **7**, which was subjected to double nucleophilic substitution with tri-*t*Bu-DO3A under classical conditions,[58–63] providing the *t*Bu-protected bis-DOTA compound **8** in good yield after column chromatography (Scheme 2).

Removal of the *t*Bu ester protecting groups of compound **8** was attempted under several conditions [1:1 trifluoroacetic acid (TFA)/CH_2Cl_2 with or without scavengers,[59] HCO_2H at

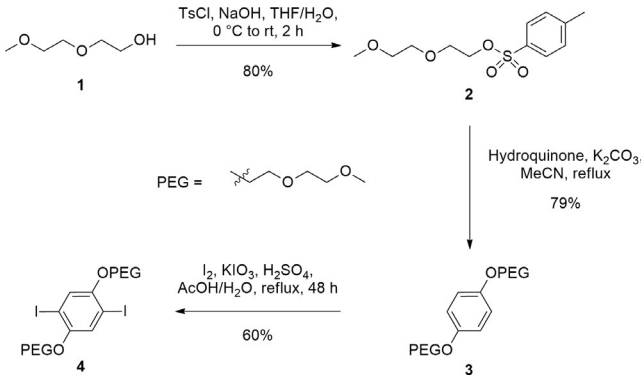

Scheme 1. Synthesis of the diiodo building block **4**. TsCl = 4-toluenesulfonyl chloride.

60 °C,[64] 6 M aqueous solution of HCl]; however, complex mixtures of unidentified products were obtained in each attempt (see HPLC profiles in Figure S1 in the Supporting Information). This deprotection step has been described to proceed smoothly, even on related compounds,[60] although low yields have sometimes been reported.[59] We surmised that the strong acidic conditions needed for the removal of the *t*Bu esters from the DOTA moieties, which is known to be sluggish,[65,66] led to the decomposition of compound **8**.

We turned our attention to the use of the more acid-labile phenylisopropyl (Pp) protecting group described by Mier et al.,[67] which could be cleaved in the presence of 2% TFA in CH_2Cl_2.[68] The Pp group has been successfully employed to generate peptides that incorporate a DOTA core with a much cleaner HPLC profile after cleavage from the resin than with the standard *t*Bu-protected DOTA.[66] Tri-Pp-DO3A **11** was synthesized in two steps from 2-phenyl-2-propanol **9** by treatment with bromoacetic acid in the presence of *N*,*N*′-dicyclohexylcarbodiimide (DCC) and 4-dimethylaminopyridine (DMAP) to give intermediate **10**, followed by reaction with 1,4,7,10-tetraazacyclododecane (cyclen; 0.33 equiv). Despite the low yield due to the concomitant formation of diversely alkylated cyclen derivatives as side products, tri-Pp-DO3A **11** was easily purified and obtained on a gram scale (Scheme 3).

The reaction between tri-Pp-DO3A **11** and bromide **7** under the conditions described above provided the Pp-protected bis-DOTA module **12**, which was cleanly deprotected in 4 h with a 2:2:96 TFA/TIS/CH_2Cl_2 cleavage cocktail, as monitored by reversed-phase HPLC (Figure S2 in the Supporting Information). The bis-DOTA-OPE model system **13** was obtained in high purity after purification by reversed-phase HPLC (Scheme 3). Due to the presence of the small PEG chains and the DOTA moieties, bis-DOTA-OPE **13** was very soluble in H_2O. The corresponding Mn^{II} complex (labeled $MnDOTA_2OPE$) was generated in situ by the addition of 1.8 equivalents of $Mn(ClO_4)_2$ to a buffered solution [4-(2-hydroxyethyl)-1-piperazineethanesulfonic acid (HEPES) 100 mM, pH 8] of **13** with 20% v/v glycerol.

The bis-TEMPO derivative **19** was also prepared by adopting a similar overall strategy. Commercially available *p*-bromobenzaldehyde (**14**) was reacted with trimethylsilylacetylene (TMSA) under Sonogashira coupling conditions to give intermediate **15** in good yield. The TMS group was then removed with K_2CO_3 in MeOH to afford *p*-ethynylbenzaldehyde **16**.[69] A double Sonogashira coupling between this compound and building block **4** gave OPE-diCOH **17** in 80% yield; compound **17** was oxidized with Oxone to generate the corresponding di-

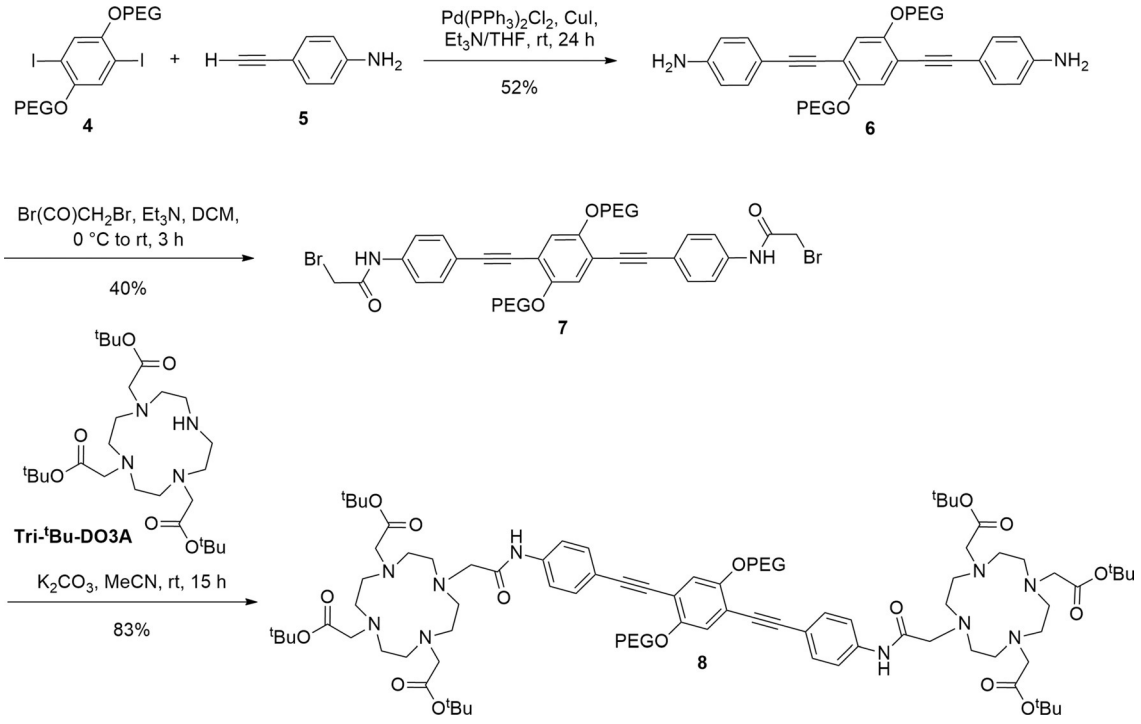

Scheme 2. Synthesis of the *t*Bu-protected bis-DOTA **8**.

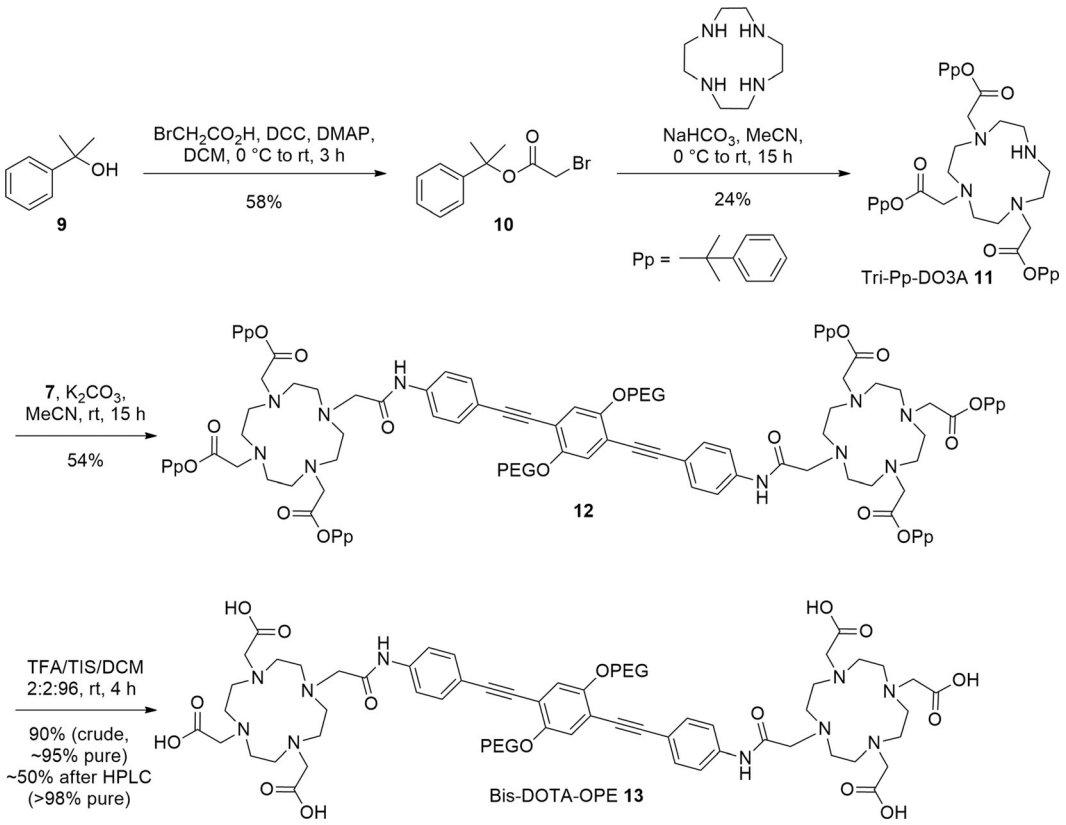

Scheme 3. Synthesis of the bis-DOTA-OPE **13**. TIS = triisopropylsilane.

carboxylic acid **18**. Amide-bond formation between OPE-diCO_2H **18** and commercially available 4-NH_2-TEMPO in the presence of DCC and 1-hydroxybenzotriazole (HOBt) gave bis-TEMPO-OPE **19** in excellent yield (Scheme 4). Interestingly, the yield obtained with this method was higher than those of standard coupling methods used to build systems incorporating two nitroxide radicals connected to a central rigid rod through ester bonds (usually in the region of 20%).[70]

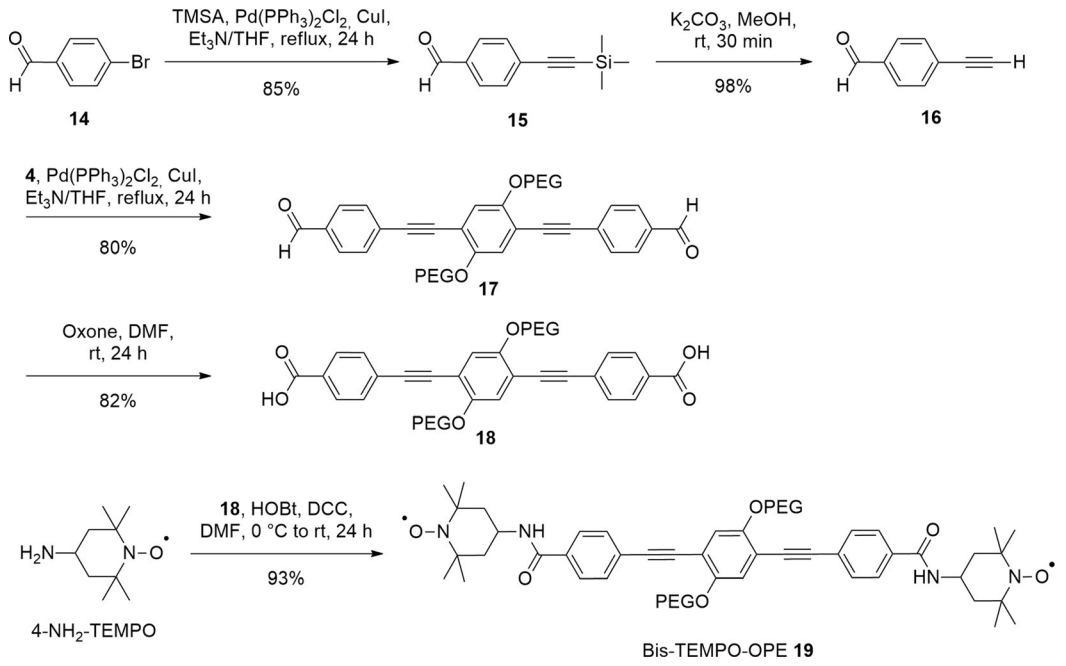

Scheme 4. Synthesis of the bis-TEMPO-OPE **19**.

2.2. X-ray Crystallography

Orange crystals of OPE-diCOH **17** suitable for XRD were obtained by slow evaporation from a 1:1 mixture of chloroform/ethyl acetate. Compound **17** crystallized in the $P\bar{1}$ space group (triclinic system). The aromatic rings were twisted relative to each other with dihedral angles of 18 and 31° relative to the central ring. The molecules were slightly bent (approximately 7°), which reflected the nonideal unidirectional arrangement of OPE spacers. No π stacking is observed, presumably because of the steric hindrance imposed by the PEG chains (Figure 1 A). The length of the OPE spacer (the C–C distance between the carbon atoms of the two aldehydes) was 1.93 nm.

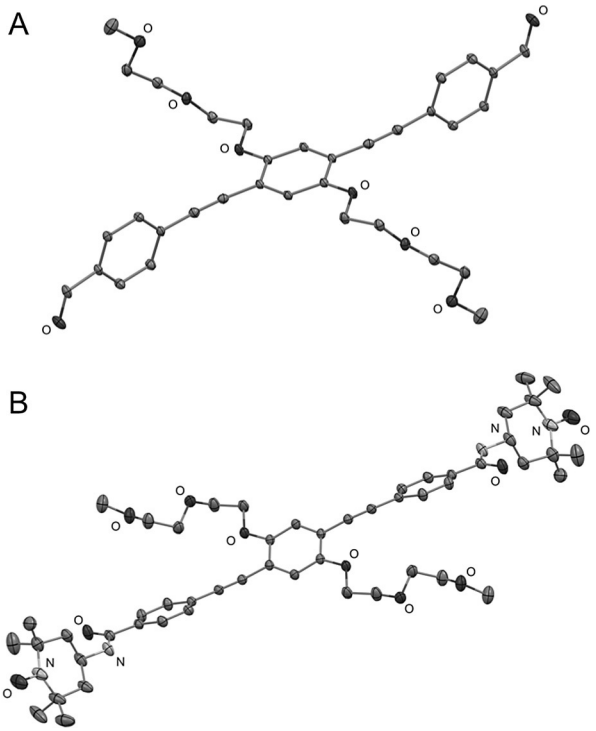

Figure 1. CSD Mercury[71] ellipsoid views of the structure of OPEs A) compound **17** and B) bis-TEMPO-OPE **19**. Ellipsoids are drawn at the 30% probability level.

Orange prisms of bis-TEMPO-OPE **19** were obtained by slow evaporation from a solution of the biradical in toluene. Compound **19** crystallized in the $P2_1/n$ space group (monoclinic system), with the three aromatic rings twisted by 39° from each other. The distance between the two N–O bonds (point-dipole approximation) was 3.02 nm (Figure 1 B) and the length of the OPE spacer (the distance between the two carbons of the amide bonds) was 1.93 nm, which was identical to that in OPE-diCOH **17** (Figure 1 B).

2.3. EPR Measurements

The W-band Hahn echo-detected field-swept EPR spectrum of $MnDOTA_2OPE$ in frozen glassy solution is depicted in Figure 2 A. A narrow sextet corresponding to the central transition superposing a broad component arising from the other transitions was observed, and was essentially the same as that of MnDOTA and MnDOTA-grafted polyprolines.[27] PELDOR measurements were performed with the pump pulse frequency (ν_{pump}) resonant with the highest field hyperfine line and the detection pulses frequency (ν_{detect}) set 70 MHz lower (Fig-

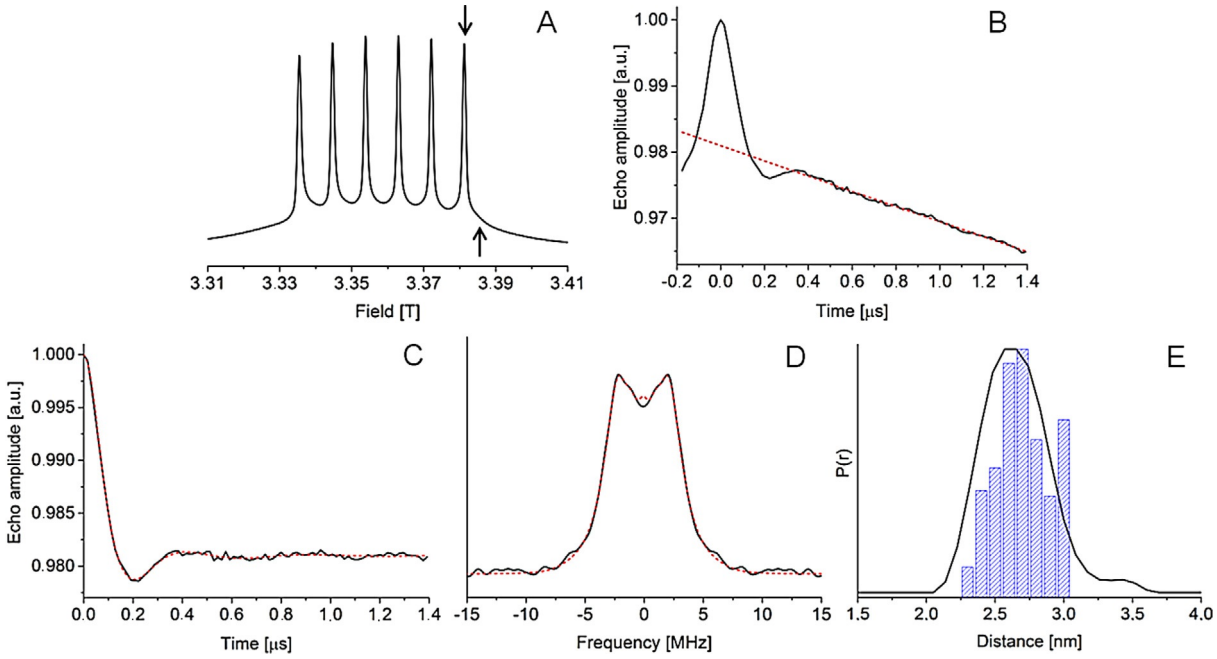

Figure 2. W-band PELDOR measurements on $MnDOTA_2OPE$ (100 μM) in HEPES (100 mM, pH 8) with 20% v/v glycerol at 10 K (black). A) Hahn echo-detected field-swept EPR spectrum with the pump and detection positions indicated schematically by the down and up arrows, respectively. B) Raw PELDOR time trace and background (dashed red). C) Background-corrected PELDOR time trace and its fit based on Tikhonov regularization (dashed red). D) Frequency-domain spectra corresponding to the experimental background-corrected time trace and its fit based on Tikhonov regularization (dashed red). E) Distance distribution profiles obtained by Tikhonov regularization and predicted by rotamer analysis (blue).

ure 2B–E). These frequency positions were chosen because previous studies suggested that the contribution from the pseudosecular term of the dipolar coupling Hamiltonian was least apparent when pumping at the hyperfine line and detecting off to the side.[27] The first modulation was clearly visible in the raw time trace and after background division the λ value was 1.9%, which was comparable to previous PELDOR measurements with MnDOTA.[27] The corresponding frequency-domain spectra showed a doublet with a splitting of 2.0 MHz. Tikhonov regularization, as conventionally implemented in DeerAnalysis,[44] gave a most probable distance of 2.6 nm. The fwhh of the distribution was 0.6 nm, which was comparable to the narrowest distance distribution profile observed in Mn^{II}–Mn^{II} PELDOR measurements.[28]

The Q-band Hahn echo-detected field-swept EPR spectrum of bis-TEMPO-OPE **19** is depicted in Figure 3A. PELDOR time traces (Figure 3B) were recorded across the whole EPR spectrum by using a constant $\nu_{detect}-\nu_{pump}$ offset of 50 MHz, with the exception of the magenta time trace for which an offset of −50 MHz was used. In the time traces, up to 7 full periods of a dampened dipolar oscillation were observed with modulation depths of up to 24%. Differences between the traces clearly indicate orientation selection.[19–21,72–76] For the orange and green time traces, the detection pulses were resonant with the lower field edge of the EPR spectrum, in which the g_{xx} component of the g tensor had a relatively large contribution to the excited orientations. In these two traces and their corresponding frequency domain spectra (Figure 3C), a large 3.6 MHz frequency component was observed. In contrast, for the other time traces, the main frequency component was at about 1.85 MHz. The orientation selection effects can be qualitatively rationalized in terms of the geometry of the biradical from its X-ray crystal structure. The g tensor of the nitroxide moieties is oriented with the g_{xx} component collinear to the mean axis of the molecule. For the orange and green time traces, the detection pulses sampled significant amounts of the g_{xx} component, such that the parallel orientation of the dipolar coupling tensor was excited to a high extent, which resulted in oscillations that were doubled in frequency (3.6 MHz) relative to the major component of the other time traces. In the green time trace, increased contributions from the g_{yy} and g_{zz} components meant that a single frequency (1.85 MHz) component was also observed. For all other time traces, the g_{xx} component only had a minor contribution to the signal, which resulted in time traces that lacked the parallel orientation of the dipolar coupling tensor. As expected, orientation selection was also observed at W-band frequencies (see Figure S4 in the Supporting Information).

The orientation selection effects were minimized by summing the Q-band PELDOR time traces (Figure 3D–F), which, in effect, provided a more uniform excitation of the dipolar coupling tensor orientations. The corresponding frequency domain spectrum resembled a complete Pake pattern. The summed time trace was analyzed by means of Tikhonov regu-

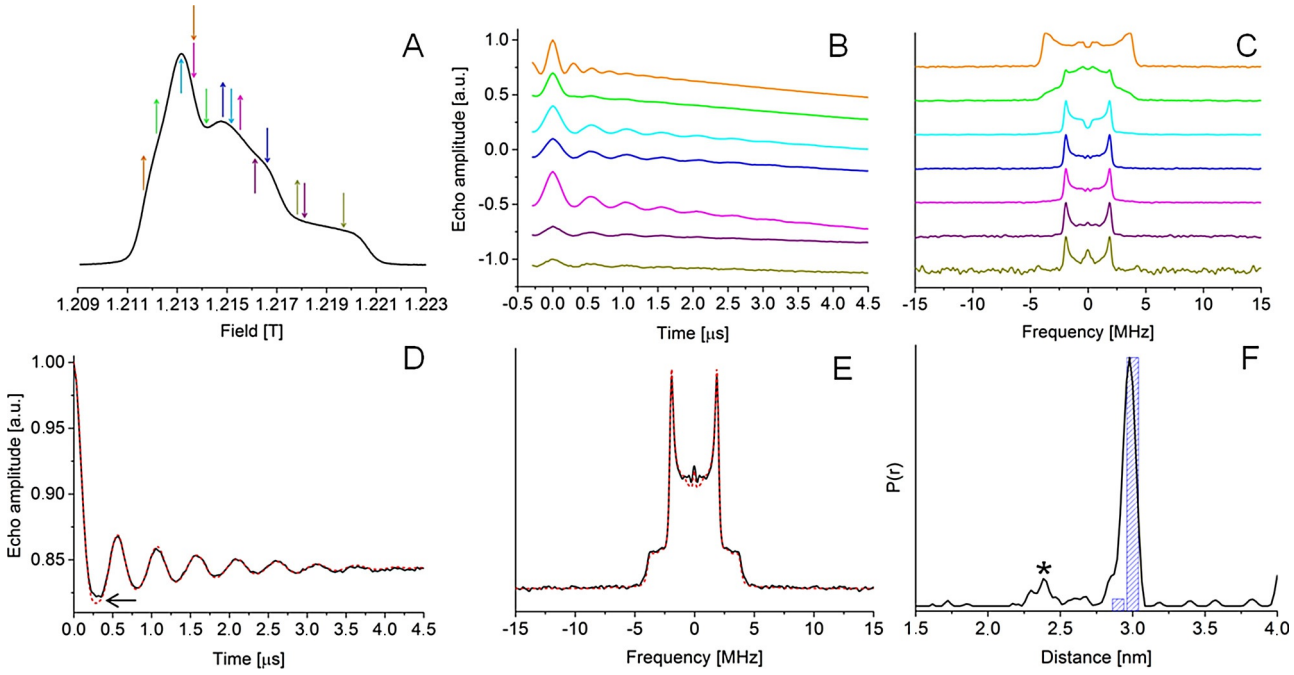

Figure 3. Q-band PELDOR measurements on bis-TEMPO-OPE **19** (100 µM) in 1:1 v/v $[D_8]$toluene/$CDCl_3$ at 50 K. A) Hahn echo-detected field-swept EPR spectrum with different pump and detection PELDOR positions indicated schematically in different colors by the down and up arrows, respectively. B) Raw PELDOR time traces recorded at different positions of the EPR spectrum, with colors corresponding to the arrows depicted in A). C) Fourier transform of the background-corrected time traces. D) The summed PELDOR time trace (black) after background correction and its fit based on Tikhonov regularization (dashed red), as implemented in DeerAnalysis.[40] The black arrow indicates a deviation due to imperfections of averaging of the orientation selection (discussed in detail in the text). E) Frequency-domain spectra corresponding to the background-corrected summed time trace (black) and its fit based on Tikhonov regularization (dashed red). F) Distance distribution profile obtained by Tikhonov regularization analysis of the summed PELDOR time trace and predicted by rotamer analysis (blue). The black asterisk indicates an artefact due to imperfection of averaging of orientation selection (details described in the text).

larization (Figure 3D–F). Small differences can be seen between the summed time trace (black) and the fit based on Tikhonov regularization (red), for example, at the first minimum of the dipolar oscillations, indicated with a black arrow in Figure 3D. This indicates that orientation selection is still present in the averaged time trace that gives rise to the small peak seen at 2.4 nm in Figure 3F. However, such imperfections are not expected to cause a significant error in the position of the main peak and the distance distribution. The most probable distance observed from the Tikhonov fit of the summed trace was 2.98 nm with a fwhh of 0.1 nm and width at 10% height of 0.2 nm.

2.4. Simulations of Distance Distribution Profiles

The Mn–Mn distance was simulated by using a rotamer analysis that accounted for the inherent flexibility of spin labels. This approach has been used to adequately predict distance distributions obtained from PELDOR measurements.[27,40,77–79] Starting from known X-ray crystal structures, we constructed a model of $MnDOTA_2OPE$ (Figure 4). Subject to certain constraints (see the Experimental Section), all possible rotamers that avoided clashes were generated and each was given the same probability. The predicted most probable Mn–Mn distance was 2.7 nm with a distribution of 0.5 nm at fwhh (Figure 2E). Similarly, starting from the X-ray structure of bis-TEMPO-OPE, its rotamers were generated and each was given the same probability. The predicted most probable spin–spin distance was 3.0 nm with a distribution of 0.1 nm at fwhh (Figure 3F).

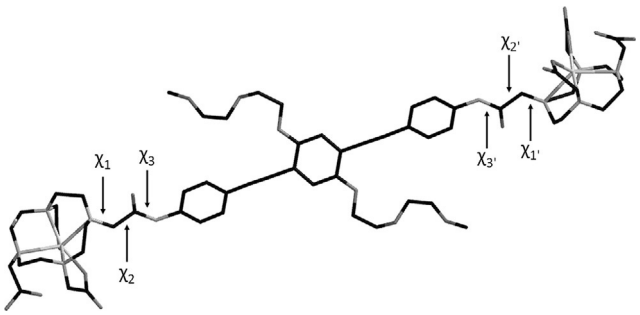

Figure 4. Schematic structure of $MnDOTA_2OPE$. The relevant dihedral angles, χ, of rotatable bonds of each MnDOTA are labeled. Hydrogen atoms have been omitted for clarity.

3. Discussion

The distance determined in the Q-band PELDOR measurements on bis-TEMPO-OPE **19** was in good agreement with that obtained from X-ray crystallography by using the point-dipole approximation and rotamer analysis. The strong orientation selection effect observed in the PELDOR time traces at these frequencies highlighted the rigidity of the molecule (and correspondingly of the OPE spacer). The determined width of the distance distribution profile was very narrow and could be attributed to bending of the OPE spacer and rotations of the single bonds of the molecule. This profile was in agreement with the prediction that had a sampling inaccuracy of 0.1 nm, but did not take into account bending of the molecule.

Compared with the bis-TEMPO-OPE results, the Mn–Mn distance obtained in W-band PELDOR measurements on $Mn\text{-}DOTA_2OPE$ were around six times more distributed. The bulk of this broadening was unlikely to have arisen from the bending of the OPE, but rather was most likely to be due to the inherent flexibility of the MnDOTA spin label. Indeed, the Mn–Mn distance distribution predicted by using a rotamer analysis was remarkably in reasonable agreement with the experimental data. Compared with PELDOR results, the predicted distance distribution profile was slightly shifted to longer distances; this was possibly due to sampling inaccuracy and/or inaccuracy of the method of modeling, such as 1) rotamer analysis did not take into account the small bending flexibility of the OPE spacer, which would give slightly shorter Mn–Mn distances; and 2) a dynamic coordination process in which the amide O atom coordinates to the Mn^{II} center,[80] which would favor shorter Mn–Mn distances. Alternatively, the differences between the experimental and predicted distance distribution profiles might also have originated from experimental data analysis, which did not take into account the pseudosecular term of the dipolar coupling Hamiltonian. For specific cases, in previous MnDOTA polyproline studies, this approach resulted in extra features at shorter distances.[27] The small feature at around 3.3 nm in the distance distribution profile, obtained in the PELDOR experiment, is possibly due to uncertainty in determining the background. Nevertheless, overall, the $MnDOTA_2OPE$ PELDOR results closely matched expectations, which suggested that MnDOTA spin labels could be used for measuring nanometric distances with relatively narrow distributions predictably, even at distances as short as 2.6 nm. Compared with the OPE spacer alone, each MnDOTA spin label only contributed around 0.3 nm to the distance and 0.3 nm to the distribution at fwhh. Although relatively small, the size and flexibility of the tethering DOTA arm appeared to outweigh the contribution from the pseudosecular term of the dipolar coupling Hamiltonian during Tikhonov regularization analysis. These advantages can potentially be further exploited by affixing MnDOTA to the biomolecule of interest in a more constrained manner, for example, by using 2,2′,2″-(10-{2-[(2,5-dioxopyrrolidin-1-yl)oxy]-2-oxoethyl}-1,4,7,10-tetraazacyclododecane-1,4,7-triyl)triacetic acid (DOTA-NHS ester), the protein backbone can be directly labeled at the N terminus,[81] or by using a derivative with short thiol-reactive tethers, similar to the Gd^{III} complexes very recently reported by Abdelkader et al.[79]

4. Conclusions

A model system incorporating two DOTA ligands on a short OPE spacer was designed, synthesized, and fully characterized. PELDOR measurements were performed on the corresponding Mn^{II} complex and on a bis-nitroxide analogue. The experimental Mn–Mn distance distribution obtained by Tikhonov regula-

rization was in good agreement with that simulated by using a simple rotamer analysis. However, there were small deviations, which might have arisen from a combination of shortcomings in the modeling and data analysis. Overall, our results suggested that PELDOR measurements with MnDOTA spin labels directly grafted on an object of interest could be used to determine nanometer distances with relatively narrow distributions predictably. Currently, we are studying the potential use of other MnDOTA derivatives as spin labels for PELDOR, as well as other dipolar EPR spectroscopic methods for Mn^{II}–Mn^{II} nanometer distance measurements, and these results will be reported in due course.

Experimental Section

Material and methods

^1H and ^{13}C NMR spectra were recorded on Bruker Avance 300 or 600 (300 or 400 MHz) spectrometers at the Ecole Normale Supérieure (ENS) in the Laboratoire des Biomolécules (LBM, UMR 7203) or at UPMC (Université Pierre et Marie Curie) in IPCM (Institut Parisien de Chimie Moléculaire, UMR 7201), with residual solvent signals as internal references. The following abbreviations were used: singlet (s), doublet (d), triplet (t), multiplet (m) and broad (br); δ indicates chemical shifts in ppm, J are coupling constants in Hz, and C_q are quaternary carbons. HRMS by using electrospray ionization (ESI) or atmospheric pressure chemical ionization (APCI) methods was performed at the Université Paris Sud in the Service de Spectrométrie de masse of the ICMMO (Institut de Chimie Moléculaire et des Matériaux d'Orsay). ESI-HRMS was also performed at UPMC (IPCM). MALDI-TOF MS was performed at UPMC in the Plate-forme de Spectrométrie de masse et Protéomique. The matrix was a saturated solution of α-cyano-4-hydroxycinnamic acid (HCCA) in MeCN/H_2O 1:1 with 0.1% TFA. Analytical TLC analysis was performed on silica gel plates (Merck 60F-254) with UV visualization at $\lambda = 254$ and 366 nm. Preparative column chromatography was performed with Merck silica gel (Si 60, 40–63 μm). Analytical HPLC measurements were performed on a Dionex Ultimate 3000 instrument by using C18A ACE columns. Preparative HPLC was performed on a Waters 600 instrument by using an XBridgeTM Prep C18 OBDTM column. Gradients of MeCN in H_2O, both containing 0.1% TFA, were employed. Products were monitored with UV detection. Unless otherwise stated, all syntheses were performed under an inert atmosphere (argon or nitrogen). Reagents and chemicals were purchased from Sigma–Aldrich, Alfa Aesar, Strem Chemicals, or Chematech. Dry solvents (CH_2Cl_2, MeCN, toluene, THF, dioxane, DMF, DMSO) were purchased from Sigma and used without further purification. EtOAc and triethylamine were dried with CaH_2, distilled under argon, and stored over 4 Å molecular sieves under argon.

2-(2-Methoxyethoxy)ethyl 4-methylbenzenesulfonate (2)

Compound **1** (39.1 mL, 332.7 mmol, 1.0 equiv) was dissolved in THF (110 mL). The resulting solution was cooled to 0 °C and NaOH (26.44 g, 661.0 mmol, 2.0 equiv) dissolved in H_2O (110 mL) was added dropwise, followed by TsCl (95.16 g, 499.0 mmol, 1.5 equiv) dissolved in THF (110 mL) dropwise. The resulting mixture was stirred at RT for 2 h and H_2O (400 mL) was added. The organic layer was recovered and washed without shaking with a 1 M aqueous solution of NaOH (2×) and H_2O (1×), dried over Na_2SO_4, filtered, and concentrated to afford **2** (72.95 g, 266.2 mmol, 80%) as a colorless oil. ^1H NMR ($CDCl_3$, 300 MHz): $\delta = 7.80$ (d, 2H, $J = 8.0$ Hz), 7.34 (d, 2H, $J = 8.0$ Hz), 4.17 (t, 2H, $J = 4.8$ Hz), 3.69 (t, 2H, $J = 4.8$ Hz), 3.61–3.54 (m, 2H), 3.51–3.44 (m, 2H), 3.35 (s, 3H), 2.44 ppm (s, 3H); ^{13}C NMR ($CDCl_3$, 75 MHz): $\delta = 144.9$ (C_q), 133.0 (C_q), 129.9 (CH), 128.1 (CH), 71.9 (CH_2), 70.8 (CH_2), 69.3 (CH_2), 68.8 (CH_2), 59.2 (CH_3), 21.8 ppm (CH_3); HRMS (ESI): m/z calcd for $C_{12}H_{19}O_5S^+$ $[M+H]^+$, $C_{12}H_{18}NaO_5S^+$ $[M+Na]^+$: 275.0948, 297.0766; found: 275.0950, 297.0767.

1,4-Bis[2-(2-methoxyethoxy)ethoxy]benzene (3)

Hydroquinone (14.64 g, 133.1 mmol, 1.0 equiv) and K_2CO_3 (73.47 g, 532.4 mmol, 4.0 equiv) were suspended in MeCN (1.1 L). The resulting suspension was heated at reflux for 30 min and cooled to RT. Compound **2** (72.95 g, 266.2 mmol, 2.0 equiv) dissolved in MeCN (220 mL) was added dropwise. The resulting mixture was heated at reflux for 72 h, cooled to RT, filtered, and concentrated. Column chromatography (SiO_2, cyclohexane/EtOAc 90:10 to 50:50) afforded **3** (32.81 g, 104.5 mmol, 79%) as an orange oil. ^1H NMR ($CDCl_3$, 300 MHz): $\delta = 6.83$ (s, 4H), 4.11–4.05 (m, 4H), 3.86–3.80 (m, 4H), 3.74–3.68 (m, 4H), 3.60–3.54 (m, 4H), 3.39 ppm (s, 6H); ^{13}C NMR ($CDCl_3$, 75 MHz): $\delta = 153.2$ (C_q), 115.6 (CH), 72.1 (CH_2), 70.9 (CH_2), 70.0 (CH_2), 68.1 (CH_2), 59.2 ppm (CH_3); HRMS (ESI): m/z calcd for $C_{16}H_{27}O_6^+$ $[M+H]^+$, $C_{16}H_{26}NaO_6^+$ $[M+Na]^+$; 315.1802, 337.1622; found: 315.1796, 337.1617.

1,4-Diiodo-2,5-bis[2-(2-methoxyethoxy)ethoxy]benzene (4)

Compound **3** (25.0 g, 79.6 mmol, 1.0 equiv), iodine (22.3 g, 87.6 mmol, 1.1 equiv), and KIO_3 (6.8 g, 31.8 mmol, 0.4 equiv) were dissolved in glacial AcOH (250 mL) and H_2O (25 mL). Concentrated H_2SO_4 (3.3 mL) was added, the resulting mixture was heated at reflux for 48 h and cooled to RT. CH_2Cl_2 and a 10% aqueous solution of $Na_2S_2O_3$ were added, the organic layer was recovered and washed with a saturated aqueous solution of $NaHCO_3$ (1×), H_2O (1×), and a saturated aqueous solution of NaCl (1×); dried over Na_2SO_4; filtered; and concentrated. Recrystallization from EtOH afforded **4** (27.27 g, 48.1 mmol, 60%) as a white solid. ^1H NMR ($CDCl_3$, 300 MHz): $\delta = 7.23$ (s, 2H), 4.14–4.07 (m, 4H), 3.92–3.86 (m, 4H), 3.80–3.74 (m, 4H), 3.61–3.55 (m, 4H), 3.40 ppm (s, 6H); ^{13}C NMR ($CDCl_3$, 75 MHz): $\delta = 153.2$ (C_q), 123.6 (CH), 86.5 (C_q), 72.2 (CH_2), 71.2 (CH_2), 70.5 (CH_2), 69.8 (CH_2), 59.3 ppm (CH_3); HRMS (ESI): m/z calcd for $C_{16}H_{25}I_2O_6^+$, $[M+H]^+$, $C_{16}H_{24}I_2NaO_6^+$ $[M+Na]^+$: 566.9735, 588.9554; found: 566.9707, 588.9544.

4,4′-({2,5-Bis[2-(2-methoxyethoxy)ethoxy]-1,4-phenylene}-bis(ethyne-2,1-diyl))dianiline (OPE-NH_2 6)

Compounds **4** (2.78 g, 5.0 mmol, 1.0 equiv) and **5** (1.17 g, 10.0 mmol, 2.0 equiv) were dissolved in dry THF (20 mL) and dry triethylamine (20 mL). Argon was bubbled for 15 min and $[Pd(PPh_3)_2Cl_2]$ (351.0 mg, 0.5 mmol, 0.1 equiv) and CuI (191.0 mg, 1.0 mmol, 0.2 equiv) were added. The resulting suspension was stirred for 24 h at RT; a saturated aqueous solution of NH_4Cl was added and the mixture was extracted with CH_2Cl_2 (3×). The combined organic layers were dried over Na_2SO_4, filtered, and concentrated. Column chromatography (SiO_2, 50:50 cyclohexane/EtOAc to 100% EtOAc) afforded **6** (1.41 g, 2.59 mmol, 52%) as an orange solid. ^1H NMR ($CDCl_3$, 300 MHz): $\delta = 7.32$ (d, $J = 8.4$ Hz, 4H), 6.99 (s, 2H), 6.63 (d, $J = 8.4$ Hz, 4H), 4.20 (t, $J = 5.0$ Hz, 4H), 3.92 (t, $J = 5.0$ Hz, 4H), 3.86–3.77 (m, 8H), 3.57–3.50 (m, 4H), 3.36 ppm (s, 6H); ^{13}C NMR ($CDCl_3$, 75 MHz): $\delta = 153.5$ (C_q), 146.9 (C_q), 133.1 (CH), 117.5

(CH), 114.9 (CH), 114.5 (C_q), 112.9 (C_q), 95.1 (C_q), 84.0 (C_q), 72.2 (CH_2), 71.2 (CH_2), 69.9 (CH_2), 69.9 (CH_2), 59.2 ppm (CH_3); HRMS (ESI): *m/z* calcd for $C_{32}H_{37}N_2O_6^+$ $[M+H]^+$, $C_{32}H_{36}N_2NaO_6^+$ $[M+Na]^+$: 545.2646, 567.2466; found: 545.2609, 567.2443.

N,N′-[({2,5-Bis[2-(2-methoxyethoxy)ethoxy]-1,4-phenylene}-bis(ethyne-2,1-diyl))bis(4,1-phenylene)]bis(2-bromoacetamide) (7)

OPE-NH_2 **6** (798 mg, 1.465 mmol, 1.0 equiv) was dissolved in dry CH_2Cl_2 (20 mL). The resulting solution was cooled to 0 °C, and triethylamine (496 μL, 3.66 mmol, 2.5 equiv) was added, followed by the dropwise addition of bromoacetyl bromide (319 μL, 3.66 mmol, 2.5 equiv) dissolved in dry CH_2Cl_2 (3 mL). The resulting mixture was allowed to warm to RT for 3 h and washed with a saturated aqueous solution of $NaHCO_3$ (1×) and a saturated aqueous solution of NaCl (1×). The organic layer was dried over Na_2SO_4, filtered, and concentrated. Compound **7** (459 mg, 0.584 mmol, 40%) was obtained after column chromatography (SiO_2, 40:60 to 20:80 cyclohexane/EtOAc) as a pale yellow solid. ^{1}H NMR ($CDCl_3$, 300 MHz): $\delta = 8.17$ (s, 2H), 7.59–7.48 (m, 8H), 7.03 (s, 2H), 4.22 (t, $J = 4.8$ Hz, 4H), 4.04 (s, 4H), 3.93 (t, $J = 4.8$ Hz, 4H), 3.83–3.78 (m, 4H), 3.57–3.52 (m, 4H), 3.37 ppm (s, 6H); ^{13}C NMR ($CDCl_3$, 75 MHz): $\delta = 163.4$ (C_q), 153.7 (C_q), 137.1 (C_q), 132.6 (CH), 120.1 (C_q), 119.7 (CH), 117.6 (CH), 114.3 (C_q), 94.7 (C_q), 86.0 (C_q), 72.2 (CH_2), 71.2 (CH_2), 69.9 (CH_2), 69.8 (CH_2), 59.2 (CH_3), 29.6 ppm (CH_2); HRMS (ESI): *m/z* calcd for $C_{36}H_{38}Br_2N_2NaO_8^+$ $[M+Na]^+$: 809.0867; found: 809.0859.

General Procedure A: Synthesis of Protected Bis-DOTA Compounds

Bromide **7** (1.0 equiv) and a DO3A derivative (tri-*t*Bu-DO3A or tri-Pp-DO3A **11**) (2.5 equiv) were mixed in dry MeCN. K_2CO_3 (10.0 equiv) was added and the resulting mixture was heated at 60 °C for 15 h and concentrated. CH_2Cl_2 was added and the mixture was washed with H_2O (1×) and a saturated aqueous solution of NaCl (1×). The organic layer was dried over Na_2SO_4, filtered, and concentrated. Column chromatography afforded the corresponding protected bis-DOTA-OPE compound as a yellow solid.

*t*Bu-Protected Bis-DOTA-OPE (8)

By using general procedure A with **7** (55 mg, 0.07 mmol), tri-*t*Bu-DO3A (100 mg, 0.174 mmol), and K_2CO_3 (96 mg, 0.7 mmol) in dry MeCN (10 mL), *t*Bu-protected bis-DOTA-OPE **8** (96 mg, 0.058 mmol, 83%) was obtained after column chromatography (SiO_2, 90:10 to 80:20 CH_2Cl_2/MeOH). ^{1}H NMR ($CDCl_3$, 300 MHz): $\delta = 11.49$ (s, 2H), 7.97 (d, $J = 8.5$ Hz, 4H), 7.34 (d, $J = 8.5$ Hz, 4H), 7.01 (s, 2H), 4.19 (t, $J = 5.0$ Hz, 4H), 3.91 (t, $J = 5.0$ Hz, 4H), 3.83–3.78 (m, 4H), 3.75 (s, 4H), 3.55–3.50 (m, 4H), 3.34 (s, 6H), 3.30–1.85 (m, 44H), 1.48 (s, 18H), 1.43 ppm (s, 36H); ^{13}C NMR ($CDCl_3$, 75 MHz): $\delta = 172.34$ (C_q), 171.6 (C_q), 153.6 (C_q), 140.1 (C_q), 131.8 (CH), 120.2 (CH), 117.6 (C_q), 114.5 (C_q), 95.9 (C_q), 84.7 (C_q), 82.4 (C_q), 82.2 (C_q), 72.2 (CH_2), 71.2 (CH_2), 69.9 (CH_2), 69.9 (CH_2), 59.1 (CH_3), 57.0 (CH_2), 55.9 (CH_2), 55.8 (CH_2), 51.3 (CH_2), 28.2 (CH_3), 28.1 ppm (CH_3); HRMS (ESI): *m/z* calcd for $C_{88}H_{136}N_{10}NaO_{20}^+$ $[M+Na]^+$: 1675.9825; found: 1675.9832.

2-Phenylpropan-2-yl 2-Bromoacetate (10)

Bromoacetic acid (10.0 g, 72 mmol, 1.0 equiv) and **9** (14.8 g, 109 mmol, 1.5 equiv) were dissolved in CH_2Cl_2 (100 mL). DMAP (880 mg, 7.2 mmol, 0.1 equiv) was added and the resulting mixture was cooled to 0 °C. DCC (15.2 g, 74 mmol, 1.03 equiv) was added portionwise and the resulting suspension was allowed to warm to RT for 3 h, filtered, and washed with CH_2Cl_2. The filtrate was washed with a 0.5 M aqueous solution of HCl (2×) and a saturated aqueous solution of $NaHCO_3$ (1×). The organic layer was dried over Na_2SO_4, filtered, and concentrated. Column chromatography (SiO_2, 95:5 cyclohexane/EtOAc) afforded **10** (10.82 g, 42.1 mmol, 58%) as a yellow oil. ^{1}H NMR ($CDCl_3$, 300 MHz): $\delta = 7.47$–7.24 (m, 5H), 3.80 (s, 2H), 1.84 ppm (s, 6H); ^{13}C NMR ($CDCl_3$, 100 MHz): $\delta = 165.1$ (C_q), 144.6 (C_q), 128.1 (CH), 127.0 (CH), 123.9 (CH), 83.4 (C_q), 28.0 (CH_3), 27.0 ppm (CH_2); HRMS (ESI): *m/z* calcd for $C_{11}H_{13}BrNaO_2^+$ $[M+Na]^+$: 278.9991; found: 278.9992.

Tris(2-phenylpropan-2-yl) 2,2′,2″-(1,4,7,10-Tetraazacyclododecane-1,4,7-triyl)triacetate (tri-Pp-DO3A 11)

Cyclen (2.41 g, 14 mmol, 1.0 equiv) was dissolved in MeCN (150 mL). The resulting solution was cooled to 0 °C and $NaHCO_3$ (3.53 g, 42 mmol, 3.0 equiv) was added. Compound **10** (10.8 g, 42 mmol, 3.0 equiv) dissolved in MeCN (40 mL) was added dropwise (≈30 min). The resulting suspension was allowed to warm to RT for 15 h and concentrated. CH_2Cl_2 was added and the mixture was washed with H_2O (1×) and a saturated aqueous solution of NaCl (1×). The organic layer was dried over Na_2SO_4, filtered, and concentrated. Column chromatography (SiO_2, 98:2 to 95:5 CH_2Cl_2/MeOH) afforded **11** (2.21 g, 3.15 mmol, 24%) as a light brown foam. ^{1}H NMR ($CDCl_3$, 300 MHz): $\delta = 9.82$ (s, 1H), 7.37–7.20 (m, 15H), 3.40–3.35 (m, 4H), 3.31 (s, 2H), 3.06–2.97 (m, 4H), 2.85–2.72 (m, 12H), 1.78 (s, 12H), 1.77 ppm (s, 6H); ^{13}C NMR ($CDCl_3$, 100 MHz): $\delta = 170.3$ (C_q), 169.3 (C_q), 145.4 (C_q), 145.2 (C_q), 128.5 (CH), 127.5 (CH), 127.4 (CH), 124.4 (CH), 124.4 (CH), 82.9 (C_q), 82.8 (C_q), 57.9 (CH_2), 52.1 (CH_2), 51.8 (CH_2), 49.7 (CH_2), 49.3 (CH_2), 47.3 (CH_2), 28.8 (CH_3), 28.8 ppm (CH_3); HRMS (ESI): *m/z* calcd for $C_{41}H_{57}N_4O_6^+$ $[M+H]^+$, $C_{41}H_{56}N_4NaO_6^+$ $[M+Na]^+$: 701.4273, 723.4092; found: 701.4315, 723.4096.

Pp-Protected Bis-DOTA-OPE (12)

By using general procedure A with **7** (71 mg, 0.09 mmol), **11** (161 mg, 0.23 mmol), and K_2CO_3 (124 mg, 0.9 mmol) in dry MeCN (8 mL), Pp-protected bis-DOTA-OPE **12** (99 mg, 0.049 mmol, 54%) was obtained after column chromatography (SiO_2, 95:5 to 85:15 CH_2Cl_2/MeOH). ^{1}H NMR ($CDCl_3$, 300 MHz): $\delta = 10.95$ (s, 2H), 7.91 (d, $J = 8.4$ Hz, 4H), 7.39 (d, $J = 8.4$ Hz, 4H), 7.34–7.08 (m, 30H), 7.04 (s, 2H), 4.21 (t, $J = 4.9$ Hz, 4H), 3.92 (t, $J = 4.9$ Hz, 4H), 3.84–3.76 (m, 4H), 3.56–3.49 (m, 4H), 3.34 (s, 6H), 3.25–1.95 (m, 44H), 1.62 ppm (s, 36H); ^{13}C NMR ($CDCl_3$, 100 MHz): $\delta = 171.6$ (C_q), 171.0 (C_q), 153.6 (C_q), 145.7 (C_q), 140.1 (C_q), 131.8 (CH), 128.4 (CH), 127.2 (CH), 124.2 (CH), 124.1 (CH), 120.1 (CH), 117.6 (CH), 117.4 (C_q), 114.5 (C_q), 95.9 (C_q), 84.8 (C_q), 83.4 (C_q), 83.3 (C_q), 72.2 (CH_2), 71.2 (CH_2), 69.9 (CH_2), 59.1 (CH_3), 56.6 (CH_2), 55.8 (CH_2), 55.7 (CH_2), 54–50.5 (CH_2, broad cluster), 50–47.5 (CH_2, broad cluster), 33–24 ppm (CH_3, broad cluster); HRMS (ESI): *m/z* calcd for $C_{118}H_{148}N_{10}Na_2O_{20}^{2+}/2$ $[M+2Na]^{2+}$, $C_{118}H_{149}N_{10}NaO_{20}^{2+}/2$ $[M+H+Na]^{2+}$: 1035.5328, 1025.0435; found: 1035.5329, 1025.0453.

Bis-DOTA-OPE (13)

Pp-protected bis-DOTA-OPE **12** was dissolved in a mixture of TFA/TIS/CH_2Cl_2 (2:2:96, 10 mg mL^{-1}). The resulting solution was stirred at RT for 4 h and concentrated. MeOH was added and the product was precipitated by slow addition of Et_2O, filtered, and dried. The

crude product was purified by preparative HPLC (30 to 50% MeCN) to afford bis-DOTA-OPE **13** as a yellow solid. HPLC: 5.02 min (5 to 100% MeCN in 10 min, >98%); MALDI-TOF MS (HCCA): *m/z* calcd for $C_{64}H_{89}N_{10}O_{20}^+$ $[M+H]^+$: 1317.62; found: 1317.43.

$MnDOTA_2OPE$

The Mn^{II} complex of bis-DOTA-OPE (**13**) was generated in situ for mass spectrometry analysis by the addition of $Mn(ClO_4)_2$ (2.0 equiv) to a buffered solution (HEPES 100 mM, pH 7.5) of **13**. MALDI-TOF MS (HCCA): *m/z* (%): 1423.46 (100) [Bis-DOTA-OPE−3H+2Mn]$^+$.

4-[(Trimethylsilyl)ethynyl]benzaldehyde (15)

Compound **14** (10.0 g, 54.05 mmol, 1.0 equiv) was dissolved in dry THF (40 mL) and dry triethylamine (20 mL). $[Pd(PPh_3)_3Cl_2]$ (380 mg, 0.541 mmol, 0.01 equiv) and CuI (103.3 mg, 0.541 mmol, 0.01 equiv) were added, and argon was bubbled for 15 min. TMSA (9.2 mL, 64.86 mmol, 1.2 equiv) was added dropwise and the resulting mixture was heated at reflux for 24 h and then cooled to RT. CH_2Cl_2 (200 mL) was added, the organic layer was recovered and washed with H_2O (1×), a 10% aqueous solution of HCl (1×), and H_2O (1×); dried over Na_2SO_4; filtered; and concentrated. Column chromatography (SiO_2, 100:0 to 90:10 cyclohexane/EtOAc) afforded **15** (9.31 g, 46.02 mmol, 85%) as a yellow solid. ^{1}H NMR ($CDCl_3$, 300 MHz): δ = 9.99 (s, 1H), 7.81 (d, 2H, J = 8.3 Hz), 7.60 (d, 2H, J = 8.3 Hz), 0.27 ppm (s, 9H); ^{13}C NMR ($CDCl_3$, 75 MHz): δ = 191.5 (CH), 135.7 (C_q), 132.6 (CH), 129.6 (CH), 129.5 (C_q), 104.0 (C_q), 99.2 (C_q), 0.1 ppm (CH_3); HRMS (ESI): *m/z* calcd for $C_{12}H_{15}OSi^+$ $[M+H]^+$, $C_{12}H_{14}NaOSi^+$ $[M+Na]^+$: 203.0887, 225.0706; found: 203.0886, 225.0668.

4-Ethynylbenzaldehyde (16)

Compound **15** (9.31 g, 46.02 mmol, 1.0 equiv) was dissolved in MeOH (450 mL). K_2CO_3 (4.77 g, 34.5 mmol, 0.75 equiv) was added and the resulting suspension was stirred at RT for 30 min. A saturated aqueous solution of NH_4Cl was added and the mixture was extracted with CH_2Cl_2 (3×). The combined organic layers were washed with H_2O (1×), dried over Na_2SO_4, filtered, and concentrated. Column chromatography (SiO_2, 100:0 to 90:10 cyclohexane/EtOAc) afforded **16** (5.87 g, 45.12 mmol, 98%) as a brown solid. ^{1}H NMR ($CDCl_3$, 300 MHz): δ = 10.02 (s, 1H), 7.87–7.81 (m, 2H), 7.67–7.60 (m, 2H), 3.29 ppm (s, 1H); ^{13}C NMR ($CDCl_3$, 75 MHz): δ = 191.5 (CH), 136.1 (C_q), 132.9 (CH), 129.6 (CH), 128.5 (C_q), 82.8 (C_q), 81.2 ppm (CH); HRMS (APCI): *m/z* calcd for $C_6H_7O_9^+$ $[M+H]^+$: 131.0491; found: 131.0493.

4,4′-({2,5-Bis[2-(2-methoxyethoxy)ethoxy]-1,4-phenylene}bis(ethyne-2,1-diyl))dibenzaldehyde (OPE-diCHO 17)

Compounds **4** (639 mg, 1.15 mmol, 1.0 equiv) and **16** (300 mg, 2.31 mmol, 2.0 equiv) were dissolved in dry THF (5 mL) and dry triethylamine (5 mL). Argon was bubbled for 15 min and then $[Pd(PPh_3)_2Cl_2]$ (81 mg, 0.115 mmol, 0.1 equiv) and CuI (44 mg, 0.23 mmol, 0.2 equiv) were added. The resulting suspension was stirred for 24 h at RT; a saturated aqueous solution of NH_4Cl was added and the mixture was extracted with CH_2Cl_2 (3×). The combined organic layers were dried over Na_2SO_4, filtered, and concentrated. Column chromatography (SiO_2, 80:20 to 0:100 cyclohexane/EtOAc) afforded OPE-diCHO **17** (528 mg, 0.925 mmol, 80%) as an orange solid. ^{1}H NMR ($CDCl_3$, 300 MHz): δ = 10.03 (s, 2H), 7.91–7.84 (m, 4H), 7.72–7.64 (m, 4H), 7.08 (s, 2H), 4.27- 4.21 (m, 4H), 3.98–3.92 (m, 4H), 3.83–3.77 (m, 4H), 3.58–3.53 (m, 4H), 3.37 ppm (s, 6H); ^{13}C NMR ($CDCl_3$, 75 MHz): δ = 191.4 (CH), 153.9 (C_q), 135.6 (C_q), 132.2 (CH), 129.7 (CH), 129.6 (C_q), 117.5 (CH), 114.3 (C_q), 94.5 (C_q), 89.9 (C_q), 72.1 (CH_2), 71.2 (CH_2), 69.9 (CH_2), 69.7 (CH_2), 59.2 ppm (CH_3); HRMS (ESI): *m/z* calcd for $C_{34}H_{35}O_8^+$ $[M+H]^+$, $C_{34}H_{34}NaO_8^+$ $[M+Na]^+$: 571.2326, 593.2146; found: 571.2315, 593.2134.

4,4′-({2,5-Bis[2-(2-methoxyethoxy)ethoxy]-1,4-phenylene}bis(ethyne-2,1-diyl))dibenzoic acid (OPE-diCO_2H 18)

OPE-diCHO **17** (1.5 g, 2.63 mmol, 1.0 equiv) was suspended in dry DMF (65 mL). $KHSO_5{\cdot}KHSO_4{\cdot}K_2SO_4$ (Oxone®; 3.23 g, 5.26 mmol, 2.0 equiv) was added and the resulting suspension was stirred at RT for 24 h. H_2O was added and the resulting precipitate was filtered and dried to afford OPE-diCO_2H **18** (1.294 g, 2.15 mmol, 82%) as a yellow solid. ^{1}H NMR ([D$_6$]DMSO, 300 MHz): δ = 13.13 (s, 2H), 8.03–7.94 (m, 4H), 7.68–7.60 (m, 4H), 7.27 (s, 2H), 4.20 (t, J = 4.5 Hz, 4H), 3.80 (t, J = 4.5 Hz, 4H), 3.71–3.64 (m, 4H), 3.48–3.41 (m, 4H), 3.21 ppm (s, 6H); ^{13}C NMR ([D$_6$]DMSO, 75 MHz): δ = 166.7 (C_q), 153.2 (C_q), 131.4 (CH), 130.6 (C_q), 129.6 (CH), 126.8 (C_q), 116.9 (CH), 113.1 (C_q), 94.3 (C_q), 88.8 (C_q), 71.4 (CH_2), 70.1 (CH_2), 69.1 (CH_2), 69.0 (CH_2), 58.1 ppm (CH_3); HRMS (ESI): *m/z* calcd for $C_{34}H_{33}O_{10}^-$ $[M-H]^-$, $C_{34}H_{32}O_{10}^{2-}/2$ $[M-2H]^{2-}$: 601.2079, 300.1003; found: 601.2076, 300.1022.

Bis-TEMPO-OPE (19)

OPE-diCO_2H **18** (57 mg, 0.094 mmol, 1.0 equiv) and 4-NH_2-TEMPO (40 mg, 0.234 mmol, 2.5 equiv) were dissolved in dry DMF (2 mL). The resulting solution was cooled to 0 °C, HOBt·H_2O (43 mg, 0.282 mmol, 3.0 equiv) and DCC (58 mg, 0.282 mmol, 3 equiv) were added, and the resulting mixture was stirred at RT for 24 h. H_2O was added and the mixture was extracted with CH_2Cl_2 (3×). The combined organic layers were dried over Na_2SO_4, filtered, and concentrated. Column chromatography (SiO_2, 30:70 to 20:80 cyclohexane/EtOAc) afforded bis-TEMPO-OPE **19** (79 mg, 0.087 mmol, 93%) as an orange solid. R_f (SiO_2): 0.39 (100% EtOAc); ^{1}H NMR ($CDCl_3$, 300 MHz; all signals broadened and some obscured due to paramagnetism): δ = 8.05–7.53 (m, 8H), 7.09 (s, 2H), 4.25 (br s, 4H), 3.96 (br s, 4H), 3.82 (br s, 4H), 3.57 (br s, 4H), 3.39 (s, 6H), 2.12–0.79 ppm (m, 32H); HPLC: 6.92 min (40 to 100% MeCN in 10 min, 95%); HRMS (ESI): *m/z* calcd for $C_{52}H_{69}N_4O_{10}^{2+}$ $[M+H]^{2+}$, $C_{52}H_{68}N_4NaO_{10}^{2+}$ $[M+Na]^{2+}$: 909.5008, 931.4828; found: 909.4968, 931.4793.

X-ray Crystallography

XRD data for compound **17** was collected by using a Kappa X8 APEX II Bruker diffractometer with graphite-monochromated MoKα radiation (λ = 0.71073 Å). XRD data for compound **19** was collected by using a Kappa VENTURE PHOTON 100 Bruker diffractometer with IμS microfocus graphite-monochromated MoKα radiation (λ = 0.71073 Å). Crystals were mounted on a CryoLoop (Hampton Research) with Paratone-N (Hampton Research) as a cryoprotectant and then flash frozen in a nitrogen gas stream at 100 K. The temperature of the crystal was maintained at the selected value (100 K) by means of a 700 series Cryostream cooling device to within an accuracy of ±1 K. The data were corrected for Lorentz polarization and absorption effects. The structures were solved by direct methods by using SIR-97[82] and refined against F^2 by full-matrix least-squares techniques by using SHELXL-2013[83] with anisotropic displacement parameters for all non-hydrogen atoms. All

calculations were performed by using the crystal structure crystallographic software package WINGX.[84]

The crystal data collection and refinement parameters are given in Table S1 in the Supporting Information.

The experimental data indicated positional static disorder of toluene of compound **19** (on inversion center). In the figures, the disordered toluene molecule is omitted for clarity.

CCDC 1431929-1431930 contains the supplementary crystallographic data for this paper. These data can be obtained free of charge from The Cambridge Crystallographic Data Centre.

EPR Measurements

W-band PELDOR measurements were performed on a Bruker Elexsys II 680 EPR spectrometer equipped with a Bruker "power upgrade 2" and an Oxford Instruments CF935 flow cryostat. For $MnDOTA_2OPE$ all experiments were performed at a sample temperature of 10 K. Spin-echo-detected EPR spectra were taken by using a Hahn-echo sequence with $\pi/2$ and π pulse durations of 12 and 24 ns, an interpulse delay time of 2500 ns, a shot repetition time of 800 μs, and a sweep width of 1000 G. For PELDOR measurements, the four-pulse, dead-time-free sequence[11,12] was used and the difference between the pump and detection frequencies was +70 MHz. The pump pulse duration was 24 ns and the duration of the $\pi/2$ and π detection pulses was 12 and 24 ns. The initial interpulse delay (between detection $\pi/2$ and π pulses) was 544 ns and the dipolar evolution window was 2226 ns. A four-step phase cycle procedure was used. The shot repetition time was 800 μs with 100 shots per point and the number of scans was 156, which equated to an accumulation time of 1.5 h. For bis-TEMPO-OPE **19**, all experiments were performed at a sample temperature of 40 K. Spin-echo-detected EPR spectra were recorded by using a Hahn-echo sequence with $\pi/2$ and π pulse durations of 40 and 80 ns, an interpulse delay time of 1500 ns, a shot repetition time of 5 ms, and a sweep width of 400 G. For PELDOR measurements, the difference between the pump and detection frequencies was +70 MHz. The pump pulse duration was 80 ns and the duration of the $\pi/2$ and π detection pulses was 40 and 80 ns. The initial interpulse delay (between detection $\pi/2$ and π pulses) was 400 ns and the dipolar evolution window was 1500 μs. A four-step phase cycle procedure was used. The shot repetition time was 5 ms with 100 shots per point and the number of scans was 25. The total accumulation time of the 3 PELDOR time traces was about 4.5 h.

Q-band PELDOR measurements were performed on a Bruker Elexsys E580 spectrometer, equipped with a 10 W AMP-Q-Band solid-state amplifier. A more detailed description of the Q-band setup is given elsewhere.[85] All experiments were performed with the ER5107D2 probe at a sample temperature of 50 K. Spin-echo-detected EPR spectra were recorded by using a Hahn-echo sequence with $\pi/2$ and π pulse durations of 16 and 32 ns, an interpulse delay time of 130 ns, a shot repetition time of 3 ms, and a sweep width of 140 G. For PELDOR measurements, the difference between the pump and detection frequencies was +50 or −50 MHz. The pump pulse duration was 22 ns and the duration of all detection pulses were 32 ns. The initial interpulse delay (between detection $\pi/2$ and π pulses) was 332 ns and the dipolar evolution window was 5 μs. To suppress deuterium modulations in the PELDOR time traces, the initial interpulse delay time was incremented by 16 ns over 8 steps (tau averaging procedure). A two-step phase cycle procedure was used. The shot repetition time was 3 ms with 20 shots per point and the number of scans was varied from 8 to 19, depending on the spectral position at which the PELDOR time traces were recorded. The accumulation time of the full set of PELDOR time traces was about 5 h.

Rotamer Analysis

Starting from the X-ray crystal structures of MnH_2DOTA[80] and the OPE spacer of bis-TEMPO-OPE **19**, a model of $MnDOTA_2OPE$ was constructed in Spartan 14 (Wavefunction Inc.) For the MnDOTA arm that linked each spin label to the OPE, dihedral angles for the C–N bond (χ_1 and $\chi_{1'}$) and C–C bond (χ_2 and $\chi_{2'}$) were restricted to staggered conformations. The values of χ_3 and $\chi_{3'}$ were fixed because previous studies showed that the acetanilide unit was overwhelmingly in the *trans* configuration.[86] Relative to each other, the two spin-labeled ends were allowed to fully rotate around the molecular axis in 30° intervals. From these parameters, all 972 possible rotamers were systematically generated and molecular mechanic force field calculations were performed on each to identify and eliminate those with clashes. For the remainder, 406 rotamers, each was given the same probability and the Mn–Mn distances were compiled in 0.1 nm boxes. Similarly, starting from the X-ray structure of bis-TEMPO-OPE, the dihedral angles of the rotatable C–N bonds were restricted to staggered conformations and, relative to each other, the two spin-labeled ends were allowed to fully rotate around the molecular axis in 30° intervals. From these parameters, all 108 possible clash-free rotamers were systematically generated. Each was given the same probability and the distances between the middle points of the N–O bonds were compiled in 0.1 nm boxes.

Acknowledgements

This work was financially supported by ANR MnHFPELDOR, ANR-DFG Chemistry 2011-INTB-1010-01 (P.D.-D. PhD studentship and H.Y.V.C. post-doctoral fellowship) and DFG (GZ: PR 294/14-1, D.A. PhD studentship). We thank the French Infrastructure for Integrated Structural Biology (FRISBI) for financial support. The W-band spectrometer was funded by the Région Ile-de-France "Sesame" program, the CEA, and CNRS. We thank UPS, IUF, Région Ile de France SESAME program 2012 no. 12018501, LabEx CHARM3AT, and CNRS for X-ray crystallography. We are very grateful to Dr. Sun Un (I2BC-CEA Saclay), Prof. Thomas Prisner (Goethe Universität Frankfurt), Dr. Burkhard Endeward (Goethe Universität Frankfurt), and Dr. Alice Bowen (Goethe Universität Frankfurt) for spectrometer access and fruitful and constructive discussions.

Keywords: EPR spectroscopy · gadolinium · manganese · pulsed electron–electron double resonance · spin labels

[1] J. R. Lakowicz, *Principles of Fluorescent Spectroscopy*, 3rd ed., Springer, New York, **2006**.
[2] M. Hong, K. Schmidt-Rohr, *Acc. Chem. Res.* **2013**, *46*, 2154–2163.
[3] H. D. T. Mertens, D. I. Svergun, *J. Struct. Biol.* **2010**, *172*, 128–141.
[4] O. Duss, M. Yulikov, G. Jeschke, F. H.-T. Allain, *Nat. Commun.* **2014**, *5*, 3669.
[5] R. R. Ernst, *Angew. Chem. Int. Ed. Engl.* **1992**, *31*, 805–823; *Angew. Chem.* **1992**, *104*, 817–836.
[6] K. Wüthrich, *Nat. Struct. Biol.* **2001**, *8*, 923–925.
[7] O. Schiemann, T. F. Prisner, *Q. Rev. Biophys.* **2007**, *40*, 1–53.
[8] G. Jeschke, *Annu. Rev. Phys. Chem.* **2012**, *63*, 419–446.

[9] Y. D. Tsvetkov, A. D. Milov, A. G. Maryasov, *Russ. Chem. Rev.* **2008**, *77*, 487 – 520.
[10] A. D. Milov, A. B. Ponomarev, Y. D. Tsvetkov, *Chem. Phys. Lett.* **1984**, *110*, 67 – 72.
[11] R. E. Martin, M. Pannier, F. Diederich, V. Gramlich, M. Hubrich, H. W. Spiess, *Angew. Chem. Int. Ed.* **1998**, *37*, 2833 – 2837; *Angew. Chem.* **1998**, *110*, 2993 – 2998.
[12] M. Pannier, S. Veit, A. Godt, G. Jeschke, H. W. Spiess, *J. Magn. Reson.* **2000**, *142*, 331 – 340.
[13] A. D. Milov, K. M. Salikhov, M. D. Shchirov, *Sov. Phys. Solid State* **1981**, *23*, 565 – 569; *Fiz. Tverd. Tela Leningrad* **1981**, *23*, 975 – 982.
[14] W. L. Hubbell, A. Gross, R. Langen, M. A. Lietzow, *Curr. Opin. Struct. Biol.* **1998**, *8*, 649 – 656.
[15] W. L. Hubbell, C. J. López, C. Altenbach, Z. Yang, *Curr. Opin. Struct. Biol.* **2013**, *23*, 725 – 733.
[16] Y. D. Tsvetkov, *J. Struct. Chem.* **2013**, *54*, 42 – 72.
[17] Y. Polyhach, E. Bordignon, R. Tschaggelar, S. Gandra, A. Godt, G. Jeschke, *Phys. Chem. Chem. Phys.* **2012**, *14*, 10762 – 10773.
[18] V. P. Denysenkov, T. F. Prisner, J. Stubbe, M. Bennati, *Proc. Natl. Acad. Sci. USA* **2006**, *103*, 13386 – 13390.
[19] Y. Polyhach, A. Godt, C. Bauer, G. Jeschke, *J. Magn. Reson.* **2007**, *185*, 118 – 129.
[20] O. Schiemann, P. Cekan, D. Margraf, T. F. Prisner, S. T. Sigurdsson, *Angew. Chem. Int. Ed.* **2009**, *48*, 3292 – 3295; *Angew. Chem.* **2009**, *121*, 3342 – 3345.
[21] A. M. Bowen, C. E. Tait, C. R. Timmel, J. R. Harmer, *Struct. Bonding (Berlin)* **2013**, *152*, 283 – 328.
[22] A. P. Jagtap, I. Krstic, N. C. Kunjir, R. Hänsel, T. F. Prisner, S. T. Sigurdsson, *Free Radical Res.* **2015**, *49*, 78 – 85.
[23] D. Goldfarb, *Struct. Bonding (Berlin)* **2014**, *152*, 164 – 203.
[24] D. Goldfarb, *Phys. Chem. Chem. Phys.* **2014**, *16*, 9685 – 9699.
[25] A. Feintuch, G. Otting, D. Goldfarb, *Methods Enzymol.* **2015**, *563*, 415 – 457.
[26] D. Banerjee, H. Yagi, T. Huber, G. Otting, D. Goldfarb, *J. Phys. Chem. Lett.* **2012**, *3*, 157 – 160.
[27] H. Y. V. Ching, P. Demay-Drouhard, H. C. Bertrand, C. Policar, L. C. Tabares, S. Un, *Phys. Chem. Chem. Phys.* **2015**, *17*, 23368 – 23377.
[28] A. Martorana, Y. Yan, Y. Zhao, Q.-F. Li, X.-C. Su, D. Goldfarb, *Dalton Trans.* **2015**, *44*, 20812 – 20816.
[29] A. M. Raitsimring, C. Gunanathan, A. Potapov, I. Efremenko, J. M. L. Martin, D. Milstein, D. Goldfarb, *J. Am. Chem. Soc.* **2007**, *129*, 14138 – 14139.
[30] A. Dalaloyan, M. Qi, S. Ruthstein, S. Vega, A. Godt, A. Feintuch, D. Goldfarb, *Phys. Chem. Chem. Phys.* **2015**, *17*, 18464 – 18476.
[31] A. Potapov, Y. Song, T. J. Meade, D. Goldfarb, A. V. Astashkin, A. Raitsimring, *J. Magn. Reson.* **2010**, *205*, 38 – 49.
[32] A. Potapov, H. Yagi, T. Huber, S. Jergic, N. E. Dixon, G. Otting, D. Goldfarb, *J. Am. Chem. Soc.* **2010**, *132*, 9040 – 9048.
[33] D. T. Edwards, T. Huber, S. Hussain, K. M. Stone, M. Kinnebrew, I. Kaminker, E. Matalon, M. S. Sherwin, D. Goldfarb, S. Han, *Structure* **2014**, *22*, 1677 – 1686.
[34] H. Yagi, D. Banerjee, B. Graham, T. Huber, D. Goldfarb, G. Otting, *J. Am. Chem. Soc.* **2011**, *133*, 10418 – 10421.
[35] E. H. Abdelkader, A. Feintuch, X. Yao, L. A. Adams, L. Aurelio, B. Graham, D. Goldfarb, G. Otting, *Chem. Commun.* **2015**, *51*, 15898 – 15901.
[36] M. Gordon-Grossman, I. Kaminker, Y. Gofman, Y. Shai, D. Goldfarb, *Phys. Chem. Chem. Phys.* **2011**, *13*, 10771 – 10780.
[37] E. Matalon, T. Huber, G. Hagelueken, B. Graham, V. Frydman, A. Feintuch, G. Otting, D. Goldfarb, *Angew. Chem. Int. Ed.* **2013**, *52*, 11831 – 11834; *Angew. Chem.* **2013**, *125*, 12047 – 12050.
[38] Y. Song, T. J. Meade, A. V. Astashkin, E. L. Klein, J. H. Enemark, A. Raitsimring, *J. Magn. Reson.* **2011**, *210*, 59 – 68.
[39] A. Martorana, G. Bellapadrona, A. Feintuch, M. Elbaum, E. Di Gregorio, S. Aime, D. Goldfarb, *J. Am. Chem. Soc.* **2014**, *136*, 13458 – 13465.
[40] M. Qi, A. Groß, G. Jeschke, A. Godt, M. Drescher, *J. Am. Chem. Soc.* **2014**, *136*, 15366 – 15378.
[41] F. Wojciechowski, A. Groß, I. T. Holder, L. Knörr, M. Drescher, J. S. Hartig, *Chem. Commun.* **2015**, *51*, 13850 – 13853.
[42] L. C. Tabares, J. Gätjens, C. Hureau, M. R. Burrell, L. Bowater, V. L. Pecoraro, S. Bornemann, S. Un, *J. Phys. Chem. B* **2009**, *113*, 9016 – 9025.
[43] C. W. Bock, A. K. Katz, G. D. Markham, J. P. Glusker, *J. Am. Chem. Soc.* **1999**, *121*, 7360 – 7372.
[44] G. Jeschke, V. Chechik, P. Ionita, A. Godt, H. Zimmermann, J. Banham, C. R. Timmel, D. Hilger, H. Jung, *Appl. Magn. Reson.* **2006**, *30*, 473 – 498.
[45] N. C. Kunjir, G. W. Reginsson, O. Schiemann, S. T. Sigurdsson, *Phys. Chem. Chem. Phys.* **2013**, *15*, 19673 – 19685.
[46] E. Brücher, G. Tircsó, Z. Baranyai, Z. Kovács, A. D. Sherry in *The Chemistry of Contrast Agents in Medical Magnetic Resonance Imaging*, 2nd ed. (Eds.: A. Merbach, L. Helm, E. Tóth), Wiley, Hoboken, **2013**.
[47] J. M. Tour, *Chem. Rev.* **1996**, *96*, 537 – 554.
[48] N. M. Jenny, M. Mayor, T. R. Eaton, *Eur. J. Org. Chem.* **2011**, 4965 – 4983.
[49] A. Godt, M. Schulte, H. Zimmermann, G. Jeschke, *Angew. Chem. Int. Ed.* **2006**, *45*, 7560 – 7564; *Angew. Chem.* **2006**, *118*, 7722 – 7726.
[50] G. Jeschke, M. Sajid, M. Schulte, N. Ramezanian, A. Volkov, H. Zimmermann, A. Godt, *J. Am. Chem. Soc.* **2010**, *132*, 10107 – 10117.
[51] A. Weber, O. Schiemann, B. Bode, T. F. Prisner, *J. Magn. Reson.* **2002**, *157*, 277 – 285.
[52] G. Jeschke, H. Zimmermann, A. Godt, *J. Magn. Reson.* **2006**, *180*, 137 – 146.
[53] G. W. Reginsson, N. C. Kunjir, S. T. Sigurdsson, O. Schiemann, *Chem. Eur. J.* **2012**, *18*, 13580 – 13584.
[54] D. Akhmetzyanov, P. Schöps, A. Marko, N. C. Kunjir, S. T. Sigurdsson, T. F. Prisner, *Phys. Chem. Chem. Phys.* **2015**, *17*, 24446 – 24451.
[55] Y. Zhao, Y. Shirai, A. D. Slepkov, L. Cheng, L. B. Alemany, T. Sasaki, F. A. Hegmann, J. M. Tour, *Chem. Eur. J.* **2005**, *11*, 3643 – 3658.
[56] H. Meier, D. Ickenroth, U. Stalmach, K. Koynov, A. Bahtiar, C. Bubeck, *Eur. J. Org. Chem.* **2001**, *2001*, 4431 – 4443.
[57] B. Sontag, M. Rüth, P. Spiteller, N. Arnold, W. Steglich, M. Reichert, G. Bringmann, *Eur. J. Org. Chem.* **2006**, *2006*, 1023 – 1033.
[58] N. Saini, R. Varshney, A. K. Tiwari, A. Kaul, M. Allard, M. P. S. Ishar, A. K. Mishra, *Dalton Trans.* **2013**, *42*, 4994 – 5003.
[59] M. Lee, M. S. Tremblay, S. Jockusch, N. J. Turro, D. Sames, *Org. Lett.* **2011**, *13*, 2802 – 2805.
[60] Y. O. Fung, W. Wu, C. T. Yeung, H. K. Kong, K. K. C. Wong, W. S. Lo, G. L. Law, K. L. Wong, C. K. Lau, C. S. Lee, W. T. Wong, *Inorg. Chem.* **2011**, *50*, 5517 – 5525.
[61] A. J. Wilkinson, D. Maffeo, A. Beeby, C. E. Foster, J. A. G. Williams, *Inorg. Chem.* **2007**, *46*, 9438 – 9449.
[62] J. Luo, W.-S. Li, P. Xu, L.-Y. Zhang, Z.-N. Chen, *Inorg. Chem.* **2012**, *51*, 9508 – 9516.
[63] J. Laakso, G. A. Rosser, C. Szíjjártó, A. Beeby, K. E. Borbas, *Inorg. Chem.* **2012**, *51*, 10366 – 10374.
[64] R. F. H. Viguier, A. N. Hulme, *J. Am. Chem. Soc.* **2006**, *128*, 11370 – 11371.
[65] M. Jamous, U. Haberkorn, W. Mier, *Molecules* **2013**, *18*, 3379 – 3409.
[66] W. Mier, K. A. N. Graham, Q. Wang, S. Krämer, J. Hoffend, M. Eisenhut, U. Haberkorn, *Tetrahedron Lett.* **2004**, *45*, 5453 – 5455.
[67] M. Jamous, U. Haberkorn, W. Mier, *Tetrahedron Lett.* **2012**, *53*, 6810 – 6814.
[68] C. Yue, J. Thierry, P. Potier, *Tetrahedron Lett.* **1993**, *34*, 323 – 326.
[69] Z. Wang, S. Yuan, A. Mason, B. Reprogle, D. J. Liu, L. Yu, *Macromolecules* **2012**, *45*, 7413 – 7419.
[70] S. Valera, J. E. Taylor, D. S. B. Daniels, D. M. Dawson, K. S. Athukorala Arachchige, S. E. Ashbrook, A. M. Z. Slawin, B. E. Bode, *J. Org. Chem.* **2014**, *79*, 8313 – 8323.
[71] C. F. Macrae, P. R. Edgington, P. McCabe, E. Pidcock, G. P. Shields, R. Taylor, M. Towler, J. van de Streek, *J. Appl. Crystallogr.* **2006**, *39*, 453 – 457.
[72] A. Marko, D. Margraf, H. Yu, Y. Mu, G. Stock, T. Prisner, *J. Chem. Phys.* **2009**, *130*, 064102.
[73] A. Marko, V. Denysenkov, D. Margraf, P. Cekan, O. Schiemann, S. T. Sigurdsson, T. F. Prisner, *J. Am. Chem. Soc.* **2011**, *133*, 13375 – 13379.
[74] A. Marko, T. F. Prisner, *Phys. Chem. Chem. Phys.* **2013**, *15*, 619 – 627.
[75] D. Abdullin, G. Hagelueken, R. I. Hunter, G. M. Smith, O. Schiemann, *Mol. Phys.* **2015**, *113*, 544 – 560.
[76] T. F. Prisner, A. Marko, S. T. Sigurdsson, *J. Magn. Reson.* **2015**, *252*, 187 – 198.
[77] G. Hagelueken, R. Ward, J. H. Naismith, O. Schiemann, *Appl. Magn. Reson.* **2012**, *42*, 377 – 391.
[78] G. Hagelueken, D. Abdullin, R. Ward, O. Schiemann, *Mol. Phys.* **2013**, *111*, 2757 – 2766.

[79] E. H. Abdelkader, M. D. Lee, A. Feintuch, M. Ramirez Cohen, J. D. Swarbrick, G. Otting, B. Graham, D. Goldfarb, *J. Phys. Chem. Lett.* **2015**, *6*, 5016 – 5021.
[80] S. Wang, T. D. Westmoreland, *Inorg. Chem.* **2009**, *48*, 719 – 727.
[81] G. Schwarz, L. Mueller, S. Beck, M. W. Linscheid, *J. Anal. At. Spectrom.* **2014**, *29*, 221 – 233.
[82] A. Altomare, M. C. Burla, M. Camalli, G. L. Cascarano, C. Giacovazzo, A. Guagliardi, A. G. Moliterni, G. Polidori, R. Spagna, *J. Appl. Crystallogr.* **1999**, *32*, 115 – 119.
[83] G. M. Sheldrick, *Acta Crystallogr. Sect. A* **2008**, *64*, 112 – 122.
[84] L. J. Farrugia, *J. Appl. Crystallogr.* **1999**, *32*, 837 – 838.
[85] P. Schöps, P. E. Spindler, A. Marko, T. F. Prisner, *J. Magn. Reson.* **2015**, *250*, 55 – 62.
[86] H. Kessler, A. Rikler, *Liebigs Ann. Chem.* **1967**, *708*, 57 – 68.

Manuscript received: March 7, 2016
Accepted Article published: March 27, 2016
Final Article published: April 18, 2016

CHEMPHYSCHEM

Supporting Information

A Bis-Manganese(II)–DOTA Complex for Pulsed Dipolar Spectroscopy**

Paul Demay-Drouhard,[a] H. Y. Vincent Ching,[b] Dmitry Akhmetzyanov,[c] Régis Guillot,[d] Leandro C. Tabares,[b] Hélène C. Bertrand,*[a] and Clotilde Policar*[a]

cphc_201600234_sm_miscellaneous_information.pdf

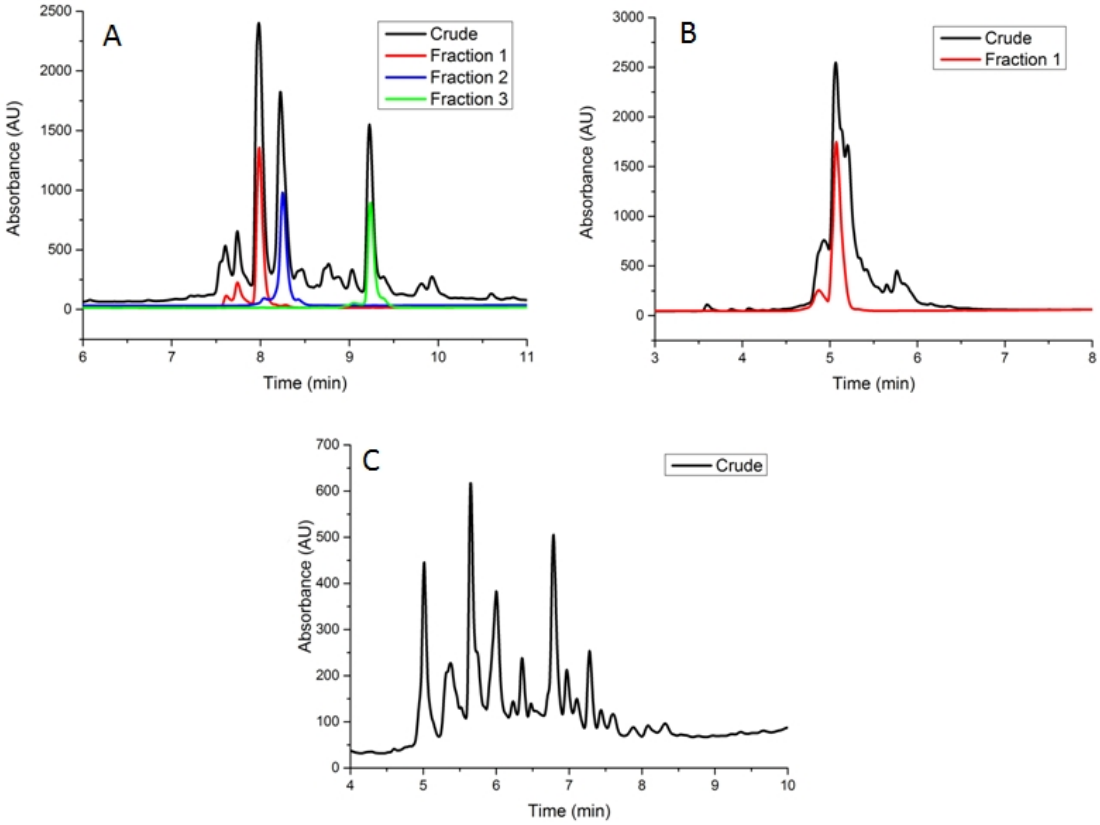

Figure S1. HPLC traces of the crude and purified products after deprotection of the protected bis-DOTA platform **8** in different conditions. A: 1:1 TFA/DCM, 24 h, 0 °C to rt. B: Aq. 6M HCl, 24 h, 0 °C to rt. C: HCO2H, 12 h, 60 °C. Gradients: 0 to 50% MeCN (A), 5 to 100% MeCN (B), 0 to 70% MeCN (C) in 10 min.

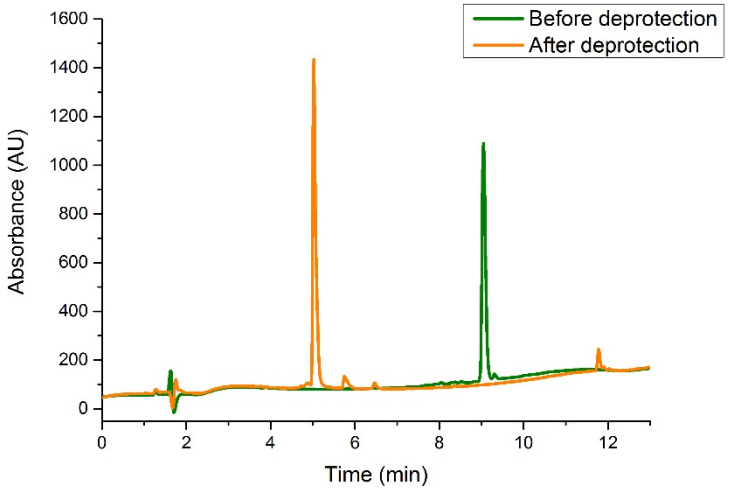

Figure S2. HPLC traces of pure Pp-protected bis-DOTA-OPE **12** (green) and of the crude mixture after completion of the deprotection (orange) containing ~95% of bis-DOTA-OPE **13**. Gradient: 5 to 100% MeCN in 10 min.

Table S1. Crystallographic data and structure refinement details for compounds.

Compound	**17**	**19**
CCDC number	1431929	1431930
Empirical Formula	C_{34} H_{34} O_8	C_{52} H_{68} N_4 O_{10}, C_7
M_r	570.61	993.17
Crystal size, mm^3	0.14 x 0.11 x 0.07	0.17 x 0.13 x 0.11
Crystal system	triclinic	monoclinic
Space group	*P -1*	*P* $2_1/n$
a, Å	8.0566(3)	12.3531(8)
b, Å	10.0504(4)	14.0252(10)
c, Å	10.2709(4)	16.2862(11)
α, °	61.8080(10)	90
β, °	74.3230(10)	100.597(2)
γ, °	81.4180(10)	90
Cell volume, $Å^3$	705.50(5)	2773.5(3)
Z	1	2
T, K	100(1)	100(1)
F_{000}	2696	1060
μ, mm^{-1}	0.095	0.081
θ range, °	2.300 – 36.031	2.219 – 30.626
Reflection collected	14 062	118 880
Reflections unique	5 697	8 521
R_{int}	0.0231	0.0276
GOF	1.026	1.081
Refl. obs. (I>2σ(I))	4 481	5 820
Parameters / restraints	191 / 0	348 / 0
wR_2 (all data)	0.1463	0.1809
R value (I>2σ(I))	0.0491	0.0977
Largest diff. peak and hole (e-.$Å^{-3}$)	-0.225 ; 1.024	-0.547 ; 0.594

Q-band PELDOR on bis-nitroxide 19

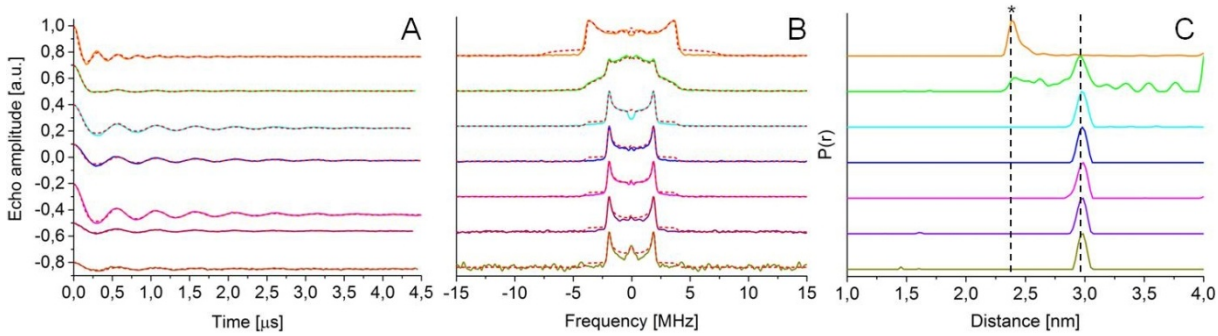

Figure S3. Q-band PELDOR measurements on bis-TEMPO-OPE **19** at seven pump-probe resonance positions indicated schematically in different colors: A) Background-corrected PELDOR time traces (solid lines) and their fits based on Tikhonov regularization analysis (dashed red lines). B) Frequency-domain spectra corresponding to the background-corrected PELDOR time traces (solid lines) and their fits based on Tikhonov regularization analysis (dashed red lines). C) Distance distribution profiles obtained by Tikhonov regularization. The peak at 2.39 nm (indicated with an asterisk) corresponding to the orange distance profile and multiple features corresponding to the green distance profile arise from orientation selection effect. Dashed black lines are guides for the eye.

W-band PELDOR on bis-nitroxide 19

At W-band frequencies the *g*-anisotropy of the nitroxide radical was resolved. PELDOR measurements were taken at the three field positions that roughly correspond to the g_{xx}, g_{yy} and g_{zz} regions of the spectrum (Figure S4). Characteristic orientation selection effects were clearly observed in the PELDOR time traces and corresponding frequency-domain spectra. For the spectral position roughly corresponding to the g_{xx} region, components at 1.7 and 3.5 MHz were observed, while for g_{yy} and g_{zz} regions only a 1.7 MHz splitting was observed.

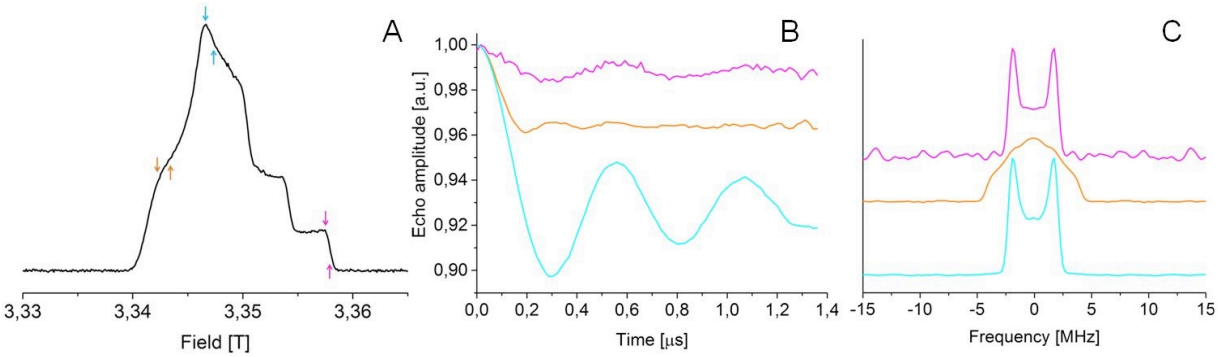

Figure S4. W-band PELDOR measurement on bis-TEMPO-OPE **19** (100 µM) in 1:1 v/v toluene-d_8/$CDCl_3$ at 40 K. A) Hahn echo-detected field swept EPR spectrum with the different pump and probe positions indicated schematically in different colors by the down and up arrows, respectively. B)

Background-corrected PELDOR time traces recorded at different positions of the EPR spectrum, with colors corresponding to the arrows depicted in panel B. C) Corresponding frequency-domain spectra.

PCCP

PAPER

View Article Online
View Journal | View Issue

Cite this: *Phys. Chem. Chem. Phys.*, 2015, **17**, 24446

Pulsed EPR dipolar spectroscopy at Q- and G-band on a trityl biradical†

D. Akhmetzyanov,‡[a] P. Schöps,‡[a] A. Marko,[a] N. C. Kunjir,[b] S. Th. Sigurdsson*[b] and T. F. Prisner*[a]

Received 24th June 2015,
Accepted 24th August 2015

DOI: 10.1039/c5cp03671b

www.rsc.org/pccp

Pulsed electron paramagnetic resonance (EPR) spectroscopy is a valuable technique for the precise determination of distances between paramagnetic spin labels that are covalently attached to macromolecules. Nitroxides have commonly been utilised as paramagnetic tags for biomolecules, but trityl radicals have recently been developed as alternative spin labels. Trityls exhibit longer electron spin relaxation times and higher stability than nitroxides under *in vivo* conditions. So far, trityl radicals have only been used in pulsed EPR dipolar spectroscopy (PDS) at X-band (9.5 GHz), K_u-band (17.2 GHz) and Q-band (34 GHz) frequencies. In this study we investigated a trityl biradical by PDS at Q-band (34 GHz) and G-band (180 GHz) frequencies. Due to the small spectral width of the trityl (30 MHz) at Q-band frequencies, single frequency PDS techniques, like double-quantum coherence (DQC) and single frequency technique for refocusing dipolar couplings (SIFTER), work very efficiently. Hence, Q-band DQC and SIFTER experiments were performed and the results were compared; yielding a signal to noise ratio for SIFTER four times higher than that for DQC. At G-band frequencies the resolved axially symmetric ***g***-tensor anisotropy of the trityl exhibited a spectral width of 130 MHz. Thus, pulsed electron electron double resonance (PELDOR/DEER) obtained at different pump–probe positions across the spectrum was used to reveal distances. Such a multi-frequency approach should also be applicable to determine structural information on biological macromolecules tagged with trityl spin labels.

Introduction

Triarylmethyl based radicals (TAM or trityl)[1] have attracted considerable attention in electron paramagnetic resonance (EPR) applications, particularly in EPR imaging[2] and pulsed EPR dipolar spectroscopy (PDS) as spin probes.[3–7] These types of carbon centred radicals have several unique properties, such as a narrow spectral width, long electron spin relaxation times (even at ambient temperatures)[8–10] as well as high stability toward redox processes.[2] These features make the utilisation of trityl radicals in EPR useful, especially for PDS applications under physiological[3,4] and *in vivo* conditions.

PDS enables the determination of nanometer-scale distances between two specifically attached spin probes through the magnitude of their magnetic dipole–dipole coupling. Hence, important information about structure, conformational changes and folding of large biomolecules can be obtained.[11,12] The choice of PDS technique should depend on the type of paramagnetic spin probes that are being used. In the case of paramagnetic centres which have EPR spectra that are significantly broader than the excitation bandwidth of the available microwave pulses, pulsed electron electron double resonance (PELDOR,[13,14] also called DEER[15,16]) is very robust, efficient and hence the most widely used PDS technique. Most commonly, a pair of nitroxide radicals, incorporated into the molecule of interest by site-directed spin labelling, has been used for these type of experiments.[17–21] On the other hand, if the excitation bandwidth of the available microwave pulses is large enough to excite the whole EPR spectrum, *e.g.* in case of trityls, the usage of single frequency techniques like double-quantum coherence (DQC),[22] or the single frequency technique for refocusing dipolar couplings (SIFTER)[23] is preferred due to higher sensitivity. Achieving this condition for nitroxides is non-trivial, due to their broad EPR spectra, although this limitation has been overcome using broadband shaped microwave pulses in a SIFTER experiment at X-band frequencies[24] and very short rectangular pulses for DQC at X- and K_u-band frequencies.[22,25]

[a] *Goethe-University Frankfurt am Main, Institute of Physical and Theoretical Chemistry and Center for Biomolecular Magnetic Resonance, Max von Laue Str. 7, 60438 Frankfurt am Main, Germany. E-mail: prisner@chemie.uni-frankfurt.de*
[b] *University of Iceland, Department of Chemistry, Science Institute, Dunhaga 3, 107 Reykjavik, Iceland. E-mail: snorrisi@hi.is*

† Electronic supplementary information (ESI) available: Chemical structure of monoradical **2**. EPR spectrum of monoradical **2** and comparison with the spectrum of biradical **1**. Q-band SIFTER and DQC raw time traces of biradical **1** with the background functions. G-band PELDOR raw time traces of biradical **1** with the background functions. Simulating the PELDOR time traces using PELDOR database approach. See DOI: 10.1039/c5cp03671b

‡ Authors contributed equally to the work.

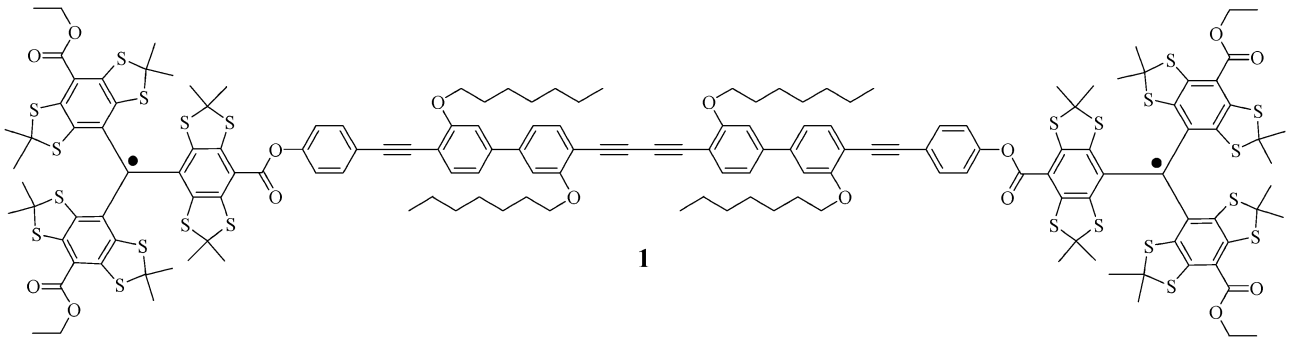

1

Fig. 1 Chemical structure of biradical **1**.

In contrast to nitroxides, trityl radicals have a significantly narrower EPR spectrum and even rectangular pulses with moderate power at X-[5,6] and Q-band frequencies can be used to excite their whole EPR spectrum. However, the width of the trityl EPR spectrum exceeds the excitation bandwidth of the available microwave pulses considerably at higher frequencies. This prefers PELDOR experiments with trityl radicals to be performed. As the EPR spectral width of trityls is significantly narrower compared to nitroxides, the sensitivity of comparable PELDOR experiments is greater for trityls.

Despite the aforementioned advantages of trityl-based radicals, only a few examples for PDS applications on biological systems[3,4,7] as well as methodological PDS studies using X-band frequencies[5,6] have been presented thus far. In the current study we investigate and describe PDS experiments on a trityl biradical **1** (Fig. 1) at Q (33.8 GHz) and G (180 GHz) – band frequencies. The results of SIFTER and DQC experiments at Q-band frequencies were compared. In addition, PELDOR experiments on biradical **1** were performed at G-band frequencies. The PELDOR time traces obtained at different pump–probe positions across the EPR spectrum exhibited orientation selection. Averaging two G-band time traces allowed Tikhonov regularisation[26] to be used to extract a distance distribution. Similar distance distributions were also obtained from the Q-band SIFTER and DQC experiments.

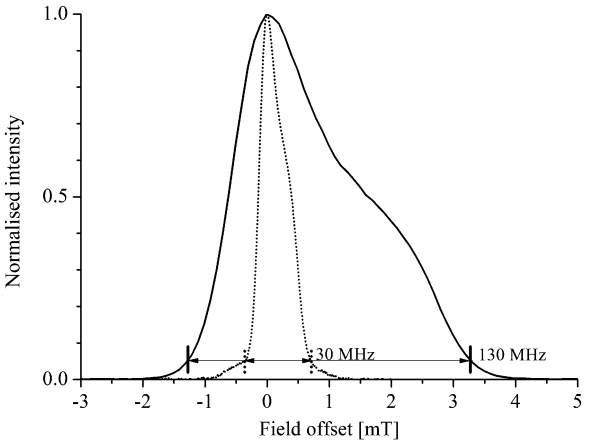

Fig. 2 Field-swept Hahn echo-detected EPR spectrum of biradical **1** obtained at Q-band frequencies at a temperature of 50 K (dotted line) and at G-band frequencies at a temperature of 25 K (solid line). The axis of abscissas corresponds to the field offset from the maximum absorption position in the spectrum. The parallel bars indicate the width of the EPR spectra.

Results and discussion

Trityl biradical 1

The trityl biradical **1**, possessing a distance between the unpaired electrons of about 4.89 nm, was synthesised according to the previously published protocol.[6]

EPR spectroscopy

Field-swept Hahn echo-detected EPR spectra of biradical 1 at Q- and G-band frequencies

The field-swept Hahn echo-detected EPR spectra of biradical **1** obtained at Q- and G-band frequencies are shown in Fig. 2. The EPR spectrum obtained at Q-band frequencies reveals a relatively narrow line with a spectral width of about 30 MHz, defined by the signal at greater than 5% echo intensity. This neglects the two weak ^{13}C satellites (including these satellites the width of the EPR spectrum is about 55 MHz). The EPR spectrum obtained at G-band frequencies shows a spectral width of about 130 MHz. The more pronounced asymmetry of the G-band EPR spectrum is due to the partially resolved ***g***-tensor anisotropy. The fact that the width of the trityl EPR spectrum scales with the microwave frequency indicates that the primary contribution to the width is the ***g***-tensor anisotropy.

The G-band field-swept Hahn echo-detected EPR spectrum of the trityl monoradical **2** (Fig. S1, ESI†) also revealed a ***g***-tensor anisotropy but with a slightly narrower spectral width of approximately 120 MHz (Fig. S2 and S3, ESI†). It is worth noting, that small changes in the chemical structure of the trityl moiety can lead to a significant change in the width of the EPR spectra and the principal values of the ***g***-tensor.[9,10,27–29]

SIFTER and DQC at Q-band frequencies

The background-corrected time traces obtained with SIFTER (Fig. 3 left) and DQC (Fig. 3 right) on biradical **1** show clear dipolar oscillations. This indicates that the biradical possess a relatively rigid structure. The raw experimental SIFTER and DQC time traces are presented in Fig. S4 (ESI†) with the corresponding background functions.

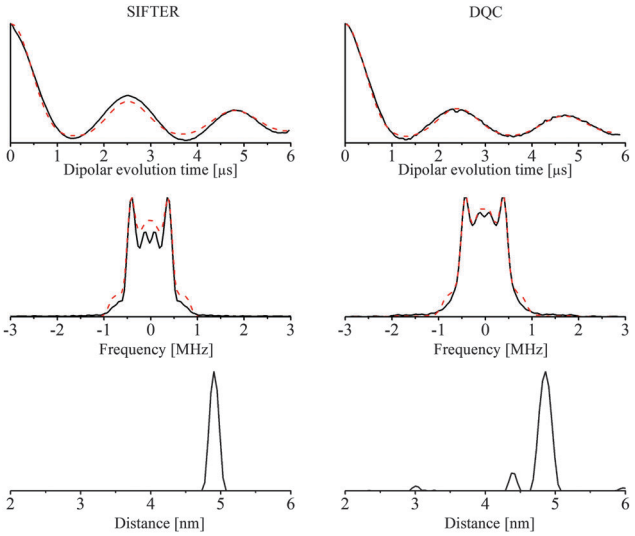

Fig. 3 Top. Background-corrected SIFTER (left) and DQC (right) time traces obtained at Q-band frequencies and a temperature of 50 K. The solid lines are experimental time traces and the dashed lines are the fits obtained by Tikhonov regularisation with the regularisation parameter of 0.1 using DeerAnalysis software.[26] The axes of ordinates are not shown, since the background-correction procedure was different for the experiments so that the *y*-axes-scaling is arbitrary in this term. For more detailed information the reader is referred to Fig. S4 (ESI†). Middle. Fourier transformation of the background-corrected SIFTER (left) and DQC (right) time traces. The solid lines are the transformation of the experimental time traces and the dashed lines are transformations of the fitted time traces. All Pake patterns are normalised. Bottom. Distance distribution functions obtained from SIFTER (left side) and DQC (right sight) time traces with Tikhonov regularisation fit.

The dipole–dipole coupling is given by the formula:[15]

$$\omega_{AB} = \frac{\mu_B{}^2 g_A g_B}{\hbar}\frac{1}{R^3}\left(3\cos^2(\theta) - 1\right) = D \cdot \left(3\cos^2(\theta) - 1\right) \quad (1)$$

where μ_B is the Bohr magneton, $\hbar$ is the Planck constant divided by 2π, g_A and g_B are the effective values of the ***g***-tensor corresponding to the excited A and B spins, R is the electron–electron distance and θ is the angle between the vector ***R*** and the external magnetic field $\boldsymbol{B}_0$. The long period of the dipolar oscillation implies a relatively large distance between the intramolecular spins.[5,6] Thus, the major part of the intramolecular spins A and B in the ensemble have a resonance frequencies difference $|\omega_A - \omega_B|$, which exceeds the absolute value of the dipole–dipole coupling $|\omega_{AB}|$, as shown already by DQC of biradical **1** at X-band frequencies.[5,6] Therefore, the pseudo-secular (flip-flop) term of the dipolar coupling Hamiltonian can be neglected in the analysis of the dipolar evolution functions.[5,6] Orientation selection is not expected to be present in the dipolar evolution functions, as the excitation bandwidth of the 22 ns π-pulse (*ca.* 37 MHz) approximately corresponds to the width of the trityl EPR spectrum (*ca.* 30 MHz), leading to almost full excitation of the spectrum. Hence, all orientations of the vector ***R*** with respect to the vector $\boldsymbol{B}_0$ contribute to the dipolar evolution function with corresponding statistical weights of $\sin(\theta)$. This leads to the well-known Pake pattern in frequency domain with singularities at $\pm D$ and $\pm 2D$. It should be noted that the Pake pattern, corresponding to the DQC time trace, showed somewhat reduced intensity at $\pm 2D$. This is attributed to imperfections in defining the background function, as described below.

Conventional Tikhonov regularisation analysis, with the complete Pake pattern as a kernel function, can be used to analyse the dipolar evolution functions.[26] The mean distances obtained from the distance distribution functions for SIFTER and DQC are 4.9 and 4.86 nm, respectively, (Fig. 3 bottom) which are in good agreement with the data obtained with DQC and PELDOR at X-band.[5,6] Very similar distance distributions were obtained by both SIFTER and DQC. The slight deviations of the mean distances as well as the widths of the distance distribution functions (Fig. 3 bottom) are most probably the result of ambiguities in the definition of the background functions. In the case of single frequency PDS techniques, these functions contain both an interspin and a relaxation-induced component. Thus far, no complete theoretical description exists for these background functions. Hence, the background-correction procedures (described in the Experimental section) were performed similarly to other published work.[23,25]

The raw experimental data for SIFTER and DQC yield different modulation depths. However, due to the different background-correction procedures, it is not possible to compare the modulation depths directly. In order to account for the different modulation depths in the analysis of the signal-to-noise ratios (SNR), it is necessary to scale the raw data to the same range. Thus, the SNR was determined from the standard deviation between the scaled raw experimental time trace and a ninth-order polynomial fit. It was found that, the SNR for SIFTER is approximately four times larger than that for DQC.

PELDOR at G-band frequencies

The EPR spectrum of biradical **1** has a width of 130 MHz at G-band frequencies, this prefers PELDOR experiments to be performed. These experiments have higher sensitivity than corresponding experiments performed on nitroxides. The G-band field-swept Hahn echo-detected EPR spectrum of biradical **1** (Fig. 2), including the pump–probe positions used for the PELDOR experiments, is depicted in Fig. 4.

The background-divided G-band PELDOR time traces obtained at pump–probe positions A, B and C (Fig. 4) show that position A yielded more pronounced high-frequency components, compared to the other two positions. The frequency domain spectrum, obtained by Fourier transformation of the background-divided PELDOR time trace at position A, has the highest intensity at $\pm 2D$ (the shoulders at about ± 1 MHz). At this position the detection pulses excite primarily the perpendicular components of the ***g***-tensor ($g_\perp$) of the trityl. Conversely at positions B and C, the detection pulses excite predominantly the parallel components of the ***g***-tensor ($g_{||}$) of the trityl (Fig. 4 upper right). The frequency domain spectra of the time traces B and C show almost vanishingly small intensity at $\pm 2D$ in comparison to the intensity at $\pm D$. These variations of the PELDOR time traces (and corresponding frequency domain patterns) with the resonance positions of the pump and probe pulses indicate the occurrence of orientation selection effects. These effects occur

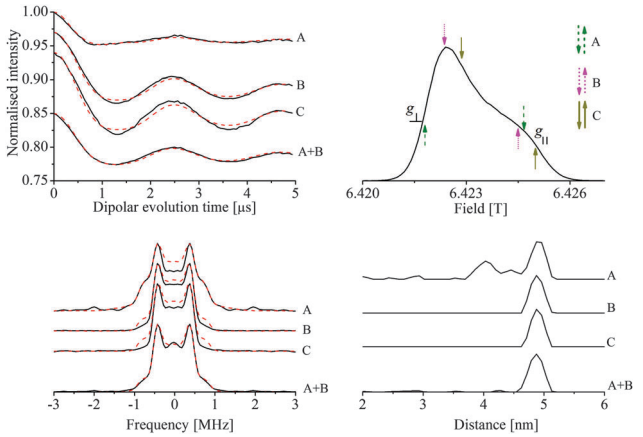

Fig. 4 Left-side (top) – Background-divided PELDOR time traces of biradical **1** obtained at G-band frequencies. Solid lines are experimental data, dashed lines are the fits obtained with Tikhonov regularisation analysis (with a regularisation parameter of 1), as implemented in DeerAnalysis.[26] Positions A, B and C correspond to the positions in the G-band spectrum depicted on the right side. The offset between the probe and pump frequencies is 80 MHz for position A and 60 MHz for positions B and C. The traces obtained at different positions are normalised and vertically shifted for better visual comparison. The raw experimental time traces with the corresponding background functions are shown in Fig. S5 (ESI†). Right-side (top) – Field-swept Hahn echo-detected EPR spectrum obtained at G-band frequencies and a temperature of 25 K depicted with pump–probe positions for PELDOR experiments. Up arrows indicate the detection positions and down arrows indicate the pump positions. Left side (bottom) – Fourier transformation of the background-divided PELDOR time traces. Solid lines are Fourier transformation of the experimental and dashed of the fitted time traces that are obtained with Tikhonov regularisation. The Fourier transformed time traces were normalised and vertically shifted for better visual representation. Positions A, B and C correspond to the positions in the G-band spectrum. Right side (bottom) – Distance distribution functions obtained with Tikhonov regularisation analysis. The distance distribution functions were normalised and vertically shifted for better visual comparison.

due to the partially resolved anisotropy of the ***g***-tensor and excitation of relatively small fractions of the spectrum with the available pulse strengths at G-band frequencies. However, the ***g***-tensor anisotropy is relatively small and combined with weakly defined relative orientations of the trityl moieties (induced by the rotation and bending of the linker segments[6]). This makes the orientation selection effects less pronounced than those seen for tyrosyl[30,31] and nitroxide[32] spin labels rigidly attached to biomolecules. For this reason the weak spectral anisotropy of the PELDOR time traces does not allow us to obtain unambiguous orientational information about the structure of this molecule. The fitting of the PELDOR time traces with a PELDOR database approach[33–36] is given in the ESI.†

The orientation selection effects observed in the three time traces can be understood in terms of the molecular structure and ***g***-tensor orientation. The ***g***-tensor in trityl is orientated with the $g_{||}$ axis perpendicular to the mean linker axis of the molecule. Therefore, when the $g_{||}$ part of the spectrum is sampled (traces B and C), mainly perpendicular orientations of the dipolar coupling tensor are excited. For this reason the PELDOR time traces obtained at positions B and C lack the parallel orientations of the dipolar coupling tensor at $\pm 2D$. However, in the PELDOR time trace obtained at position A (Fig. 4), in which the $g_{\perp}$ portion of the spectrum is detected, the parallel orientations of the dipolar coupling tensor are excited, giving rise to signal in the frequency pattern at $\pm 2D$. Addition of the time trace at position A to the time trace at position B reduces orientation selection effects further by providing a more uniform excitation of all vector ***R*** orientations with respect to magnetic field vector $\boldsymbol{B}_0$. The frequency domain spectrum of the sum of time traces A and B resembles a full Pake pattern (Fig. 4 bottom left).

Tikhonov analysis of the time traces was performed to generate distance distributions. Analysis of the summed (A + B) time trace yields a distance distribution in good agreement with those obtained from the SIFTER and DQC experiments (and also literature[6]), with a mean distance of 4.88 nm. The distance distribution function at position A reveals a mean distance at about 4.92 nm and additional features probably due to orientation selection effects. However, the distance distribution functions, obtained by Tikhonov regularisation analysis of the time traces at position B and C, reveal only insignificant difference with respect to that obtained by Tikhonov analysis of the A + B time trace (Fig. 4).

Experimental

The concentrations of biradical **1** and monoradical **2** were 200 and 400 μM, respectively, in toluene-d_8 solvent.

Q-band pulsed EPR experiments

Pulsed EPR experiments at Q-band frequencies were performed on a Bruker Elexsys E580 spectrometer, equipped with 10 W AMP-Q-Band solid state amplifier. A more detailed description of the Q-Band setup is given elsewhere.[24] All experiments were performed using the ER5107D2 probe at a temperature of 50 K. For the measurements the samples were transferred into 1 mm inner diameter quartz tubes. To avoid the formation of microcrystals the samples were rapidly frozen in liquid nitrogen before inserting them into the probe. With this setup a π pulse length of 22 ns could be achieved and was used for SIFTER and DQC. The applied SIFTER pulse sequence was $\pi/2–\tau_1–\pi–\tau_1–\pi/2–\tau_2–\pi–\tau_2$. Unwanted echoes were eliminated by performing a 16 step phase cycle.[23] For the SIFTER time trace a background function was determined by carrying out the experiment on monoradical **2**. The background-correction procedure was performed by a division of the experimental biradical **1** time trace by a Gaussian least-square fit to the monoradical **2** time trace, similarly as performed for SIFTER on nitroxides.[23] The DQC experiment was performed by using the six pulse sequence $\pi/2–\tau_1–\pi–\tau_1–\pi/2–\tau_3–\pi–\tau_3–\pi/2–\tau_2–\pi–\tau_2$ and a 64 step phase cycle.[22] τ_3 was kept constant at 35 ns. The background correction for the DQC time trace was performed by a subtraction of a baseline, obtained by an exponential fit function.[25] The raw DQC and SIFTER time traces are depicted in Fig. S4 (ESI†) with the corresponding background functions. For both, DQC and SIFTER experiments τ_1 and τ_2 were changed in 20 ns steps

with initial values of τ_1 = 120 ns and τ_2 = 6000 ns, the microwave frequency was set to the maximum absorption position in the spectrum, the shot repetition time was set to 5000 μs and the measured echo was integrated over 100 ns in 1 ns steps. To suppress deuterium modulations a tau averaging procedure of 8 measurements with steps of $\Delta\tau_1 = \Delta\tau_2$ = 16 ns was performed.

G-band pulsed EPR experiments

Pulsed EPR experiments at G-band frequencies were performed on a home built G-band EPR spectrometer[37,38] at a sample temperature of 25 K. The temperature of 25 K, rather than 50 K, was chosen for pulsed G-band experiments, as an increase of 15 percent in the transversal relaxation time (T_2) was observed at the lower temperature. For the measurements the samples were transferred into 0.4 mm inner diameter tubes. The field-swept Hahn echo-detected EPR spectrum was recorded with pulse lengths of 10 ns and 60 ns (a pulse length of 60 ns corresponds to the flip angle of π) for the first and second pulses, respectively. The length of the first pulse was reduced to 10 ns in order to avoid saturation of the spectrometer receiver by the large signal intensity. For this reason, the shot repetition time was also reduced to 15 ms. The interpulse delay time was set to 200 ns and the number of shots per point was 80. The raw PELDOR time traces are depicted in Fig. S5 (ESI†) with the corresponding exponential background functions. For the G-band PELDOR experiment obtained at position A, the detection pulse lengths were 27.5 ns and 52.5 ns, for the π/2 and π pulses, respectively, and 55 ns for the pump pulse. The initial π/2 and π pulse delay time was 250 ns and kept the same for all PELDOR experiments. The dipolar evolution time window was set to 6.4 μs and the pump–probe frequency offset to 80 MHz. The number of shots per point was 25 and kept the same for all PELDOR experiments; the shot repetition time was 25 ms and the number of scans 51. For the PELDOR experiment obtained at position B the detection pulse lengths were 30 ns and 55 ns, for the π/2 and π pulses, respectively and 50 ns for the pump pulse. The dipolar evolution time window was set to 6.2 μs and the pump–probe frequency offset to 60 MHz. The shot repetition time was 39 ms and the number of scans 55. For the PELDOR experiment obtained at position C the detection pulse lengths were 27.5 ns and 52.5 ns, for the π/2 and π pulses, respectively. The pump pulse length, the dipolar evolution time window and the pump–probe frequency offset were the same as in the case of position B. The shot repetition time was 25 ms and the number of scans 26. The microwave power for the PELDOR experiments was about 60 mW.

Conclusions

SIFTER and DQC experiments at Q-band frequencies and PELDOR experiments at G-band frequencies were performed on a trityl biradical with a known interspin distance of 4.89 nm.[5,6] The narrow spectral width of the trityl biradical of about 30 MHz at Q-band frequencies enabled almost complete excitation of the EPR spectrum with commercially available microwave components. Fulfilment of this condition is necessary for the optimal performance of single frequency dipolar spectroscopy techniques, like SIFTER and DQC. Both methods revealed a distance agreeing with the literature.[5,6] However, the signal-to-noise ratio achieved with SIFTER is about a factor of 4 higher compared to that achieved with DQC. At G-band frequencies the axially symmetric ***g***-tensor anisotropy of the trityl biradical was resolved, preferring the performance of PELDOR experiments. By using Tikhonov regularisation analysis[26] of the averaged PELDOR time trace, the distance that is in agreement with SIFTER and DQC at Q-band frequencies was obtained.

The multi-frequency approach presented here could be useful for biological applications using trityl spin tags on nucleic acids or proteins in cells under physiological conditions.

Acknowledgements

The authors acknowledge Dr Vasyl Denysenkov for the technical support with the G-band EPR spectrometer and Dr Alice Bowen for useful discussions and for proof reading the manuscript. This work is supported by SPP 1601 New Frontiers in Sensitivity for EPR Spectroscopy: from Biological Cells to Nano Materials from the German Research Society DFG, the Cluster of Excellence Frankfurt (CEF) Macromolecular Complexes and the Icelandic Research Fund (120001021), which are all gratefully acknowledged.

References

1 T. J. Reddy, T. Iwama, H. J. Halpern and V. H. Rawal, *J. Org. Chem.*, 2002, **67**, 4635.
2 J. H. Ardenkjær-Larsen, I. Laursen, I. Leunbach, G. Ehnholm, L.-G. Wistrand, J. S. Petersson and K. Golman, *J. Magn. Reson.*, 1998, **133**, 1.
3 G. Y. Shevelev, O. A. Krumkacheva, A. A. Lomzov, A. A. Kuzhelev, O. Y. Rogozhnikova, D. V. Trukhin, T. I. Troitskaya, V. M. Tormyshev, M. V. Fedin, D. V. Pyshnyi and E. G. Bagryanskaya, *J. Am. Chem. Soc.*, 2014, **136**, 9874.
4 Z. Yang, Y. Liu, P. Borbat, J. L. Zweier, J. H. Freed and W. L. Hubbell, *J. Am. Chem. Soc.*, 2012, **134**, 9950.
5 N. C. Kunjir, G. W. Reginsson, O. Schiemann and S. Th. Sigurdsson, *Phys. Chem. Chem. Phys.*, 2013, **15**, 19673.
6 G. W. Reginsson, N. C. Kunjir, S. Th. Sigurdsson and O. Schiemann, *Chem. – Eur. J.*, 2012, **18**, 13580.
7 G. Yu. Shevelev, O. A. Krumkacheva, A. A. Lomzov, A. A. Kuzhelev, D. V. Trukhin, O. Yu. Rogozhnikova, V. M. Tormyshev, D. V. Pyshnyi, M. V. Fedin and E. G. Bagryanskaya, *J. Phys. Chem. B*, 2015, DOI: 10.1021/acs.jpcb.5b03026.
8 R. Owenius, G. R. Eaton and S. S. Eaton, *J. Magn. Reson.*, 2005, **172**, 168.
9 A. J. Fielding, P. J. Carl, G. R. Eaton and S. S. Eaton, *Appl. Magn. Reson.*, 2005, **28**, 231.
10 L. Lumata, Z. Kovacs, A. D. Sherry, C. Malloy, S. Hill, J. van Tol, L. Yu, L. Song and M. E. Merritt, *Phys. Chem. Chem. Phys.*, 2013, **15**, 9800.
11 G. Jeschke, *Annu. Rev. Phys. Chem.*, 2012, **63**, 419.
12 O. Schiemann and T. Prisner, *Q. Rev. Biophys.*, 2007, **40**, 1.

13 A. D Milov, K. M. Salikhov and M. D. Shchirov, *Soviet Physics – Solid State*, 1981, **23**, 565.
14 A. D. Milov, A. B. Ponomarev and Y. D. Tsvetkov, *Chem. Phys. Lett.*, 1984, **110**, 67.
15 M. Pannier, S. Veit, A. Godt, G. Jeschke and H. W. Spiess, *J. Magn. Reson.*, 2000, **142**, 331.
16 R. G. Larsen and D. J. Singel, *J. Chem. Phys.*, 1993, **98**, 5134.
17 W. Hubbell, A. Gross, R. Langen and M. Lietzow, *Curr. Opin. Struct. Biol.*, 1998, **8**, 649.
18 I. Krstic, B. Endeward, D. Margraf, A. Marko and T. F. Prisner, *Top. Curr. Chem.*, 2012, **321**, 159.
19 S. Shelke and S. Sigurdsson, *Struct. Bonding*, 2013, **152**, 121.
20 W. Hubbel, C. Lopez, C. Altenbach and Z. Yang, *Curr. Opin. Struct. Biol.*, 2013, **23**, 725.
21 G. Fanucci and D. Cafiso, *Curr. Opin. Struct. Biol.*, 2006, **16**, 644.
22 P. P. Borbat and J. H. Freed, *Chem. Phys. Lett.*, 1999, **313**, 145.
23 G. Jeschke, M. Pannier, A. Godt and H. W. Spiess, *Chem. Phys. Lett.*, 2000, **331**, 243.
24 P. Schöps, P. E. Spindler, A. Marko and T. F. Prisner, *J. Magn. Reson.*, 2015, **250**, 55.
25 P. Borbat, H. Mchaourab and J. Freed, *J. Am. Chem. Soc.*, 2002, **124**, 5304.
26 G. Jeschke, V. Chechik, P. Ionita, A. Godt, H. Zimmermann, J. Banham, C. Timmel, D. Hilger and H. Jung, *Appl. Magn. Reson.*, 2006, **30**, 473.
27 D. Banerjee, J. C. Paniagua, V. Mugnaini, J. Veciana, A. Feintuch, M. Pons and D. Goldfarb, *Phys. Chem. Chem. Phys.*, 2011, **13**, 18626.
28 B. D. Armstrong, D. T. Edwards, R. J. Wylde, S. A. Walker and S. Han, *Phys. Chem. Chem. Phys.*, 2010, **12**, 5920.
29 J. H. Ardenkjær-Larsen, S. Macholl and H. Johannesson, *Appl. Magn. Reson.*, 2008, **34**, 509.
30 V. Denysenkov, T. Prisner, J. Stubbe and M. Bennati, *Proc. Natl. Acad. Sci. U. S. A.*, 2006, **103**, 13386.
31 V. P. Denysenkov, D. Biglino, W. Lubitz, T. F. Prisner and M. Bennati, *Angew. Chem., Int. Ed.*, 2008, **47**, 1224.
32 A. Marko, V. P. Denysenkov, D. Margraf, P. Cekan, O. Schiemann, S. T. Sigurdsson and T. F. Prisner, *J. Am. Chem. Soc.*, 2011, **133**, 13375.
33 A. Marko and T. F. Prisner, *Phys. Chem. Chem. Phys.*, 2013, **15**, 619.
34 T. F. Prisner, A. Marko and S. Th. Sigurdsson, *J. Magn. Reson.*, 2015, **252**, 187.
35 D. Abdullin, G. Hagelueken, R. I. Hunter, G. M. Smith and O. Schiemann, *Mol. Phys.*, 2015, **113**, 544.
36 C. Abe, D. Klose, F. Dietrich, W. H. Ziegler, Y. Polyhach, G. Jeschke and H.-J. Steinhoff, *J. Magn. Reson.*, 2012, **216**, 53.
37 M. Rohrer, O. Brügman, B. Kinzer and T. Prisner, *Appl. Magn. Reson.*, 2001, **21**, 257.
38 V. Denysenkov, T. Prisner, J. Stubbe and M. Bennati, *Appl. Magn. Reson.*, 2005, **29**, 375.

Pulsed EPR Dipolar Spectroscopy at Q- and G-band on a Trityl Biradical

Supplementary Information

D. Akhmetzyanov,‡[a] P. Schöps,‡[a] A. Marko,[a] N. C. Kunjir,[b] S. Th. Sigurdsson*[b] and T. F. Prisner*[a]

[a] Goethe-University Frankfurt am Main, Institute of Physical and Theoretical Chemistry and Center for Biomolecular Magnetic Resonance, Max von Laue Str. 7, 60438 Frankfurt am Main, Germany.
E-mail: prisner@chemie.uni-frankfurt.de
[b] University of Iceland, Department of Chemistry, Science Institute, Dunhaga 3, 107 Reykjavık, Iceland.
E-mail: snorrisi@hi.is
‡ Authors contributed equally to the work
* Corresponding authors

Table of contents

1. Chemical structure of trityl monoradical **2**

Chemical structure of trityl monoradical is presented in Fig. S1. Synthesis of the monoradical is described elsewhere.[1]

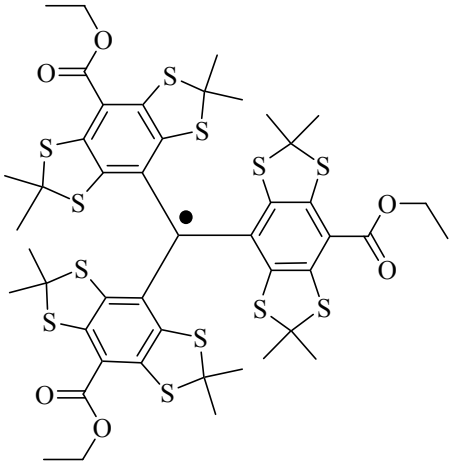

2

Fig. S1. Chemical structure of trityl monoradical **2**.

2. G-band EPR spectrum of monoradical **2**

The field-swept Hahn echo-detected G-band EPR spectrum of monoradical **2** and the simulated spectrum, obtained with EasySpin software,[S1] are depicted in Fig. S2.

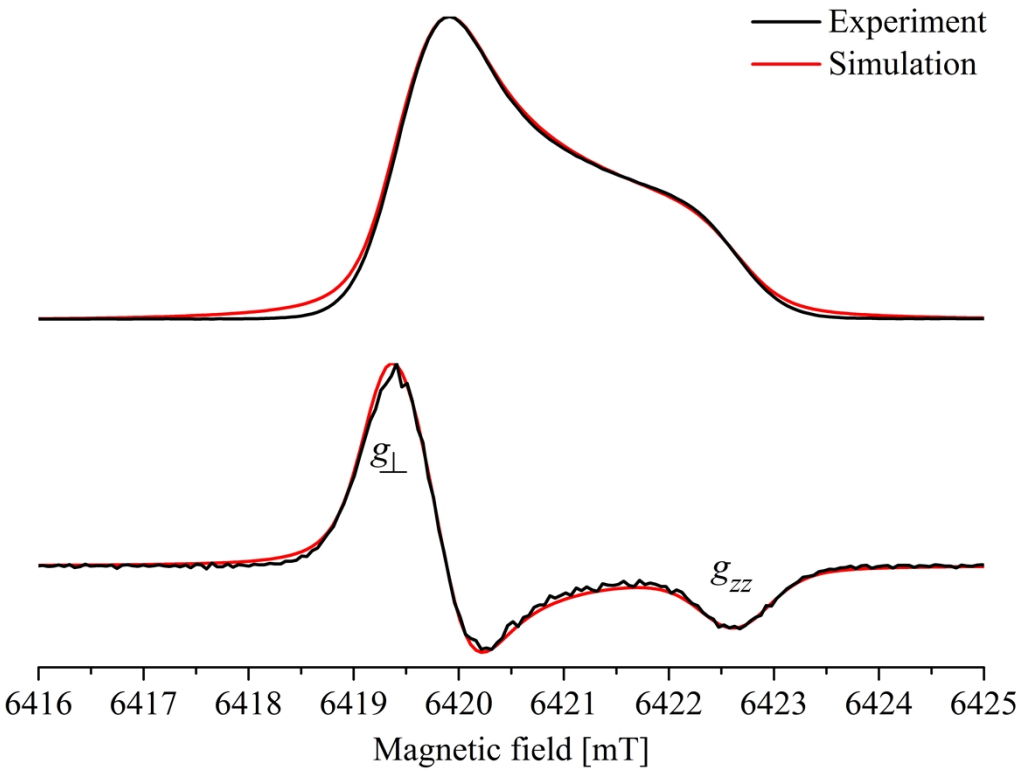

Fig. S2. **Top.** Field-swept Hahn echo-detected EPR spectrum obtained at G-band frequencies on monoradical **2** (black curve) with corresponding simulated spectrum (red curve) obtained with EasySpin. The temperature of the sample was 100 K. The concentration was 200 μM in toluene solvent. The field was calibrated with Mn^{2+} doped MgO standard sample.
Bottom. Numerical differentiation of the experimental (black curve) and simulated (red curve) EPR spectra.

Parameters used for the simulation are represented in Table S1.

Table S1. Parameters of the EasySpin simulation

g-values			lwpp, mT		HStrain, MHz			A*,MHz		
g_{xx}	g_{yy}	g_{zz}	Gauss	Lorentz	x	y	z	Axx	Ayy	Azz
2.0034(1)	2.0032(4)	2.0023(7)	0.2	0.2	10	12	16	20.6	20.6	160.1

*Principal values of the central ^{13}C hyperfine coupling tensor are obtained from another study.[S2]

3. Comparison of G-band EPR spectra of **1** and **2**

The field-swept Hahn echo-detected EPR spectra of trityl mono- and biradical obtained at G-band frequencies are depicted in Fig. S3.

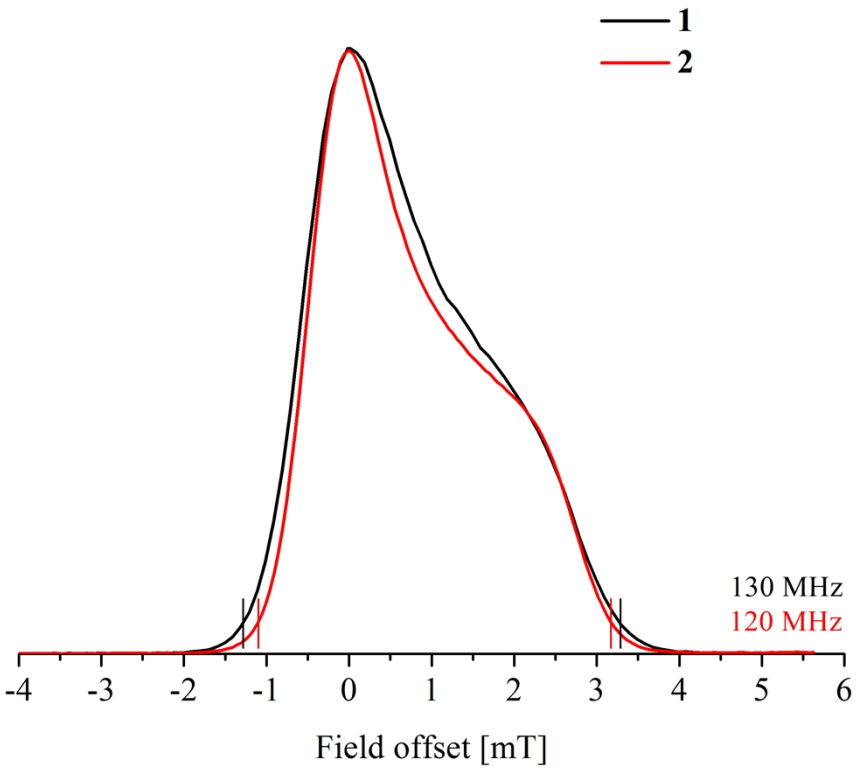

Fig. S3. Field-sweep Hahn echo-detected G-band EPR spectra of trityl mono- and biradical. The EPR spectrum of biradical **1** is obtained at 25 K with a concentration of 200 μM in toluene-d_8 solvent. The EPR spectrum of monoradical **2** is obtained at 100 K with a concentration of 200 μM in toluene solvent. The axis of abscissas represents the field offset from the maximum absorption position in the spectra. The field for the EPR spectrum of biradical **1** was not calibrated. The field for the EPR spectrum of monoradical **2** was calibrated with Mn^{2+} doped MgO standard sample. Parallel bars indicate the boundaries that define the width of the EPR spectra of the trityl mono- and biradical (5 % of echo intensity).

4. Raw Q-band SIFTER and DQC time traces with the corresponding background functions

The Q-band SIFTER and DQC raw time traces of biradical **1** with the corresponding background functions are depicted in Fig. S4.

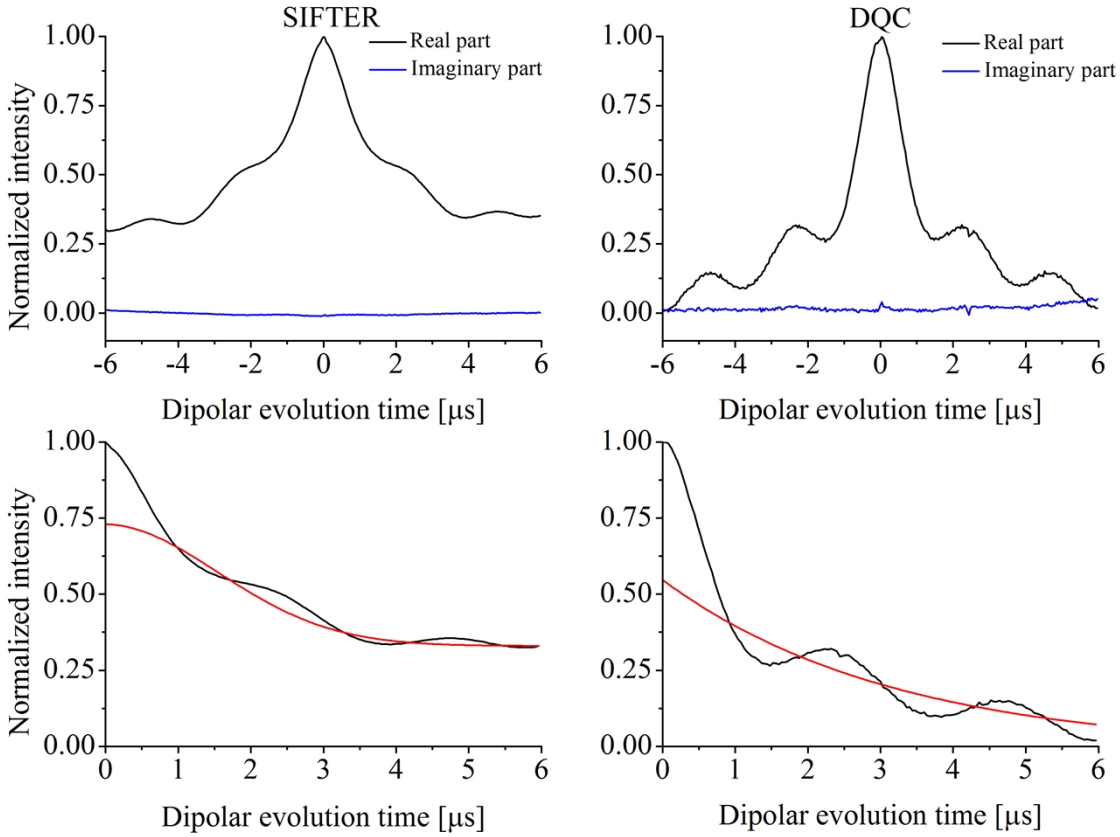

Fig. S4. **Top.** SIFTER (left) and DQC (right) raw experimental time traces obtained at Q-band frequencies at a temperature of 50 K.
Bottom. Black curves are the raw time traces obtained as a sum of the part of the time trace with the positive dipolar evolution time and the mirror symmetric part of the time trace with negative dipolar evolution time. Red curves are the background functions. For the SIFTER time trace the background function is obtained by a Gaussian fit of the SIFTER time trace of monoradical **2**. For the DQC time trace the background function is obtained by an exponential fit of the time trace using the EasySpin exponfit function.

5. G-band PELDOR experimental data and corresponding background functions

The experimental G-band PELDOR time traces obtained on biradical **1** are depicted in Fig. S5 with the corresponding exponential background functions.

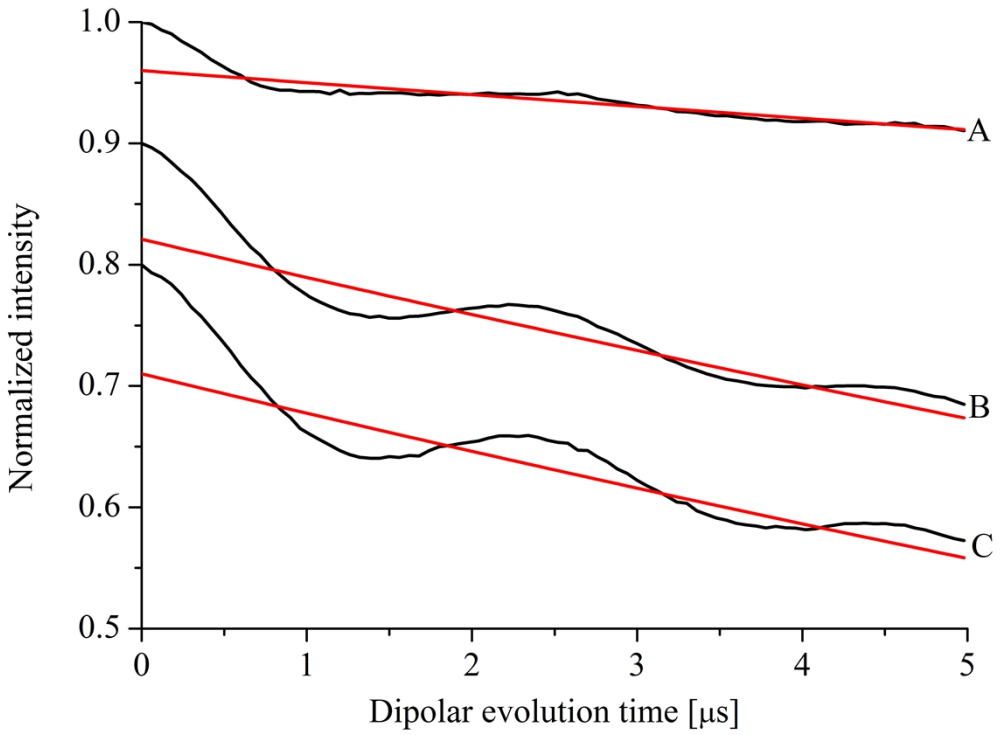

Fig. S5. PELDOR time traces obtained at G-band frequencies at a temperature of 25 K (black curves) and the corresponding exponential background functions (red curves). The positions A, B and C correspond to the positions in the spectrum depicted in Fig. 4.

6. Fitting of the G-band PELDOR time traces using the PELDOR database

Simulation of the full set of the G-band PELDOR time traces was performed with the PELDOR database approach.[33] For the creation of the PELDOR database three cartesian coordinate systems $\{x_1,y_1,z_1\}$, $\{x_2,y_2,z_2\}$ and $\{x,y,z\}$ were defined. The coordinate systems $\{x_1,y_1,z_1\}$ and $\{x_2,y_2,z_2\}$ correspond to the trityl g-tensor frame (Fig. S6). The z_1 and z_2 - axes are collinear to the pseudo-C_3 symmetry axis of the trityl moieties. The x_1 and x_2 - axes are chosen collinear to the σ-bonds of the central trityl carbon atoms that are aligned along the linker axis. The y_1 and y_2 - axes are orthogonal to the x_1 and x_2 - axes, respectively. The third, reference coordinate system $\{x,y,z\}$, that is associated with the biradical linker, is held constant (Fig. S7). The z-axis of the reference frame is aligned along the mean linker axis, and the x-axis is aligned orthogonally to the plane, containing two axes z_1 and z. The coordinate systems $\{x_1,y_1,z_1\}$ and $\{x_2,y_2,z_2\}$ rotate with respect to this reference frame and the orientations of $\{x_1,y_1,z_1\}$ and $\{x_2,y_2,z_2\}$ with respect to $\{x,y,z\}$ are described by the Euler angles $\{\alpha_1,\beta_1,\gamma_1\}$ and $\{\alpha_2,\beta_2,\gamma_2\}$ in ZXZ-convention shown in Fig. S6.

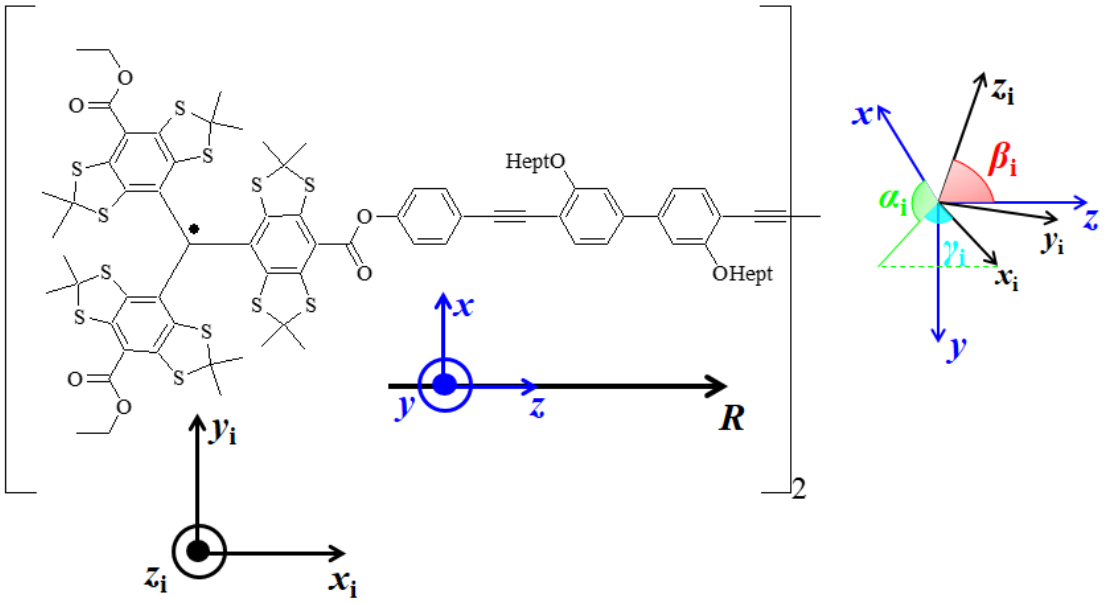

Fig. S6. Left. Schematic representation of the trityl moiety g-tensor frame $\{x_i,y_i,z_i\}$with the fixed reference frame $\{x,y,z\}$ **Right.** Euler angles $\{\alpha_i,\beta_i,\gamma_i\}$, describing the rotation of the trityl g-tensor frame with respect to the fixed reference frame.

The Euler angle α_i is the angle between the line of nodes N_i (the intersection line of the planes x_i-y_i and x-y) and the x axis. According to our definition, the angle α_1 is equal to zero for all biradicals. The β_i is the angle between the trityl g-tensor frame z_i-axis and the reference frame z-axis. In the simplified schematic representation depicted in Fig. S6 (left) the β_i angle equals to $\pi/2$. The γ_i is the angle between the line of nodes N_i and trityl x_i-axis. This angle describes the rotation of the trityl moiety around the g-tensor frame z_i-axis. Due to the invariance of the PELDOR signal with respect to a permutation of the two identical radicals, the Euler angles have only to be varied in a restricted angle parameter space: ($\alpha_1 = 0$, $0 \le \beta_1 \le \pi/2$, $0 \le \gamma_1 < \pi$) and ($0 \le \alpha_2 < \pi$, $0 \le \beta_2 \le \pi/2$, $0 \le \gamma_2 < \pi$) in order to generate PELDOR time traces of all possible forms. Within this 5-dimensional angle parameter space, a set of 172800

PELDOR time traces S_i were calculated for each interspin distance *R* with a resolution of 10° for β_1 and β_2 angles and 15° for the angles γ_1, γ_2 and α_2. These calculated PELDOR time traces, which constitute the elements of the PELDOR database, were compared to the set of the experimental time traces. In order to account for possible modulation depths inaccuracies in the simulated PELDOR time traces, caused either by incorrectly adjusted pump and detection pulse lengths or by uncertainties in the calculation of the excitation profile of the pulses, the value given by expression (2) was minimised:

$$\left\|(1 - S_{exp}) - f(1 - S_i)\right\|^2 \underset{f,i}{\rightarrow} min \qquad (2)$$

The procedure was performed with respect to the parameter *f* within the range ($0.8 < f < 1.2$) and parameter *i* which denotes the number of the spin label conformer. S_i and S_{exp} represent computed and experimental signals, respectively. The procedure (2) yielded numbers i_1 and f_1. In the next step the fit of the experimental traces was improved further by minimising the value given by (3)

$$\left\|(1 - S_{exp}) - f\left(1 - \frac{S_{i1} + S_i}{2}\right)\right\|^2 \underset{f,i}{\rightarrow} min \qquad (3)$$

with respect to *i* and *f*. This gives the conformer number i_2. The procedure was iteratively repeated 50 times, yielding each time a set of Euler angles of (β_1, γ_1, β_2, γ_2, α_2) and a distance *R*. Note, that a dataset from the PELDOR database can be chosen several times, thereby increasing its statistical weight.

Two types of simulations using the concept of the PELDOR database were performed. In the first approach a *model free* search of the conformations has been incorporated, using the full database of the PELDOR signals. In the second approach additional constrains on the selection of the conformations have been imposed in order to reflect the free rotation of the linker segments.

The fitted PELDOR time traces and distance distribution function obtained with the *model-free* approach are depicted in Fig. S7 (Top). The main peak at 4.9 nm and the shape of the distance distribution function are in a good agreement with the result of Tikhonov regularization analysis of the DQC, SIFTER and PELDOR data. However, the *model-free* fitting procedure did not yield uniform distribution of the Euler angle α_2 (see Fig. S7 bottom left). The Euler angle α_2 is defined as the angle between the plane containing the vectors *z* and z_1 and the plane containing vectors *z* and z_2. For biradical **1** it is expected that this angle is uniformly distributed from 0° to 360° due to the free rotation of the linker segments.[6]

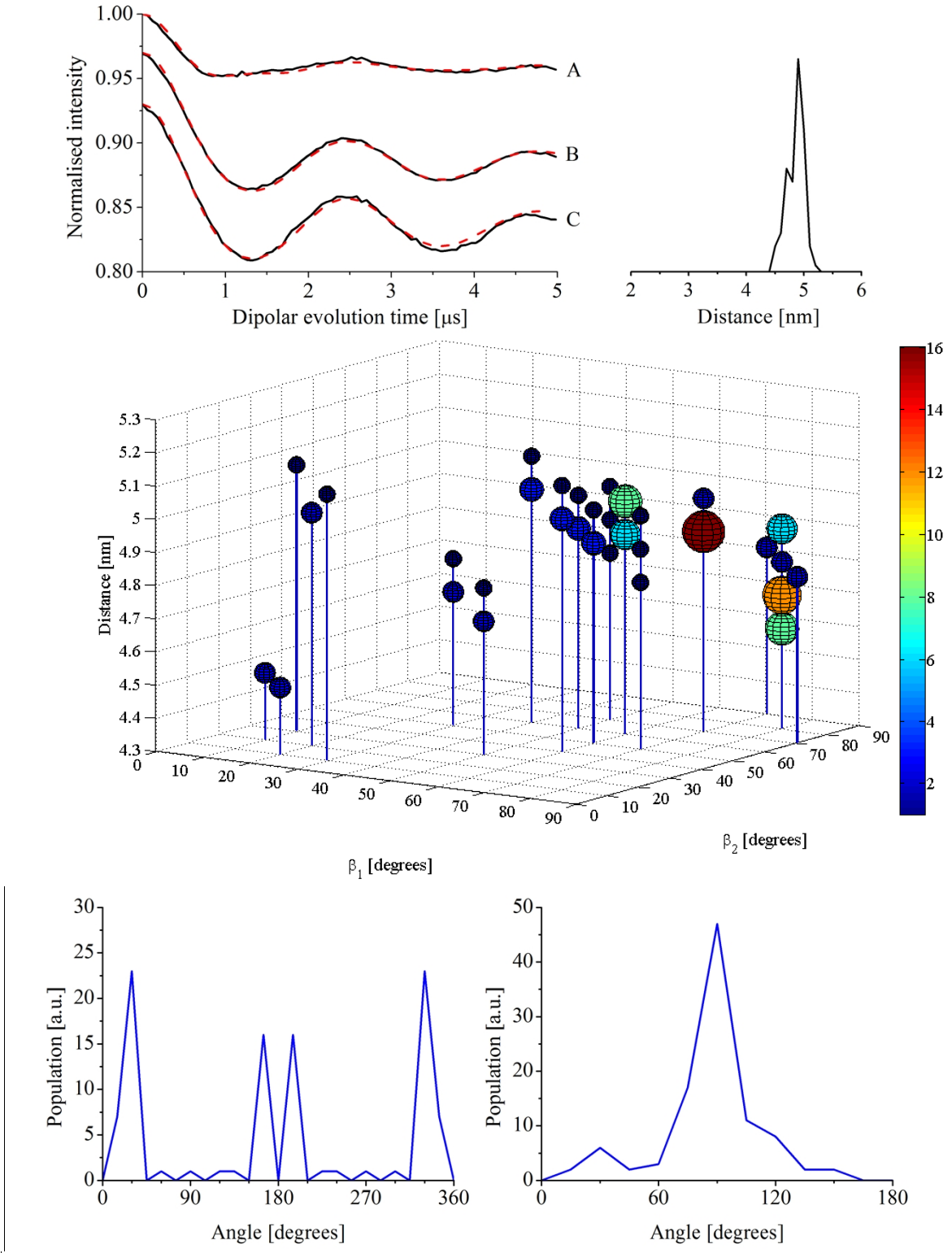

Fig. S7. Top. Left-side - Background-divided PELDOR time traces of biradical **1** obtained at G-band frequencies. Solid lines are experimental data, dashed lines are the fits obtained with the first PELDOR database approach (*model-free* approach). Positions A, B and C correspond to the positions in the G-band spectrum depicted in Fig. 4. Right-side - Distance distribution function obtained from the PELDOR database *model-free* fit approach.

Middle. Set of the biradical **1** conformers, characterised with the angles β_1, β_2 and a distance *R*, obtained with the PELDOR database *model-free* approach. The colour code and size of the balls represent the statistical weights of the distinct conformer.

Bottom. Corresponding set of the biradical **1** conformers, characterised with the α_2 angles (left-side) and γ_i angles (right-side). Axes of ordinates correspond to the statistical weight of the conformers.

In the second fitting approach, the PELDOR database was averaged over this angle α_2 leading to a smaller signal database that contains only 14400 signals for various Euler angles (β_1, γ_1, β_2, γ_2).

The fitted PELDOR time traces, distance distribution function and a set of the biradical **1** conformers with their statistical weights are depicted in Fig. S8. In this approach a good fit of the experimental PELDOR signals was achieved as well. However, the statistical weight of the relative spin label orientations and distance distribution function differ from the result obtained in the first, *model-free* approach. This led to the conclusion, that a set of the three G-band PELDOR time traces with their weak spectral anisotropy is not enough to gain information about the trityl biradical conformational flexibility unambiguously.

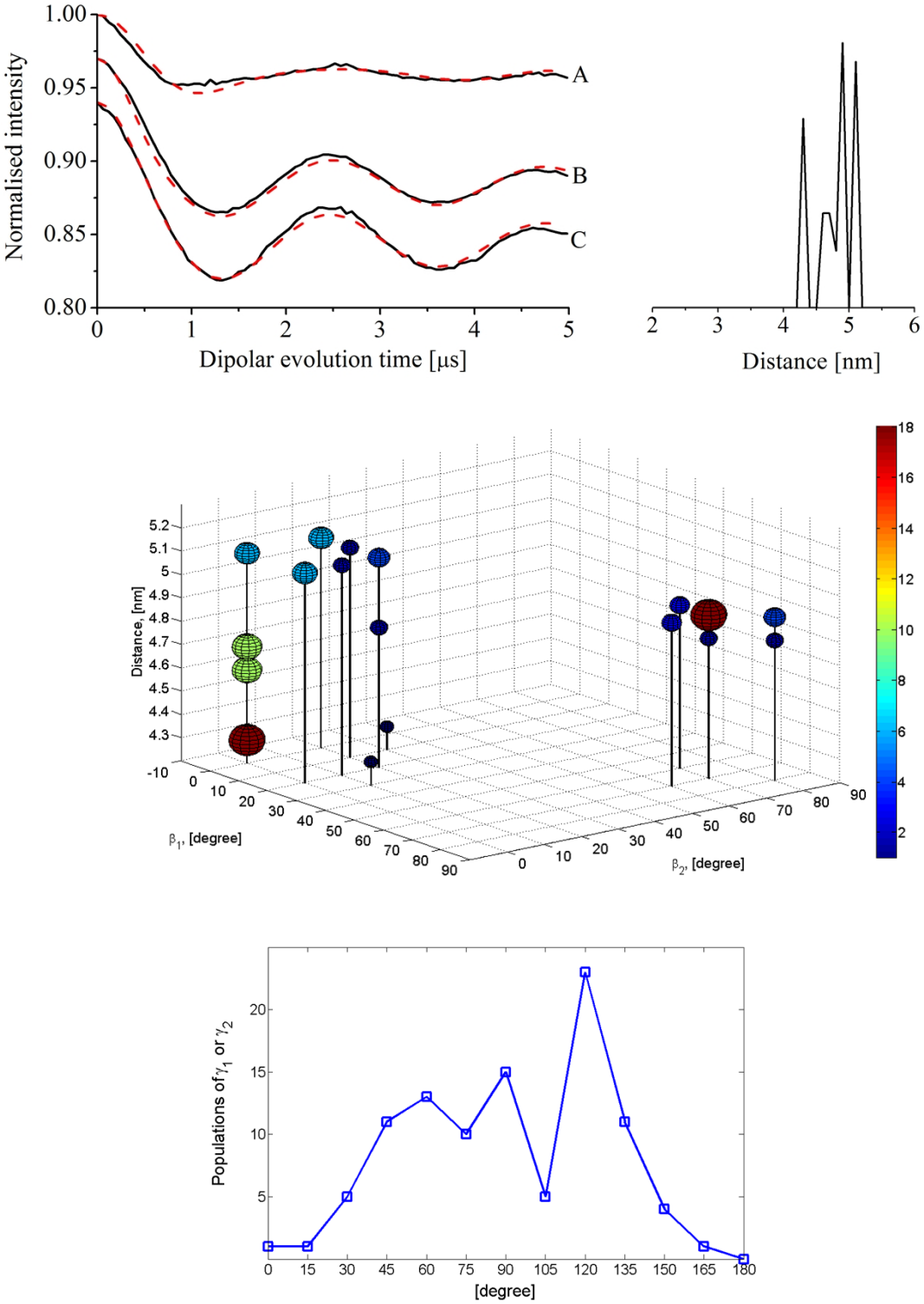

Fig. S8. Top. Left-side - Background-divided PELDOR time traces of biradical **1** obtained at G-band frequencies. Solid lines are experimental data, dashed lines are the fits obtained with the second PELDOR database fit approach. Positions A, B and C correspond to the positions in the G-band spectrum depicted in Fig. 4. Right-side - Distance distribution function obtained from the second PELDOR database fit approach.

Middle. Set of the biradical **1** conformers, characterised with the angles β_1, β_2 and a distance *R*, obtained with the second PELDOR database approach. The colour code and size of the balls represent the statistical weights of the distinct conformer.

Bottom. Corresponding set of the biradical **1** conformers, characterised with γ_i angle. Axes of ordinates correspond to the statistical weight of the conformers.

7. References

S1 S. Stoll and A. Schweiger, *J. Magn. Reson.*, 2006, **178**, 42.

S2 M. K. Bowman, C. Mailer and H. J. Halpern, *J. Magn. Reson*., 2005, **172**, 254.

PCCP

PAPER

View Article Online
View Journal | View Issue

Cite this: *Phys. Chem. Chem. Phys.*, 2015, **17**, 6760

Pulsed electron–electron double resonance spectroscopy between a high-spin Mn^{2+} ion and a nitroxide spin label†

D. Akhmetzyanov, J. Plackmeyer, B. Endeward, V. Denysenkov and T. F. Prisner*

Received 18th November 2014,
Accepted 3rd February 2015

DOI: 10.1039/c4cp05362a

www.rsc.org/pccp

Pulsed Electron–Electron Double Resonance (PELDOR) has attracted considerable attention for biomolecular applications, as it affords precise measurements of distances between pairs of spin labels in the range of 1.5–8 nm. Usually nitroxide moieties incorporated by site-directed spin labelling with cysteine residues are used as spin probes in protein systems. Recently, naturally occurring cofactors and metal ions have also been explored as paramagnetic spin species for such measurements. In this work we investigate the performance of PELDOR between a nitroxide spin label and a high-spin Mn^{2+} ion in a synthetic model compound at Q-band (34 GHz) and G-band (180 GHz). We demonstrate that the distances obtained with high-frequency PELDOR are in good agreement with structural predictions. At Q-band frequencies experiments have been performed by probing either the high-spin Mn^{2+} ion or the nitroxide spin label. At G-band frequencies we have been able to detect changes in the dipolar oscillation frequency, depending on the pump–probe positions across the ***g***-tensor resolved nitroxide EPR spectrum. These changes result from the restricted mobility of the nitroxide spin label in the model compound. Our results demonstrate that the high-spin Mn^{2+} ion can be used for precise distance measurements and open the doors for many biological applications, as naturally occurring Mg^{2+} sites can be readily exchanged for Mn^{2+}.

Introduction

Determination of distances in the nanometer range is an important issue for structural characterisation of macromolecules. Pulsed Electron–Electron Double Resonance (PELDOR)[1] has become a valuable method for such applications in material science and structural biology[2,3] allowing the determination of distances in the 1.5–8 nm range from measurement of the magnetic dipole–dipole coupling between two paramagnetic sites. So far, nitroxide spin labels specifically attached to proteins[4] or nucleic acids[5] have been used as paramagnetic probes in biological systems. Only a few examples have been reported, where naturally occurring paramagnetic cofactors, for example, amino acid radicals,[6] metal ions[7] or iron–sulfur clusters[8,9] were used for PELDOR measurements. Recently, chelate complexes with Gd^{3+} (ref. 10 and 11) or Mn^{2+} ions[12] have been used as paramagnetic tags attached to proteins. Due to the high electronic spin multiplicity of these metal ions, it is beneficial to perform EPR experiments at higher magnetic field strengths.[13]

The Mn^{2+} ion is especially attractive for biological applications, since several enzymes[14] and membrane proteins naturally contain this paramagnetic marker. Moreover, due to the very similar ionic radius and identical electric charge of Mn^{2+} and Mg^{2+} ions, Mn^{2+} can easily replace Mg^{2+}, an essential cofactor for many enzymes, nucleic acid molecules and nucleotide binding domains.[15] Thus, PELDOR in combination with Electron-Nuclear Double Resonance (ENDOR) spectroscopy, is an ideal tool for structural characterisation of such intrinsic metal sites in biomolecules, which in many cases undergo long range structural rearrangements and changes in the ligand sphere within the catalytic function.[16,17]

The high-spin Mn^{2+} ion has an electronic spin of $S = 5/2$. In addition the 100% naturally abundant ^{55}Mn isotope has a nuclear spin of $I = 5/2$. Such high-spin multiplicities lead to rather complex EPR spectra in disordered systems at low magnetic fields.[18] However, at higher magnetic field, when the electron Zeeman splitting is considerably larger than the

Goethe University Frankfurt am Main, Institute of Physical and Theoretical Chemistry and Center for Biomolecular Magnetic Resonance, Max von Laue Str. 7, 60438 Frankfurt am Main, Germany. E-mail: prisner@chemie.uni-frankfurt.de

† Electronic supplementary information (ESI) available: EPR spectrum of compound **6**. Phase memory time measurements on compound **4** at Q-band and G-band frequencies and on compound **6** at Q-band frequencies. PELDOR time traces without background subtraction of compound **4** at Q-band, experimental parameters, background functions, experimental and fitted Pake patterns. Q-band EPR experiments upon pumping and detecting on Mn^{2+} ion spin system on compound **4** and on compound **6**. Simulated PELDOR time traces at G-band frequencies on compound **4** without background function, parameters of simulations. MS spectrum of compound **4**. See DOI: 10.1039/c4cp05362a

Zero-Field Splitting (ZFS), the six allowed hyperfine lines of the central electron spin transition ($|m_S = -1/2, m_I\rangle \rightarrow |m_S = 1/2, m_I\rangle$) become narrow and indicative. The line narrowing of the central transition can be assessed by second-order perturbation theory. This reveals that the linewidth scales inversely with the external magnetic field as D^2/B_0, assuming a ZFS asymmetry parameter of $E = 0$.[18] Moreover, the intensities of the forbidden hyperfine transitions ($\Delta m_S = \pm 1$ $\Delta m_I = \pm 1$ and $\Delta m_S = \pm 1$ $\Delta m_I = \pm 2$) become significantly reduced.[18] Thus, the EPR spectrum of a disordered Mn^{2+} system simplifies considerably at higher magnetic field.

The EPR signals resulting from the different electron spin sublevels ($|m_S,m_I\rangle \rightarrow |m_S \pm 1,m_I\rangle$) of the Mn^{2+} ion all have different transition moments. Therefore, the Rabi oscillation frequency of the central electron spin transition of an Mn^{2+} ion spin system is 3 times higher compared to a nitroxide electron spin ($S = 1/2$) at high magnetic fields. These differences in transition moments can be used to separate the different electron spin transitions by their Rabi nutation frequencies.[19] However, this phenomenon further complicates pulsed EPR experiments, especially at low magnetic fields, as spectrally overlapping allowed and forbidden transitions are all excited simultaneously by the microwave pulses, although to a different extent.

Here we performed PELDOR measurements at two magnetic field strengths (1.2 T and 6.4 T corresponding to electron excitation frequencies of 33.7 GHz (Q-band) and 180 GHz (G-band), respectively) on a nitroxide–Mn^{2+} model compound in order to investigate in detail the performance of this experiment while pumping either on the nitroxide spin system or Mn^{2+} ion spin system.

Results and discussion

Synthesis

The synthesis of the model compound **4** with a distance of approximately 2.7 nm between the unpaired electron of the nitroxide and the Mn^{2+} ion[20–22] is schematically represented in Fig. 1. Sonogashira coupling of **1** with 4′-(4-ethynylphenyl)-2,2′:6′,2″-terpyridine **2** yielded the nitroxide substituted terpyridine ligand **3**. The heteroleptic Mn^{2+}-terpyridine complex **4** was obtained as the hexafluorophosphate by mixing equimolar amounts of **3** with [Mn(terpyridine)Cl_2] and precipitation under excess of NH_4PF_6.

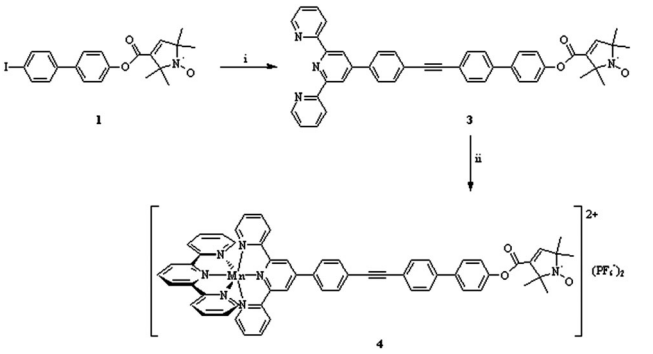

Fig. 1 Scheme of the synthesis of the ligand **3** and the model compound **4**. Reagents and conditions: (i) 4′-(4-ethynylphenyl)-2,2′:6′,2″-terpyridine **2**, $Pd(PhCN)_2Cl_2$, CuI, TBAB, $P(Ph)_3$, Et_2NH/THF, room temperature, 16 h. (ii) (a) [Mn(terpyridine)Cl_2], MeOH/CH_2Cl_2, 45–50 °C, 1.5 h; (b) NH_4PF_6, MeOH.

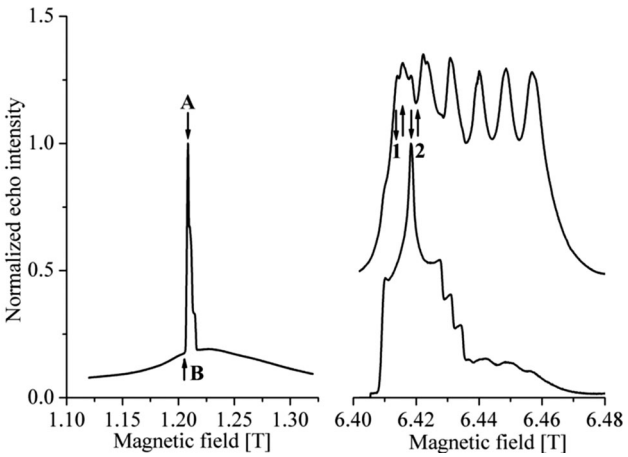

Fig. 2 Field-swept echo-detected EPR spectrum of the heteroleptic Mn^{2+}-terpyridine complex **4**. Left – spectrum recorded at Q-band frequencies and a temperature of 5 K; arrows at the field positions A and B illustrating the probe and pump positions for the PELDOR experiments. Pulse lengths and repetition time of the pulse sequence are optimised for the Mn^{2+} ion spin system at field position B. Right – spectra recorded at G-band frequencies and a temperature of 10 K. Upper spectrum: pulse lengths and repetition time of the pulse sequence are optimised for the Mn^{2+} ion spin system at one of the central hyperfine lines. Lower spectrum: pulse lengths and repetition time of the pulse sequence are optimised for the nitroxide spin system at the position of maximum absorption in the nitroxide spectrum. The sets of arrows at field positions 1 and 2 illustrate the pump and probe excitation positions used for the PELDOR experiments. Within each set (1 or 2) the arrows up and down represent the probe and pump positions respectively.

EPR spectroscopy

The PELDOR experiments on the heteroleptic Mn^{2+}-terpyridine complex **4** were performed at Q-band (33.7 GHz) and G-band (180 GHz) frequencies. The field-swept echo-detected EPR spectra at both frequencies are shown in Fig. 2. At Q-band frequencies (Fig. 2 left) a broad and featureless EPR signal from the Mn^{2+} ion spin system can be observed with the comparably narrow nitroxide EPR signal superimposed. Despite the fact that pulse lengths (32 ns) and repetition time (0.8 ms) were optimised for the much faster relaxing Mn^{2+} ion spins in this experiment, the nitroxide signal still shows a larger relative intensity. The sample temperature was set to 5 K in order to achieve longer transversal relaxation (T_2) time for Mn^{2+} ion spins, as the latter limits the length of the observable time window. The Mn^{2+} ions hyperfine lines of the central electron spin transition $|-1/2, m_I\rangle \rightarrow |1/2, m_I\rangle$ are not resolved at Q-band frequencies which indicates the presence of relatively large ZFS parameters for this molecule. In another study of Mn^{2+} bis(terpyridine) complexes it was found that the ZFS parameter D is strongly dependent on the structure of the terpyridine moiety and on the solvent.[23,24] ZFS parameters for the Mn^{2+} bis(terpyridine) complex in acetonitrile were given as: $D = -1.54$ GHz and $E = 0.3$ GHz.[23] Attaching a nitroxide linker to one of the terpyridine moieties, as is the case with the heteroleptic

Mn^{2+}-terpyridine complex **4** and using 2-methyltetrahydrofuran as solvent may lead to different ZFS parameters. An EPR spectrum of compound **6** (scheme is presented in Fig. S1, ESI†) a derivative of compound **4** without the nitroxide moiety is shown in Fig. S2 (ESI†).

Field-swept echo-detected EPR spectra of the heteroleptic Mn^{2+}-terpyridine complex **4** at G-band frequencies are shown in Fig. 2 on the right side. As described previously, the linewidth of the central electron spin transitions narrow at higher fields. Therefore, the sextet of hyperfine lines for this transition can clearly be resolved at G-band frequencies (Fig. 2 upper right spectrum). Since the overall Mn^{2+} ion spectral shape is very smooth and reveals no characteristic features related to the ZFS, a broad statistical distribution of the ZFS parameters of the Mn^{2+} ion of the compound **4** must exist. A similar broad statistical distribution of the ZFS parameters was also observed for the Gd^{3+} complexes in frozen solution.[25] The overlapping EPR spectra corresponding to the Mn^{2+} ion and nitroxide spins can be distinguished by changing the length of the pulses and the experimental repetition time because of the different transition moments and longitudinal relaxation times (T_1) of the two species. Such a procedure has already been demonstrated for the Gd^{3+}–nitroxide spin system at X- and Q-band frequencies.[26]

PELDOR experimental time traces of the heteroleptic Mn^{2+}-terpyridine complex **4** at Q-band frequencies are presented in Fig. 3 together with respective fits. In both cases, when probing either on the Mn^{2+} ion or nitroxide spin systems, pronounced dipolar oscillations are visible, reflecting the rigid structure of compound **4**.

For PELDOR experiments at Q-band frequencies a 90 MHz offset between pump and probe frequencies was used. This separation is the upper limit that could be achieved with the experimental setup. This value was chosen such that when probing the Mn^{2+} ion spins and pumping on the maximum of the nitroxide spectrum, a negligible amount of nitroxide spins are excited by the detection pulses. Excitation of the nitroxide spins by the detection pulses would reduce the modulation depth. Moreover, we assume that level mixing of the dipolar coupled Mn^{2+}–nitroxide spin system, due to the pseudo-secular terms of the dipolar coupling Hamiltonian, could be significantly minimised by choosing a pump–probe frequency offset that considerably exceeds the dipolar coupling constant. In general, the contribution from the pseudo-secular terms is larger for a dipolar coupled pair of high-spin centres compared to a pair of spin-1/2 centres, as demonstrated for a Gd^{3+}–Gd^{3+} system.[27] However, if only one centre in the pair has a high spin quantum number, the contribution from the pseudo-secular terms is reduced, as proposed for a Gd^{3+}–nitroxide pair compared to a Gd^{3+}–Gd^{3+} system.[28] It is assumed, that this situation will also apply for the Mn^{2+}–nitroxide system studied here.

Orientation selection effects at Q-band frequencies are expected to be negligible. When pumping and probing at the maximum of the nitroxide EPR spectrum the orientation selectivity is poor at this frequency. In the case of pumping and probing Mn^{2+} the orientation selectivity is also assumed to be small due to a broad statistical distribution of the ZFS parameters. Therefore, a Tikhonov regularisation with the complete Pake pattern as the integral kernel function[29] can be used to determine the distance between two spins within the molecule. DeerAnalysis[29] has been used to obtain the distance distribution functions in both cases.

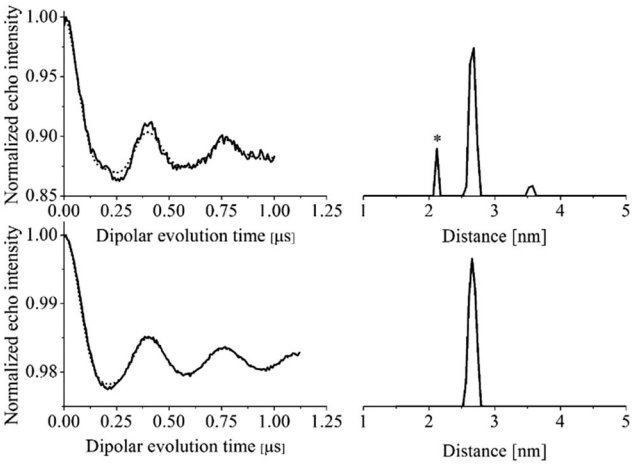

Fig. 3 Background-corrected PELDOR time traces obtained at Q-band frequencies. The solid lines are experimental time traces, the dotted lines are the fits by Tikhonov regularisation.[29] The upper row shows the PELDOR time traces and distance distribution functions obtained by pumping on position A (nitroxide, as depicted in Fig. 2) and probing on position B (Mn^{2+}). The lower row shows the traces for pumping on position B (Mn^{2+}) and probing on position A (nitroxide). The pump–probe frequency difference is 90 MHz in both cases. Both experiments are performed at 5 K. The peak at 2.1 nm marked by the asterisk is described in the text.

The PELDOR time trace obtained by probing the nitroxide and pumping on the Mn^{2+} spins (Fig. 3 lower row), revealed a narrow distance distribution with a single distance of 2.65 nm and a full width at half maximum of only 0.15 nm (the Fourier-transformed Pake pattern is shown in Fig. S3, ESI†). When pumping on the nitroxide and probing the Mn^{2+} spins (Fig. 3 upper row), the same distance of 2.65 nm was extracted from the dipolar evolution function. A Tikhonov regularisation, performed with DeerAnalysis 2013 with a regularisation parameter of 0.01, was used in both cases. Validation using different fitting conditions for the background function provided an error of about 0.05 nm. Hence, the extracted distance is in good agreement with the predicted interspin distance of 2.7 nm.

The distance distribution pattern obtained from the PELDOR time trace by probing the Mn^{2+} spins contains a ghost peak at a 2.1 nm (asterisk in Fig. 3). A possible explanation of this is the occurrence of nuclear modulation effects in the PELDOR trace (a two-pulse ESEEM experiment is depicted in Fig. S2 of the ESI†). Due to the short transversal relaxation time of Mn^{2+} spins, tau-averaging was not used in the PELDOR experiment, as it would reduce the signal/noise ratio. Control experiments were performed where pump and probe pulses were applied only on the Mn^{2+} of compound **4** or compound **6**. A detailed explanation of these experiments is given in Section 4 of the ESI.† These experiments revealed oscillations which are likely to also be present in the PELDOR time trace obtained by probing the Mn^{2+} spins. Another possible explanation may be insufficient fulfillment of the high-field approximation at Q-band frequencies, so that ZFS induced contributions to the secular term of the

dipolar coupling Hamiltonian,[28] occur in the PELDOR time trace when probing the Mn^{2+} spins. Such effects are not included in the standard analysis of PELDOR time traces.

The appearance of additional satellite peaks in the distance distribution pattern has also been observed at X- and Q-band PELDOR experiments of a Gd^{3+}–nitroxide spin system.[26] The features were attributed to a violation of the high-field approximation and, for a part of the molecular ensemble, to effects arising from excitation of transitions other than the $|-1/2\rangle \leftrightarrow |1/2\rangle$.[26] In the case of the Mn^{2+}–nitroxide system studied here it is assumed that the central electron spin transition, including forbidden ^{55}Mn hyperfine transitions, is excited to a much larger extent than the other electron transitions. A detailed study of the distortions in PELDOR induced by ZFS and ZFS distribution when the high-field approximation is violated has been performed on Gd^{3+} species.[28] It was shown, that the ratio $3D/g\mu B_0$ defines the magnitude of distortions appearing in PELDOR for the Gd^{3+}–nitroxide spin system. Larger ZFS parameters induce a higher degree of level mixing and thus deviations from the normal undistorted case. This is particularly dramatic when the external magnetic field is not aligned along the canonical orientations of the ZFS frame. Nevertheless, for the cases where the ratio $3D/g\mu B_0$ is 2/3 (corresponding to a D value of 2 GHz at X-band frequencies) it was shown that the dipolar frequency pattern reveals only modest deviation from the expected pattern. These distortions appear as an artificial broadening of the distance distribution without significant shifts of the mean distance. For the D values $\leq$600 MHz at X-band frequencies the distortions are negligibly small. For the data obtained at Q-band frequencies distortions of the distance distribution were expected to be negligible, and a conventional analysis of the PELDOR time traces can be safely applied for values of $D < 2$ GHz.[28] The values given above are specific for Gd^{3+} however analogous results are expected for high-spin Mn^{2+}.[28]

The Q-band data presented here indicate that for the Mn^{2+}–nitroxide complex only weak distortions in the PELDOR trace are induced by ZFS. This does not lead to a shift of the mean distance within the experimental error, nor to broadening of the distance distribution. However, a detailed study of the high-field approximation violation in high-spin Mn^{2+} systems has yet to be performed in more detail.

As expected, the modulation depth λ is much lower when pumping on Mn^{2+}. In this case a modulation depth of only 2% was achieved under our experimental conditions. A detailed calculation of the excitation efficiency is complicated because of spectral overlap and the fact that spectral shape, population and nutation frequencies differ for all the individual electron spin transitions. In addition, the hyperfine coupling of the Mn^{2+} electronic spin system with the ^{55}Mn nuclear spin system and ZFS causes level mixing ($|m_S,m_I\rangle$ and $|m_S,m_I \pm 1\rangle$; $|m_S,m_I\rangle$ and $|m_S,m_I \pm 2\rangle$)[18] further complicating the picture especially at Q-band frequencies. Nevertheless, a rough approximation can be done by comparing the pump pulse excitation width with the overall spectral width. A pump pulse length of 20 ns corresponds to an excitation bandwidth of about 40 MHz and the overall Mn^{2+} linewidth is $8D + 5A$ (from first order perturbation theory). Assuming a ZFS parameter D of about 1.5 GHz and hyperfine coupling of about 250 MHz, this corresponds to a Mn^{2+} spectral width of 13.25 GHz. This rough analysis predicts a value of $\lambda = 1\%$. Although, this approximation is rather imprecise, it roughly corresponds to the experimentally observed value of 2%.

In the other case, when pumping on the nitroxide spin system, a modulation depth of 11% was experimentally achieved. At Q-band frequencies the nitroxide spectral width is about 280 MHz, leading to a pump efficiency of about 30% when pumping on the maximum of the spectrum. B_1 inhomogeneity of the Q-band resonator leads to a value of 25% for the modulation depth. This has been experimentally observed for nitroxide biradicals with our experimental setup. Therefore, the experimental λ value observed on the heteroleptic Mn^{2+}-terpyridine complex **4** is roughly a factor of 2 less than expected.

To investigate orientation selection effects for a high-spin Mn^{2+} ion coupled with a nitroxide spin, we performed PELDOR experiments at G-band frequencies, where the anisotropy of the nitroxide ***g***-tensor is fully resolved (as shown in Fig. 2 lower right spectrum). Two PELDOR experimental time traces for different pump positions on the nitroxide spectrum and probing the Mn^{2+} (Fig. 2) spins are depicted in Fig. 4 together with corresponding simulations based on the geometry of the molecule.

The experimentally observed modulation depths at both pump positions at G-band are a factor of 2.8 smaller compared to the predictions (analysis is described below). The fact that the observed modulation depths upon pumping on the nitroxide are smaller compared to the predictions both at Q- and G-band frequencies, indicates that the sample might also contain Mn^{2+} complexes that are not covalently coupled to the nitroxide moiety. This is supported by the appearance of a peak with m/z corresponding to Mn^{2+} bis(terpyridine) complex in the ESI mass spectrum (Fig. S7, ESI†). A reduced modulation depth was also observed for a Gd^{3+}–Gd^{3+} spin system.[27] It has been hypothesised that for this spin system the effect is caused by the influence of pseudo-secular terms of the dipolar coupling Hamiltonian that contribute to the PELDOR signal. However, in the case of the Mn^{2+}–nitroxide system studied here this effect is assumed to be negligible.

In the G-band data the modulation depth and frequency differ between the two PELDOR time traces taken at positions 1 and 2. This indicates orientation selection in the time traces when pumping on the nitroxide. Therefore, the analysis of the PELDOR time traces cannot be done by Tikhonov regularisation with the complete Pake pattern as the integral kernel function. Thus, simulations of the two PELDOR time traces at G-band frequencies were performed using the known orientation of the nitroxide moiety compared to the direction of the linker[22] and the excited orientations of the nitroxide with respect to B_0 (calculated with EasySpin[30] software, shown as insets in Fig. 4) upon pumping at position 1 or 2 (Fig. 4). The simulations used a fixed interspin distance of 2.7 nm (dotted lines in Fig. 4) and a Gaussian distance distribution width of 0.15 nm. The modulation depths of the simulations were corrected to those achieved experimentally to allow better visualisation (dash-dotted lines in Fig. 4).

For the simulation of the orientationally selective G-band experiments the geometry between the nitroxide moiety and the

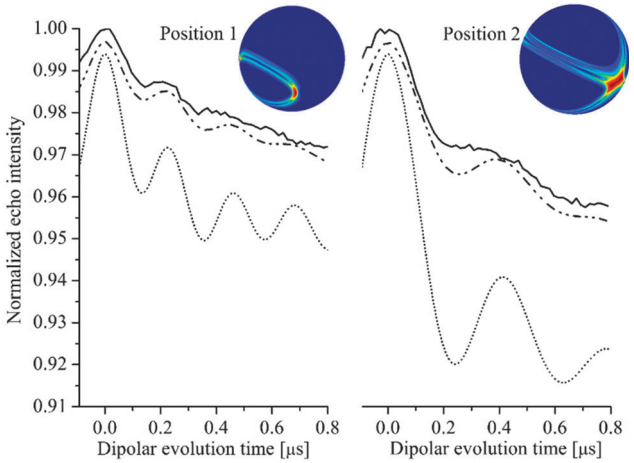

Fig. 4 PELDOR time traces at G-band without background subtraction. The solid lines represent experimental data; the dotted lines represent the simulation with calculated modulation depths and with the fixed interspin distance of 2.7 nm; the dash-dotted lines is the simulation where Gaussian distance distribution was included and experimental modulation depths were adapted to the experimental values. The pump–probe frequency offset is set to 60 MHz. The intermolecular background function used for the simulations is adjusted to fit the experimental data. Insets to the figure show the excited orientations of the nitroxide spin system in the ***g***-tensor frame.

dipolar axis was taken from the structure predictions (Fig. 1). Flexibility of the linker and the rotation of the nitroxide moiety around the linker axis of the complex was not explicitly included but only modeled by a Gaussian distance distribution, adjusted to fit the experimentally observed damping of the dipolar oscillations. Nevertheless the dipolar oscillation frequencies observed experimentally upon pumping on different positions in the nitroxide spectrum as well as the relative modulation depths are reproduced nicely by the simulations (the simulated time traces without background are depicted in Fig. S8, ESI†).

It is important to note, that the orientation selection analysis, which takes only the secular term of the dipolar coupling Hamiltonian into account, reproduced very well the experimentally observed dipolar oscillation frequencies and the ratio of the modulation depths at different selected spectral positions of the pumped nitroxide spin system.

Experimental

Synthesis of the heteroleptic Mn^{2+}-terpyridine complex 4

General. All reactions were performed with exclusion of air under argon, employing standard Schlenk techniques. Reagent-grade solvents and chemicals were used without further purification, except where stated otherwise. Dry solvents were purchased (Aldrich, ACROS) and thoroughly degassed prior to use. Diethylamine (ACROS) was freshly distilled from CaH_2. Solvents and reagents for Sonogashira cross-couplings were degassed by freeze–pump–thaw cycles. 4′-(4-Bromophenyl)-2,2′:6′,2″-terpyridine **5**,[31] [Mn(terpy)Cl_2][32] were synthesised according to the literature cited. 4′-(4-Ethynylphenyl)-2,2′:6′,2″-terpyridine **2** was obtained from 4-ethynylbenzaldehyde[33] by the method of Winter and coworkers.[34] Synthesis of 1-oxyl-2,2,5,5-tetramethyl-pyrrolin-3-carboxylic acid 4′-iodobiphenyl-4yl-ester **1** as well as the equipment for analytic observations were already described elsewhere.[35]

(1-Oxyl-2,2,5,5-tetramethyl-pyrrolin-3-carboxylic acid-(4′-(4-[2,2′:6′,2″]terpyridin-4′-yl-phenylethynyl)-biphenyl-4-yl)-ester) 3. Bis(benzonitrile)dichloropalladium(II) (43 mg, 0.11 mmol) and 1-oxyl-2,2,5,5-tetramethyl-pyrrolin-3-carboxylic acid 4′-iodobiphenyl-4yl-ester (367 mg, 0.75 mmol) were suspended in 150 mL diethylamine. Addition of 15 mL THF resulted in a yellow solution. To the stirred mixture CuI (26 mg, 0.13 mmol) and tetrabutylammoniumbromide (50 mg, 0.15 mmol) were added, followed by a solution of 4′-(4-ethynylphenyl)-2,2′:6′,2″-terpyridine (250 mg, 0.75 mmol) and triphenylphosphine (28 mg, 0.11 mmol) in 50 mL diethylamine and 10 mL THF. The resulting orange solution was stirred for 16 h at room temperature. All solvents were removed *in vacuo* and the remaining orange solid was treated with NH_4Cl solution (1 M, 150 mL) and dichloromethane (150 mL). The organic phase was washed with water and brine, dried (Na_2SO_4) and stripped from the solvent. The residue was recrystallised from methanol. A pale yellow solid was finally obtained by filtration. Yield: 313 mg (0.46 mmol, 62%). Anal. calcd for **3** ($C_{44}H_{35}O_3N_4$ (667.78)): C, 79.14; H, 5.28; N, 8.39. Found: C, 78.68; H, 5.78; N, 7.76. ESI-MS: *m*/*z* 668.17 ($[M + H]^+$).

([4′-(4-Bromophenyl)-2,2′:6′,2″-terpyridine][2,2′:6′,2″-terpyridine]-manganese(II)-bis-hexafluorophosphate) 6. 4′-(4-Bromophenyl)-2,2′:6′,2″-terpyridine **5** (39 mg, 0.10 mmol) and [Mn(terpy)Cl_2] (36 mg, 0.10 mmol) were dissolved in 15 mL of methanol by stirring for 1 h. The resulting yellow mixture was heated to reflux for 4 h and filtered while still warm. To the filtrate 2 eq. of NH_4PF_6 (33 mg, 0.20 mmol) were added, which gave a pale yellow precipitate. After filtration the yellow solid was washed with methanol and diethyl ether and air dried. Yield: 52 mg (0.05 mmol, 50%). Anal. calcd for **6** ($C_{36}H_{25}MnN_6P_2F_{12}Br$ (966.41)): C, 44.74; H, 2.61; N, 8.69. Found: C, 44.50; H, 2.56; N, 8.68.

([1-Oxyl-2,2,5,5-tetramethyl-pyrrolin-3-carboxylic acid-(4′-(4-[2,2′:6′,2″]terpyridin-4′-yl-phenylethynyl)-biphenyl-4-yl)-ester]-[2,2′:6′,2″-terpyridine]manganese(II)-bis-hexafluorophosphate) ([Mn(terpy)(3)]$(PF_6)_2$) 4. [Mn(terpy)Cl_2] (14.7 mg, 0.041 mmol) was dissolved in 8 mL of methanol by warming up the mixture slightly. The ligand **3** (27.1 mg, 0.041 mmol) dissolved in dichloromethane (3 mL) was added dropwise, resulting in an intensified yellow colour of the reaction mixture. The solution was warmed up to 45–50 °C for 30 min, after which a yellow solid precipitated. Stirring was continued at the same temperature for additional 60 min. After cooling to room temperature the solution was filtered. A solution of 4 eq. NH_4PF_6 (26.7 mg, 0.164 mmol) in methanol (1 mL) was added to the filtrate and a yellow precipitate was formed. For complete precipitation the mixture was stored over night at 4 °C. A yellow solid was obtained by filtration, washed with cold methanol and dried *in vacuo*. Yield: 27 mg (0.022 mmol, 53%). Anal. calcd for **4** ($C_{59}H_{46}MnN_7O_3P_2F_{12}$ (1245.91)): C, 56.88; H, 3.72; N, 7.87. Found: C, 57.74; H, 3.89; N, 7.37. ESI-MS: *m*/*z* 477.1 ($[M - 2PF_6]^{2+}$); 1100.7 ($[M - PF_6]^+$).

Pulsed EPR experiments

Pulsed EPR experiments were performed on a Bruker Elexsys E580 spectrometer using a ER5107D2 Q-band probehead and on a home built G-band EPR spectrometer.[36,37]

Q-band experiments were performed at a temperature of 5 K. The field-swept echo-detected EPR spectrum was recorded with pulses of 32 ns length, the power of the $\pi/2$ and π pulses, respectively, was adjusted for maximum echo intensity of the Mn^{2+} ion spin system at the detection position B (see Fig. 2); the pulse separation (here the time between front edges of the pulses) was 120 ns; the experimental repetition time was 0.8 ms. The four-pulse PELDOR sequence[38] was used for both Q- and G-band experiments. A Q-band PELDOR experiment in which the nitroxide spin system was pumped (at the maximum of the spectrum, position A in Fig. 2) was performed with pulse lengths of 20 ns (pump pulse) and 32 ns (detection pulses); the dipolar evolution time window was 1.6 μs. The power of the pump pulse was adjusted for maximum inversion efficiency of the nitroxide spins and the power of detection pulses were adjusted for maximum echo intensity at position B. The experimental repetition time was 0.408 ms. Identical pulse lengths and pulse separations were used for the Q-band PELDOR experiment where the Mn^{2+} spin system was pumped (corresponding to the position B in Fig. 2 left). The power of the pump pulse was adjusted for maximum inversion efficiency of the Mn^{2+} spin system, whereas the power of the detection pulses were optimised for maximum echo intensity of the nitroxide signal. The experimental repetition time was 8.16 ms.

All G-band EPR experiments were performed at 10 K. The field-swept echo-detected EPR spectrum, optimised for Mn^{2+} spin system (the upper spectrum in Fig. 2, right) were recorded with pulse lengths of 22.5 and 32.5 ns for $\pi/2$ and π pulses, respectively. The length of the $\pi/2$ pulse is more than half the length of the π pulse due to relatively long (about 5 ns) rise and fall time for pulses on the G-band spectrometer. The microwave power was 30 mW for both pulses. The pulse separation (here the time between falling edge of the first pulse and front edge of the second pulse) was set to 300 ns and the repetition time to 1.1 ms. The adjustment of the pulse lengths was performed for maximum echo intensity at one of the ^{55}Mn hyperfine lines of the Mn^{2+} central transition. For the field-swept echo-detected EPR spectrum optimised for the nitroxide spin system, the pulse lengths were 40 and 75 ns for $\pi/2$ and π pulses, respectively. The pulse separation was set to 300 ns and the experimental repetition time to 77.5 ms. For PELDOR experiments the detection pulse lengths were 20 and 27.5 ns and the pump pulse length was 65 ns. The microwave power was 60 mW for all pulses. The dipolar evolution time window was 1.5 μs and the experimental repetition time was 1.1 ms.

Sample preparation for the EPR experiments

2-Methyltetrahydrofuran (MTHF) was used as a solvent (Sigma-Aldrich). Dissolution of the compound **4** was achieved by counter ion exchange with the non-coordinating tetrakis [3,5-bis(trifluoromethyl)phenyl] borate ($BAr^{F-}{}_4$). Sodium tetrakis [3,5-bis(trifluoromethyl)phenyl] borate ($NaBAr^{F-}{}_4$), obtained from Alfa Aesar, was added to a mixture of the heteroleptic Mn^{2+}-terpyridine complex **4** and MTHF with 30 to 40-fold excess. After adding $NaBAr^{F-}{}_4$ the solution became yellow coloured and was fully dissolved after 15 to 20 minutes of vortex mixing. The concentration of the compound for the EPR measurements was approximately 200 μM. For EPR measurements the sample was transferred to 1 mm inner diameter quartz tubes (Q-band) and 0.4 mm inner diameter tubes (G-band).

Conclusions

PELDOR experiments on a molecule containing a high-spin Mn^{2+} ion and a nitroxide spin system were performed at Q- and G-band frequencies. Analysis of the PELDOR data recorded at Q-band reveals an interspin distance of 2.65 nm, which is in good agreement with the distance derived from the crystal structures of similar compounds. The PELDOR data recorded at G-band frequencies show a dependence of the dipolar oscillation frequency on the position of the pump pulse within the spectrum. Simulations taking the orientation selection of the nitroxide spin system into account are in good agreement with the experimentally observed orientationally selective PELDOR oscillation frequencies. Our results demonstrate that the high-spin Mn^{2+} ions can be used in conjunction with nitroxide spin labels for accurate distance determination. This provides interesting possibilities for applications to nucleotide binding domains of proteins and other biological systems. Extension of such studies to Mn^{2+}–Mn^{2+} spin pairs is under investigation in our laboratory.

Acknowledgements

The authors thank Dr Philipp Spindler for assistance with first Q-band PELDOR measurements, Dr Andriy Marko and Dr Björn Corzilius for discussions and Dr Alice Bowen for proofreading of the manuscript. The authors acknowledge financial support from the German Research Society DFG (GZ: PR 294/14-1).

References

1 A. Milov, A. Ponomarev and Y. Tsvetkov, *Chem. Phys. Lett.*, 1984, **110**, 67.
2 G. Jeschke, *Annu. Rev. Phys. Chem.*, 2012, **63**, 419.
3 O. Schiemann and T. Prisner, *Q. Rev. Biophys.*, 2007, **40**, 1.
4 W. Hubbell, A. Gross, R. Langen and M. Lietzow, *Curr. Opin. Struct. Biol.*, 1998, **8**, 649.
5 I. Krstic, B. Endeward, D. Margraf, A. Marko and T. Prisner, *Top. Curr. Chem.*, 2012, **321**, 159.
6 V. Denysenkov, T. Prisner, J. Stubbe and M. Bennati, *Proc. Natl. Acad. Sci. U. S. A.*, 2006, **103**, 13386.
7 I. van Amsterdam, M. Ubbink, G. Canters and M. Huber, *Angew. Chem., Int. Ed.*, 2003, **42**, 62.
8 C. Elsässer, M. Brecht and R. Bittl, *J. Am. Chem. Soc.*, 2002, **124**, 12606.

9 M. Roessler, M. King, A. Robinson, F. Armstrong, J. Harmer and J. Hirst, *Proc. Natl. Acad. Sci. U. S. A.*, 2010, **107**, 1930.
10 A. Potapov, H. Yagi, T. Huber, S. Jergic, N. Dixon, G. Otting and D. Goldfarb, *J. Am. Chem. Soc.*, 2010, **132**, 9040.
11 L. Garbuio, E. Bordignon, E. Brooks, W. Hubbell, G. Jeschke and M. Yulikov, *J. Phys. Chem. B*, 2013, **117**, 3145.
12 D. Banerjee, H. Yagi, T. Huber, G. Otting and D. Goldfarb, *J. Phys. Chem. Lett.*, 2012, **3**, 157.
13 A. Raitsimring, C. Gunanathan, A. Potapov, I. Efremenko, J. Martin, D. Milstein and D. Goldfarb, *J. Am. Chem. Soc.*, 2007, **129**, 14138.
14 I. Fridovich, *Annu. Rev. Biochem.*, 1995, **64**, 97.
15 T. Schweins, K. Scheffzek, R. Aßheuer and A. Wittinghofer, *J. Mol. Biol.*, 1997, **266**, 847.
16 P. Manikandan, R. Carmieli, T. Shane, A. Kalb (Gilboa) and D. Goldfarb, *J. Am. Chem. Soc.*, 2000, **122**, 3488.
17 M. Bennati, M. Hertel, J. Fritscher, T. Prisner, N. Weiden, M. Spörner, R. Hofweber, G. Horn and H. Kalbitzer, *Biochemistry*, 2006, **45**, 42.
18 G. Reed and G. Markham, in *Biological Magnetic Resonance*, ed. L. Berliner and J. Reuben, 1984, vol. 6, p. 73.
19 A. Astashkin and A. Shweiger, *Chem. Phys. Lett.*, 1990, **174**, 595.
20 A. Rompel, A. Bond and C. McKenzie, *Acta Crystallogr., Sect. E: Struct. Rep. Online*, 2004, **60**, m1759.
21 H.-G. Liu, Y.-C. Qiu and J.-Z. Wu, *Acta Crystallogr., Sect. E: Struct. Rep. Online*, 2007, **63**, m2393.
22 D. Margraf, D. Schuetz, T. Prisner and J. Bats, *Acta Crystallogr., Sect. E: Struct. Rep. Online*, 2009, **65**, o1784.
23 J. Gätjens, M. Sjödin, V. Pecoraro and S. Un, *J. Am. Chem. Soc.*, 2007, **129**, 13825.
24 C. Duboc, M. Collomb, J. Pecaut, A. Deronzier and F. Neese, *Chem. – Eur. J.*, 2008, **14**, 6498.
25 A. Raitsimring, A. Astashkin, O. Poluektov and P. Caravan, *Appl. Magn. Reson.*, 2005, **28**, 281.
26 P. Lueders, G. Jeschke and M. Yulikov, *J. Phys. Chem. Lett.*, 2011, **2**, 604.
27 A. Potapov, Y. Song, T. Meade, D. Goldfarb, A. Astashkin and A. Raitsimring, *J. Magn. Reson.*, 2010, **205**, 38.
28 M. Yulikov, P. Lueders, M. Warsi, V. Chechik and G. Jeschke, *Phys. Chem. Chem. Phys.*, 2012, **14**, 10732.
29 G. Jeschke, V. Chechik, P. Ionita, A. Godt, H. Zimmermann, J. Banham, C. Timmel, D. Hilger and H. Jung, *Appl. Magn. Reson.*, 2006, **30**, 473.
30 S. Stoll and A. Schweiger, *J. Magn. Reson.*, 2006, **178**, 42.
31 W. Spahni and G. Calzaferri, *Helv. Chim. Acta*, 1984, **67**, 450.
32 C. Mantel, C. Baffert, I. Romero, A. Deronzier, J. Pecaut, M.-N. Collomb and C. Duboc, *Inorg. Chem.*, 2004, **43**, 6455.
33 W. Austin, N. Bilow, W. Kelleghan and K. S. Lau, *J. Org. Chem.*, 1981, **46**, 2280.
34 A. Winter, A. M. van den Berg, R. Hoogenboom, G. Kickelbick and U. Schubert, *Synthesis*, 2006, 2873.
35 B. Bode, J. Plackmeyer, T. Prisner and O. Schiemann, *J. Phys. Chem. A*, 2008, **112**, 5064.
36 M. Rohrer, O. Brügman, B. Kinzer and T. Prisner, *Appl. Magn. Reson.*, 2001, **21**, 257.
37 V. Denysenkov, T. Prisner, J. Stubbe and M. Bennati, *Appl. Magn. Reson.*, 2005, **29**, 375.
38 M. Pannier, S. Veit, A. Godt, G. Jeschke and H. Spiess, *J. Magn. Reson.*, 2000, **142**, 331.

Electronic Supplementary Material (ESI) for Physical Chemistry Chemical Physics.

Pulsed Electron-Electron Double Resonance Spectroscopy between a High-Spin Mn^{2+} Ion and a Nitroxide Spin Label

Supporting information

D. Akhmetzyanov,[a] J. Plackmeyer,[a] B. Endeward,[a] V. Denysenkov[a] and T. F. Prisner[a]

[a] *Goethe-University Frankfurt am Main, Institute of Physical and Theoretical Chemistry and Center for Biomolecular Magnetic Resonance, Max von Laue Str. 7, 60438 Frankfurt am Main, Germany.*
E-mail: prisner@chemie.uni-frankfurt.de

1. Chemical Structure of Compound 4 and 6

The synthesis of the compounds is described in the main text of the manuscript. The schematic representations of compounds **4** and **6** are given in Fig. S1.

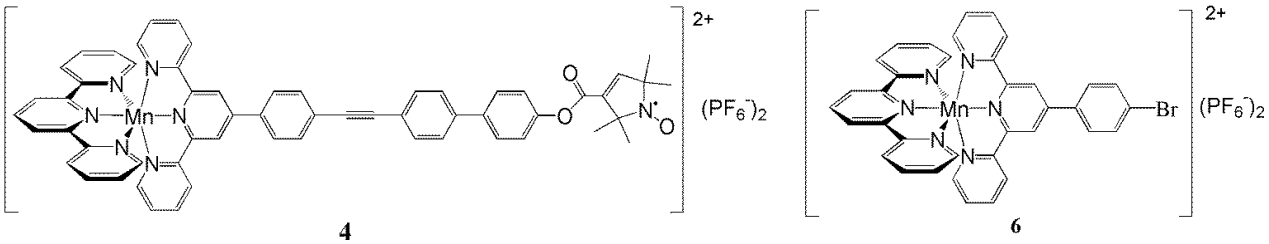

4 **6**

Fig. S1. Heteroleptic Mn^{2+}-terpyridine complex (compound **4**) and a Reference Mn^{2+}-terpyridine complex (exact name is given in the main text) (compound **6**)

2. EPR spectra and Hahn-echo phase memory time measurements of compounds 4 and 6

Field-swept echo-detected EPR spectra on compounds **4** and **6** at Q-band and a temperature of 5 K are presented in Fig. S2. The spectra were normalized to the maximum of the Mn^{2+} ion spin system spectrum. The nitroxide line in the spectrum of compound **4** was artificially cut. The broad and featureless line, corresponding to the Mn^{2+} ion spin system practically does not change between compound **4** and **6**, however, to detect the change between ZFS parameters of these complexes is not possible in this experiment, because the Q-band frequencies are not high enough.

In Fig. S2 the phase memory time measurements obtained from the Hahn-echo decay is presented. The temperature used for Q-band measurements is 5 K. The G-band measurements on compound **4** were obtained at 10 K. The estimated phase memory times for both frequencies and both compounds are roughly 1 μs. Pronounced hyperfine coupling induced modulation of the echo evolution function (ESEEM modulation) could be observed at Q-band frequencies (probably due to the coupling to the close-by nitrogen nuclei of the terpyridine moieties), whereas at G-band frequencies this modulation is absent.

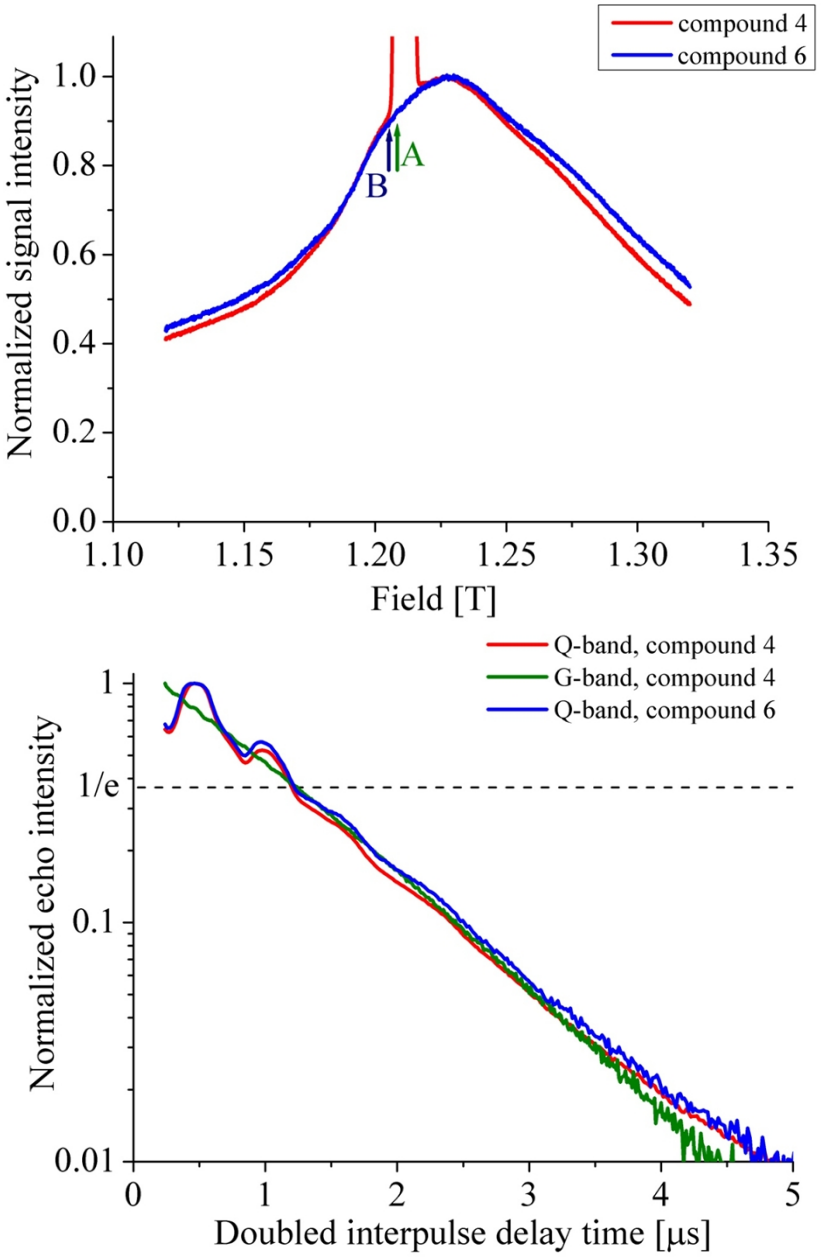

Fig. S2. Up - Field swept echo detected EPR spectra of compounds **4** and **6** at Q-band frequencies. The microwave frequency was 33.769 GHz. The pulse settings were optimized for Mn^{2+} ion spin system at the position B. The length of the pulses was set to 32 ns, the interpulse delay time was 120 ns; repetition time was 0.8 ms. The label A and B indicate the pump and probe positions, respectively, used for the experiment when pumping and detecting on the Mn^{2+} ion spin system of compound **6** (Fig. S6), control for testing nuclear modulation effects.
Down - Hahn-echo decay as a function of the double interpulse delay time. Compound **4**: the position in the spectrum was the position B; The pulse lengths were set to 32 ns, the initial interpulse delay time was 120 ns; repetition time was 0.8 ms. Compound **6**: the position on the spectrum was chosen roughly the same as for compound **4**, and all other parameters were identical. For the G-band experiment: the position in the spectrum was the position marked by up arrow at position 2 (Fig. 2 of the article - right upper spectrum); the temperature was 10 K; the pulses were 22.5 ns and 32.5 ns, the initial interpulse delay time was 300 ns; repetition time was 3 ms.

3. PELDOR experiments of compound 4 at Q-band frequencies

The 4-pulse PELDOR sequence was used. In Table S1 the experimental settings are given for pumping on the nitroxide (position A) and Mn^{2+} ion (position B), respectively.

Table S1. Experimental settings for the PELDOR experiments at Q-band

	Pump A detect B				Pump B detect A			
Pulses	$(\pi/2)_x$	$(\pi)_y$	$(\pi)_y$	π-pump	$(\pi/2)_x$	$(\pi)_y$	$(\pi)_y$	π- pump
Position of the pulses, ns	0	142	1784	190*	0	142	1784	190*
Length of the pulses, ns	32	32	32	20	32	32	32	20
Repetition time, μs	408				8160			
Shots per point	50				20			
Number of scans	1678				937			
Detection pulses frequency, GHz	33.85924				33.67894			
Pump pulse frequency, GHz	33.76910				33.76910			
Duration of the experiment	~ 4 hours				~ 16 hours			

*For the π-pump pulse the initial position of the pulse is given.

The power of the pulses was adjusted for the detection pulses by maximizing the echo intensity and for the pump pulse by obtaining the maximum inversion efficiency. A two-step phase cycling has been used: $(\pi/2)_x\ (\pi)_y\ (\pi)_y - (\pi/2)_{-x}\ (\pi)_y\ (\pi)_y$.

Raw experimental PELDOR traces including the intermolecular background functions as well as the Pake patterns derived by Fourier transformation of the background divided time traces are depicted in Fig. S3.

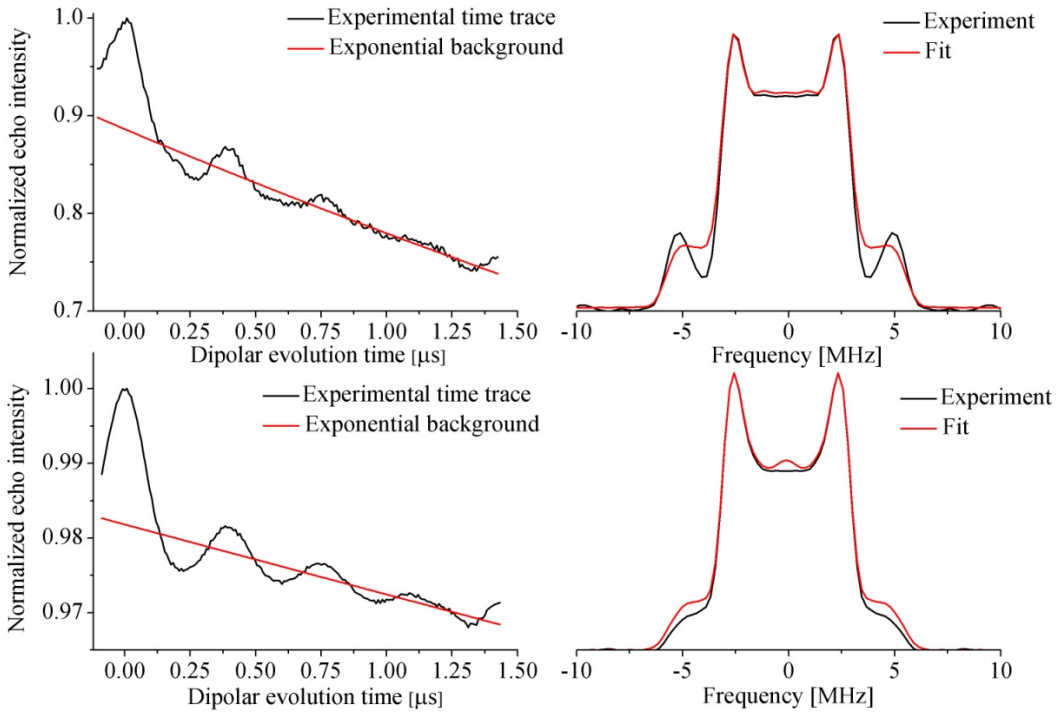

Fig. S3. Experimental PELDOR time traces including intermolecular background (red) and experimental Pake pattern obtained by Fourier transformation of the background divided time traces (black) and by Tikhonov regularization (red). Upper figures - pump position A, detect position B. Lower figures - pump position B, detect position A. The fits were obtained by DeerAnalysis 2013.

4. Control experiments with pump and detect frequency on the Mn^{2+} ion spin system

To check for artifacts by hyperfine coupling induced modulations or connected to the high-spin multiplicity of the Mn^{2+} ion two types of control experiments were performed:

1) Pump and detection was performed only on the Mn^{2+} ion spin system (positions C and D in Fig. S4, respectively) on compound **4**;

2) Pump and detection was performed only on the Mn^{2+} ion spin system approximately at the positions A and B (Fig. S2) on compound **6**.

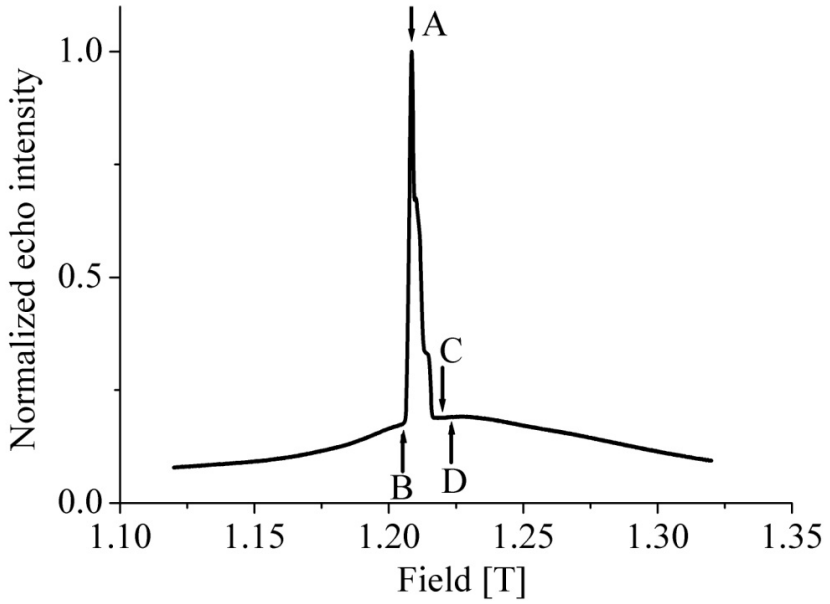

Fig. S4. Field swept echo detected EPR spectrum of compound 4. The spectral positions for probe and pump frequencies for the control experiments are shown.

Experiment 1

The experimental time trace upon pumping on position C and detection on the position D is depicted in Fig. S5. The parameters of the experiment are presented in Table S2. The power of the pulses was optimized with the strategy described in section 3.

Table S2. Experimental settings for the PELDOR-type experiment

	Pump C detect D			
Pulses	$(\pi/2)_x$	$(\pi)_y$	$(\pi)_y$	π- pump
Position of the pulses, ns	0	142	1784	190
Length of the pulses, ns	32	32	32	20
Repetition time, μs	816			
Shots per point	50			
Number of scans	1245			
Detection pulses frequency, GHz	33.67891			
Pump pulse frequency, GHz	33.76910			
Duration of the experiment	~ 5 hours			

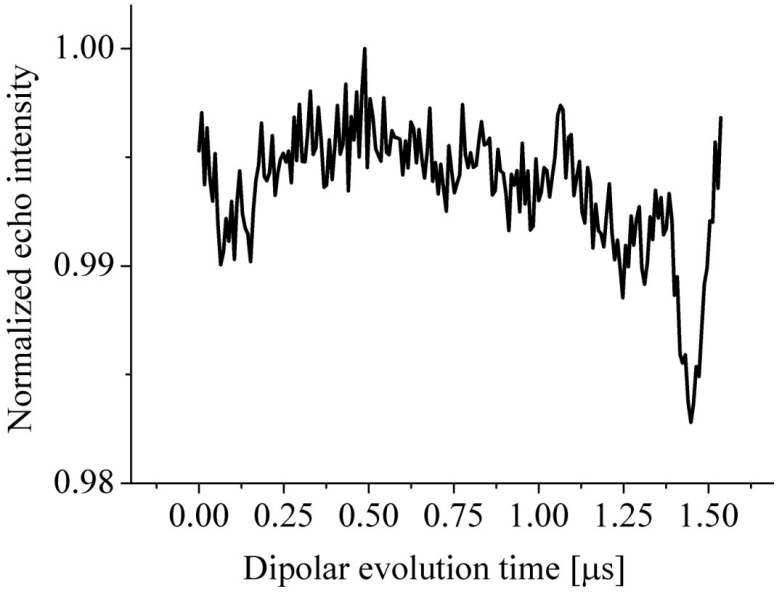

Fig. S5. Pumping and detecting on the Mn^{2+} ion spin system of compound **4** at Q-band frequencies and a temperature of 5K. The pump-detect frequency offset was set to 90MHz (positions C and D in Fig. S4).

Since none of the nitroxide spins are excited by the pump pulse at position C no dipolar oscillations are observed. The remaining weak oscillations could be caused by nuclear modulation effects.

Experiment 2

For this experiment pumping and detection was performed at positions A and B (Fig. S2) of compound **6**, containing no nitroxide. Pumping was performed on the Mn^{2+} ion spin system, however, the power of the pump pulse was the same as in the experiment with compound **4**, where pumping was performed on the nitroxide spin system. The power of the detection pulses was optimized for maximum echo intensity. All parameters of this experiment are given in Table S3.

Table S3. Experimental settings for the PELDOR-type experiment

	Pump A detect B			
Pulses	$(\pi/2)_x$	$(\pi)_y$	$(\pi)_y$	π- pump
Position of the pulses, ns	0	142	1784	190
Length of the pulses, ns	32	32	32	20
Repetition time, μs	816			
Shots per point	50			
Number of scans	2724			
Detection pulses frequency, GHz	33.85919			
Pump pulse frequency, GHz	33.76910			
Duration of the experiment	~ 12 hours			

The time trace for this experiment is shown in Fig. S6.

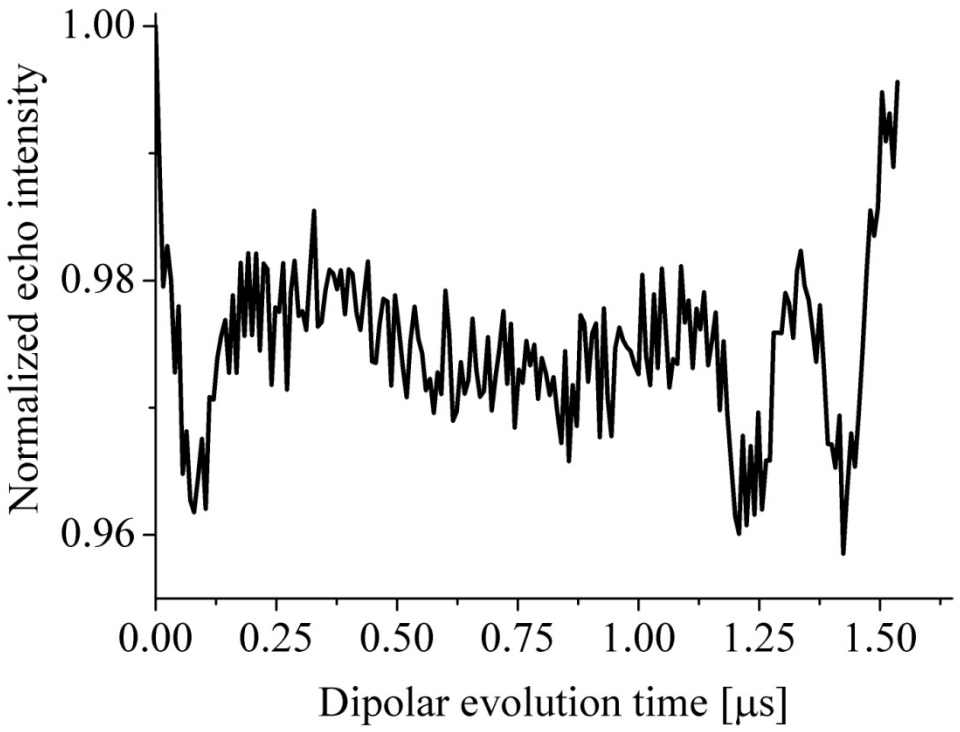

Fig. S6. Pumping and detecting on the Mn^{2+} ion spin system of compound **6** at Q-band frequencies and a temperature of 5 K. The pump-detect frequency offset was set to 90MHz.

More pronounced oscillations can be seen in the time trace under these experimental conditions. As it was discussed above, nuclear modulation effect cannot be ruled out from the consideration, assuming complexity of the high-spin Mn^{2+} ion spin system. These oscillations may be present in the PELDOR time trace when probing on Mn^{2+} spin system (Fig. S3 – upper trace). When probing on the nitroxide spin system this was not observed.

5. ESI mass spectrum of the heteroleptic Mn^{2+}-terpyridine complex (compound 4)

The ESI mass spectrum of compound **4** (Fig. S7) was obtained on a VG Platform II spectrometer, using an ionizing voltage of +3 kV. The solvent was a mixture of water:methanol 1:1, (v:v). Despite the fact, that solvent used for the EPR experiments was 2-methyltetrahydrofuran, the results obtained by mass spectroscopy give some qualitative information about the sample.

The peak with the m/z of 477.1 (double charged), corresponds to the expected mass of compound **4** without counter ions (m/z of 954.58±2.32 calculated 955.30). The peak with m/z of 1100.7 corresponds to the mass of compound **4** with only one counter ion (calculated m/z: 1100.27), so the complex appears as single charged.

The peak with the m/z of 666.0 most probably corresponds to a single charged Mn^{2+} bis-terpyridine complex $[(terpy)_2MnPF_6]^+$ (calculated m/z of 666.09). However, it is worthwhile to mention that this is also close to the calculated m/z of 667.27 corresponding to ligand **3** (see article Fig. 1). The main peak with the m/z of 539 might be attributed to a single charged Mn^{2+} bis-terpyridine complex (calculated mass 521.13) solvated with one water molecule from the solvent: $[(terpy)_2Mn(H_2O)]^+$. The double charged complex can attract an electron and become single charged, so that it also appears with actual m/1 in the spectrum.

In summary, from the mass spectrum the presence of another Mn^{2+} bis-terpyridine complex in solution besides of compound **4** cannot be excluded.

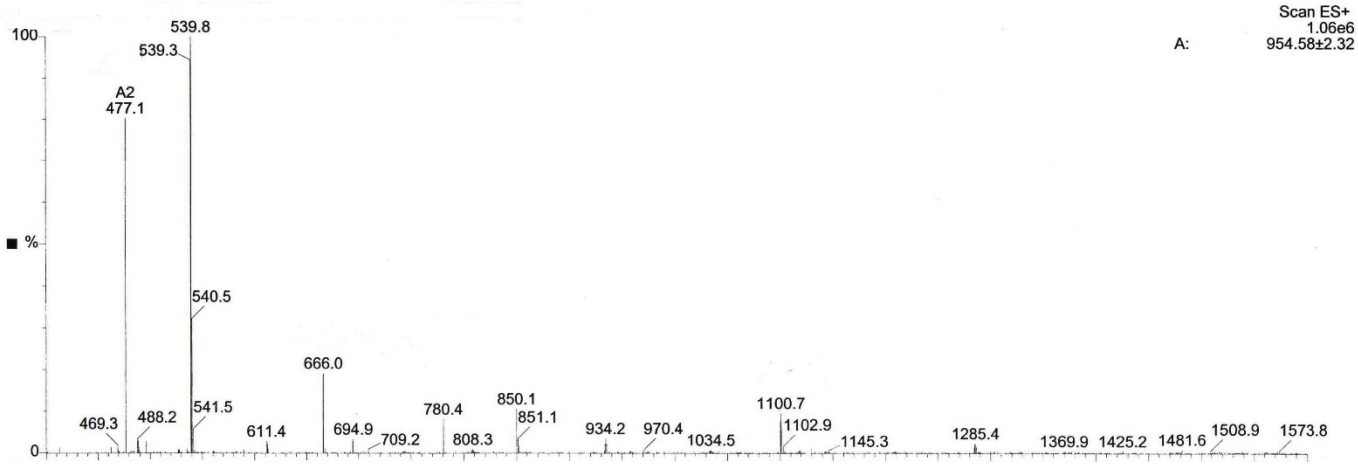

Fig S7. ESI mass spectrum of compound **4**.

6. Simulations of the G-band PELDOR time traces

The simulated dipolar evolution functions upon pumping on positions 1 and 2 (article Fig. 2 - right) are depicted in Fig S8.

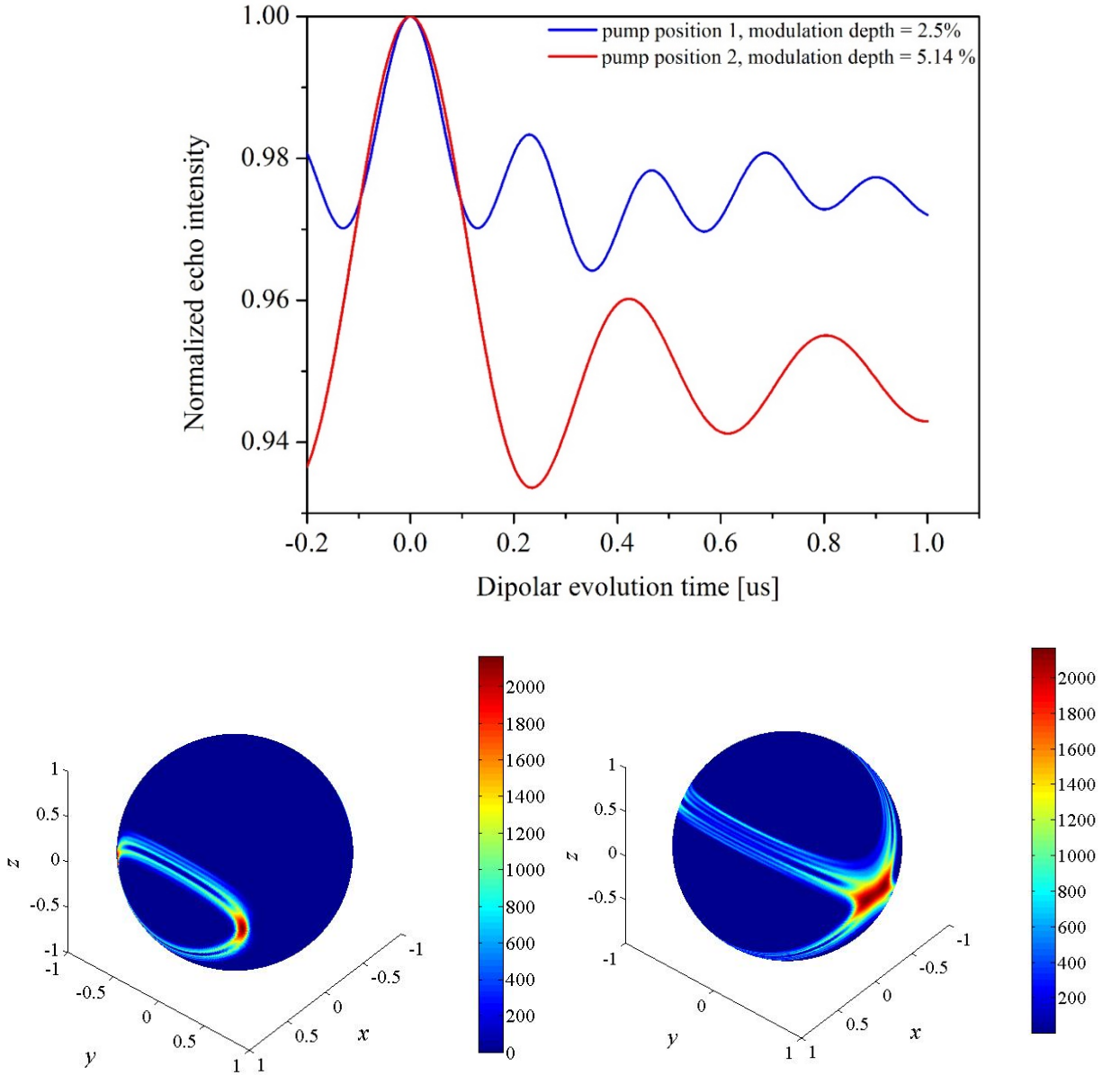

Fig. S8. Upper panel: simulated dipolar evolution functions upon pumping on the nitroxide spin system at positions 1 and 2 (Fig 2-left) with a fixed distance of 2.7 nm between the Mn^{2+} ion and the unpaired electron of the nitroxide; Lower panel - excited orientations of the nitroxide spin system upon pumping at position 1 (Left) and upon pumping at position 2 (Right). The *x*-, *y*-, *z*- axis represent the main axis of the g-tensor of the nitroxide spin system and the given colour bar represent the relative weight of the orientations excited by a pump pulse with pump pulse with 10 MHz bandwidth assuming an inhomogeneous linewidth of the nitroxide spin system of 10 MHz.

The excited orientations of the nitroxide spin system was obtained by the EasySpin function “orisel”.